Atomic-Scale Insights into Light Emitting Diode

Mansoor Ali Khan

A thesis submitted in fulfilment of

the requirements for the Degree of

Doctor of Philosophy

The School of Physics

The University of Sydney

2018

A Thesis for the Degree of Doctor of Philosophy

Atomic-Scale Insights into Light Emitting Diode

Supervisor: A/Prof. Rongkun Zheng

Co-Supervisors: Prof. Simon Ringer and Prof. Catherine Stampfl

Submitted by: Mansoor Ali Khan

Date of submission: 30/01/2018

Date of approval: ...../. ..../2018

The School of Physics

The University of Sydney

Certificate of Originality

This is to certify that the content of this dissertation, to the best of my knowledge, is my own work. The dissertation contains no materials previously published or written by another person, nor material which to a substantial extent has been accepted for the award of any other degree or diploma at the University of Sydney or any other educational institution, except where the due acknowledgement is made in this thesis. Any contribution made to the research by others, with whom I have worked at The University of Sydney or elsewhere, is explicitly acknowledged in the thesis.

I also declare that the intellectual content of this dissertation is the product of my own work, except to the extent that assistance from others in the project's design and conception or in style, presentation, and linguistic expression is acknowledged.

Signed by Mansoor Ali Khan

25 June 2018

Acknowledgements

2 years of work in microelectronics field persuaded me to further research on the remarkable and innovative technology of Gallium Nitride. I got that opportunity in the form of postgraduate research through Australian Government IPRS/APA scholarship, where A/Prof. Rongkun Zheng selected me as PhD candidate in his group. Firstly, I wish to express my sincere gratitude to my primary supervisor A/Prof. Rongkun Zheng, who provided me a big picture of microelectronics and visionary research path to work on semiconductor devices, and how to contribute in its grooming era. At the initial stage of PhD, good advice is a key to target valuable project, at that critical point, I found Zheng has excellent qualities of both advisor and supervisor. Zheng offered invaluable assistance, support and supreme guidance throughout my research work. I am thankful to him for being engaging in useful meetings and open discussions. Apart from professional life, Zheng being technically sound also supported me morally as well. I remember his words that "*difficulties do not break you, in fact, they make you strong*". Throughout my PhD research, Zheng has been my motivation and I have great respect for him in all aspects.

I am highly indebted to my co-supervisors Prof. Simon Ringer and Prof. Catherine Stampfl for their auxiliary supervision, advice, encouragement, and admiration shown for my work. I am also very grateful to the facilities, scientific and technical assistance provided by Australian Centre for Microscopy and Microanalysis at the University of Sydney, especially Dr. Patrick Trimby, Mr. Steve Moody, Dr. Hongwei Liu, Dr. Limei Yang, Dr. Matthew Foley, Mr. Adam Sikorski, Ms. Lisa Abraham and Dr. Thomson Chow. I would also like to thank my wonderful group members Dr. Jiangtao Qu, Mr. Hansheng Chen, Pengju Bian and Ms. Fan Yun for their help and kind coordination.

Finally, yet importantly, I would like to express my heartfelt thanks to my beloved late mother and father whose prayers always work as a catalyst and without their support this journey would not have been possible. Other than my parents, I would likely to express my sincere gratitude to everyone who helps me during my Doctorate's research work.

Publications

(1) **M. A. Khan**, S. P. Ringer, and R. K. Zheng, "Atom Probe Tomography on Semiconductor Devices," Adv. Mater. Interfaces, vol. 3, 1500713, Apr. 2016. *DOI: 10.1002/admi.201500713.*

(2) **M. A. Khan**, P. W. Trimby, H. W. Liu, and R. K. Zheng, "On the Metallic Bonding of GaN-based Vertical Light-emitting Diode," Mater. Sci. Semicond. Process., vol. 63, pp. 237–247, Jun. 2017. *DOI: 10.1016/j.mssp.2017.02.025.*

(3) **M. A. Khan**, H. Chen, J. Qu, P.W. Trimby, S. Moody, Y. Yao, S. P. Ringer, and R. K. Zheng, "Insights into the Silver Reflection Layer of a Vertical LED for Light Emission Optimization," ACS Appl. Mater. Interfaces, vol. 9, no. 28, pp. 24259–24272, Jul. 2017. *DOI: 10.1021/acsami.7b04854.*

(4) **M. A. Khan**, H. Chen, J. Qu, F. Yun, H. W. Liu, J. Cairney, S. P. Ringer, and R. K. Zheng, "Insights into p-n junction of GaN-based Vertical LED using Aberration-Corrected Electron Microscopy," Submitted to APS Phys. Rev. Materials. *Manuscript ID: MT10018.*

(5) **M. A. Khan**, P. Bian, J. Qu, H. Chen, H. W. Liu, Y. Yao, S. P. Ringer, and R. K. Zheng, "Non-destructive Analysis on Nano-Textured Surface of the Vertical LED for Light Enhancement," Submitted to Ultramicroscopy. *ID: ULTRAM_2018_61.*

(6) **M. A. Khan** and R. K. Zheng, "Nanostructural Analysis of CMOS-MEMS-Based Digital Microphone for Performance Optimization," IEEE Trans. Nanotechnol., vol. 15, no. 6, pp. 849–855, Nov. 2016. *DOI: 10.1109/TNANO.2016.2554602.*

(7) J. Qu, D. Su, T. Wang, C. Cui, et al., **M. A. Khan**.; S. P. Ringer; R. K. Zheng. "3D Atomic-Scale Insights into Anisotropic Core-Shell-Structured InGaAs Nanowires Grown by Metal-Organic Chemical Vapor Deposition, "Adv. Mater. 2017, 1701888. *DOI: 10.1002/adma.201701888.*

Conference Presentations

(1) **M. A. Khan**, H. Chen, J. Qu, F. Yun, H. W. Liu, J. Cairney, S. P. Ringer, and R. K. Zheng, "Insight into Multiple Quantum Wells of GaN-based Vertical LED using Aberration-Corrected Electron Microscopy," Oral presentation at the International conference of 2017 Materials Research Society (MRS Fall) Meeting and Exhibit at Boston, Massachusetts, United States of America. Paper #: EM04.03.10, 28 November 2017.

(2) **M. A. Khan**, F. Yun, R. K. Zheng, "Nanocharacterization of Organic Polymer Solar cells," Oral and poster presentations at the International Summit of the MRS chapters on 'Nanotechnology and Sustainability' of 2017 Materials Research Society (MRS Fall) Meeting and Exhibit at Boston, Massachusetts, United States of America., Paper #: ISUCNS-16, 30 November 2017.

(3) **M. A. Khan**, P. Bian, and R. K. Zheng, "AFM and Raman Characterization on Nano-Textured Surface of Vertical LED for Light Enhancement," Oral presentation at the International Conference on Nanoscience and Nanotechnology (ICONN 2018), University of Wollongong, NSW, Australia, Paper #: 580, 2 Feb 2018.

(4) **M. A. Khan**, H. Chen, J. Qu, P.W. Trimby, S. Moody, Y. Yao, S. P. Ringer, and R. K. Zheng, "Insight into GaN-based blue VLED using SEM-TKD and TEM," poster presentation at the 24th Australian Conference on Microscopy and Microanalysis (ACMM) 2016, Melbourne, Australia, Paper #: 230, 3 Feb 2016.

(5) **M. A. Khan** and R. K. Zheng, "Insight into CMOS-MEMS device using Energy Dispersive X-Ray Spectroscopy," Oral presentation at the 11th Australasian Conference on Vibrational Spectroscopy (ACOVS11) and the 5th Asian Spectroscopy Conference (ASC5), Sydney, Australia, 1 October 2015.

Certifications

(1) **M. A. Khan**, "Material Behavior," Course Certification from Georgia Institute of Technology, Coursera, 2 Feb 2017. coursera.org/verify/QBEMA5NTUHNJ.

(2) **M. A. Khan**, "Organic Solar Cells – Theory and Practice," Course Certification from Technical University of Denmark (DTU), Coursera, 13 December 2017. coursera.org/verify/V3PQULLTPLVS.

Dissertation Authorship Attribution Statement

This dissertation consists of seven chapters. The first chapter presents a literature review of the light emitting diodes (LED). Chapter two presents vertical LED (VLED) fabrication and its sample preparation methodology for microscopy characterization, all the provided figures, and protocols to prepare the VLED specimen are from my own experimental work.

Chapters from three to six constitute nano/atomic-scale characterization of the VLED, and all provided figures/results are based on my own experimental work. In chapters, three to six, each VLED stack layers, i.e., wafer (metallic) bonding, silver (Ag) reflection, active (MQWs), and top textured surface layers are systematically investigated. Chapter seven of this dissertation provides summary, conclusion, and prospective work on organic solar cells.

Chapter 1 of this thesis is partially published as:

M. A. Khan, S. P. Ringer, and R. K. Zheng, "Atom Probe Tomography on Semiconductor Devices," Adv. Mater. Interfaces, vol. 3, 1500713, Apr. 2016. *DOI: 10.1002/admi.201500713.*

This work highlights the basics of atomic-scale characterization on semiconductor devices, especially the focus was on the GaN-based optoelectronic devices, for instance, light-emitting diode (LEDs). On my supervisor's guidance, the literature review was compiled independently by me and has motivated me to work on GaN-based VLEDs.

Chapter 2 of this thesis is partially published in:

M. A. Khan, P. W. Trimby, H. W. Liu, and R. K. Zheng, "On the Metallic Bonding of GaN-based Vertical Light-emitting Diode," Mater. Sci. Semicond. Process., vol. 63, pp. 237–247, Jun. 2017. *DOI: 10.1016/j.mssp.2017.02.025.*

M. A. Khan, H. Chen, J. Qu, P.W. Trimby, S. Moody, Y. Yao, S. P. Ringer, and R. K. Zheng, "Insights into the Silver Reflection Layer of a Vertical LED for Light Emission Optimization," ACS Appl. Mater. Interfaces, vol. 9, no. 28, pp. 24259–24272, Jul. 2017. *DOI: 10.1021/acsami.7b04854*.

In this work, VLED fabrication and sample preparation (bulk/thin) methodologies for microscopy characterization are presented. All the provided figures and protocols to prepare the VLED specimen are based on my experimental work.

Chapter 3 of this thesis is published as:

M. A. Khan, P. W. Trimby, H. W. Liu, and R. K. Zheng, "On the Metallic Bonding of GaN-based Vertical Light-emitting Diode," Mater. Sci. Semicond. Process., vol. 63, pp. 237–247, Jun. 2017. *DOI: 10.1016/j.mssp.2017.02.025*.

In this manuscript, metallic bonding in GaN-based vertical LED was systematically characterized by using a combined methodology of SEM-based TKD/EDX and HR-STEM. This publication has been independently composed by me and all results in that manuscript have been obtained from my own experimental work in support with supervisor discussion and coauthors assistance.

Chapter 4 of this thesis is published as:

M. A. Khan, H. Chen, J. Qu, P.W. Trimby, S. Moody, Y. Yao, S. P. Ringer, and R. K. Zheng, "Insights into the Silver Reflection Layer of a Vertical LED for Light Emission Optimization," ACS Appl. Mater. Interfaces, vol. 9, no. 28, pp. 24259–24272, Jul. 2017. *DOI: 10.1021/acsami.7b04854*.

This publication provides in detail analysis on the silver reflection layer of the GaN-based vertical LED. The experimental setup and applied methodologies of this work were performed independently by me. Data acquisition, data analysis and key findings from different microscopy tools were figured out by me, my supervisors and coauthors discussion, especially Patrick Trimby expertise in SEM-TKD data analysis was significant.

Chapter 5 of this thesis has been submitted to a journal and presented orally as:

M. A. Khan, H. Chen, J. Qu, F. Yun, H. W. Liu, J. Cairney, S. P. Ringer, and R. K. Zheng, "Insight into Multiple Quantum Wells of GaN-based Vertical LED using Aberration-Corrected Electron Microscopy," Submitted to APS Phys. Rev. Materials. *Manuscript ID: MT10018.*

In this submitted work, key active layer (MQWs) of the VLED was investigated by the powerful technique of aberration-corrected scanning transmission electron microscope (AC-STEM). The sample preparation was independently done by me, and AC-STEM experiments were performed in collaboration with FEI Company. Dr. Hongwei Liu expertise provided technical assistance in data acquisition. Data analysis and manuscript drafting were independently done by me in coordination with my supervisor and coauthors Jiangtao Qu and Hansheng Chen.

Chapter 6 of this thesis is submitted to the journal and presented orally as:

M. A. Khan, P. Bian, J. Qu, H. Chen, H. W. Liu, Y. Yao, S. P. Ringer, and R. K. Zheng, "Non-destructive Analysis on Nano-Textured Surface of the Vertical LED for Light Enhancement," Submitted to Ultramicroscopy.

M. A. Khan, P. Bian, and R. K. Zheng, "AFM and Raman Characterization on Nano-Textured Surface of Vertical LED for Light Enhancement," Oral presentation at the International Conference on Nanoscience and Nanotechnology (ICONN 2018), University of Wollongong, NSW, Australia, Paper #: 580, 2 Feb 2018.

In this work, the applicability of non-destructive techniques to perform surface analysis on the vertical LED was independently done by me in coordination with coauthor Pengju Bian. Data analysis and manuscript drafting were done by myself. Yin Yao provided technical assistance in AFM data acquisition.

Chapter 7 of this thesis is presented orally as:

M. A. Khan, F. Yun, R. K. Zheng, "Nanocharacterization of Organic Polymer Solar cells". Oral and poster presentations at the International Summit of the MRS chapters on 'Nanotechnology and Sustainability' of 2017 MRS Fall Meeting and Exhibit at Boston, Massachusetts, United States of America. Paper #: ISUCNS-16, 30 November 2017.

In this chapter prospective project of organic solar cells, experimental methodologies, sample preparation protocols were done by me independently. APT data acquisition and analysis were performed in coordination with coauthor Fan Yun.

In support of above statements, permission to include the published material has been granted by the corresponding author and coauthors.

Signed by Mansoor Ali Khan
25 June 2018

List of Figures

Table of Contents

List of Abbreviations

GaN	gallium nitride
LED	light-emitting diode
VLED	vertical light-emitting diode
LEE	light-extraction efficiency
MOCVD	metalorganic chemical vapor deposition
ROI	region of interest
WZ	wurtzite
MQWs	multiple quantum wells
3D	three dimensional
TKD	transmission Kikuchi diffraction
AFM	atomic force microscopy
QW	quantum well
IQE	internal quantum efficiency
EQE	external quantum efficiency
EBL	electron blocking layer
EDX	energy dispersive x-ray spectroscopy
AC-STEM	aberration-corrected scanning transmission electron microscope
HAADF	high-angle annular dark field
ABF	annular bright field

XRD	X-ray diffraction
PL	photoluminescence
NDT	non-destructive techniques
APT	atom probe tomography
SEM	scanning electron microscopy
SIMS	secondary ion mass spectrometry
STEM	scanning transmission electron microscopy
HRTEM	high-resolution transmission electron microscopy
FEEM	field emission electron microscope
FIB	focused ion beam
GB	grain boundary
WB	wafer bonding
EELS	electron energy loss spectrometry
FOV	field-of-view
AOI	area of interest
EBSD	electron backscattering diffraction
SPM	scanning probe microscopy

Abstract

In solid-state lightning, light-emitting diode (LED) technology is considered extensively as industry-focused optoelectronic devices for illumination in high-value applications, such as smartphones, traffic lights, automotive headlights, full-color displays, home lighting, backlighting source in liquid-crystal displays (LCDs), and other medical and commercial devices.

In the LED technology, GaN-based thin-film or vertical light-emitting devices have attracted tremendous attention because their luminous efficacy (~150-250 lm/W) has surpassed the traditional lightning technologies (~10-110 lm/W), even the 2014 Nobel Prize in Physics was awarded for the invention of efficient blue LEDs, which enabled eco-friendly and energy-saving white lighting sources. Despite today's GaN-based blue VLEDs can produce internal quantum efficiency (IQE) of 90% and external quantum efficiency (EQE) of 70-80%, still there exist a major challenge of efficiency droop (the substantial decrease of quantum efficiency with increasing drive current). Nonetheless, state-of-the-art material characterization and failure analysis tools are inevitable to address that issue.

In this context, although LEDs have been characterized by different microscopy techniques, they are still limited to either its semiconductor (GaN) layer or active (quantum wells) region, which mainly contributes towards the IQE. This is also one of the reason that today's LEDs IQE exceeded above 80% but EQE of 70-80% remains. Therefore, to scrutinize the efficiency droop or low EQE issue of the LED, this research work focused on developing a novel strategy to investigate semiconductor-metal interfaces, and to explore metallic layers of the LED structure, which play critical role in enhancing the EQE and directly or indirectly impact its light-extraction efficiency (LEE) and IQE factors, i.e., EQE = IQE x LEE.

Based on that strategy, wafer (metallic) bonding, reflection (Ag mirror), semiconductor-metal (GaN-Ag) interface, active (multiple quantum wells), top textured n-GaN layers have

been systematically investigated under the framework of powerful advanced microscopy techniques of SEM-based transmission Kikuchi diffraction (TKD)/energy dispersive X-ray spectroscopy (EDX)/electron backscatter diffraction (EBSD), high-resolution scanning transmission electron microscope (HR-STEM), aberration-corrected STEM (AC-STEM), atomic force microscopy (AFM), Raman spectroscopy, X-ray diffraction (XRD) and photoluminescence (PL). Further, based on these correlative microscopy results, optimization suggestions on LEE are given for performance enhancement in the LEDs.

The objective of this research is to perform atomic or nano-scale characterization on the vertical LED layers/interfaces to scrutinize their surface morphology, chemical composition, elemental diffusion, surface topography, crystallographic information, atomic structure with polarity, interfaces abruptness and carrier localization mechanism in quest of efficiency droop issue of the LED.

Overall the purpose of this work is to evaluate the quality control of each LED layer, and on the basis of that optimize the fabrication process of the LED. Also, it includes correlating microscopy results with the structure-property-process-performance paradigm of the LED, i.e., link the data analysis that is interpreted from advanced microscopy techniques with the efficiency droop and reliability issues of the LED.

The outcome of this research advances in optimization engineering of LED by competitive and failure analysis. Our results from microscopy techniques provide unparalleled insight into metallic bonding, reflection, quantum wells, and textured layers of the LED. By correlating the results from microscopy technologies, we are able to understand LED device physics, grain morphology, interfacial diffusion, chemical composition, surface topography, stress-state, and impurity levels on the atomic or nano-scale. The competitive and failure analysis in this research will not only impact various device optimization techniques but also incorporating standardization in a product design for better manufacturability.

Lastly, this dissertation also provides vital guidance and references for scientists and design engineers in the field of optimization of advanced smart optoelectronics devices.

Keywords: Gallium nitride, vertical LED, atomic-scale, microscopy techniques, light extraction efficiency.

Dissertation Outline

Considering stated above objectives, seven chapters have been compiled in this dissertation.

In the first chapter, the state-of-the-art GaN-based light emitting diode (LED) is reviewed to explore its device physics to develop an understanding of atomic-scale interfaces in it. Industrial LED as a semiconductor product has been scrutinized in light of surface morphologies, chemical compositions, dopant distributions, grain boundaries and interface characteristics.

In the second section, vertical LED (VLED) fabrication and protocols for sample preparation for microscopy characterization are presented. Also, the approach to use diverse microscopy platform is discussed that allows for the further optimization of LED device.

In the third part of this dissertation, metallic bonding in GaN-based VLED is systematically characterized by using the combined methodology of TKD and EDX in a SEM. SEM-based TKD with EDX identifies chemical composition, grain morphology, orientation, and phases at metallic bonding, while TEM provides nanoscale characteristics of metallic diffusion bonding, and its interface-related defects and nano-twinned boundaries. Our results from SEM-TKD and TEM techniques provide unparalleled insight into the metallic bonding and its future optimization.

In the fourth section, silver (Ag) as a highly reflective mirror layer of GaN-based blue VLED has been systematically investigated by correlating SEM-based EDX/TKD)/EBSD, AC-STEM, and AFM techniques. In the context of high-efficiency lighting, three critical aspects: 1) chemical diffusion, 2) grain morphology and 3) surface topography of Ag layer has been scrutinized at the nanoscale. We found that nanoscale inhomogeneous distribution

of indium (In) in InGaN/GaN multiple quantum wells (MQWs), interfacial diffusion (In/Ga out-diffusion into Ag layer, the diffusion of Ag into p-GaN and quantum wells), and the Ag agglomeration deteriorate the light reflectivity, which account for the decreased luminous efficiency in VLED. Meanwhile, surface morphology and topographical analyses revealed nano-morphology of Ag layer, where nanograined size with special nanotwinned boundaries and an extremely smooth surface are strongly desired for better reflectivity. Further, based on these microscopy results, suggestions on light extraction optimization are given to improve the performance of GaN-based blue VLED.

Fifth part of this dissertation presents an atomic-scale insight into MQWs of the blue VLED by using the powerful technique of AC-STEM. AC-STEM at atomic resolution of 0.7 Å with an EDX demonstrates interesting results across four InGaN MQWs and GaN quantum barriers (QBs) by providing compositional inhomogeneity of indium distribution, structural defects, and nanoscale interfacial chemical migration. STEM-based EDX results reveal that InGaN is a random alloy with indium fluctuations at multiple QWs and superlattice (SL) layers. Similarly, on the p-GaN side, Al-based electron blocking layer (EBL) shows non-uniform profile. Also, high-resolution STEM images determine that inhomogeneity of indium distribution results in QW width variations and random indium fluctuations on an atomic-scale due to compositional pulling effect. In addition, ultra-high resolution STEM images identify that InGaN QWs and GaN QBs interfaces are not atomically smooth but are somewhat diffused. Moreover, the Ga-Ga atomic columns separated by 75 pm are resolved by STEM high-angle annular dark field (HAADF) imaging whereas the annular bright field (ABF) technique is utilized for a light element (N) imaging with sub-angstrom resolution. Simultaneously recorded AC-STEM HAADF and ABF images scrutinize the GaN active region exhibit hcp-wurtzite crystal structure with validation of N-polarity. Furthermore, electron microscopy results are correlated with various aspects of degradation in LED performance. Lastly, based on AC-STEM nanostructural characterization and analytical results, further optimization prescriptions and remedies are given to mitigate critical issues of efficiency droop, quantum-confined Stark effect and structural defects in order to enhance the performance of LEDs.

In the sixth section, the nano-textured surface of the GaN-based VLED is characterized using a unified framework of non-destructive techniques (NDT) incorporating SEM, AFM, Raman spectroscopy, Photoluminescence (PL) and XRD to optimize the light output efficiency. The surface roughness of ~ 300 nm is revealed by AFM. Compression stress state of 0.667 GPa in the GaN surface is indicated by the E2(high) and A1(LO) phonon peak values at 569 cm−1 and 736 cm−1, respectively, in Raman spectrum and the wavelength at 442 nm rather 450 nm in PL spectrum. Surface analysis by NDT helps to advance the understanding of optimized angular redistribution of light subject to the high-roughness surface, and negative impacts of stress induced in the top GaN layer leads to degrading the optical efficiency of the VLED. Furthermore, the impact of texturing on underneath n-GaN and MQWs layers is investigated via SEM-based TKD and AC-STEM, and demonstrates a smooth surface morphology and good crystalline quality, indicating the etch-induced damage by texture engineering does not impair the active region of VLED. Accordingly, prospective optimizations are suggested in the context of surface engineering for light enhancement in VLEDs.

In the last section of this dissertation, a compact summary of keys results of this research work is presented with the conclusion. Also, a prospective future research project on organic solar cells (OSC) and OLEDs will be briefly explained, their importance and methodologies to characterize them at the nanoscale are demonstrated.

Chapter One

Literature Review

1.1 Background and Motivation

1.1.1 Introduction to Light emitting diodes (LEDs)

Light-emitting diode (LED) is an eco-friendly electroluminescence device which converts electricity into visible light for illumination, as illustrated in Figure 1.1. With the increasing traditional energy resource crisis and environmental pollution arising from electrical production, the appealing LEDs have become a competitive candidate for next-generation solid-state lighting devices because of their small size, high-energy efficiency, high-color rendering index, reliable life-time, and wide spectral line width from deep ultra violet to yellow [1]–[3]. Also, LED technology has many advantages over traditional light sources in terms of compact size, lifetime, variable intensity control, low voltage requirement, instant on/off, high energy saving capability, and so forth [3]–[6].
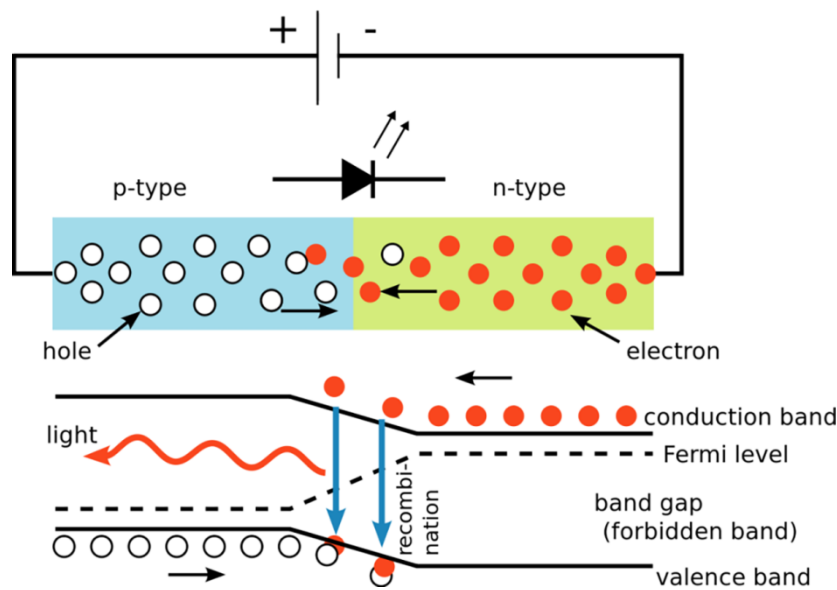
Figure 1.1 Working principle of the light emitting diode (LED).

Currently, LEDs are considered extensively as industry-focused optoelectronic devices for illumination in high-value applications, such as traffic lights, automotive headlights, full-color displays, home lighting, backlighting source in smartphones, liquid-crystal displays (LCDs), LED displays, and other medical and commercial devices, [7]–[10], as shown in Figure 1.2.

31

Figure 1.2 Industrial applications of the LED.

Also, the 2014 Nobel Prize in Physics was given to Shuji Nakamura's and Akasaki's groups for the invention of efficient blue LEDs, which has enabled bright and energy-saving white light sources [11]. This invention recognizes the significance of environment-friendly LEDs, and attained considerable attention in further optimization. Although nowadays the luminous efficacy (~150-250 lm/W) of most of the LEDs has surpassed the traditional incandescent, line and compact fluorescent technologies (~10-110 lm/W) [12], [13], as shown in Figure 1.3, still cost-effective design of high-power and high-efficiency LEDs is essential to penetrate in the general illumination market.
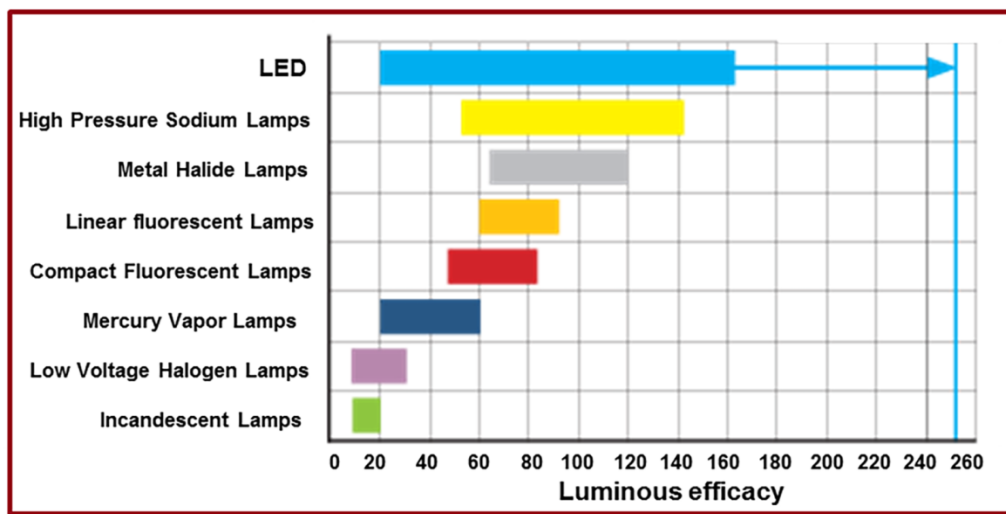
Figure 1.3 Comparison of LED efficacy with traditional light sources [14].

Currently, a modern white LED lightbulb converts more than 50% of the electricity remarkably superior to its incandescent counterparts with 4% conversion efficiency, and therefore are regarded as a green solution to counter the global energy crisis [15]–[17]. With 20-30% of the world's electricity used for lighting, it's been estimated that optimal use of LED lighting could reduce this to 4% [18], as depicted in Figure 1.4.
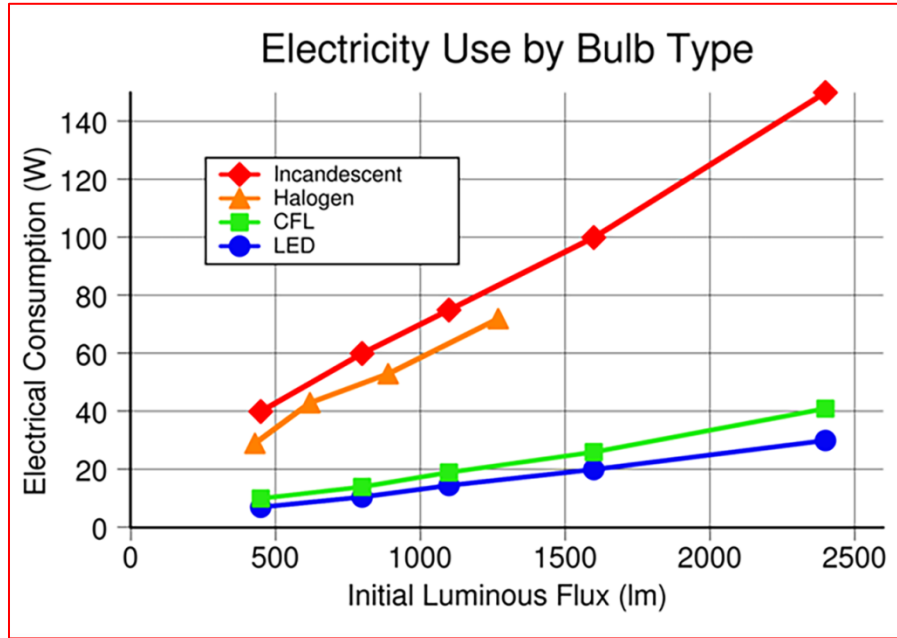
Figure 1.4 Comparison of LED electrical consumption with traditional light sources [18].

1.1.2 Why GaN-based LEDs?

In III-V compound semiconductors, gallium nitride (GaN) has manifested its superior material properties compared to conventional Si or GaAs [19]–[21], as summarized in Table 1.1. The potential for solid-state lighting based on LED technology to reduce energy usage is made possible through the development of GaN and its alloys. GaN is a fundamental material for a vast range of optoelectronic devices because it has demonstrated prominent light emission capabilities ranging from ultra-violent (undoped) to green and red (doped with indium or aluminum) [12], [22], as shown in Figure 1.5.

GaN as a wide bandgap material can be integrated with other compound semiconductors such as InGaN and InGaAlP to form a potential minimum or well structure with a discrete

33

Table 1.1 GaN comparison with other semiconductor materials *(Source: Mansoor Khan at 11th International Conference on Nano technologies, 2013, Seoul, South Korea).*

Characteristics	Si	GaAs	InP	SiC	GaN		
Bandgap (eV)	1.1	1.42	1.35	3.26	3.49	→ High Voltage	→
Critical Breakdown Field (MV/cm)	0.3	0.4	0.5	3	3.3		
Electron Mobility at 300 K (cm²/Vs)	1500	8500	5400	700	1000-2000	→ High Frequency	High Power High RF Functionality
Saturation Electron Velocity (x10⁷cm/s)	1	1.3	2.2	2	2.5		
Charge Density (x10¹³ /cm²)	0.3	0.3	0.35	0.4	1	→ High Power Handling	
Thermal Conductivity (W/cm-K)	1.5	0.5	0.7	4.5	>1.5		
Wide Band Gap and Polarization (No Dopants)	–	–	–	–	Yes	→ Low Noise, Low Loss, Higher RF current	
Relative Dielectric Constant (Εr)	11.8	12.8	12.5	10	9		
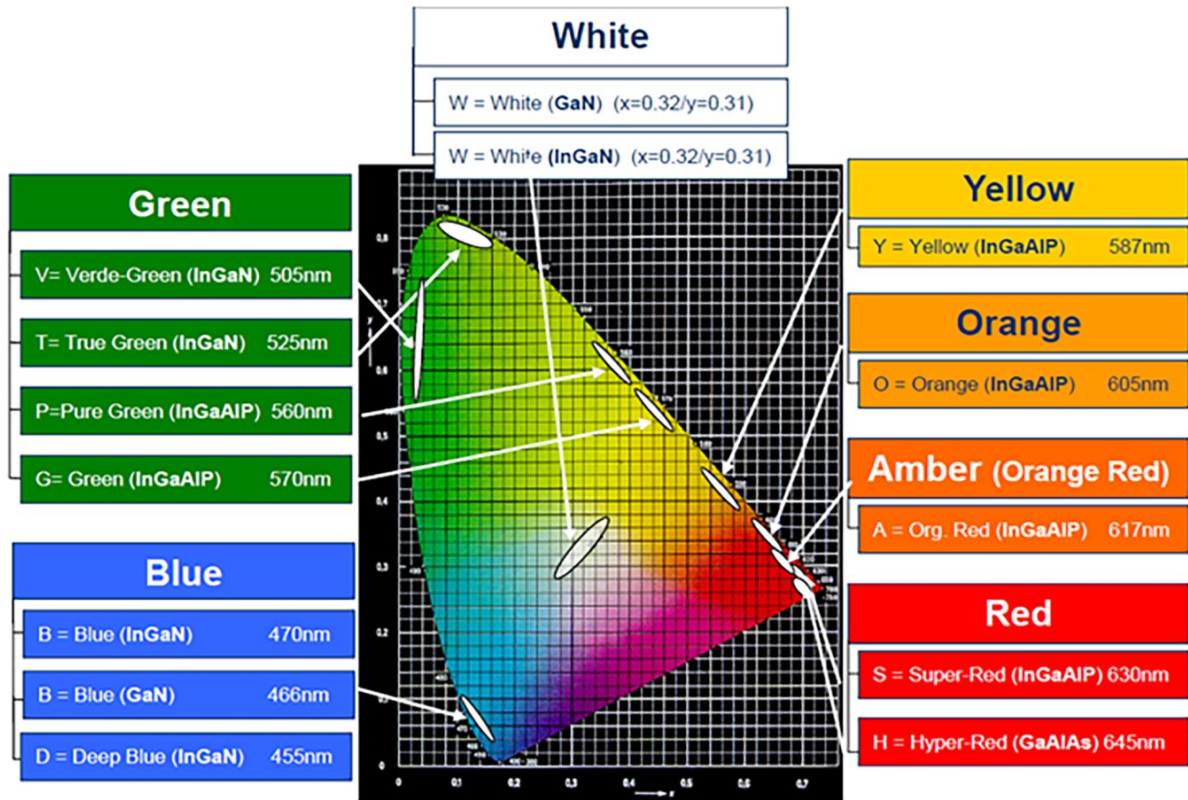
Figure 1.5 Different colors (wavelength) of the LED [13], [23].

34

energy values by virtue of quantum-confinement effect (QCE). The QCE takes place when the quantum well (QW) thickness approaches less than or equal to the de Broglie wavelength of the carriers (electrons and holes) [20]. In fact, the QCE is due to changes in the atomic structure as a result of the direct influence of ultra-small length scale on the energy bandgap structure, where the length scale ranges from 1 to 25 nm for typical semiconductor III-V, IV and II-VI groups. In QCE, QW is a type of structure in which charge carriers are confined to move in a plane and have free motion in a two-dimensional.
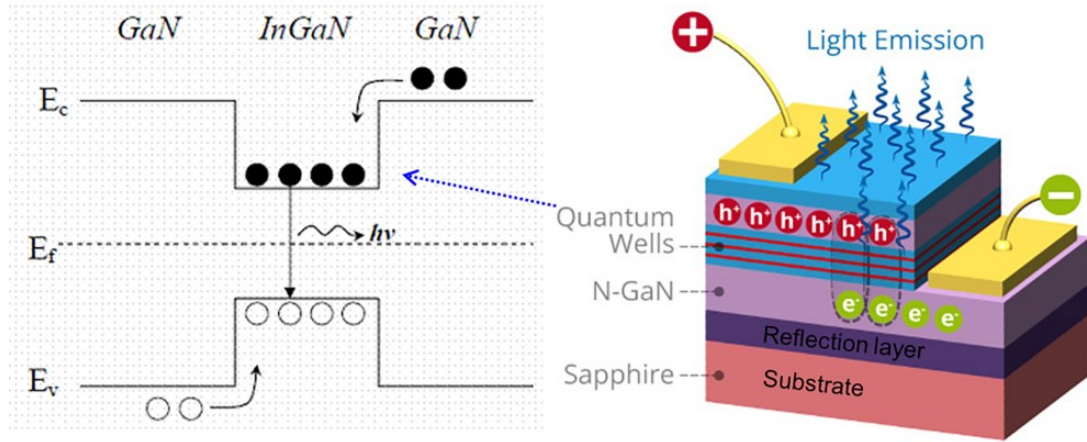
Figure 1.6 The concept of quantum wells in LEDs [29], [30]

As illustrated in Figure 1.6, a single QW is formed from one semiconductor (e.g., InGaN) sandwiched between two layers of a second semiconductor (e.g., GaN) having a larger band gap. The center layer with the smaller band gap semiconductor forms the QW, while the two layers sandwiching the center layer create the potential barriers (Figure 1.6). If the barrier thickness between adjacent wells is sufficient to prevent significant electronic coupling between the wells, then each well is electronically isolated; this form a structure called multiple quantum wells (MQWs). These MQWs structures consist of a series of QWs (i.e. a series of alternating layers of wells and barriers), which generate active regions to produce LEDs and laser diodes [24], [25]. Also, MQWs are the source for the production of thin-film LEDs and depend mostly on the concentration of compound semiconductors to

produce different colors of LED (Figure 1.5). For instance, varying the indium (In) concentration in the InGaN material can produce different colors in the LED, as shown in Figure 1.7 [26]–[28].
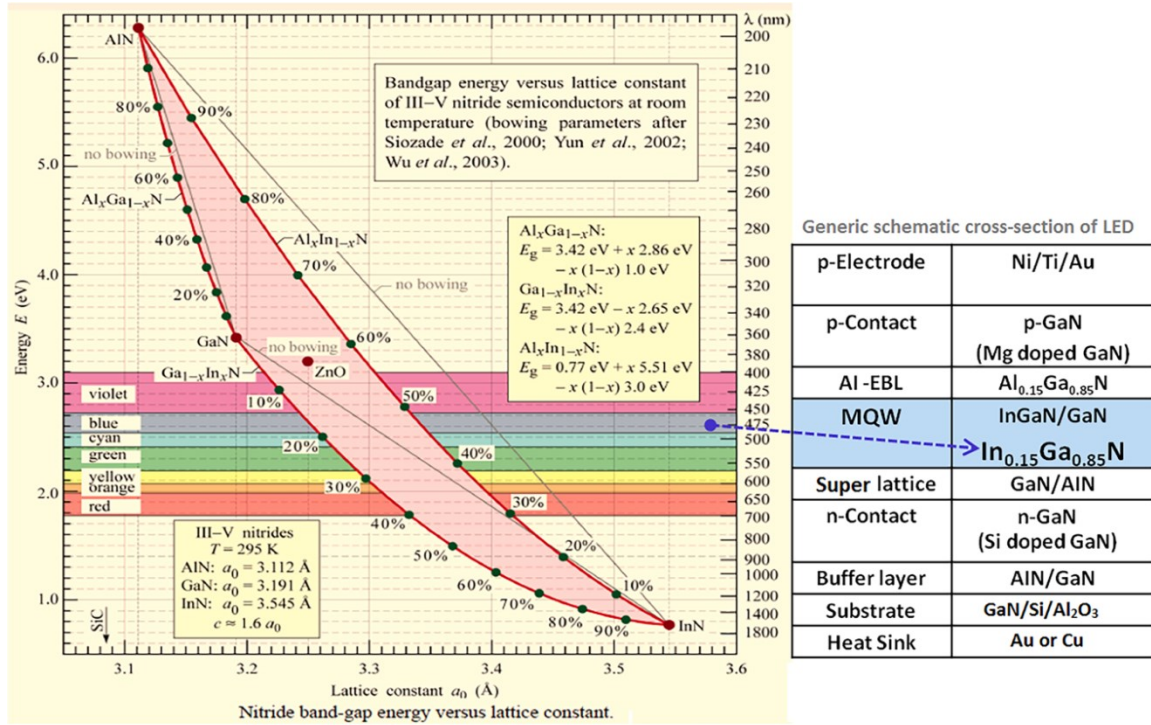
Figure 1.7 The impact of GaN-based alloy concentration on different colors (wavelength) of LED. An example of indium (In) concentration at MQW for the blue color LED [31].

Contrary to other compound semiconductors (e.g., InGaAlP or AlInGaP), the InGaN/GaN-based LEDs are the dominating candidates in illumination market with merits of a wide range of wavelengths, high efficacy [26], [32]–[34] (Figure 1.8). They also have merits in saving over 10% of worldwide electricity usage and reduction in global warming by decreasing at least 10% in fuel consumption, CO_2 emissions from power stations and mercury pollution [3], [35]. Hence, it is due to the superb figure of merits among various III-nitrides system, GaN-based LEDs has attracted tremendous attention in various industrial applications including back-lighting for smartphones and liquid crystal displays, traffic signals, automotive lights, and other outdoor commercial full-color displays [7], [8], [12], [35].
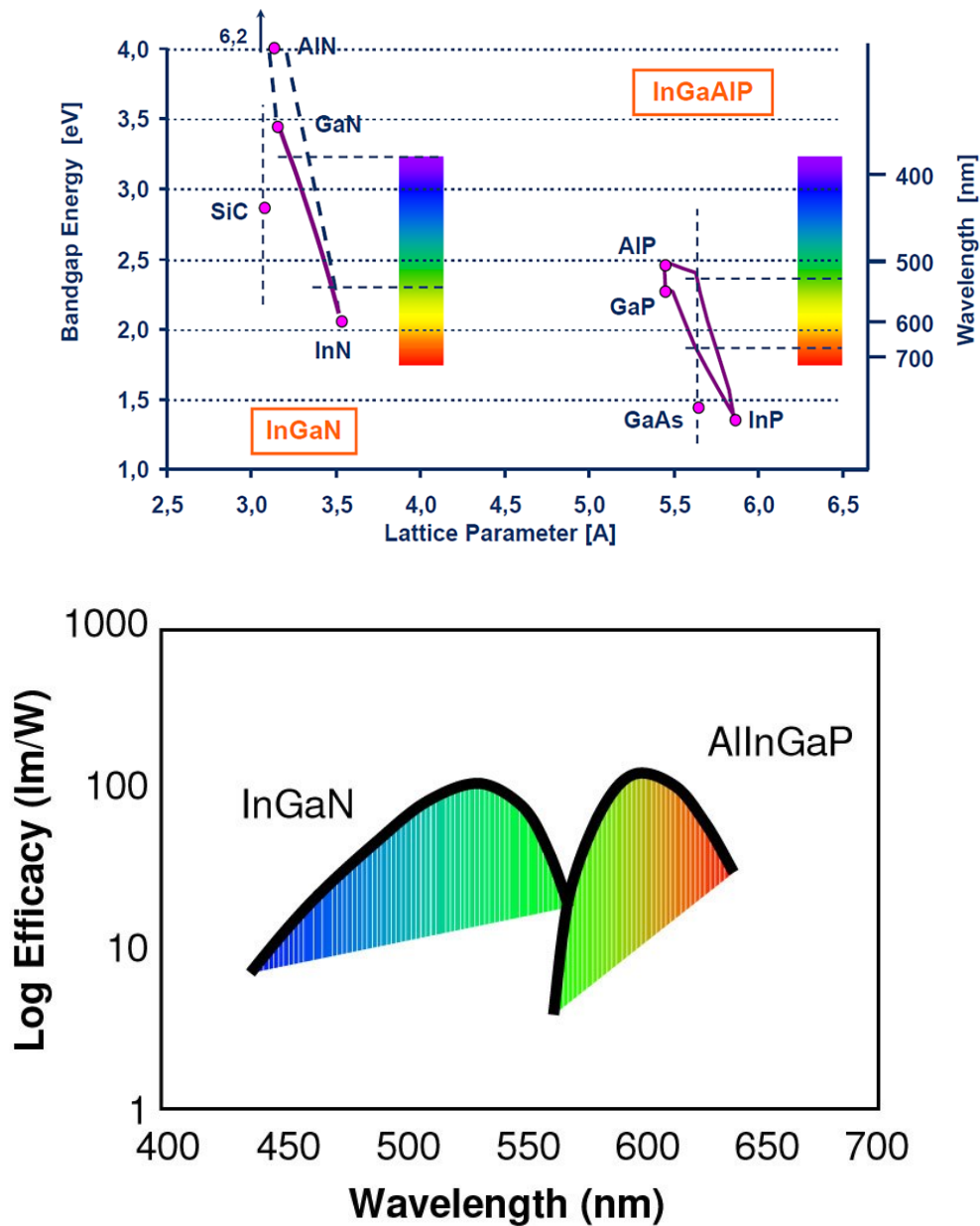
Figure 1.8 Comparison of InGaN and InGaAlP LEDs in terms of bandgap energy and efficacy [20].

1.1.3 Why GaN-based Vertical LEDs (VLEDs)?

In optoelectronics devices, GaN has prominent light emission capabilities with a wide range of wavelengths, from ultra-violet (being undoped) to red (doped) [26], [32]–[34]. Further, GaN-based thin or vertical light emitting diode (VLED) have been developed

because they possesses superior light emission property compared with the conventional lateral LED (LLED) architecture (Figure 1.9), including large light-emitting area by using one top electrode (n-side up and p-side down), mitigation of current-crowding problem, small series resistance (vertical current injection), better heat dissipation via a metal-based substrate or bendable substrateless techniques, higher light-extraction efficiency (LEE) by roughening the top n-GaN surface, and a better reflection of downward-absorbing light by placing a mirror layer on the top of the substrate [36]–[42].
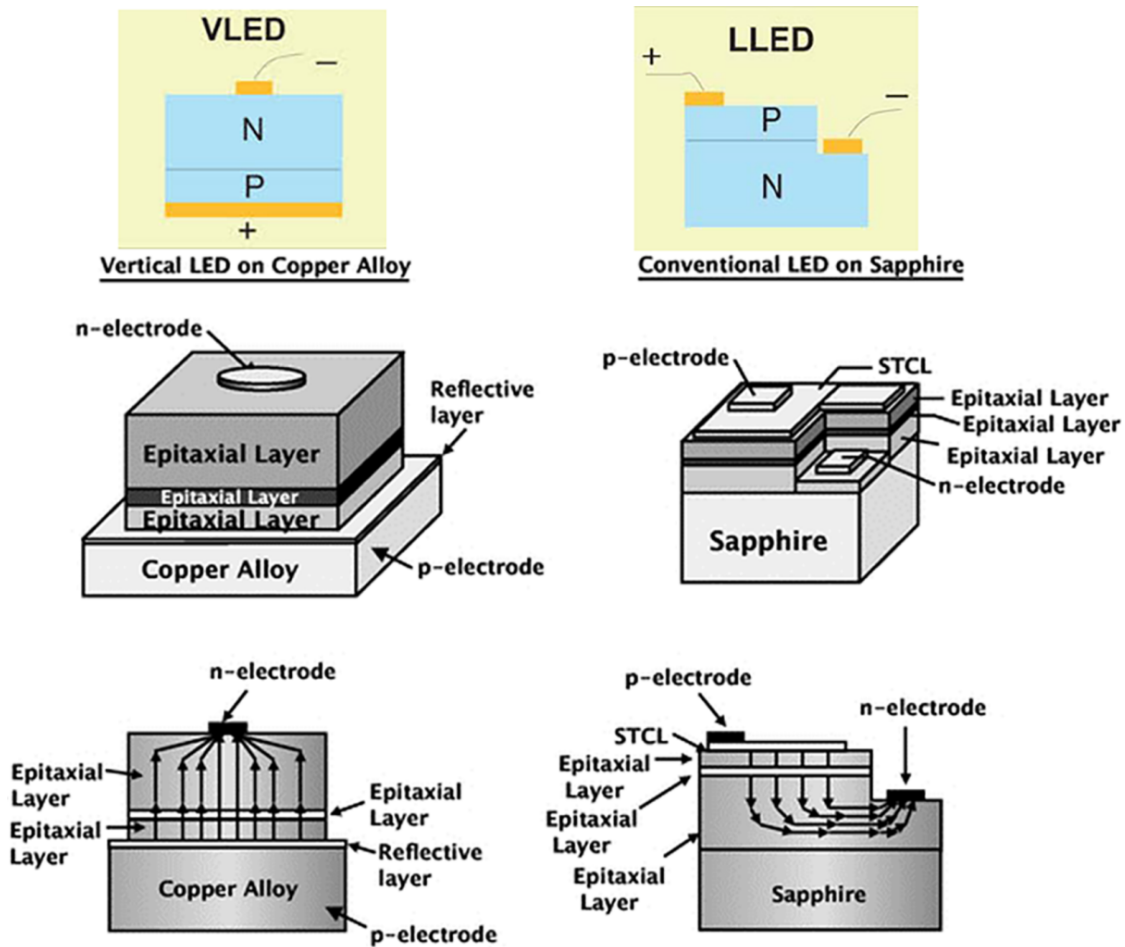
Figure 1.9 Comparison of vertical LED (VLED) and lateral LED (LLED) structures [39].
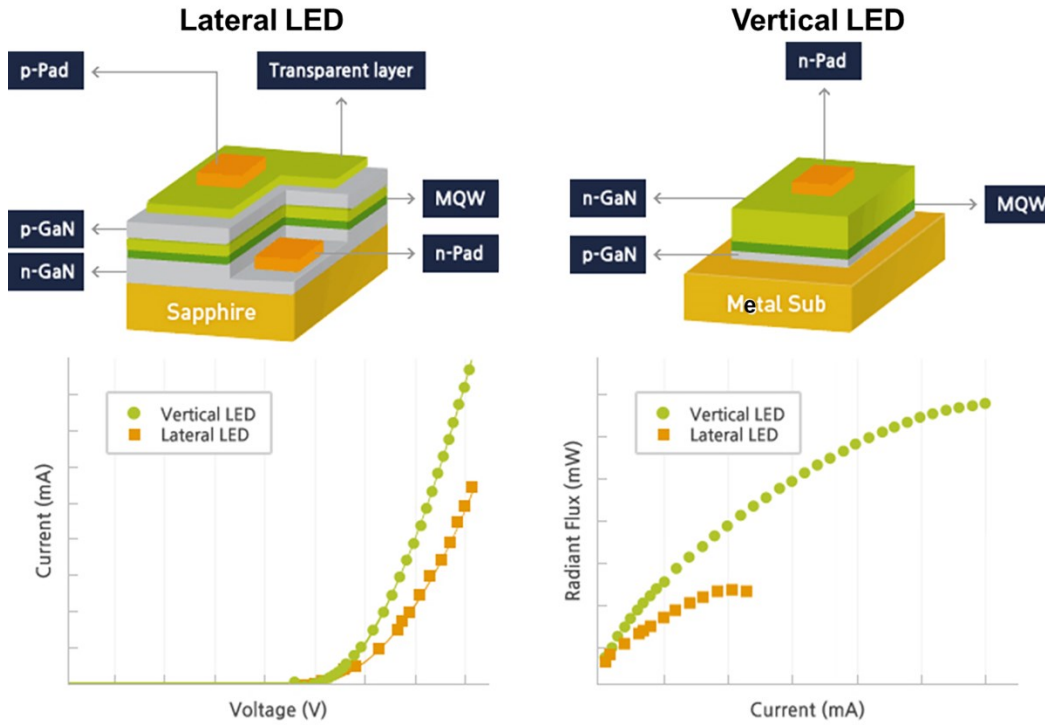
Figure 1.10 Radiation flux and I-V comparison of VLED and LLED structures [43].

The VLEDs do not exhibit the current-crowding problem on the top emission area, which is attributed to the relatively larger effective light-emitting area by using only one electrode at the top. VLEDs also have a better reflection of the downward-absorbing light by the reflection metal layer (e.g., Ag or Al), and enhanced LEE by roughening of the top n-GaN surface [43]–[45]. Furthermore, the current can spread uniformly in the VLED structure because p-side or p-electrode is down and n-side up, with a top single n-metal electrode, as illustrated in Figure 1. 9 and Figure 1.10.

Previous research groups reported that the light output powers for the LLED and VLED were 127.2mW and 156.4mW, respectively, at 350mA injection current and 298K temperature [14], [36], [46], [47]. In Figure 1.11, we can observe that the VLED structure has better performance in output power and LEE as compared to LLED [48], [49] due to better extraction of light from the surface roughening (top) and the reflective metal layers (at the base) of the device [50]–[53]. Such advancements are difficult to implement in the LLED since the top layer of p-GaN is thin and there is a lack of base reflectors to avoid light entering and being trapped in the sapphire substrate. Furthermore, conventional LLED

39

grown on the sapphire substrates are forced to use a lateral conduction scheme since the substrate is insulating. However, in case of VLEDs, particularly with nitrides, perform better with vertical conduction, where the current density is uniform [54]. This unique features is achieved by wafer bonding technology, which separates the nitride semiconductor films from the substrate (sapphire, silicon, or any metal alloy) on which the device layers were grown [55]–[57].
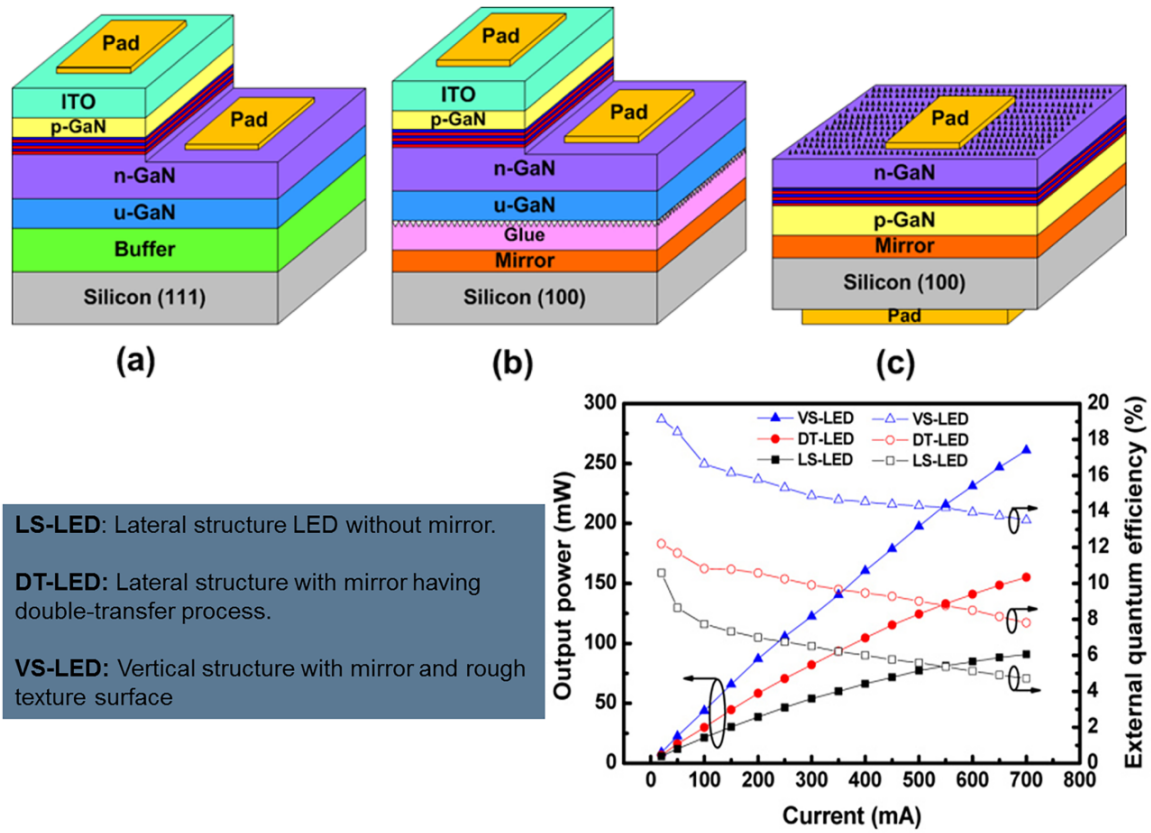
Figure 1.11 Comparison of lateral LED and vertical LED in terms of output power and EQE [48].

In recent years, the GaN-based VLEDs market is booming fast and has demonstrated high internal quantum efficiency (IQE) of 90% by developing good epitaxy or high crystalline MQWs [15], [58], [59]. However, their external quantum efficiency (EQE), which is equal to IQE × LEE, has achieved only 60-80% and there is still room for further improvement. To achieve the required benchmark for next-generation solid-state lighting, vertical LEDs are facing major challenges of low LEE and high cost [60], [61].

1.1.4 Current Challenges for LED?

Despite InGaN/GaN-based QWs for blue VLEDs can produce IQE of 90% and EQE of 60-80% [59], [62], [63] (Figure 1.12), there exist many key challenges, for instance, the efficiency droop (the substantial decrease of quantum efficiency with increasing drive current) [64], [65], the green gap (the relatively low efficiency of green LEDs in comparison to blue) [65], [66], the quantum-confined Stark effect (large piezo-electric and polarization fields arising at polar interfaces) [67], carrier (electrons and holes) injection efficiency [68], [69], Auger recombination [70], [71], carrier delocalization [72], impurity diffusion [52], [73], structural and crystal defects (lattice mismatch, dislocations) [74]–[76].
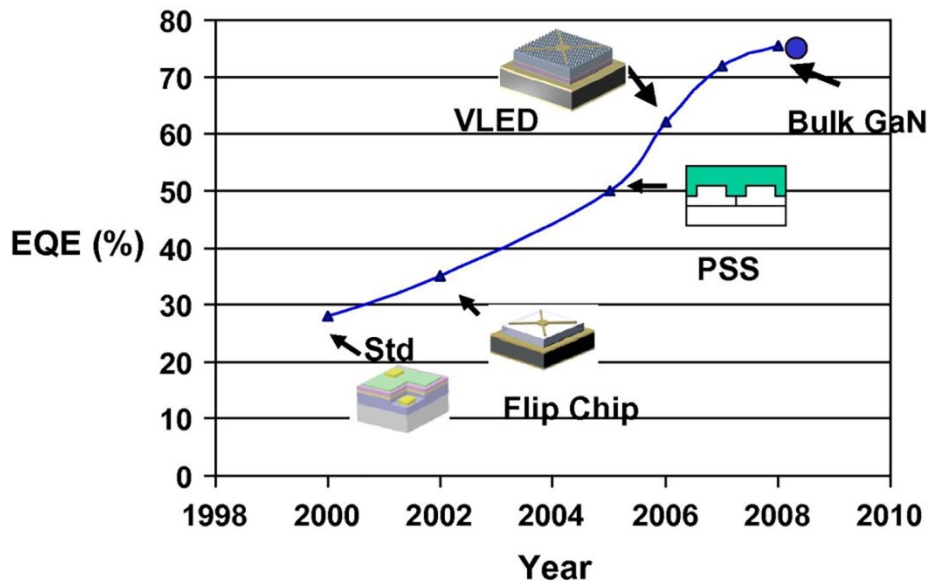
Figure 1.12 Comparison of different structures of LEDs in terms of EQE [25].

In spite of research work on GaN/InGaN or GaN/InGaAlP bandgap engineering [77]–[82], a major challenge is "efficiency droop" or roll-off of EQE while operating LEDs at higher current densities (>10 A cm^{-2}) when trying to increase the luminous flux (currently ~160 lumens per power LED chip), as show in Figure 1.13. Thus, VLED still needs improvement, particularly on the luminous efficacy and admittedly EQE. To understand that critical challenge of "efficiency droop" or low EQE, we need to know the basic concepts of EQE, IQE and the factors on which they rely. The EQE (η_{EQE}) is the product of the injection

41
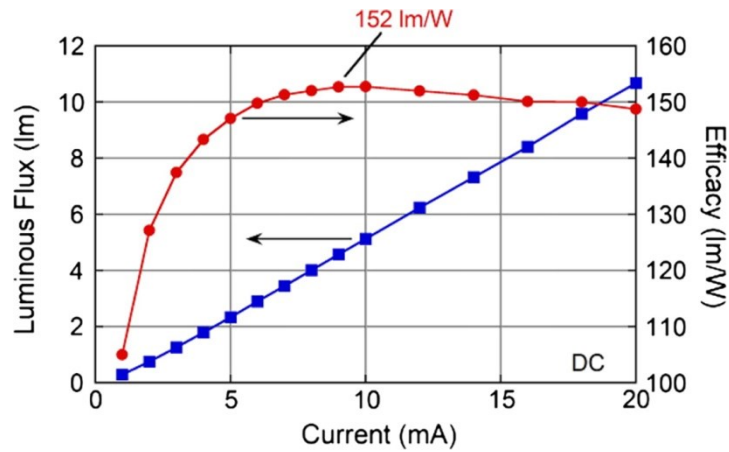
Figure 1.13 The efficiency droop in the LED [25].

efficiency η_{inj}, the IQE (η_{IQE}), and the LEE (η_{extr}), i.e., $\eta_{EQE} = \eta_{inj} \cdot \eta_{IQE} \cdot \eta_{extr}$ [83]. The LEE or η_{extr}, which is the ratio between the externally emitted photons and the internally generated photons in the active region, is mainly determined by the LED architecture (chip design), surface roughening, patterned substrates (PSs), material absorption and reflection, and so forth, whereas η_{IQE}, which is the ratio between the electrically injected carriers and the internally emitted photons is mainly connected to the quality of the active layer and is
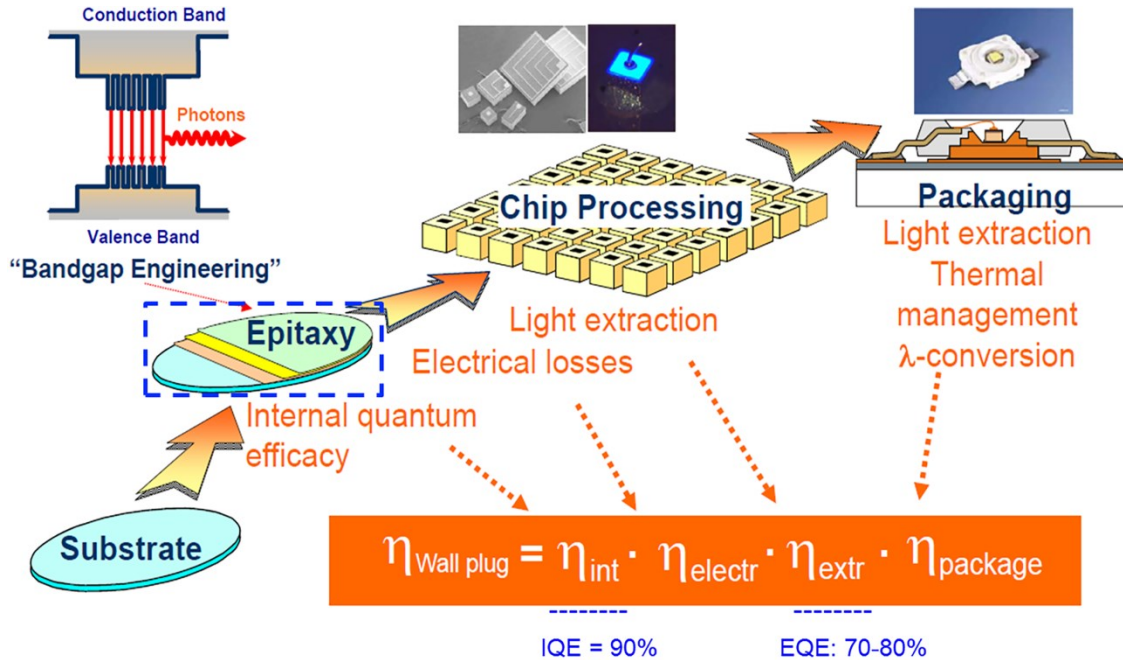
Figure 1.14 Dependence of different types of efficiencies in the LED on epitaxial layers, fabrication and chip packaging processes (*Source: Semi LED*).

42

evaluated by its growth conditions, impurity incorporation (diffusion), doping profile, defect density of the material and surface morphology [83], [84]. Consequently, two factors: (1) IQE and (2) LEE mainly contribute to overall wall plug efficiency of LED, as illustrated in Figure 1.14. Thus, it is of great importance to correlate LEE and IQE, consequently to enhance the overall EQE in the LEDs.

Hence, the EQE considered to be the main criterion for LED performance, and has been approaching 60-80% in recent LED products [25], [59], [84], [85]. Therefore, optimization across these aspects needs to be explored systematically in detail for further improvement in the EQE.

1.2 Strategies Adopted to Address Challenges of VLED

Although the IQE of today's best LEDs has reached values > 80% for blue 450 nm LEDs at low current densities (<30 A cm^{-2}) and EQE of 70-80%, still further improvements towards 100% for both IQE and EQE are required. In fact, optimization engineering in both fabrication and characterization sectors is inevitable in producing high-performance LEDs to fully replace traditional incandescent and compact fluorescent technologies. In this regard, atomic or nanoscale characterization of "*each LED stack layers*" is necessary to reveal their pertinent internal physics and chemistry, which facilitates in understanding the detailed surface morphology, chemical composition, elemental diffusion, surface topography, crystallographic information, atomic structure with polarity, interfaces abruptness and carrier localization mechanism.

In this context, LED have been characterized by different groups using microscopy techniques of scanning electron microscopy (SEM) [86], atom probe microscopy (APM) [87], secondary ion mass spectroscopy (SIMS) [88], [89], transmission electron microscopy (TEM) or electron tomography (ET) [90]–[92], atomic force microscopy (AFM) [93], Raman spectroscopy [94], [95], X-ray diffraction (XRD) [96], and Photoluminescence (PL) [97], and so forth. Few examples of these microscopy techniques applied on the LED are shown below in Figure 1.15 to Figure 1.23.
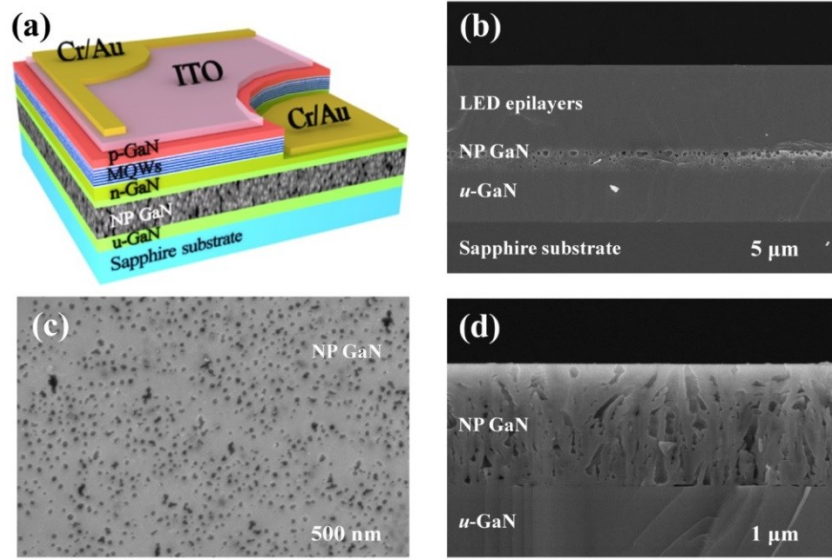
Figure 1.15 (a) Schematic diagram of LEDs grown on a nanoporous (NP) GaN layer. (b) SEM image of NP GaN-embedded LED structure. (c) Top, and (d) Cross-sectional SEM images of NP GaN [86].

For instance, in Figure 1.15(b)-(d), SEM images indicates top and cross-sectional view of nanoporous (NP) GaN-embedded LED structure etched at an applied voltage of 17 V. Such images are vital to cross-check the quality of electrochemically etched NP GaN layer, which attributes to increase LEE by light scattering effect by NP [86].

Figure 1.16 illustrates a competitive analysis of a GaN-based commercial LED chip by using APT technique [31], [87]. APT has the unique capability of determining chemical compositions in three-dimensional (3D), where it shows four MQWs layers are composed of In/Ga, while Al as an electron blocking layer (EBL) and Mg doping form p-type layers of LED. Also, the mass spectrum and one-dimensional (1D) elemental compositional profiles generated from within the reconstructed volume shows that the device is composed of a number of elements, majorly Ga, N, In and Mg along with their counts and concentration (at.%), respectively. The ID profiles confirm that concentration of Al EBL is about 10-14 at.%, and the average In concentration within the five QWs is determined as 8 at.%., whereas it varies periodically between 0.5 at.% and 1.5 at.% at 21 In-rich superlattice layers. Although APT provides the chemical composition in 3D, still it has a limited volume of data (~100 nm^3 compared to SIMS larger area of ~100 x 100 μm^2), hence complimentary SIMS calibrations are necessary to analyze dopant distributions [31].
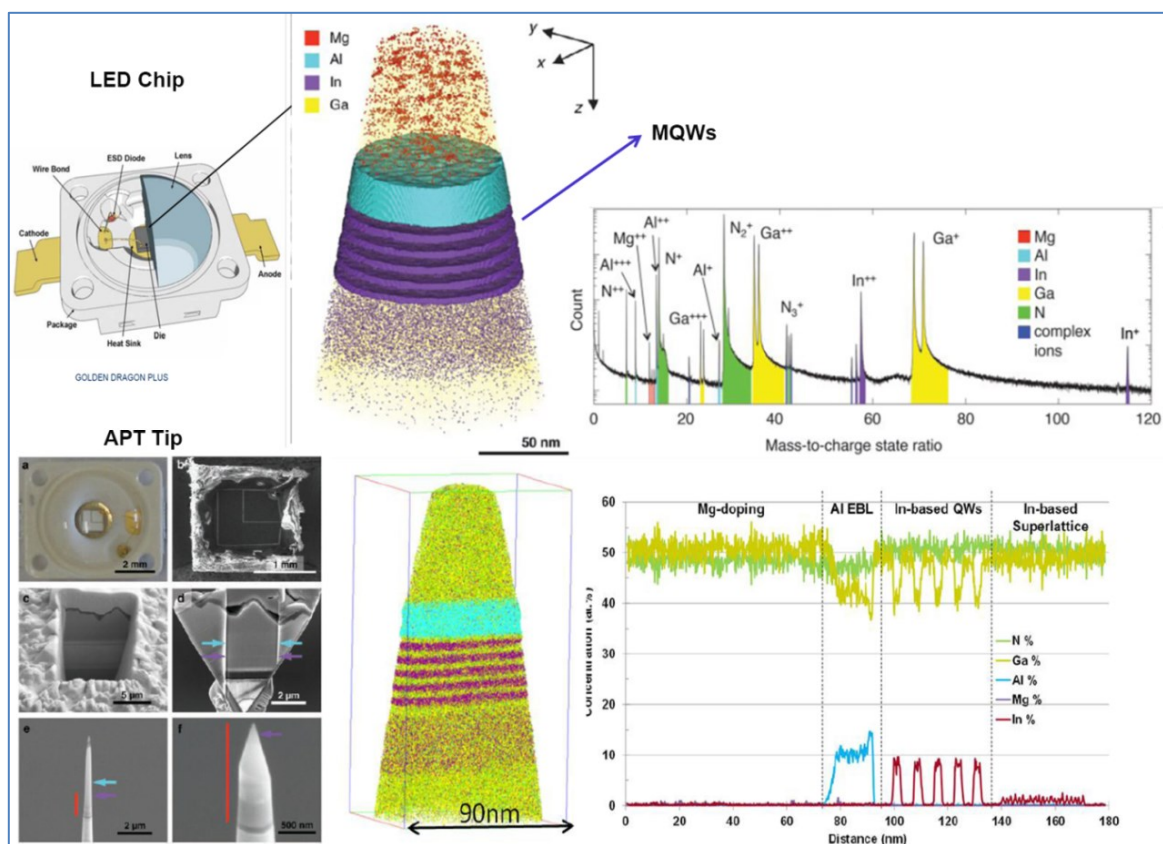
Figure 1.16 3D chemical composition (atom map), mass spectrum, 1D composition profile by APT on the commercial OSRAM 455 nm Golden Dragon@ Plus blue GaN-based blue vertical LED chip [31], [87].

SIMS is another key analytical technique used to analyze the composition of thin films or solid surfaces by sputtering their surface with the primary ion beam of few keV energy, collecting and analyzing ejected secondary ion (particles) from the specimen. SIMS works mainly in two modes: (1) static mode and (2) dynamic mode. The former concentrates on the first top monolayer by providing mostly molecular characterization, while in the later mode, bulk composition and in-depth distribution of trace elements are investigated with a depth resolution ranging from sub-nm to tens of nm [88], [89]. In Figure 1.17, using dynamic SIMS, a depth profile of p-type (Mg) and n-type (Si) dopants was obtained in the GaN-based LED. Also, seven MQWs consist of In element, whereas Al profile is noticed for EBL. In impurity control and failure analysis of the LEDs, particularly depth profiling data is routinely recorded for both matrix and dopant species, where undesirable contamination of H, C, and O causes defects into GaN crystalline structure, which majorly affects the electrical properties and shift the intended emission wavelength.

Figure 1.17 SIMS analysis showing p- and n-type dopant profiles in AlGaN/GaN LED structure [88], [89].

In order to have a better lateral spatial resolution (atomic-planes) and crystallographic information, electron microscopy or TEM is mostly applied. In Figure 1.18(a), cross-sectional TEM images determine that visible LED stack on graphene/SiC is composed of three periods of III-nitride MQWs (InGaN well and GaN barrier) sandwiched between p-GaN and n-GaN. The high-resolution (HR) TEM images taken at the GaN/graphene/SiC interface shows well aligned, ordered GaN crystal lattice on a recycled graphene/SiC substrate and released by a Ni stressor/handling tape, respectively (Figure 1.18(b)-(d)). A selected area electron diffraction pattern taken from the released LED stack indicates a well-aligned single crystal (see inset of Figure 1.18(d)). A I–V curve and blue light emission from the released LED stack was observed (inset of Figure 1.18(f)). The electroluminescence spectra (Figure 1.18(f)) confirmed the light emission peaking at $\lambda \approx 440$ nm which is typical for III-nitride blue LEDs.

Furthermore, in Figure 1.19(a),(b), scanning TEM analysis indicates the absence of major defects such as cracks or V-shaped ones in the 10 pairs heterostructures corresponding to GaN and $Al_xGa_{1-x}N$:Mn Bragg layers, respectively. The defined Z-contrast in the high-angle annular dark field (HAADF)/STEM image of (Figure 1.19(c)) recorded on the $[11\bar{2}0]$ zone axis is an indication of the atomically sharp interface between the $Al_xGa_{1-x}N$:Mn and

46
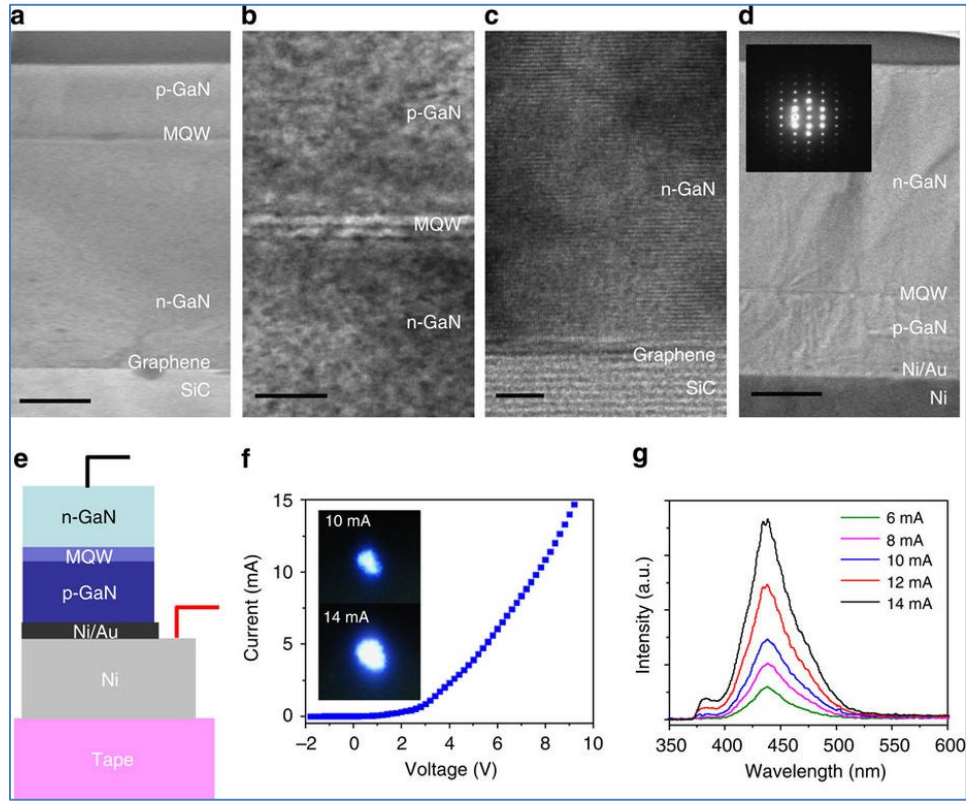
Figure 1.18 Cross-sectional TEM image of LED stacks (p-GaN/MQW/n-GaN) on a graphene/SiC substrate (scale bar, 1 μm). (**b**) High-resolution (HR) TEM image magnified at MQW (scale bar, 100 nm). (**c**) HRTEM image magnified at a GaN/graphene/SiC interface (scale bar, 5 nm). (**d**) Cross-sectional TEM image of a released LED stack from a graphene/SiC substrate: n-GaN/MQW/p-GaN/Ni (scale bar, 1 μm). A selected area electron diffraction pattern from p-GaN/MQW/n-GaN is displayed in an inset. (**e**) Schematic of a transferred LED device (**f**) $I-V$ characteristic of a transferred LED stack measured by applying positive bias on Ni and negative bias on n-GaN. The pictures of the blue LED are displayed in an inset. (**g**) Electroluminescence (EL) spectra of a transferred LED stack taken as a function of injection current [90].

and the GaN layers. However, threading dislocations can be seen in Figure 1.19(b) and are dominated by defects due to structural and thermal mismatch of the $Al_xGa_{1-x}N$ nucleation layer with respect to the sapphire substrate. The strain state around the $Al_xGa_{1-x}N$:Mn/GaN interface also evidenced by x-ray diffraction (XRD) in Figure 1.19(d). In Figure 1.19 (extreme right end), the cross-sectional HAADF TEM image of the active region of another LED shows that it has five pairs of MQWs, each of which consists of an $In_{0.2}Ga_{0.8}N$ QW (2.5 nm) and a quaternary $Al_{0.04}GaIn_{0.12}N$ QB (3.5 nm), which are sandwiched by two GaN cap layers.

47
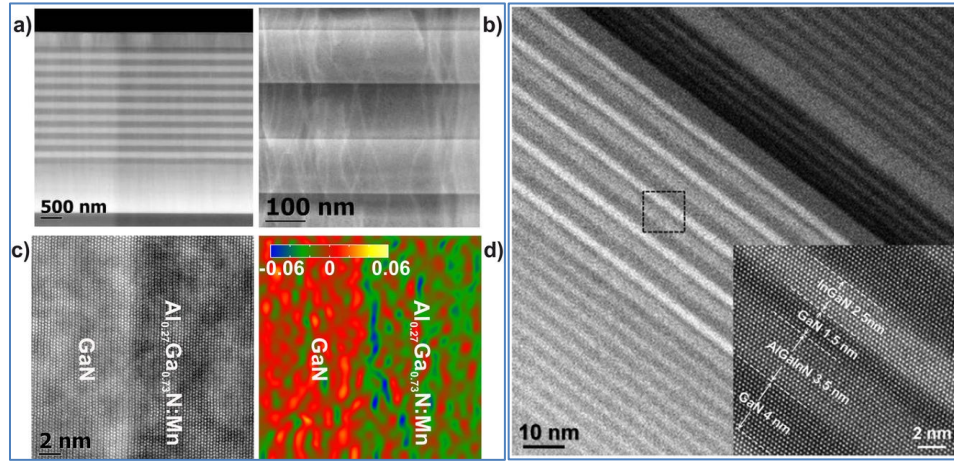
Figure 1.19 (a,b) STEM images of the active region of LED. Light and dark alternating areas correspond to the GaN and $Al_xGa_{1-x}N$:Mn regions of the Bragg pairs, respectively. In (a) the 130 nm thick GaN:(MN, Mg) active layer is also distinguishable at the top of the structure. (c) HR-STEM acquired along the interface between the GaN and $Al_xGa_{1-x}N$:Mn layers of one Bragg pair. (d) Strain mapping for the interface reported in (c) Annular dark-field STEM image showing the MQWs of LED device. The active region consists of 5 pairs of MQWs), which are InGaN QWs and quaternary AlGaInN QBs sandwiched by GaN cap layers with different thicknesses. The inset shows a higher resolution image of the square region [91], [92].

On comparing APT, SIMS and TEM techniques, we can observe that the powerful spatial resolution of the APT known to be anisotropic (being better in depth than laterally) and limited by the physics of field evaporation. It is also revealed that contrary to the pure metals, lateral resolution for semiconductor (SC) may no longer be on at atomic-planes, which explains why it is not always possible to have structural (crystallographic) information like TEM while working with SC materials [31]. Also, the detection limit for APT ($\sim$5x 10^{17} at cm^{-3}) is less than the one of SIMS due to analysis volume but APT has a better depth resolution, gives a unique 3D profile.

Apart from the APT peculiar approach in 3D compositional imaging, it can image and analyze hundreds of millions of atoms, which is currently impossible in ET. Furthermore, APT accomplishes analysis at the atomic-scale with high analytical sensitivity ($\sim$10–100 ppm compared to 1 ppm in SIMS or 10000 ppm in TEM) [31]. Nevertheless, TEM provides crystallographic information, high lateral spatial resolution for high-fidelity imaging, chemical and compositional information from the energy-dispersive x-ray spectroscopy (EDX) and electron energy loss spectrometry (EELS), but unable to

determine the unique 3D positions of every atomic species in a selected region. Also, TEM lacks the attribute of discrete 3D imaging (tomographic images) and faces a particular challenge when features of interest are smaller than the thickness of the specimen (~10–100 nm). Although recent improvements in ET have reached comparable scale to APT, the atomic-scale has not yet fully achieved or less distinct and detailed 3D quantitative compositional data of complex (nano-scale or multilayer) structures is less developed so far in ET as compared to APT. Hence, each microscopy technique has its own advantage, and correlatives techniques must be applied to provide more detailed structural and compositional information about the relevant device. More discussion about microscopy tools is in section 2.3 "Microscopy Techniques on the Vertical LED".

Figure 1.20 reveals a schematic of the high-power VLED chip with Si submount die-bonded to a high-temperature co-sintered ceramic (HTCC) lead frame substrate encapsulated in copper films. Roughening processes were applied to the surface of the lead frame to form a diffusely reflecting surface that would significantly improve the out-coupling of rays. The surface roughness is measured by AFM technique, which is inevitable to analyze surface topography of the LED without damaging the sample. More about AFM is detailed in section 2.4 of this thesis.
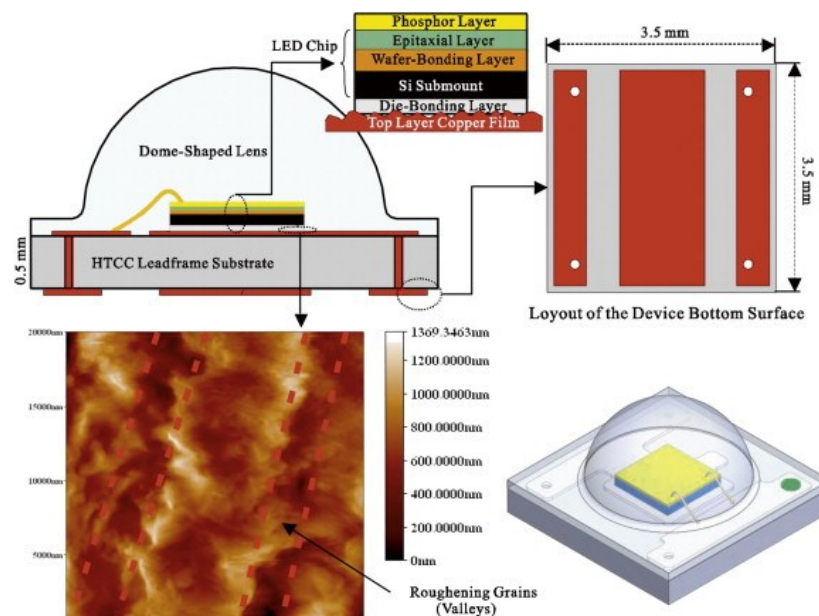
Figure 1.20 AFM image showing surface topography of the lead-frame substrate [93].

49

Strain analysis of grown GaN microstructures was determined by micro-Raman scattering spectroscopy as shown in Figure 1.21. The 3D structures, such as nanowires and micro-rods, can be used to overcome the issues of planar 2D growth of GaN on a foreign substrate (such as suffers from strain energy accumulation in the film resulting essentially from the lattice mismatch, a difference in thermal expansion coefficient, and wafer bowing). The 3D GaN structures can be grown with good crystal quality despite the large lattice mismatch and thermal expansion coefficient difference between GaN structures and substrates, leading to the growth of almost strain-free 3D structures through lateral strain relaxation. These 3D structures have also attracted considerable interest for their potential application to a number of technologies including nanoelectronics, optoelectronics, photovoltaics, and sensors.
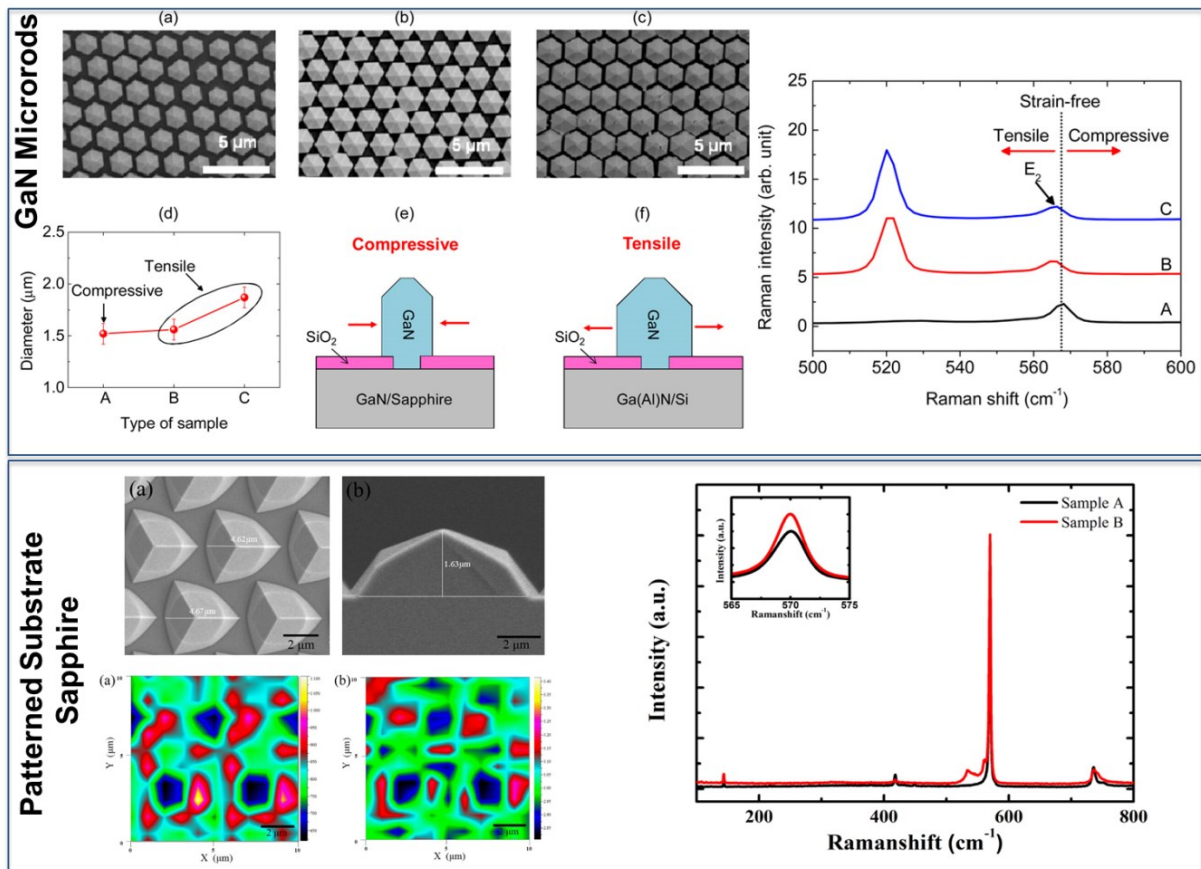
Figure 1.21 Raman spectroscopy (stress state analysis) on GaN micro-rods and patterned sapphire substrate of the LED [94], [95].

Figure 1.21(a)-(c) shows the growth of GaN micro-rods on various strain-induced templates: samples A, B, and C are GaN/sapphire, GaN/AlN/Si(111), and AlN/Si(111) substrates, respectively. According to group theory [20], hexagonal GaN belonging to the space group holds six first-order Raman-active optical modes at Γ point: A_1 (LO) + A_1 (TO) + E_1 (LO) + E_1 (TO) + E_2 (low) + E_2 (high) in various scattering geometry configurations. Under Z-geometry, only E_2 (low), E_2 (high) and A_1 (LO) mode peaks are allowed to appear in the spectra. The E_2^h (high) mode peak is considered to be the most sensitive to stress and always used to characterize the residual stress in GaN thin films (more discussion about it is in section 2.4 of this thesis).

The Raman spectra for the three samples showed the intense peak at ~521 cm^{-1} for samples B and C is attributed to the Si substrate, as shown in Figure 1.21. Also, the E_2^h peaks can be observed at 564.46 and 566 cm^{-1} for samples B and C, respectively. Compared with the Raman shift of strain-free bulk GaN shown by the dotted line at 567.5 cm^{-1}, redshift of the E_2^h phonon mode for samples B and C clearly reflects the residual tensile strain of grown GaN micro-rods. On the other hand, sample A showed the Raman shift at 568.1 cm^{-1}, indicating slight compressive strain or almost no strain. Hence, the commonly induced compressive strain of GaN/sapphire templates was almost fully relaxed by the selective-area growth by hydride vapor phase epitaxy and careful selection of the template is necessary to control the diameter of GaN 3D micro-rods.

Similarly, in Figure 1.21 (bottom), micro-Raman measurements have been carried out to investigate the spatial variations in crystal quality of n-type GaN grown on the planar substrate (a) and the PSS (b). Three peaks located at about 142 cm^{-1}, 570 cm^{-1} and 734 cm^{-1} appear in all spectra which represent to the E_2 (low), E_2 (high) and A_1 (LO) mode peak, respectively. The peaks at about 418 cm^{-1} and 748 cm^{-1} are corresponding to sapphire Raman peaks. It can be noticed from the insets that all the E_2 (high) mode peaks in the two samples are larger than 567.6 cm^{-1}, which indicate that both samples are under compressive stress, just as predicted for GaN epilayers grown on sapphire substrates. Also, other useful information on spatial distributions of crystalline quality in n-type GaN grown on PSS could be obtained through a spatial mapping of the E_2 (high) mode. The color mapping in Figure 1.21 (bottom images), shows the intensity and the full width at half maximum

(FWHM) maps of the E_2 (high) mode in a $10 \times 10\ \mu m^2$ zone measured in sample B. The mapping scans data ranging from black for the weakest to yellow for the highest intensity. The blue regions with the lowest intensity corresponding to the center parts of the patterns (minimum FWHM, meanwhile the yellow and red regions with the highest intensity refer to the rest part of the patterns (largest FWHM). In fact, the intensity and FWHM variations of E_2 (high) mode peak could effectively provide the crystalline quality of GaN epilayers. The smaller FWHM of E_2 (high) indicates a better crystalline quality of material with lower dislocation density.

In Figure 1.22, the crystalline quality and the variation of stresses during the fabrication of p-electrode LEDs on Cu are characterized by HR-XRD. The $2\theta/\omega$ scans around GaN (0002) of the LED wafer on Si before and after etching by inductively coupled plasma reactive ion etching (ICP-RIE), and the embedded wide p-electrode LED on Cu, respectively. The satellite peaks show that no obvious deteriorations are found in the MQWs after the LEDs transferred from Si substrate onto Cu. According to the 2θ values, the LED on Si shows a tensile stress, while after the Si substrate removal, an almost fully strain relaxation is observed in the embedded wide p-electrode LED on Cu. This strain relaxation is in favor of
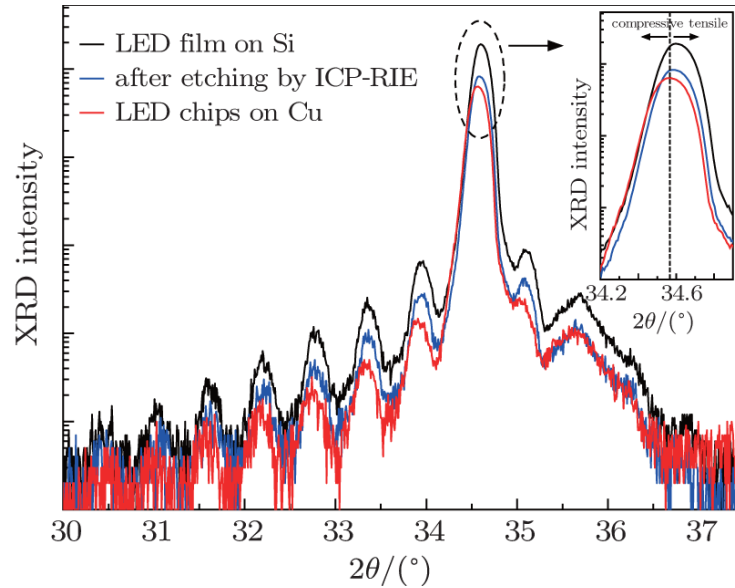
Figure 1.22 HR-XRD $2\theta/\omega$ scans around GaN (0002) of the LED film on Si before and after etching by ICP-RIE, and the embedded wide p-electrode LED on Cu, respectively. The diffraction peaks of GaN (0002) are shown in the inset [96].

the reduction of QCSE and the enhancement of IQE.

GaN-based LEDs on Si (111) substrates with different interlayer structures were investigated using PL technique, as shown below in Figure 1.23. Although low-temperature AlN (LT-AlN) single interlayer was commonly used in growing high-performance GaN-based LEDs on Si substrates to mitigate the issues of large mismatch in lattice constant (16.9%) and thermal expansion coefficients (57%) between GaN and Si, still its variation in thickness and temperature causes new dislocations and crack density (stress), respectively. Thus, there is a motivation to explore alternate interlayer structures, which can not only improve stress and but also minimize dislocation formation for high-performance GaN-based LEDs on Si substrates.
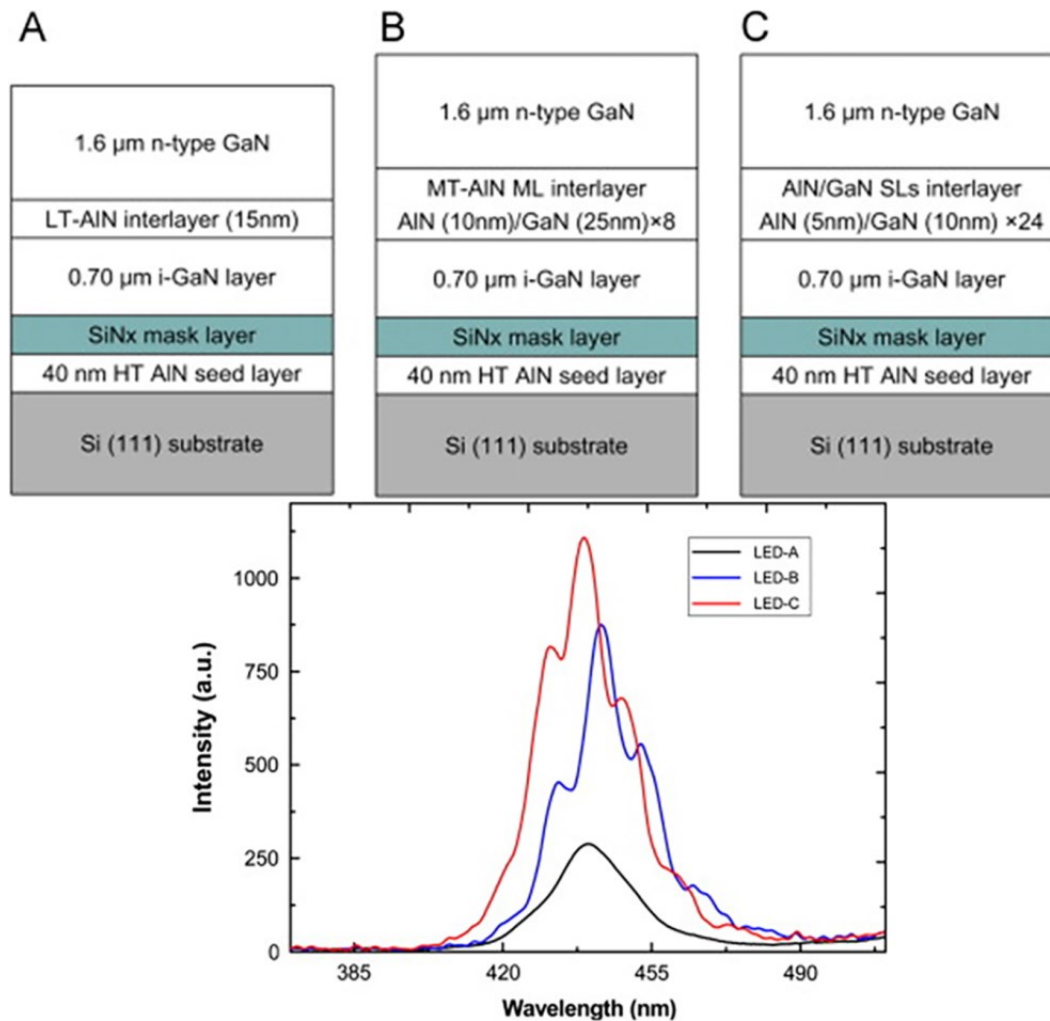
Figure 1.23 PL spectrums of LEDs with different buffer (interlayer) configurations [97].

In this context, PL for the three LED samples: (1) LT-AlN (sample A at 830 °C), (2) medium-temperature AlN multilayer (MT-AlN ML) (sample B at 1020 °C), and (3) AlN/GaN superlattice (SL) (sample C at 1070 °C) were performed to determine the influence of the interlayers upon the LED optical properties, as illustrated in Figure 1.23 (a)-(c). All the LED samples emit at a wavelength of around 440 nm. The best PL peak intensity can be observed for LED-C. This is because the SL interlayer can effectively reduce the dislocations density and the probability for dislocations propagating into the MQWs, resulting in better internal quantum efficiency. Hence, the PL and micro-Raman measurements reveal not only the crystal quality of the GaN micro-rods but also strain distribution as well.

1.3 Objectives of this Research?

In previous reports on the LEDs, it can be observed that majority of groups focused either on the semiconductor (GaN) film or active region (MQWs) of the LED, which mainly contributes towards the IQE. This is the reason that today's LEDs IQE exceeded above 80% but EQE still remains at 70-80%. Thus, to address the efficiency droop (low EQE) issue of
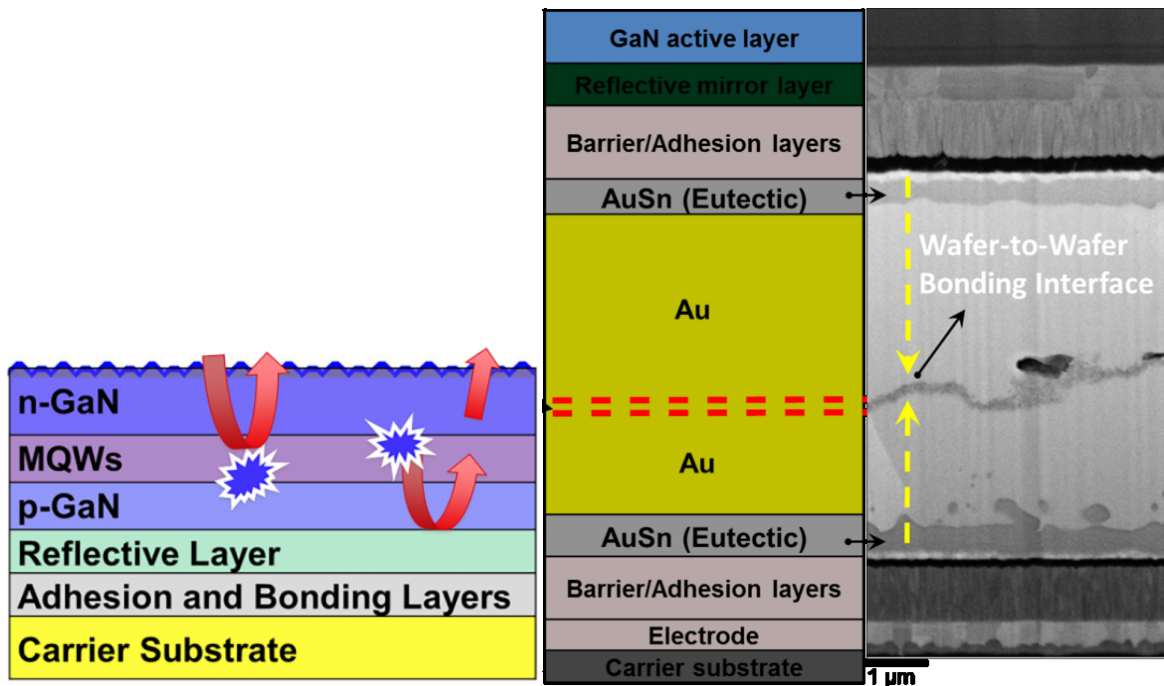
Figure 1.24 Cross-sectional schematic of VLED.

54

the LED, my research work focused on developing a novel strategy to explore underneath metallic layers and investigate their semiconductor-metal interfaces in the LED stack layers well, which plays a critical role in enhancing the EQE and directly or indirectly impacts the LEE and IQE factors. The stack layers of our VLED are shown in below Figure 1.24.

Based on that strategy, wafer-metallic bonding, silver-mirror reflection, GaN active-MQWs, textured n-GaN layers have been systematically investigated using SEM-based transmission Kikuchi diffraction (TKD)/EDX, HR TEM/scanning transmission electron microscope (STEM)-based-EDX, aberration-corrected STEM (AC-STEM), AFM, Raman spectroscopy, XRD and PL techniques.

The key objectives of our research are summarized below:

(1) Perform atomic or nanoscale characterization on the LED stack layers (Figure 1.24) to scrutinize their surface morphology, chemical composition, elemental diffusion, surface topography, crystallographic information, atomic structure with polarity, interfaces abruptness and carrier localization mechanism.

(2) Systematically apply those microscopy techniques on the LED, which are advanced, powerful, high lateral/spatial resolution, robust and sophisticated to characterize LED at the atomic or nanoscale.

(3) Correlate microscopy results with the structure-property-process-performance paradigm of the LED.

(4) To perform quality control (QC) and quality analysis (QA) by competitive and failure analysis to evaluate fabrication process of VLED, and link that data analysis with the efficiency droop and reliability issues of the LED.

(5) Further, based on these microscopy results, optimization suggestions on light extraction (EQE= IQE x LEE) to be given to improve the performance of VLEDs.

Chapter Two

Fabrication Method and Microscopy Techniques on VLED

2.1 Fabrication Process of Vertical LED

The process flow of fabricating GaN-based blue VLED involved four steps: (1) growth of metal-organic chemical vapor deposition (MOCVD) epitaxial layers on a device wafer (DW), that constitutes sapphire/silicon substrate, and deposition of a reflective mirror by electron-beam evaporation, diffusion barrier, adhesive, and bonding metal layers, (2) wafer-to-wafer (W-W) bonding, i.e., transferring of DW and integrating it to a carrier wafer (CW), (3) removal of the temporary grown substrate (sapphire) from DW by laser lift-off, and lastly (4) surface structuring or pattering (top textured surface) of the VLED die [38], [52], [57]. Figure 2.1 illustrates the summary of mentioned above steps.
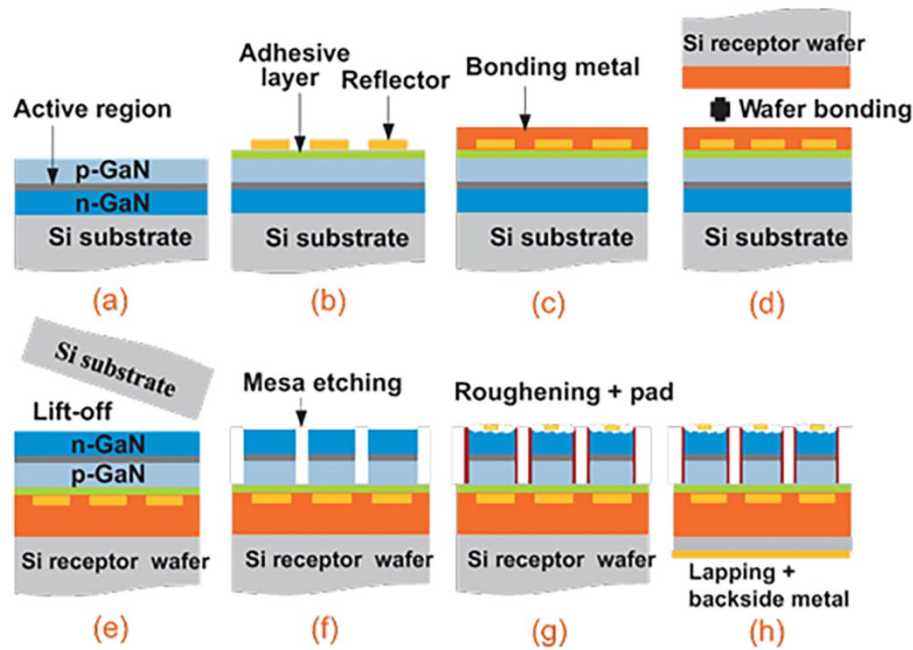
Figure 2.1 Fabrication process of VLED.

In step (1), the GaN-based blue vertical LED structure was fabricated on a 2-inch (0001) sapphire wafer using metal-organic vapor-phase epitaxy (MOVPE) or MOCVD method, and the cross-sectional schematic diagram is shown in Figure 2.2. In the growth process, trimethyl gallium (TMGa), trimethyl indium (TMIn), bis-cyclopentadienyl magnesium (Cp$_2$Mg), silane (SiH$_4$), and ammonia (NH$_3$) were used as sources for Ga, In, Mg, Si, and N, respectively. Prior to the growth of GaN epitaxial layers, the sapphire wafer was exposed to
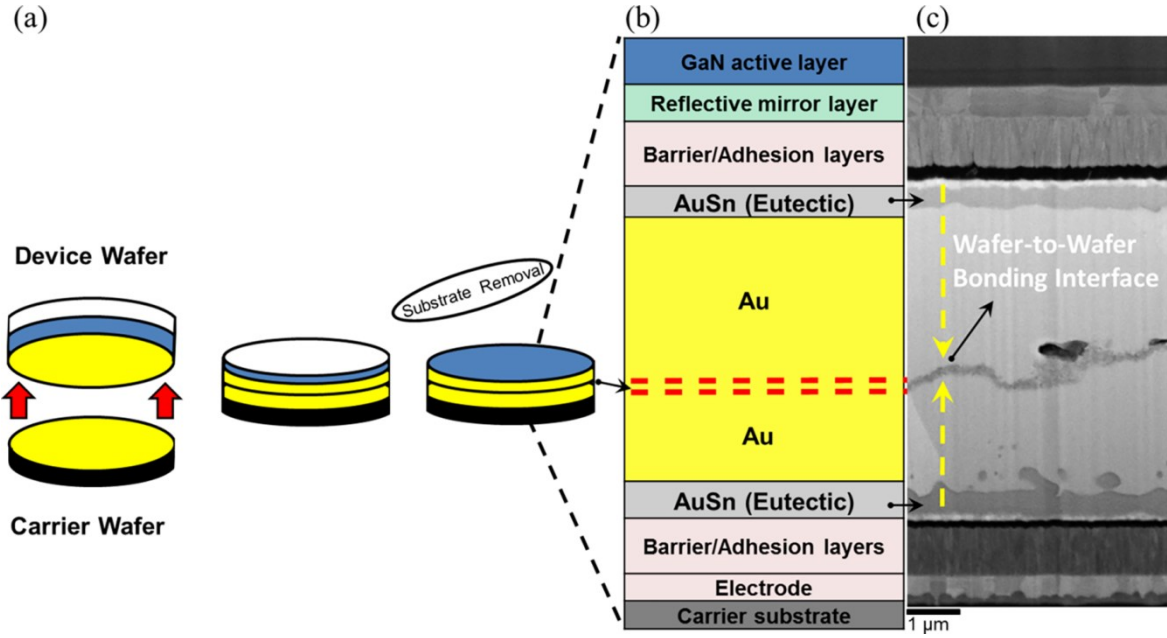
Figure 2.2 (a) Schematic diagram of fabrication steps, (b) and (c) Cross-sectional schematic and corresponding SEM image of VLED [57].

H_2 gas at 1100 °C to remove surface contamination. Firstly, the 25-nm-thick GaN nucleation layer was deposited at 550 °C, followed by the growth of a 2.5-µm-thick undoped GaN and a 3-µm-thick Si-doped n-type GaN layer. A 60-nm-thick superlattice (SL) containing alternating layers of InGaN/GaN (1nm/1nm), and four periods of InGaN QWs with 2.5-nm-thick wells each separated by 3.5-nm-thick GaN quantum barriers (QB) were used for blue light emission in the wavelength of ~455-470 nm. The growth temperature for four pairs of InGaN QWs and GaN QBs were kept between 750 and 850 °C, respectively. On the top of InGaN/GaN-based MQWs, a 20-nm-thick p-AlGaN electron blocking layer (EBL) was incorporated, and finally a deposition of 200-nm-thick Mg-doped p-type GaN. Prior to silver and other metals deposition, the sample is treated with HCL to remove surface native oxides formed during MOCVD process. The high-reflectance silver (Ag) as a reflective mirror and ohmic contact metal was deposited on p-type GaN by electron-beam evaporation followed by thermal annealing (300-600°C) in the oxygen ambient to produce a low resistance ohmic contact, i.e., a low-contact resistivity in the order of 10^{-5} Ω cm^2. Afterward, the deposition of the diffusion barrier, adhesive, and

bonding metal sublayers constitute layers of the device wafer. Later on, the device and carrier wafers were bonded together.

In step (2), W-W bonding for VLED structure, standard semiconductor wafers typically having a wafer size of 2-inch (50 mm) diameter with thickness ~275-430 μm were used for each CW and DW. Initially, CW consists of the conductive carrier (Si or Ge), p-side electrode (Au/Pt), barrier/adhesion metal layers (Ti/W/Pt/Ni) and bonding metal layers, i.e., Au layer (1.5 μm) formed on eutectic AuSn (300 nm) sublayer. On the other hand, DW is constituted by GaN-based epitaxial (active) layers on sapphire or Si substrate, reflective mirror layer (Ag or Al), barrier/adhesion metal layers (Ti/W/Pt/Ni) and bonding metal layers, i.e., Au layer (1.5 μm) formed on eutectic AuSn (200 nm) sublayer. The total thickness of bonding medium (Au-AuSn at CW and AuSn-Au at DW) was about 3.5-4 μm. Prior to wafer bonding, both wafers were aligned (mechanically) while loading into the bond chamber. In the next step, CW structure was bonded to the DW structure through a cycle of the thermocompression wafer bonding process, which involved three key parameters: 1) pressure, 2) heat (temperature), and 3) bonding duration. CW was pressed against DW with a pressure of approximately 0.3227 to 1.0 MPa and the pressed wafers were heated together at the temperature of 310-400 °C for the duration of 5-30 minutes, consequently, the Au-Au bond formation was achieved through the atomic contact, pressure and temperature impact [39]. The resulting wafer bonded structure was then flipped, i.e., DW (top) and CW (down), as shown in Figure 2.2 (a).

In step (3), the sapphire or Si substrate was removed from DW by laser lift-off or reactive ion etching techniques [98]. In the last step (4), the roughening for the textured surface at the top DW was performed by photoelectrochemical etching (or heated KOH solution) and finally SiO_2 as passivation layer was deposited by plasma-enhanced chemical vapor deposition (PECVD) to facilitate the escape of light from the VLED device. The final product of GaN-based VLED has an optical efficiency of 50-55% with blue light emission in the wavelength of ~455-470 nm and its cross-sectional layers is shown in Figure 2.2 (b) and (c).

2.2 VLED Specimen Preparation Methodologies for Microscopy Characterization

To obtain information from microscopy tools, three steps were involved: (1) specimen preparation, (2) data collection, and (3) data analysis [99]–[104]. The major challenge was in the first step, where it was necessary to prepare a good bulk and fine thin specimens from the LED die. Most of specimen preparation methods for semiconductor devices [105]–[107], which have been developed for TEM lamella were applied to our LED specimen. However, in wedge-shaped lamella additional steps were required in its final thinning for analyzing under SEM-TKD/electron backscatter diffraction (EBSD), TEM and AC-STEM techniques.

To understand LED stack layers, it is necessary to investigate the morphology and chemical composition of each layer first under the SEM and later by TEM microscopy tools. Thus,
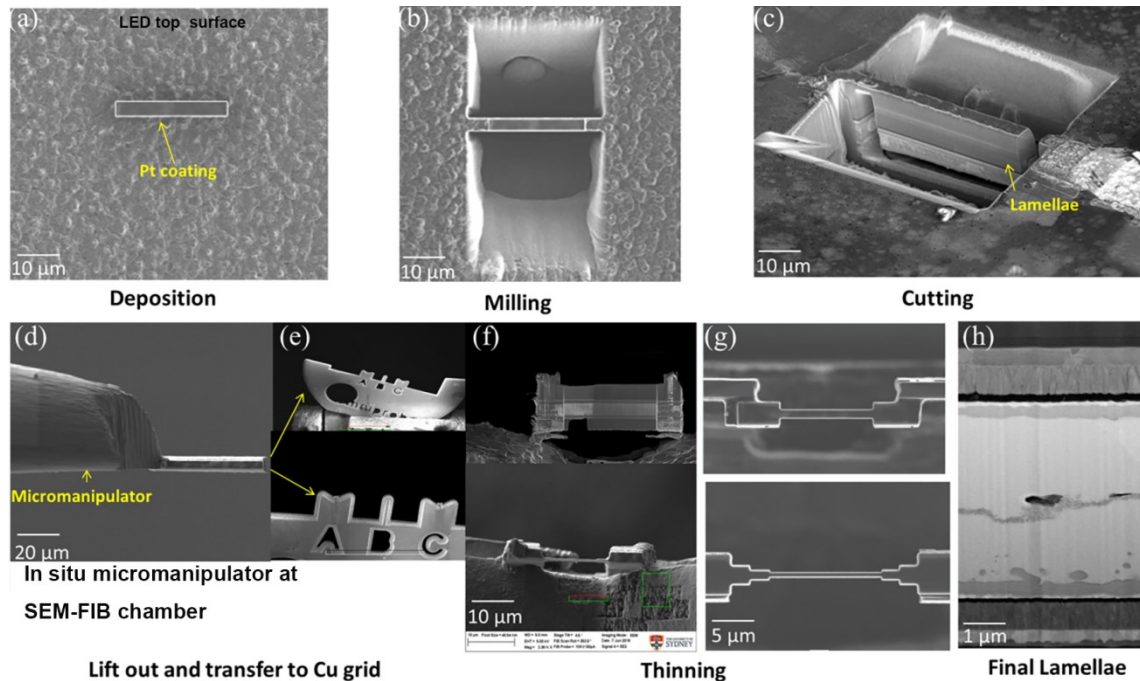
Figure 2.3 LED lamella preparation by FIB for SEM-TKD and TEM analyses. (a) Pt coating of the sample to avoid Ga damage, (b), (c) FIB lamella wedge definition by milling and cutting. (d)-(e) Lift-out of TEM lamella by in-situ micromanipulator and transfer to Cu/Mo grid. (g) final thin lamella (80-100 nm), (h) SEM micrograph showing cross-sectional schematic layers of VLED [57].

for that particular region of interest (ROI), a cross-sectional thin (80-100 nm) lamella specimen was prepared, and using in situ micromanipulator it was mounted on a Cu/Mo grid in accordance with the standard TEM foil preparation protocols based on focused ion beam (FIB) lift-out techniques [108], the summarized steps are shown in Figure 2.3. This approach normally works well for SEM and TEM analyses.
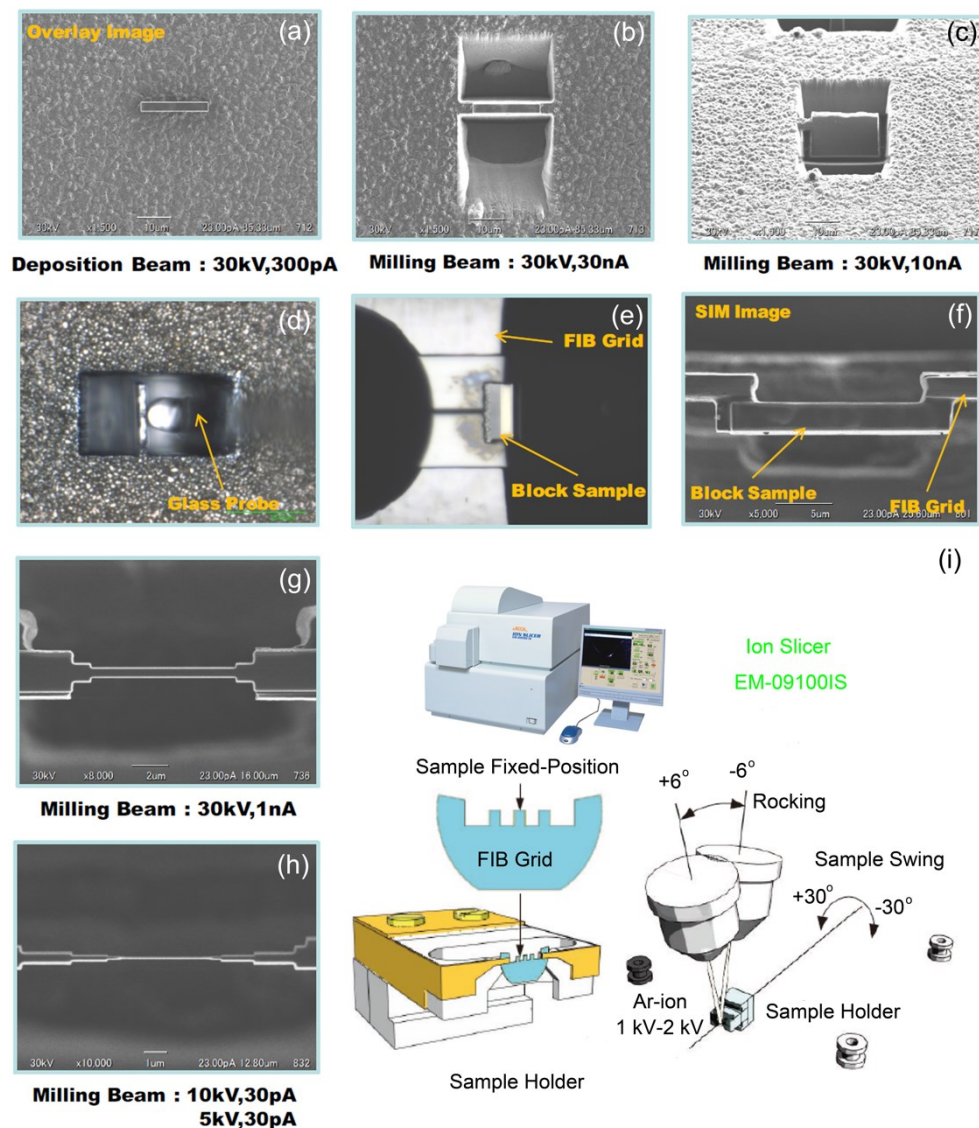
Figure 2.4 LED lamella preparation by FIB for HRTEM and AC-STEM analyses. (a) Pt coating of the sample to avoid Ga damage, (b), (c) FIB lamella wedge definition by milling and cutting. (d)-(f) Lift-out of TEM lamellae by ex-situ micromanipulator and transfer to Cu/Mo grid. (g), (h) Thinning of lamella to 100-120 nm at 10 and 5kV by Ga-ion milling, (i) Final lamella thinning to 60-80 nm by Ar-ion milling at 1kV-2kV.

61

In the second approach, we adopted additional steps to prepare very fine thin lamella of thickness 60-80 nm: (1) use of ex-situ glass micromanipulator, and (2) at final stage perform Ar-ion milling rather than Ga-ion milling at FIB, as shown in Figure 2.4. Both of these steps facilitated damage-free (Ga-ion) lamellae for HR-STEM and AC-STEM analyses in order to investigate sub-nm active layers (MQWs) and other semiconductor-metal interfaces. In fact, in the second approach, after FIB milling with a Ga-ion beam at 30 kV and 5 kV performed, subsequent Ar-ion milling by JEOL EM-09100IS Ion Slicer at 1-2 kV was performed for final thinning of the lamellae to 60-80 nm to minimize the FIB-induced damages or artefacts. Further, the lamella was examined under JEOL JEM-ARM300F and FEI Titan Themis Z300 AC-STEMs to obtain the crystallographic structure, high lateral spatial resolution for high-fidelity imaging and chemical compositional information from the key epitaxial layers of the GaN-based blue VLED.

2.3 Microscopy Techniques on the Vertical LED

To optimize the performance of solid-state lighting devices, nano or atomic-scale characterization is necessary to reveal their pertinent internal physics and chemistry. The reason for that is the continuing miniaturization as described by Moore's law [109], [110], where transistors shrink from microns to the nano-scale, as shown in Figure 2.5 (a) and (b).
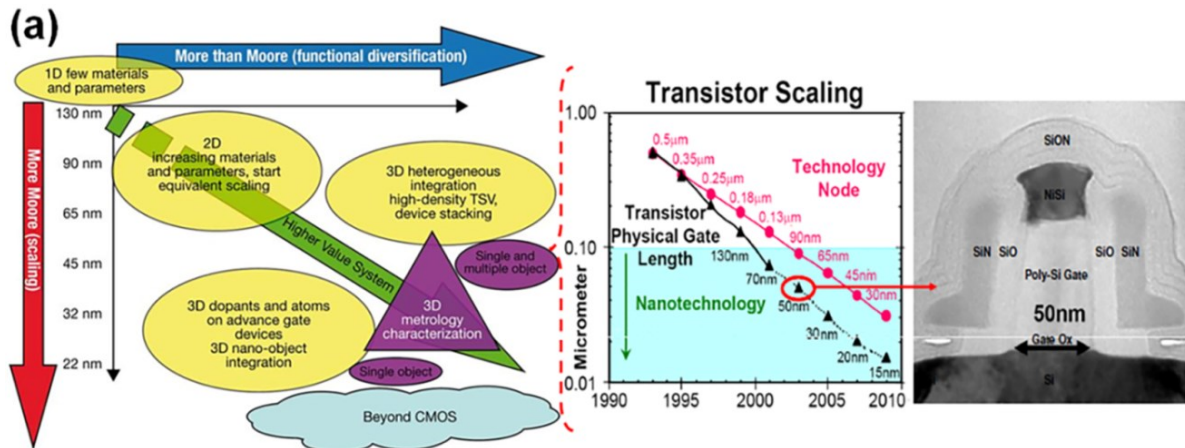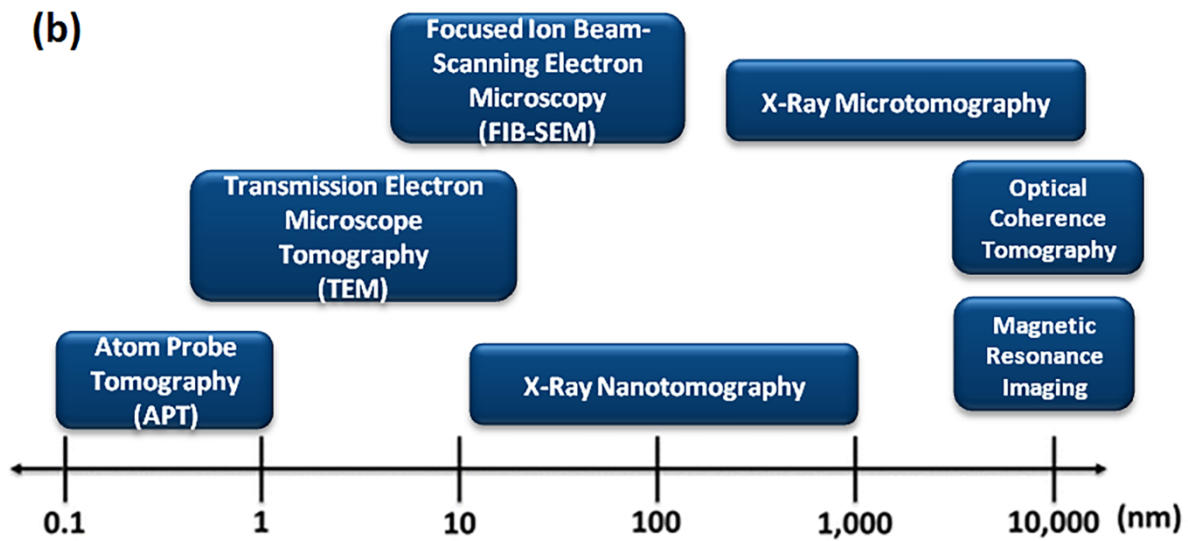
Figure 2.5 (a) Moore's law and transistor scaling [109], [110]. (b) Microscopy techniques capable of device scaling [31].
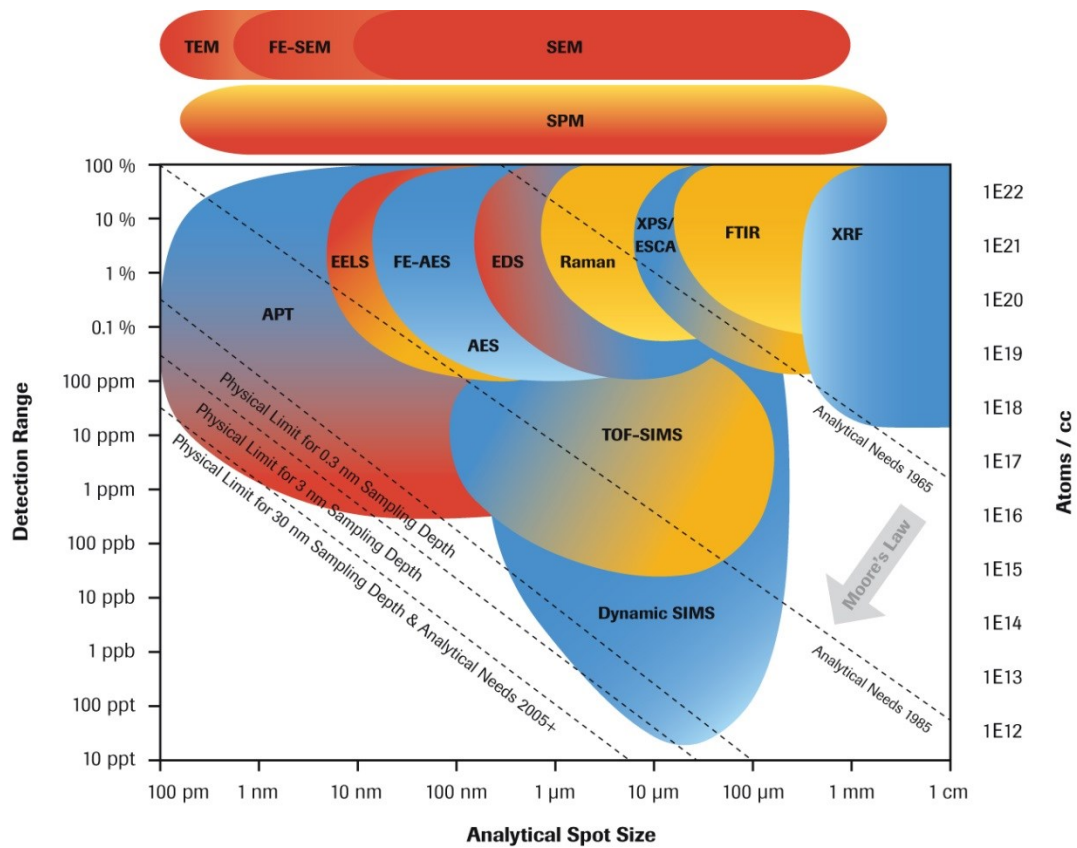
Figure 2.6 Comparison of microscopy techniques [117] (*Source: Prof. Simon Ringer*).

In these techniques, SEM is a microscope that works on the principle of particles with a negative charge (electrons) instead of light. The electrons are released from field emission source gun and accelerated in a high electrical field within vacuum column. These primary electrons are focused and deflected by electronic lenses to produce narrow scan beam (primary electron beam) that hits the specimen or object. As a result, secondary electrons (SE) are emitted, which are observed by relevant detectors. Depending on the primary electron beam (energy) intensity and sample depth (thickness), other electrons such as backscattered electrons (BSE) and characteristic X-rays can be generated, which can be used in EBSD and EDX analyses for further information, as illustrated in Figure 2.7.
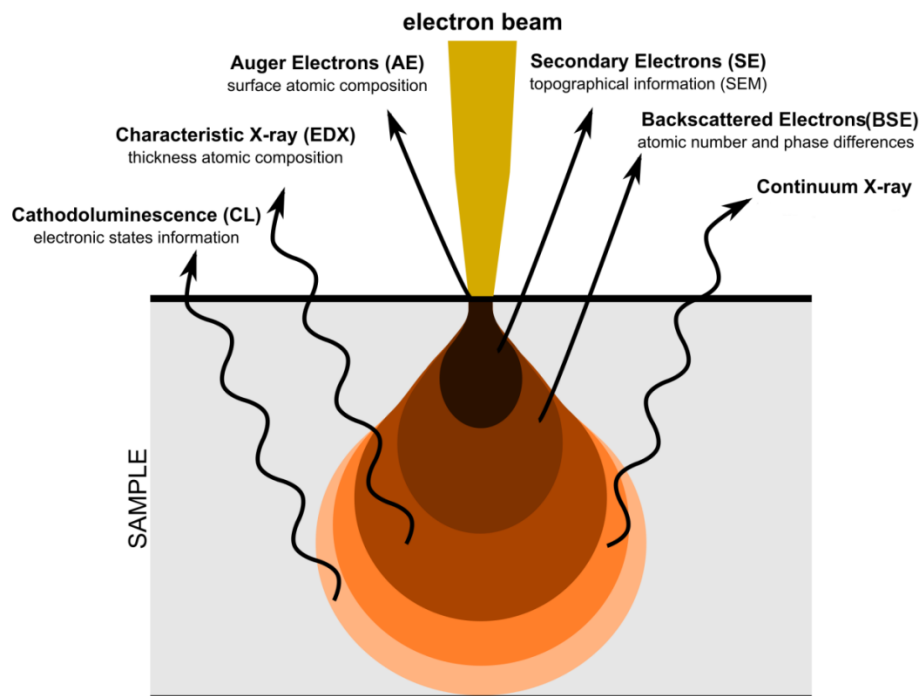
Figure 2.7 Principles of SEM operation.

Compared with conventional SEM, field-emission SEM (FE-SEM) produces more clearer, less electrostatically distorted images with high-spatial resolution down to ~1-1.5 nm (almost three to six times better), this is because the field-emission cathode in the electron gun produces narrower probing beams with high electron energy, resulting in improved spatial resolution, less charging and minimized damage to the sample [118].

In case of our VLED sample, FE-SEM imaging provided topographical information (structure uniformity determination, small contamination, features geometry), cross-sectional analyses of LED stack layers, as shown in Figure 2.8.
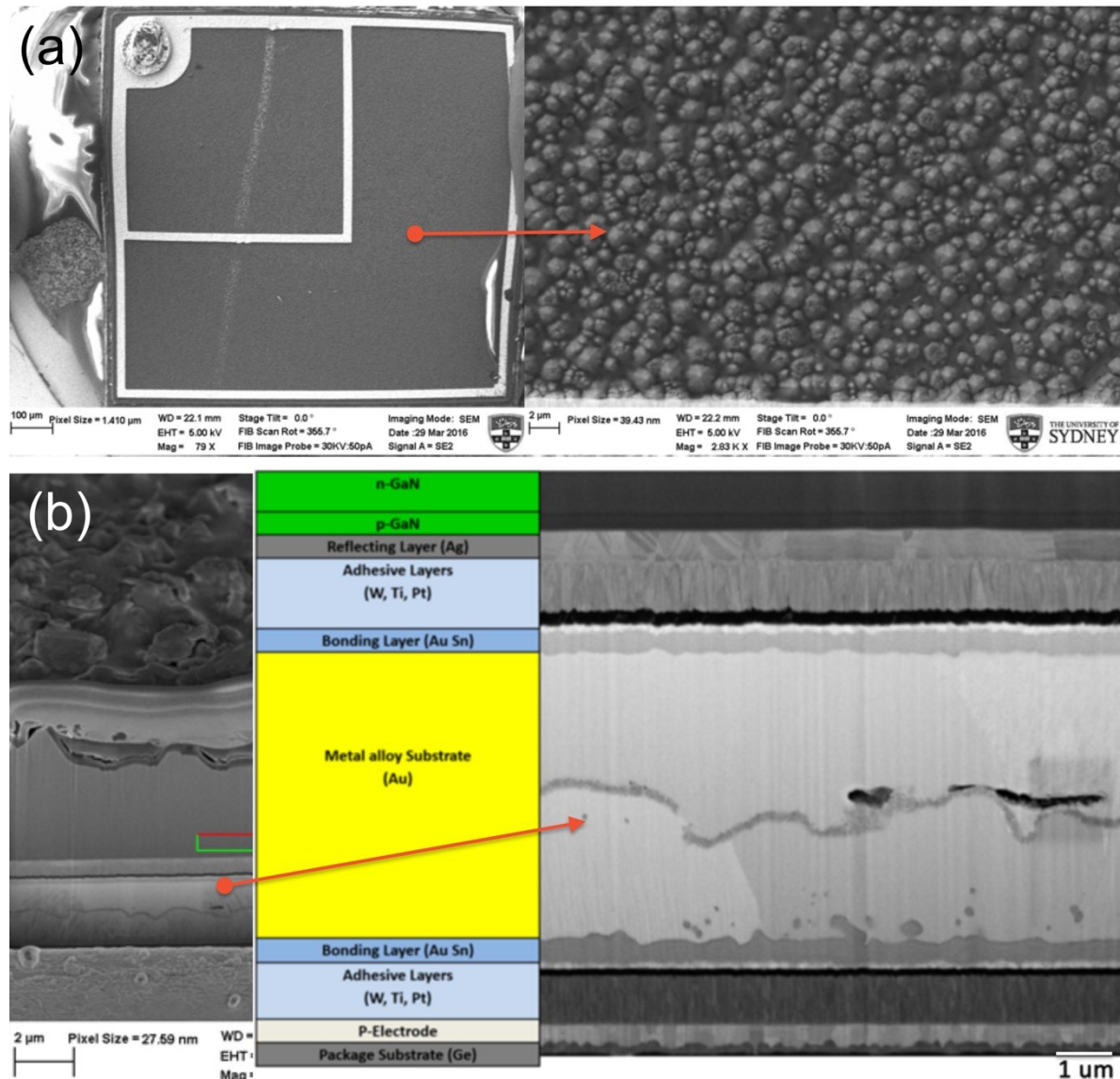
Figure 2.8 SEM micrographs (a) Top bulk textured surface. (b) Cross-sectional layers of VLED [52].

Also, SEM-based EDX is a powerful and less-destructive analytical technique for identifying unknown elements, elemental composition measurements and performed well in bulk (thick) areas of the LED sample. In these results, SEM-EDX allowed us for rapid identification and characterization of surface imperfections, and lateral compositional

variations (Figure 2.9). Thus, SEM-EDX as an analytical technique was used to determine the chemical composition (quantitative and qualitative) of the LED (more description about these SEM and EDX results are in subsequent chapters of this dissertation).
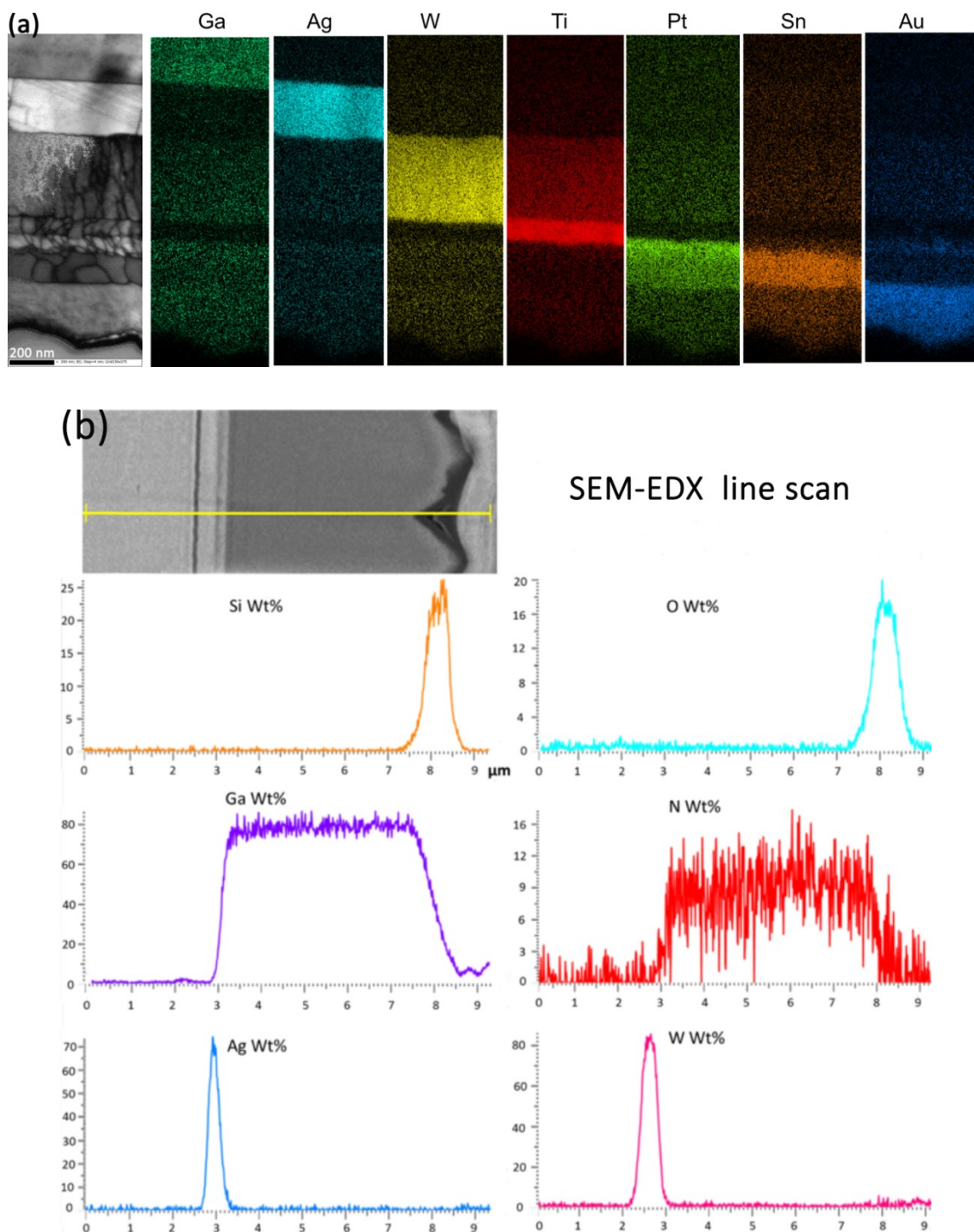
Figure 2.9 SEM-EDX analysis on the cross-sectional layers of the VLED [52].

Furthermore, in SEM tool, new techniques of TKD and EBSD can be used. The working principle and experimental setup are illustrated in Figure 2.10. The powerful SEM-based TKD with a spatial resolution of 2-15 nm provides key nanostructural information, such as orientation mapping (OM), grain size analysis, poles figures (PFs, texture), and Kikuchi diffraction patterns [118]. Both TKD and EBSD works on the same principle, however, SEM-TKD cannot be performed on a bulk or thick specimen, as it requires electron transparent thin samples (by electropolishing or using a focused ion beam SEM). Moreover, SEM-TKD or transmission EBSD (t-EBSD) has better spatial resolution (2-15 nm) compared with conventional EBSD technique (30-100 nm) [52], [119]. SEM-TKD/EBSD also less destructive technique compared to TEM [120].
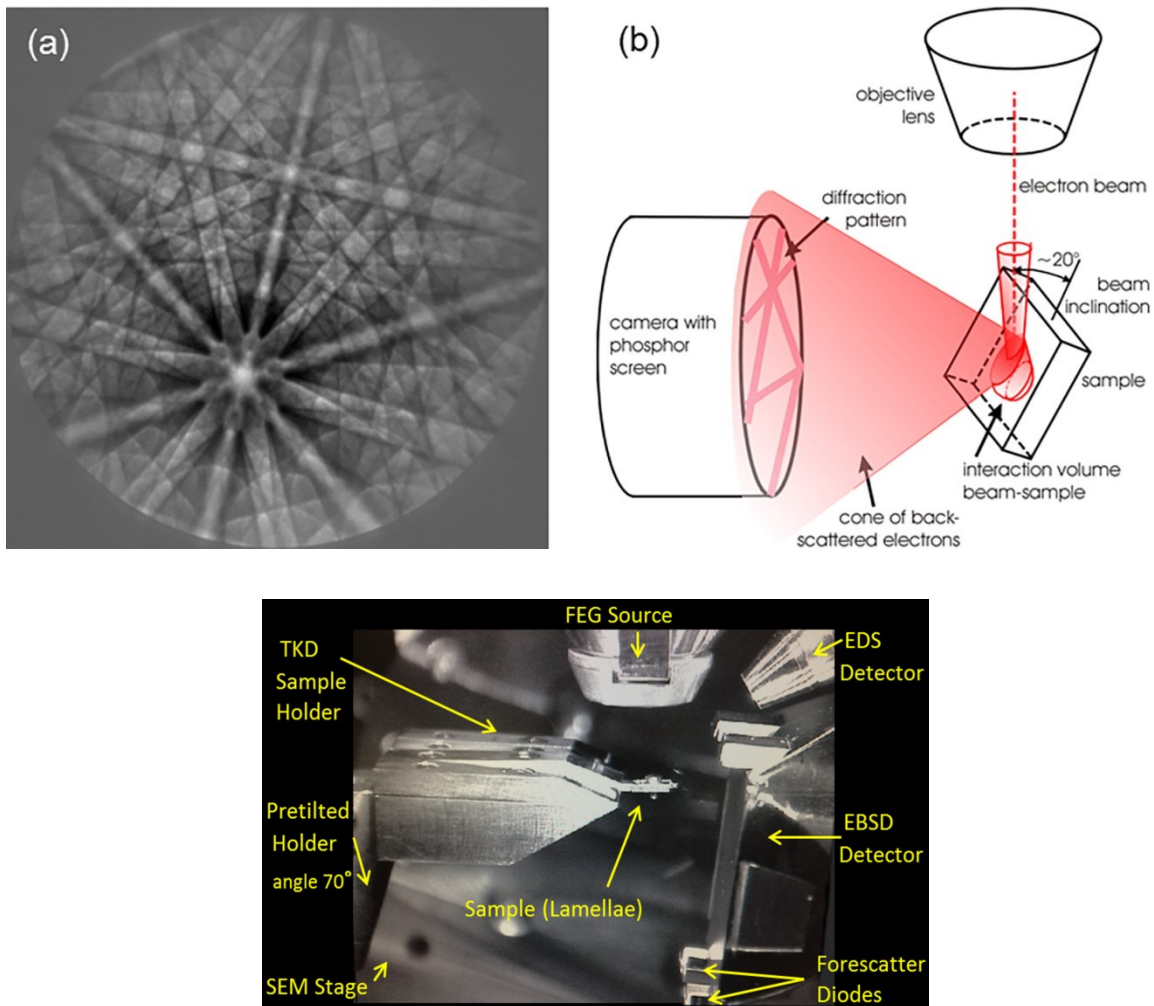
Figure 2.10 Principle and experimental setup of SEM-EBSD and TKD operation [52] (*top image source: A/Prof. Rongkun Zheng*).

67

For instance, in case of our VLED sample, PF (texture) and grain morphology of the Ag reflective layer were analyzed by SEM-TKD (cross-sectional wise) and EBSD technique (top bulk surface). Few exemplary results from our VLED are depicted in below Figure 2.11 and Figure 2.12 (more description of them are in subsequent chapters of this dissertation).
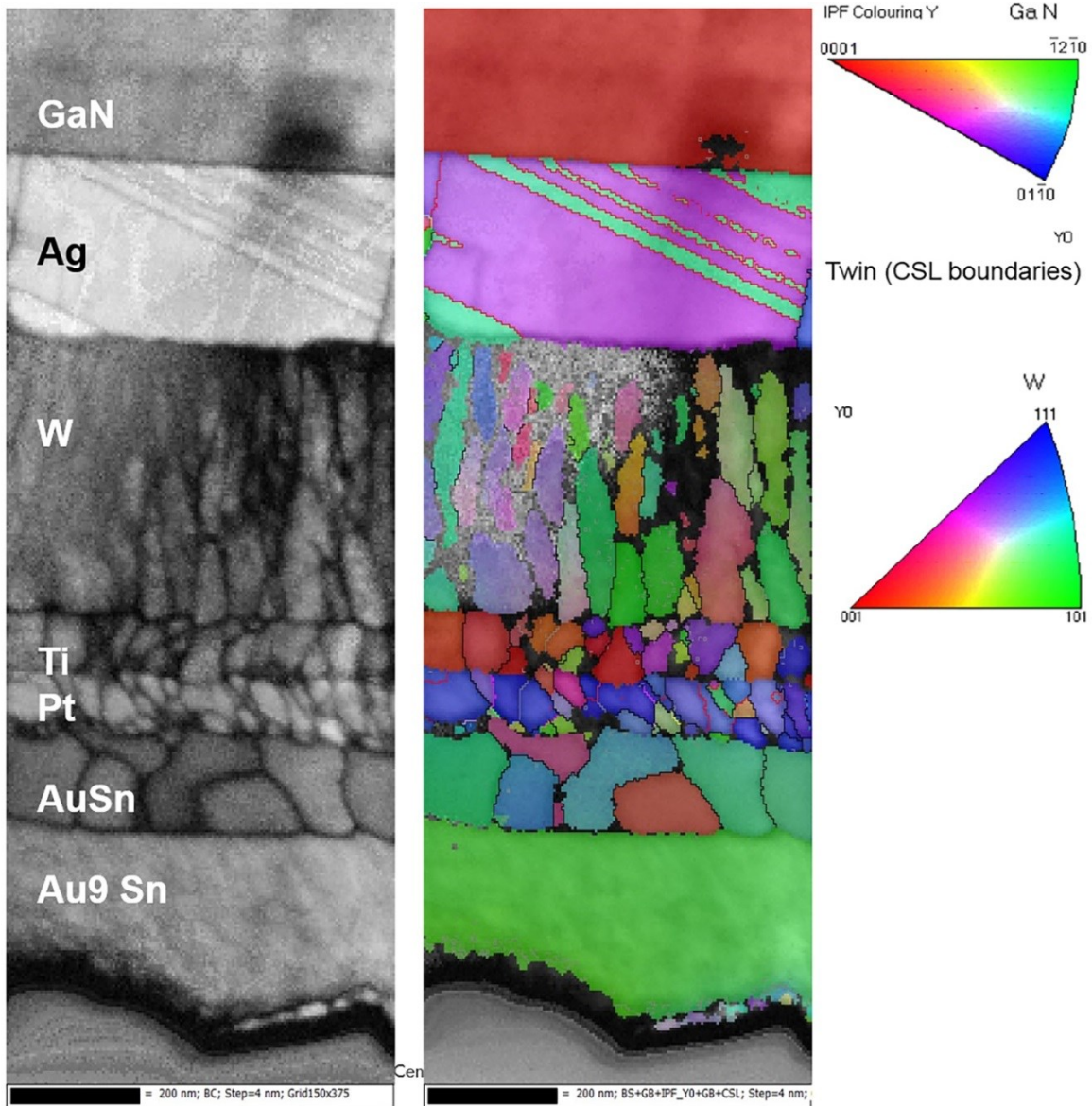
Figure 2.11 SEM-TKD analysis on the cross-sectional layers of the VLED [52].

For TKD analysis, FIB technique was used to prepare fine thin lamellae (60-100 nm) on the VLED, as stated in section 2.2 of this dissertation.

= 2 μm; BC+GB+IPF; Step=0.025 μm; Grid465x689

= 2 μm; BC+CSL+Twin (Σ3) <111> 60° GB; Step=0.025 μm; Grid465x689

= 2 μm; CSL+TC; Step=0.025 μm; Grid465x689

IPF colouring Z0

{100} {110} {111}

Special boundaries (SB), texture and IPF maps from silver (mirror) layer in GaN-based VLED
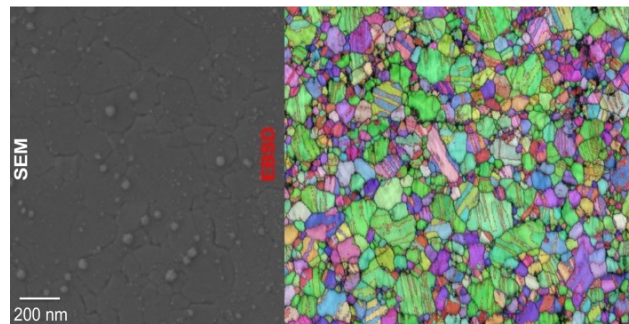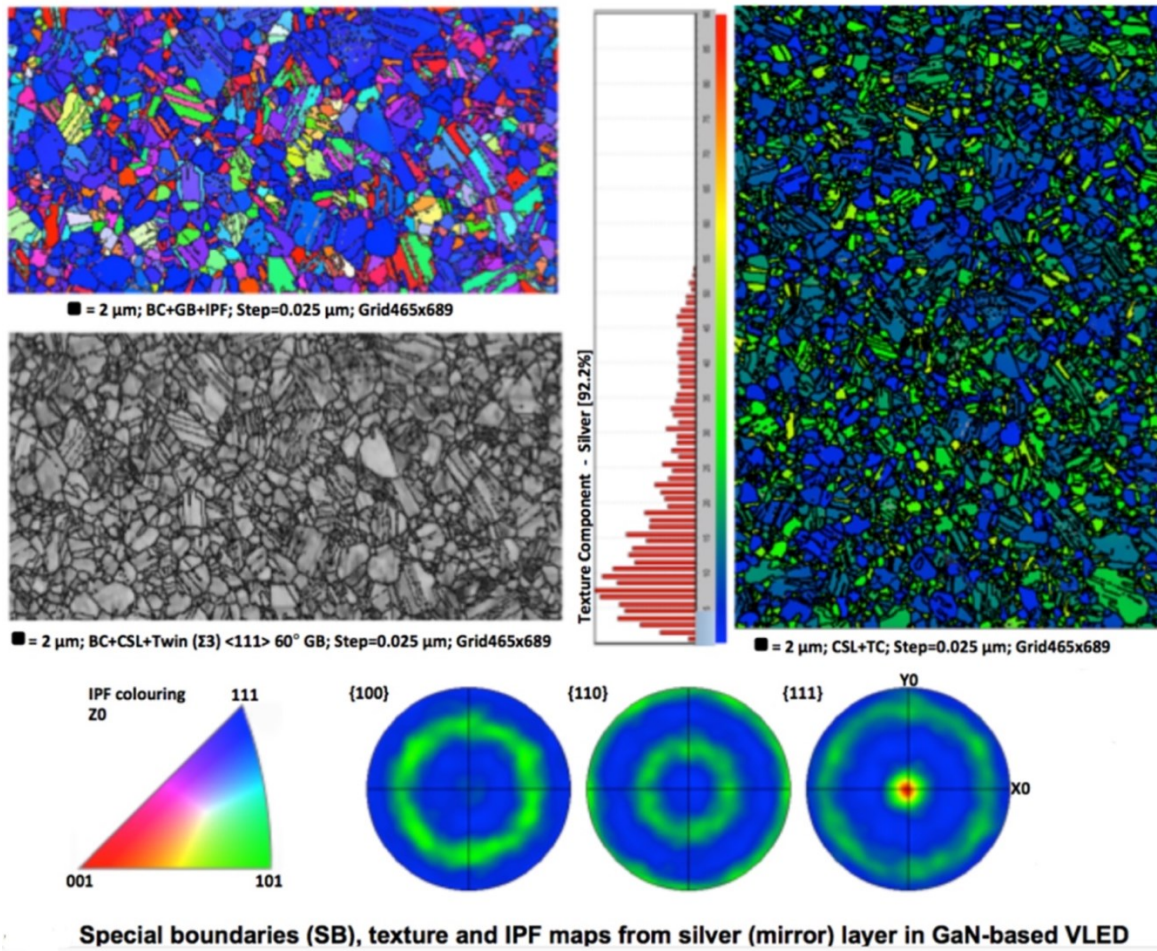
Figure 2.12 SEM-EBSD analysis on the top bulk surface of the reflection layer in the VLED [52].

Although SEM-based EDX and TKD/EBSD are powerful and less destructive techniques compared to TEM [120] but suffers from limitations, such as no absolute chemical state information can be verified and limited in obtaining discrete diffraction patterns or grains (texture) for a very thin film layers (below <10 nm). However, these limitations can be mitigated in correlation with EDX in TEM technique.

69

In TEM or electron microscopy technique, the beam of electrons is transmitted through a transparent thin sample to form an image (like in case of SEM-TKD). The working principle of TEM is illustrated in Figure 2.13. However, TEM with high beam intensity has a unique capability by providing crystallographic information at the high lateral spatial resolution for high-fidelity imaging along with compositional information from the EELS and EDX [121]–[123]. Also, high-resolution (HR)-STEM showed better spatial resolution (atomic-planes) compared to APT [31], [124]. Furthermore, these complementary techniques (TEM and APT) are combined to correlate the analytical sensitivity and three-dimensionality of APT with TEM spatial fidelity [125], [126].
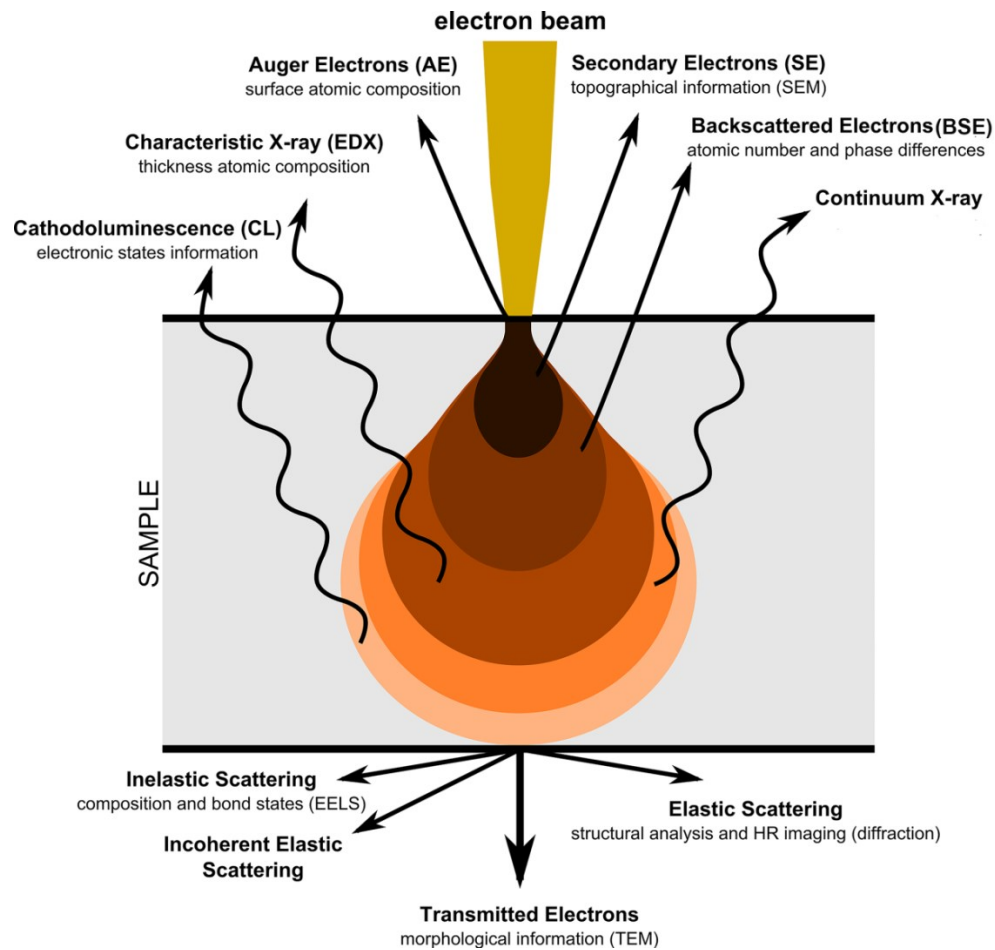
Figure 2.13 Principles of TEM operation.

In TEM, two main types of imaging exit: (1) phase contrast imaging in conventional TEM (CTEM) or HR-TEM, and (2) Z-contrast imaging in the STEM (Figure 2.14).
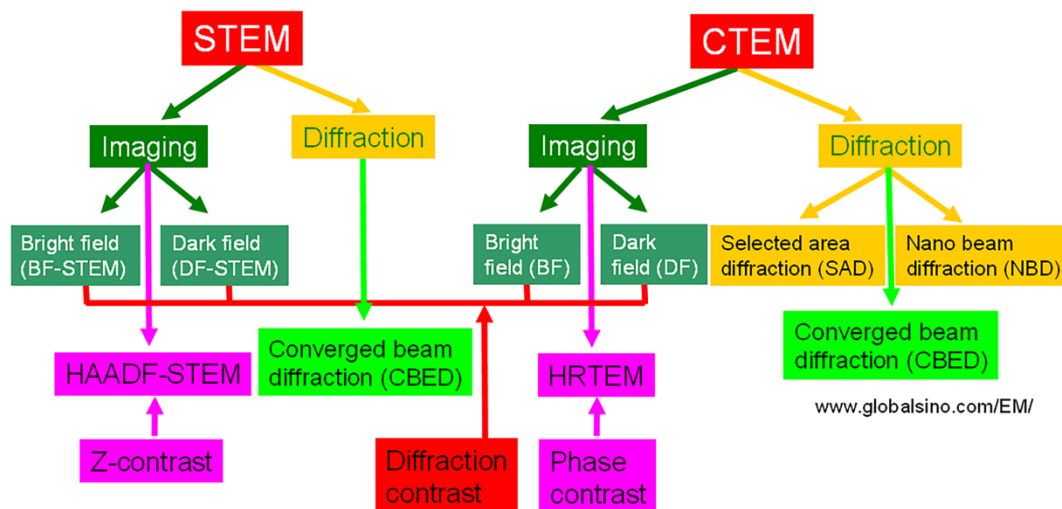
Figure 2.14 Types of imaging in TEM technique.

For the VLED case, robust compositional analysis across its multilayered structure through SEM-EDX was very beneficial to locate the elemental inter-diffusion on a micron-scale for a broad field of view. However, the spatial resolution of SEM-based EDX was not high enough to investigate the sub-nm scale MQWs layers and elemental inter-diffusion or interfacial diffusion (metal-semiconductor). Therefore, high-resolution AC-STEM was used to measure the accurate compositions on the nano or atomic-scale.

The development of AC-STEM by adding Cs correctors provides new dimensions to state-of-the-art electron microscopy, enabling to perform a structural analysis at the sub-angstrom resolution [127]–[129], as illustrated in Figure 2.15. The evolution of aberration correctors has improved the sensitivity and spatial resolution of both phase contrast imaging in HR-TEM and Z-contrast imaging in STEM [130], [131]. This peculiar capability of AC-STEM has opened a new realm to understand materials properties by correlating their atomic-scale changes in composition with the structure of interfaces and defects [132]. For instance, by HAADF STEM method, a resolution of 45-pm separated Si-Si dumbbells imaging were performed [133]. Other applications of AC-STEM are summarized in Figure 2.16.

71
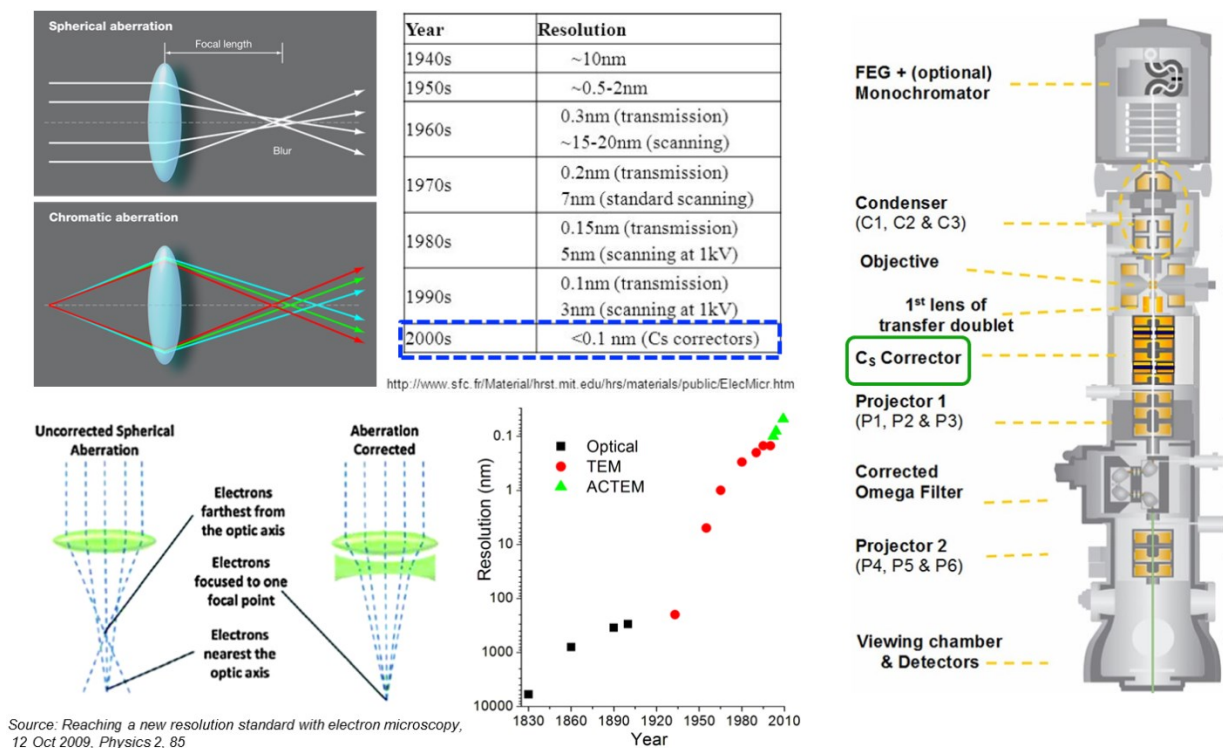
Figure 2.15 Principles of AC-STEM (*Source: Mansoor Khan @MRS conference 2017, Boston, USA*).

Figure 2.16 Applications of AC-STEM (*Source: Mansoor Khan @MRS conference 2017, Boston, USA*).
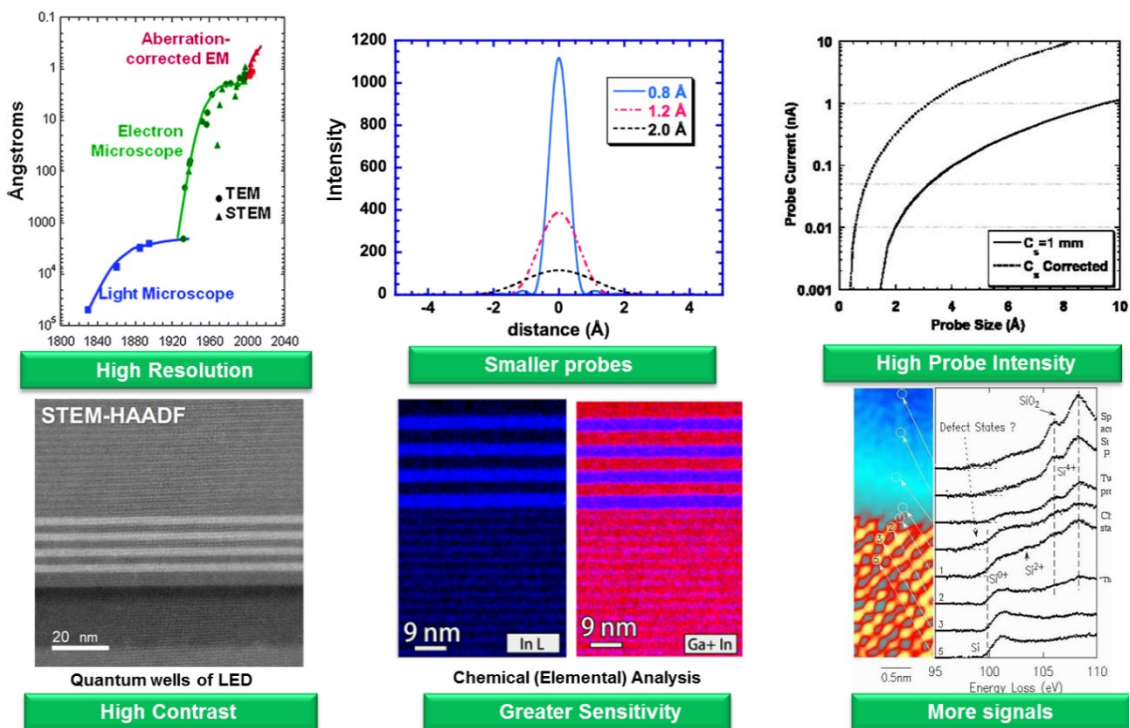
In case of our VLED sample, high-resolution AC-STEM is able to locate delicate nanostructures (MQWs) and absolute chemical state information can be verified as shown in Figure 2.16 (above) and Figure 2.17 (below) showing MQWs and their chemical composition profile.

Furthermore, using HAADF STEM method, a resolution of 75-pm separated Ga-Ga dumbbells imaging was performed. Also, for the light elements (N), the sub-angstrom distance between Ga-N atomic columns in a GaN sample was resolved by an annular bright field (ABF) imaging technique, as shown below in Figure 2.17.
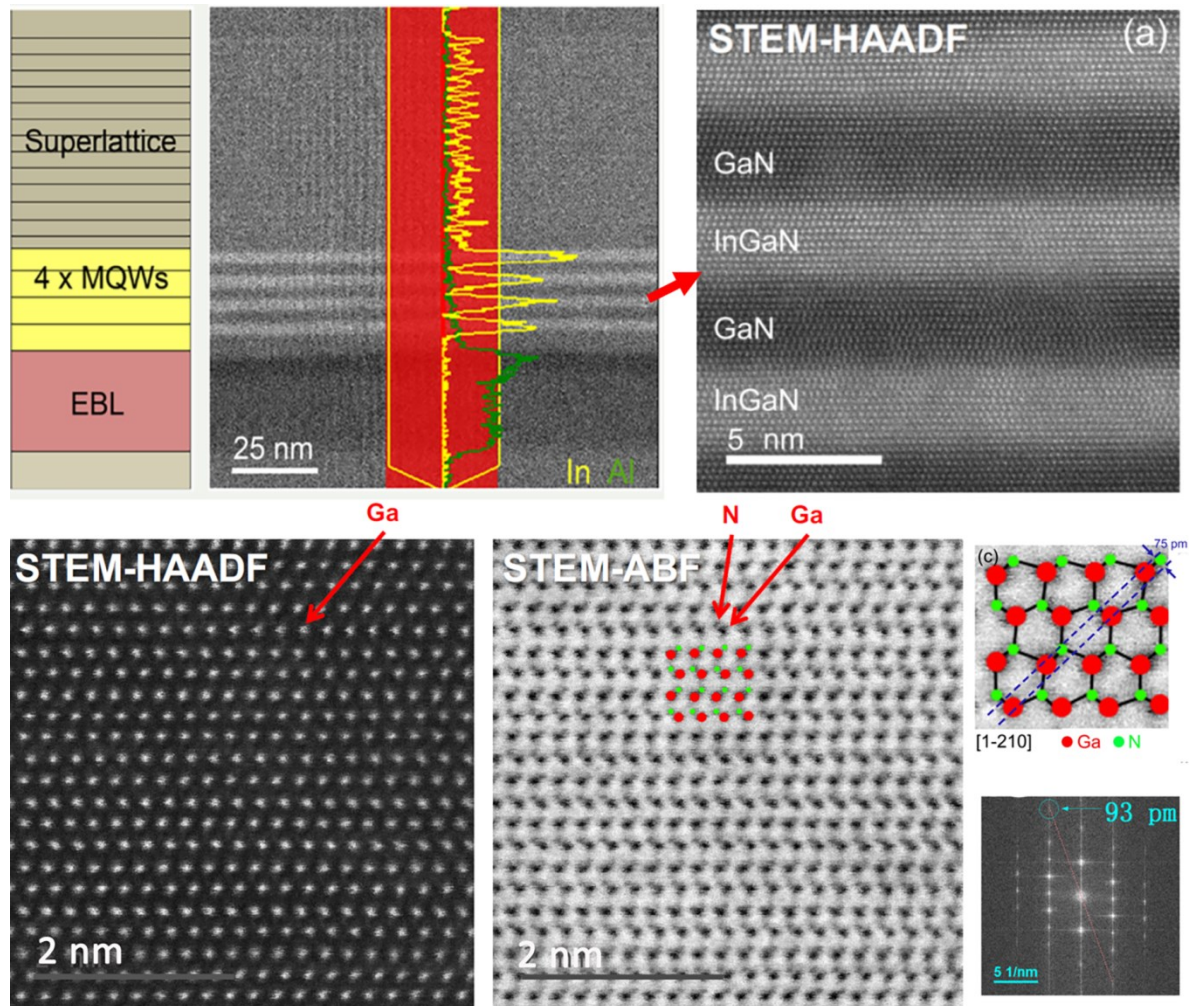
Figure 2.17 TEM analysis on the VLED.

In AFM technique, a cantilever with a very sharp tip (probe) is used to scan over a sample surface, also called SPM, as depicted in Figure 2.18. APM can perform different functions, e.g., force measurements and manipulations but its specific imaging capability allows it to form an image of the 3D shape (topography) of a sample surface on the order of fractions of a nanometer. AFM vertical resolution can be up to 0.1 nm but the lateral resolution is low (~30 nm) due to the convolution.
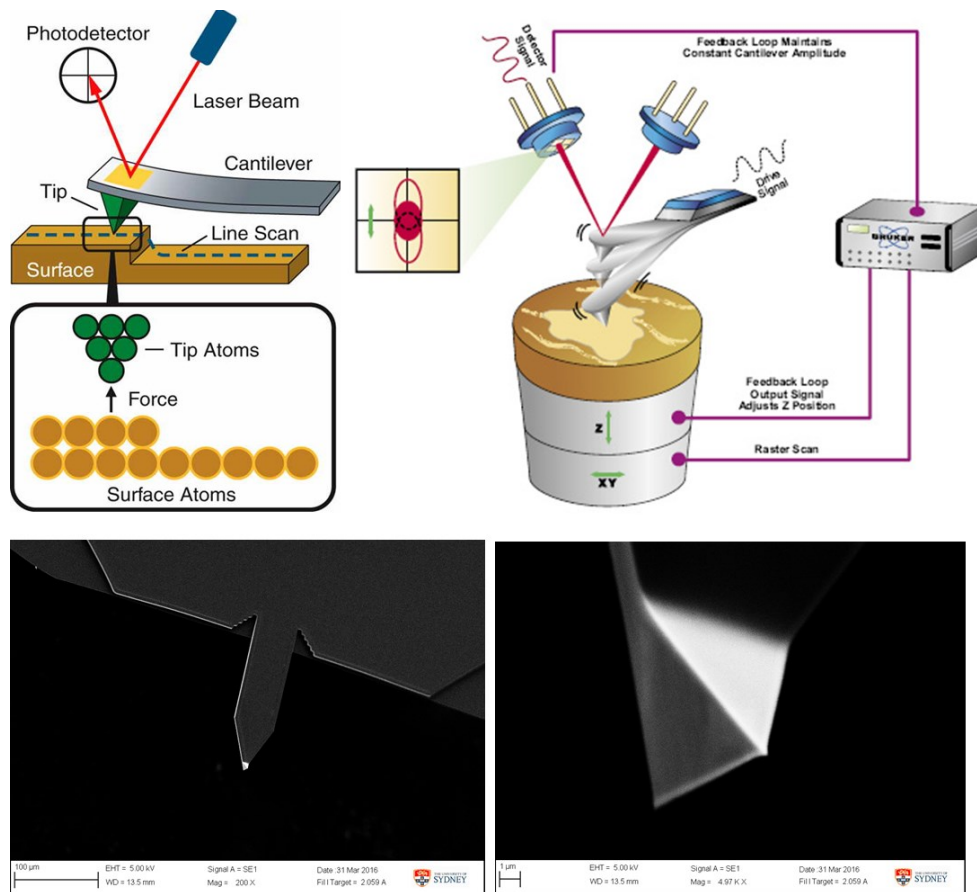
Figure 2.18 Principles of AFM operation.

In case of our VLED, we used tapping mode rather contact mode to avoid damage to surface of the LED sample. Tapping mode is a primary AFM mode and provides surface morphology and topography in the form of surface roughness. The probe has cantilever with a sharp tip, where a drive signal is applied it, the tapping piezo mechanically oscillates the probe at or near its resonance frequency (the fundamental resonance) and detector signal is cantilever oscillation amplitude or phase. In feedback mode, output signal usually

adjusts the Z position of the scanner to maintain an (rms) amplitude set point [134] (Figure 2.18). Taping mode enables numerous secondary modes, including phase imaging and surface topographical imaging in 2D and 3D form, as shown below in Figure 2.19.
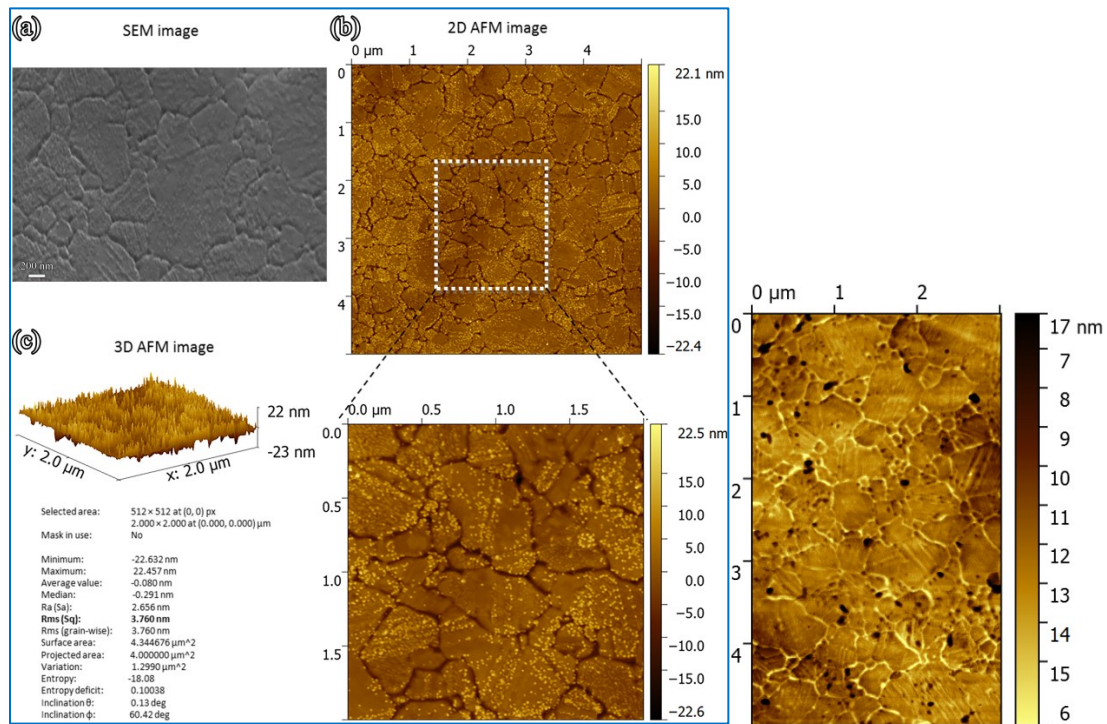
Figure 2.19 AFM analysis on the silver reflection layer of the VLED [52].
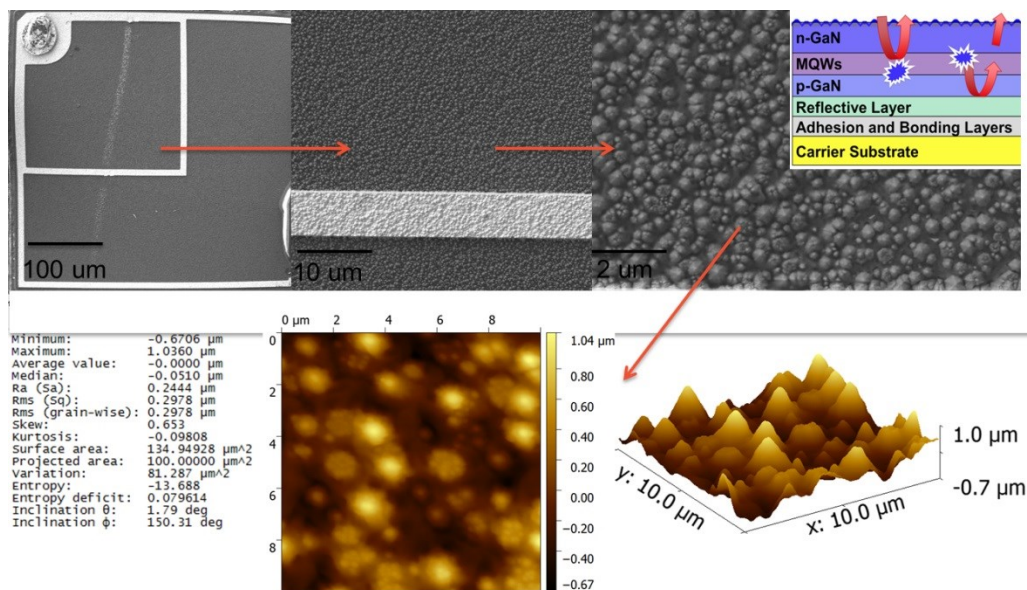
Figure 2.20 AFM analysis on the top textured surface of the VLED.

75

2.4 Other Non-destructive Characterization Techniques on the Vertical LED

Raman spectroscopy is a non-destructive surface analysis technique, which works on the principle of light (photon) scattering. When a light (usually monochromatic laser beam) interacts with the molecule (molecular vibrations) or crystal or phonons of the system, resulting excitation put molecule or phonons into a virtual energy state for a short time before the photon is emitted, as illustrated in Figure 2.21. Raman scattering is different from Rayleigh scattering because later is an example of elastic scattering, where the frequency (wavelength) of the Rayleigh scattered light is the same as that of the incoming electromagnetic radiation. Contrary to that, in Raman scattering the resulting inelastically scattered photon, which is either emitted/scattered can be of either lower stokes or higher (anti-Stokes) energy than the incoming photon (Figure 2.21).
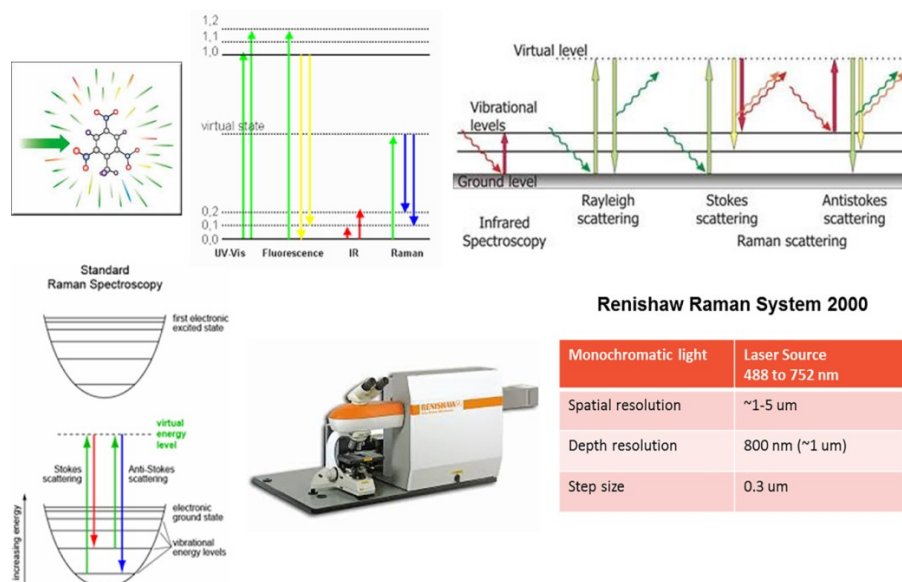
Figure 2.21 Principles of Raman spectroscopy.

Raman spectroscopy is useful to observe vibrational, rotational, and other low-frequency modes in a certain crystal system. In case of our GaN-based VLED, the Raman shift at approximately $565–568 \text{ cm}^{-1}$ corresponds to the E2 phonon mode, which is sensitive to the amount of stress inside the GaN layer. In GaN films, the E_2 high ($E_2{}^{\text{H}}$) and A$_1$ longitudinal

optical (LO) phonon modes are widely used to evaluate the stress-related property of III-nitrides [135], [136], as shown in Figure 2.22 (more detail about results are in Chapter 6).
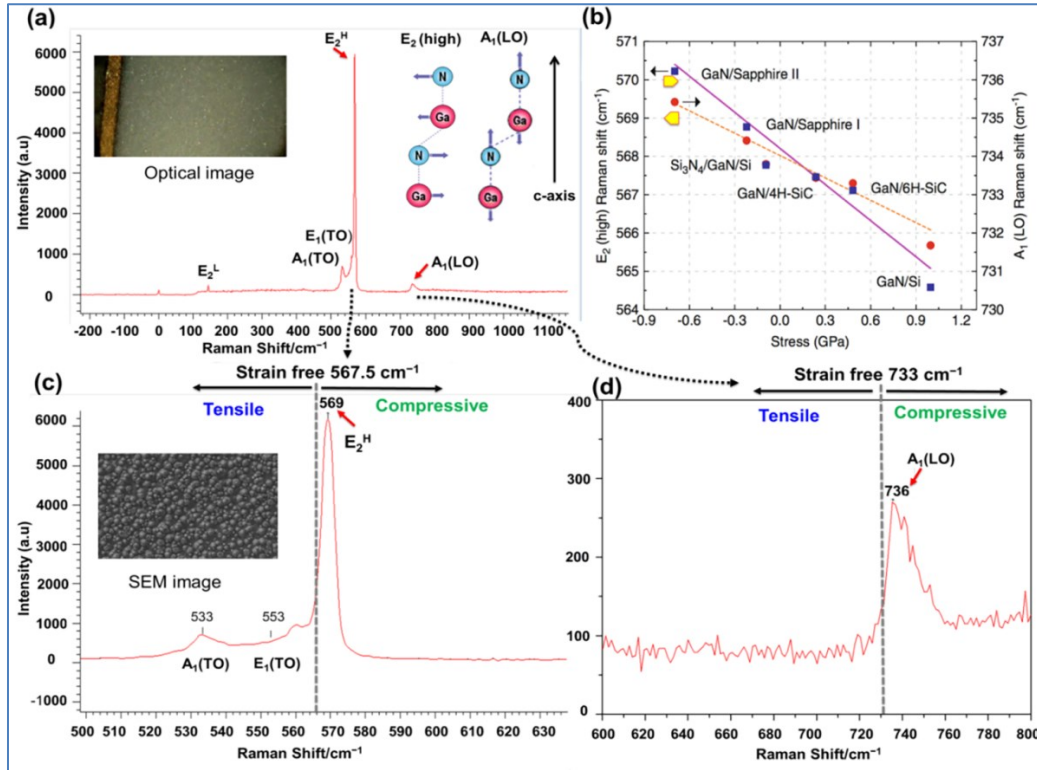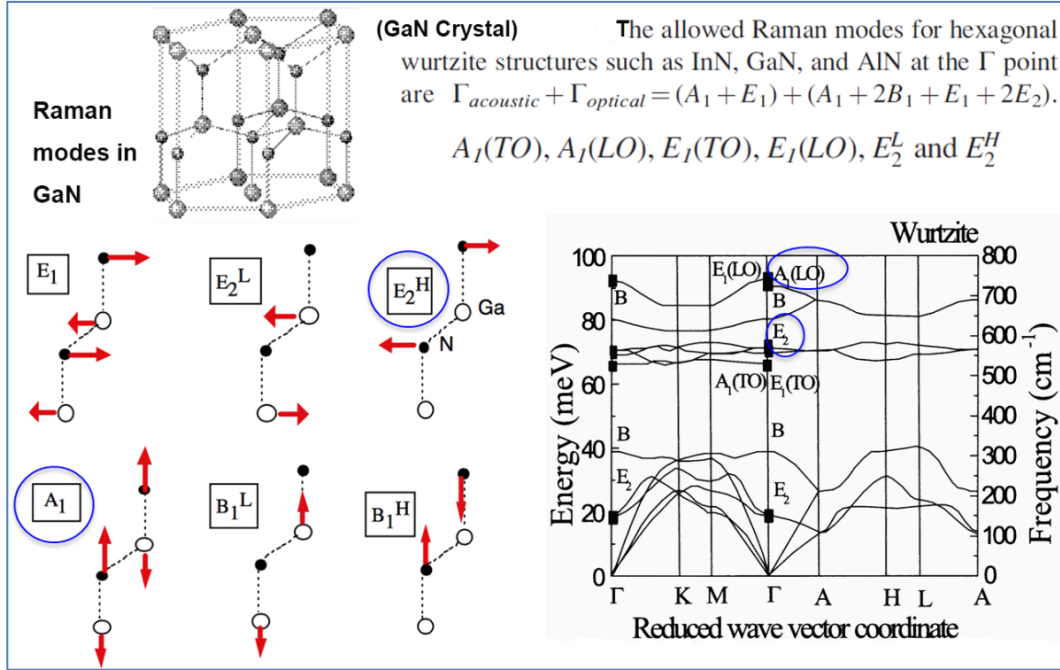
Figure 2.22 Raman modes in GaN system. (a)-(d) Raman analysis on the textured n-GaN surface of VLED.

XRD is another non-destructive technique (NDT) based on constructive interference of monochromatic X-rays and a crystalline sample, in which the crystalline atoms cause a beam of incident X-rays to diffract into many specific directions. A cathode ray tube is a source to generate X-rays, they get filtered to produce monochromatic radiation, collimated to concentrate, and directed towards the target sample, as shown in Figure 2.23. XRD is a robust analytical technique primarily used for phase identification of crystalline materials and analysis of unit cell dimensions (lattice constant) in terms of stress-strain analysis.
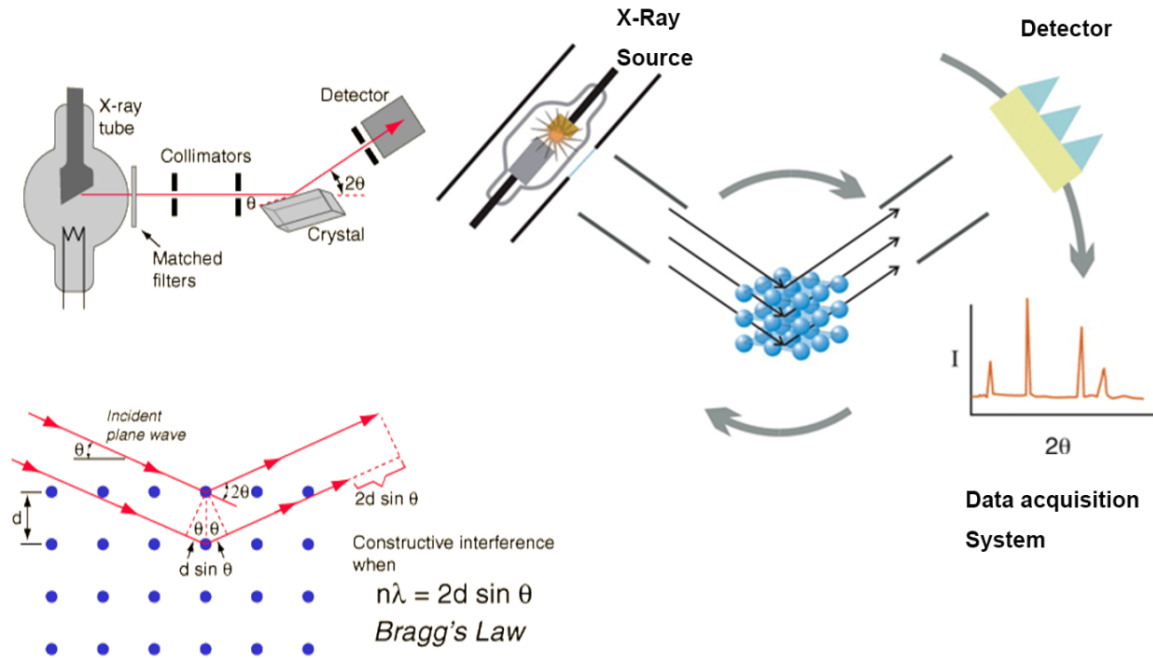
Figure 2.23 Principles of XRD techniques

We used XRD technique on the top textured GaN surface of VLED to analyze the stress-strain analysis on the GaN material system to validate the Raman spectroscopy results. By scanning the LED sample through a range of 2θ angles, all possible diffraction directions of the lattice can be attained due to the random orientation of the textured surface of VLED. Conversion of the diffraction peaks to d-spacings (obtained by solution of the Bragg equation for the appropriate value of λ, i.e., $n\lambda = 2d\ sin\theta$) allows identification of the material in VLED because each material has a set of unique d-spacings, for instance, in Figure 2.24 significant X-ray reflection by the hexagonal GaN (0002) occurred at ~35°, while the reference stress-free GaN locates such reflections at 34.6°.

78
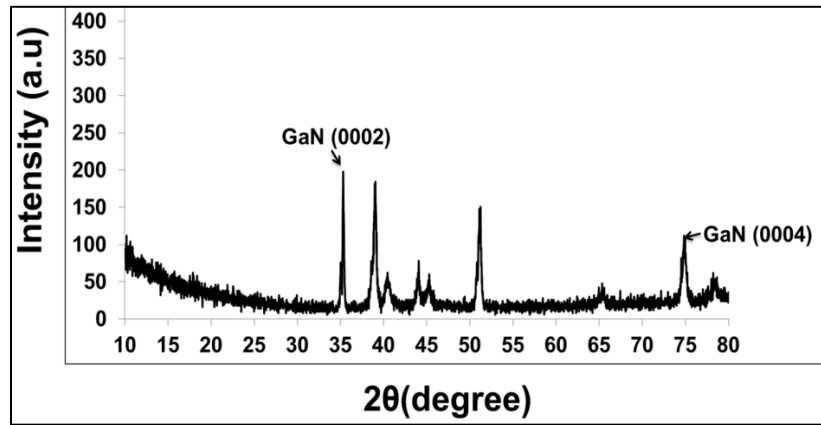
Figure 2.24 XRD analysis on the VLED.

PL spectroscopy like Raman spectroscopy is also non-contact, nondestructive techniques but former is many times stronger than later [137]. In PL, a light is directed onto a sample, where it is absorbed and photo-excitation occurs. The photo-excitation causes the electrons to be excited to a higher energy level, but to achieve relaxation stage, they release energy in form of photons on returning to back to a lower energy level. The emission process of photons (light) or luminescence is PL, as shown in Figure 2.25 (a).

PL applications include assessing impurity levels, emission property (Figure 2.25 (b)), material quality by inspecting variations of stress level in the GaN system since the energy band gap is strongly sensitive to the state of stress [138], [139]. Mostly, PL and XRD measurements were taken to substantiate Raman spectroscopy results.
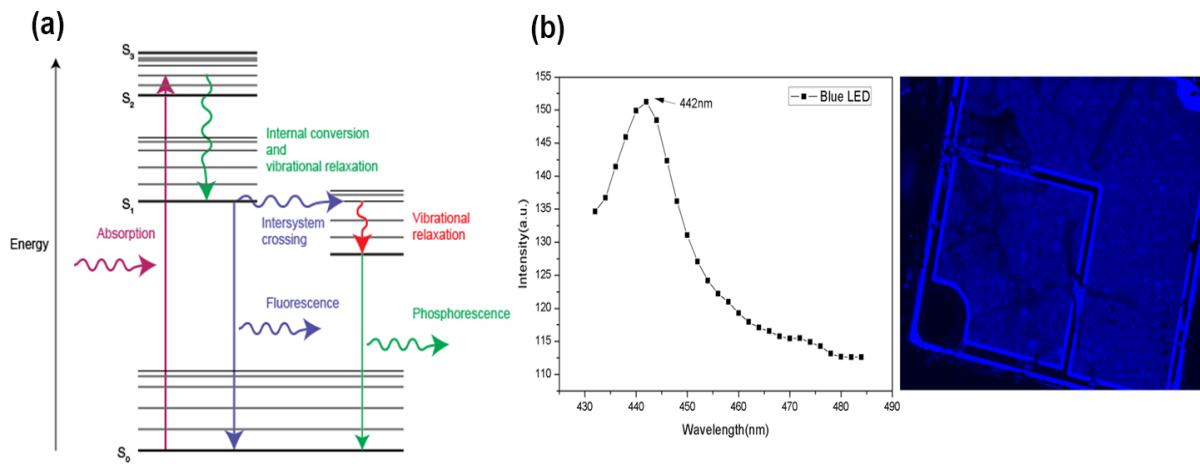
Figure 2.25 (a) Principles of the PL. (b) PL analysis on the VLED (*Source: Mansoor Khan@ ICONN 2018*).

79

2.5 Summary and Conclusions

Below is the summary of microscopy techniques employed on the VLED device.
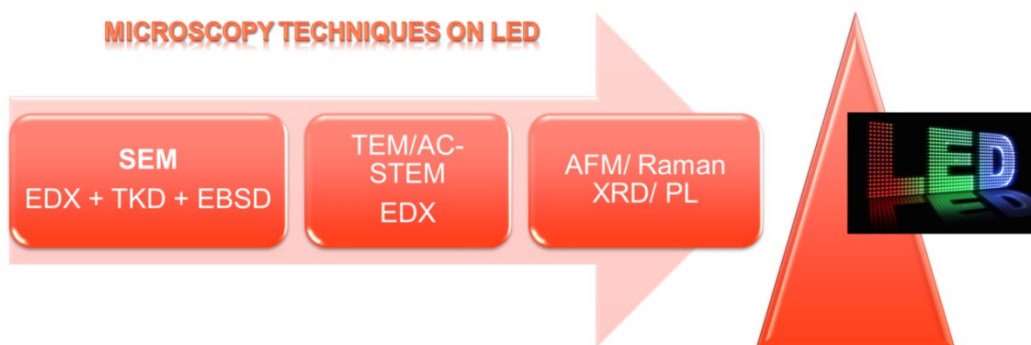
Table 2.1 Summary of microscopy techniques applied to the VLED with their specifications

Device and Microscopy Techniques		Specifications	Purpose
Vertical LED Chip		GaN: 440-490 nm, η_{opt} : 50%	Blue Light
Zeiss Auriga SEM-FIB		5 kV-30 kV, 50 pA-2 nA	Milling
Zeiss Ultra plus FEG-SEM		10-30 kV, 1-3 nA	EDX
		WD: 6-10 mm	EBSD
		Oxford Intr. AZTec Nordlys-nano EBSD detector system	TKD
TEM	JEOL 2200FS/ JEM-ARM300F	200 kV	STEM
	FEI Titan Themis Z aberration-corrected with Super-X EDX	80-300 kV	EDX AC-STEM
Bruker SPM/AFM		Dimension ICON SPM with ScanAsyst® image system	AFM
Renishaw Raman System 2000		Laser source: 488 to 752 nm	Raman
Olympus FluoView FV1000 Confocal		405 nm laser diode	PL
Schimadzu XRD 6000		Cu X-ray tube, 6-40 kV, scan range: 10-80	XRD

In conclusion, nanostructural investigations have been performed on the LED by applying advance powerful microscopy tools. SEM technique has provided the surface morphology of the LED top surface and cross-sectional layers. Combined SEM-EDX and TKD analysis revealed elemental segregation, characterization of the grain morphology (grain size, grain orientation, and grain boundary types) and crystallographic (texture) orientations of the LED stack layers. At the preliminary stage of examining any semiconductor device, the combination of SEM-TKD/EBSD with EDX proved to be a robust and sophisticated methodology for nanocharacterization of the LED.

In addition, to prepare fine electron transparent lamella specimen (50-80 nm) for SEM-TKD and TEM analysis, the FIB technique in SEM should use appropriate currents and accelerating voltages for milling to avoid damage as much as possible the Ga+ ions contamination (sample-amorphization or implantation) [106], [140], [141]. In the context of specimen-yield, to reduce the stress on the specimens, suggested methods include change the specimen orientation (plan view to cross-section view) and do Pt/Au or carbon coatings.

Furthermore, TEM technique on the VLED showed its unique capability to explore the structural and chemical properties of devices at atomic-scale resolution. LEDs, which are mostly based on compound semiconductors, TEM revealed the composition of III-V MQWs or semiconductor (GaN) and metal (Ag) interfaces at the atomic-level. Particularly, AC-STEM yields distinctive potential to quantify the distribution of chemical species (Ga and light N elements) at the atomic-scale) and provides polarity of the device in atomic-planes (Figure 2.17), thereby having the advantage over three-dimensional (3D) APT techniques [142], [143]. This is because TEM provides crystallographic information at the high lateral spatial resolution (atomic-planes). However, TEM has limitations as it lacks the ability to determine the unique 3D positions of every atomic species in a selected region and faces the particular challenge when features of interest are smaller than the thickness of the specimen (~10-100 nm) [144]. Although recent improvements in ET have reached comparable scale to APT [145], [146], the atomic-scale has not yet fully achieved or less distinct, and detailed 3D quantitative compositional data of complex (nano-scale or multilayer) structures is less developed so far in ET as compared to APT [147], [148].

In addition to above microscopy techniques, surface analysis of the VLED by non-NDT of AFM, Raman spectroscopy, XRD and PL provided surface topography, stress-state, phase identification of a crystalline material, and emission properties, respectively.

In general, microscopy characterization on the VLED demonstrated that the interface quality strongly influences the properties of the epitaxial layers, and interfaces are linked to heterostructures properties, such as carrier density or mobility and recombination rates, which directly affect the efficiency droop of the VLED. Nevertheless, microscopy analysis has been essential to map chemical composition, surface morphology, elemental diffusion or impurity levels, surface topography, and grain boundaries that impact the electronic properties of the device under test (DUT). Indeed, microscopy techniques are capable of performing component-level and device-level analysis and offers unique information for LED optimization to play a vital role in the electronic materials industries.

Furthermore, inside the microscopy instruments, appropriate choice of experimental parameters, such as specimen temperature (K), vacuum pressure (mbar or Torr), electron/ion-beam intensity (FIB), working distance (SEM/EDX/TKD/EBSD), laser pulse or X-ray energy (AFM/PL/Raman/XRD) and other sample preparation protocols are also taken into account for reliable data collection (reconstruction) and data analysis. These parameters are critical for the semiconductor (SC) materials (like LEDs) because to analyze SC materials with poor thermal diffusivity, rapid cooling is the key in achieving good data [31]. Also, it is important to mention that the spatial resolution (key criteria for any microscopy performance) is material-dependent.

Moreover, in the field of semiconductors (SC), sample preparation is challenging because some microscopy techniques (e.g. SEM-FIB) suffers from somewhat limitations when applied to 3D structures composed of regions with different layers with different evaporation/milling rate. Also, it is plausible that the spatial resolution in SC materials deteriorates more with e-beam intensity compared with pure metals, because electric fields could penetrate much deeper into SC materials than for metals due to the difference in band-structures [149]. Particularly, in compound SC, milling rate varies with chemical composition, material density, crystallography, interfaces, and phases.

To mitigate these difficulties, several methodologies and new protocols are in the development phase. Correlative microscopy (TEM/SEM/TKD combine with APT or another microscopy) considered being helpful in obtaining high-quality 2D/3D data. Indeed, complementary techniques (such as TEM and APT) will likely to develop a closer relationship in the future, where the TEM spatial fidelity is combined with the analytical sensitivity and three dimensionality of APT [150], [151]. Further, instruments that combine these techniques into a single instrument are currently being pursued by the "ATOM project" [152], [153] in the form of STEM-APT microscopy to develop true and ultimate metrology tool namely "atomic-scale tomography" (AST) [154].

Also, in the near future, technological advancements in SEM/TEM, EBSD/EDX, and AFM/XRD/PL detectors (hardware) and automated sample procedures will make beneficial techniques to induct into competitive and failure analysis tools. Hence, the unified framework of microscopy techniques on the vertical LED will facilitate to investigate device physics and structure-property relationships.

Chapter Three

On the Metallic Bonding of GaN-based Vertical Light-Emitting Diode
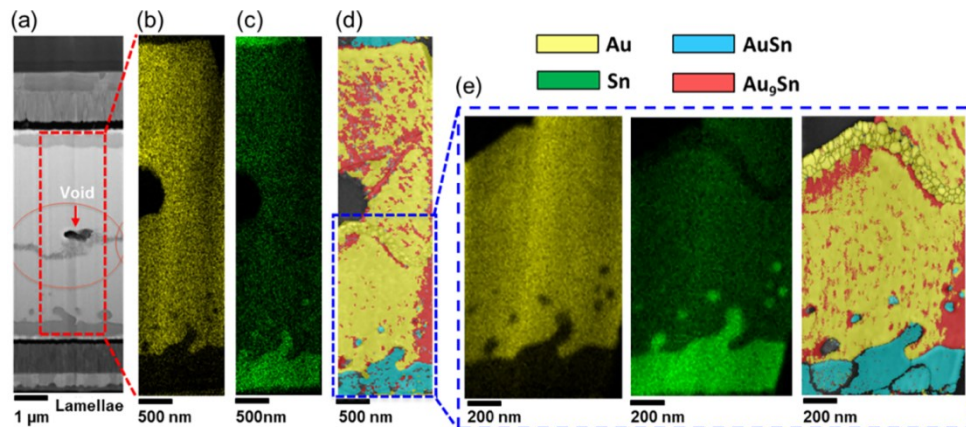
3.1 Role of Wafer Bonding?

Wafer bonding is the most prominent joining technology used in optoelectronics, micro-electro-mechanical systems (MEMS), nanophotonics and other industrial semiconductor devices [55], [56], [155]–[157]. Wafer bonding plays a critical role in the fabrication of cost-effective LEDs and development of today's 3D integrated circuits (ICs) [39], [158]–[160]. In wafer-to-wafer (W-W) bonding numerous approaches exist, e.g., direct fusion, anodic, glass frit, adhesive bonding and transient liquid phase (TLP). However, metal-based wafer bonding (WB) namely: (1) eutectic (solid-liquid phase), and (2) thermo-compression or diffusion bonding (diffusion of metal atoms) are dominant in electronics products [161]–[164]. As these metallic bonding includes provisions for good electrical interconnects (conductive bonds) with a high degree of hermeticity, and device scaling. In eutectic bonding, intermediate bonding material forms a eutectic alloy at a specific composition and temperature [162], [165]. Those eutectic metals include Au-Sn, Au-Si, Pb-Si, Au-In and Au-Ge, etc. alloys that transform from solid to liquid state, or vice versa [166], [167]. The bonding interfaces will be fused together due to intermetallic phase formation, for instance, Au/Sn alloy system forms a eutectic solder at the composition of Au71 at.% Sn29 at.% at melting temperature of ~278 °C or solid-liquid interdiffusion (SLID) bonding for high-temperature (~600 °C) applications [168], [169].

On the other hand, in thermocompression bonding (TCB) technique, the two metal surfaces adhere to each other by the simultaneous application of pressure and temperature [170], [171]. In fact, bonding interfaces will fuse together due to atomic interaction under heat and pressure. To clarify, eutectic bonding is solid-liquid diffusion, while TCB is solid-state diffusion, where a solid phase direct bonding process is realized without an intermediate phase or intermetallic compounds (IMC). TCB is also referred as metal diffusion bonding, pressure joining, or solid-state welding. Almost any metal can be bonded via thermocompression technique, however, the requisite temperature or pressure may not be in a suitable or practical range for all metals. In metals, mostly Au is selected as an ideal bonding material because contrary to Cu-Cu/Al-Al, Au-Au bonding is known to have superior resistance to oxidation and contaminations [172]–[175]. In literature, Au-based TCB has been performed at both chip or wafer-level that holds varying temperature ranges

85

from 260-450°C and pressure of 0.1-20 MPa with bonding duration in ~2-60 minutes [176]–[179]. Au-based TCB is an interesting technology for achieving chip or wafer-level bonding at low temperature without the requirement of an electric field (anodic bonding) or complicated pre-bond cleaning procedure (plasma-assisted silicon direct bonding) [170]. Further, lowering the temperature and pressure requirements of Au-Au metal bonding will allow its applicability for more diverse and economical MEMS, IR sensors and 3D-ICs products.

3.2 Wafer Bonding in Vertical LEDs

In the context of III-nitride-based optoelectronics, thin-film or VLEDs fabricated by laser lift-off and metallic, i.e., eutectic and thermocompression WB processes have demonstrated improved optical, thermal and electrical properties over conventional lateral LEDs [5], [180], [181]. In fact, the concept and design of VLED is indebted to WB technology. This is because metallic WB technology provides good thermal conductivity (for heat dissipation), lower electrical resistance, uniform current spreading, and reduction of light absorption losses [85], [182]. Thus, metallic WB has gained interest in solid-state lighting market to enhance the LEE and/or luminous efficiency of GaN-based VLEDs [39], [183]. Good thermal conductivity, adequate mechanical strength, and electrical conductivity are known criterial parameters for high-quality metallic WB [184]. Nonetheless, state-of-the-art material characterization and failure analysis tools are inevitable to ensure high-yield bonding process. In this regard, several groups have adopted different visualization methods, such as infrared (IR) transmission, ultrasonic, X-ray topography, SEM and TEM [185]–[188]. However, these approaches lack either in providing detailed information about the nature of bond interface (interfacial microstructures, micro-voids) or have complex experimental setup and manual analysis. Hence, a sophisticated microanalytical tool is required that can scrutinize bonding interface. SEM-based TKD technique combined with EDX provides a robust collection of orientation and pattern quality maps at the effective spatial resolution of 2-10 nm [118]. Also, its automated analysis of grain morphology with electron diffraction system has the non-trivial advantage over other conventional counterparts.

This work reports on a detailed microstructural characterization of the bonding between the device and carrier wafers of LED by means of advanced electron microscopy techniques. Firstly, a metal-based WB of GaN-based vertical LED is characterized at the nanoscale by using the combined methodology of SEM-based TKD and EDX. Peculiar SEM-TKD provides valuable insight into metallic-bond chemistry and reveals its grain morphology, i.e., grain-size distribution, grain orientation (texture), grain boundaries (GBs), and special twin boundaries (TBs). In parallel, high-resolution (HR)-TEM explicates defects (voids, diffusions) at the interface of metallic diffusion or thermocompression bonding. Based on SEM-TKD and TEM microstructural characterization and analytical results, further optimization prescriptions are given for performance enhancement of metallic bonding in the VLED.

3.3   Materials and Methods

3.3.1 Fabrication Steps in Wafer Bonding of the Vertical LED

Section 2.1 of this thesis provides a detailed explanation of fabrication steps, and Figure 2.2 illustrates the summary of wafer bonding mechanism [164], [180].

3.3.2 Experimental Setup for SEM-TKD and TEM

In SEM image (Figure 2.2(c)), we can observe that DW (top) and CW (bottom) are connected together by metallic WB (dotted lines towards bonding interface), wherein the post-bond thickness of the bond pair measured to be ~3.1-3.3 μm, i.e. Au (~1.35 μm)-AuSn (~240-280 nm) at CW, and Au (~1.4 μm)-AuSn (~170-180 nm) at DW. The slight variation of thickness in bonding medium is due to wafer's flatness deviations or surface imperfections, material's melting or reflow (inter-metal diffusions) or compression (deformation) and defects (voids, irregular interfaces) as of non-uniform distribution of pressure and thermal equilibrium, respectively [189]. Further, on both CW and DW, multiple stacks of adhesion/barriers sublayers are located and the functionality of these layers is to stop bonding metals diffusions, enhance adhesion and relax stress during the W-W bonding process. For instance, the non-reactive barrier layer (Ti) at CW is used to prevent Sn diffusion (from AuSn sublayer) into either Si or Ge substrates, while at DW it

blocks Sn migration (from AuSn sublayer) into the reflective and GaN active layers. Also, generally Au does not bond well to conductive Si carrier, but Ti facilitates it [177].

Moreover, from SEM cross-sectional image (Figure 2.2(c)), three interesting features can be noticed in the fabricated VLED structure: (1) eutectic bonding possesses stable interface without any Kirkendall voids, however, (2) At Au-Au thermocompression bonding few interfacial irregularities are emerged in the form of micro-voids, and (3) Au-Au bonding forms zig-zag (non-liner) interface. To understand them, it is necessary to investigate the morphology and chemical composition of metallic bonding under the SEM and TEM microscopy tools. Thus, for that particular region of interest (ROI), a cross-sectional thin (50-60 nm) electron transparent lamella specimen was prepared from a VLED die by using focused ion beam (FIB) process. FIB-prepared lamella steps are shown in Figure 3.1. Next, to investigate the metallic-bond chemistry and grain morphology, a powerful tool of Carl Zeiss Ultra Plus FEG-SEM with NordlysNano EBSD detector system was setup on the FIB-prepared lamella, as shown in Figure 3.2. The Oxford Instruments Aztec software was used to process TKD data and Kikuchi patterns. Further, the sample was examined under the JEOL 2200FS TEM. Table 2.1 summarizes experimental details.
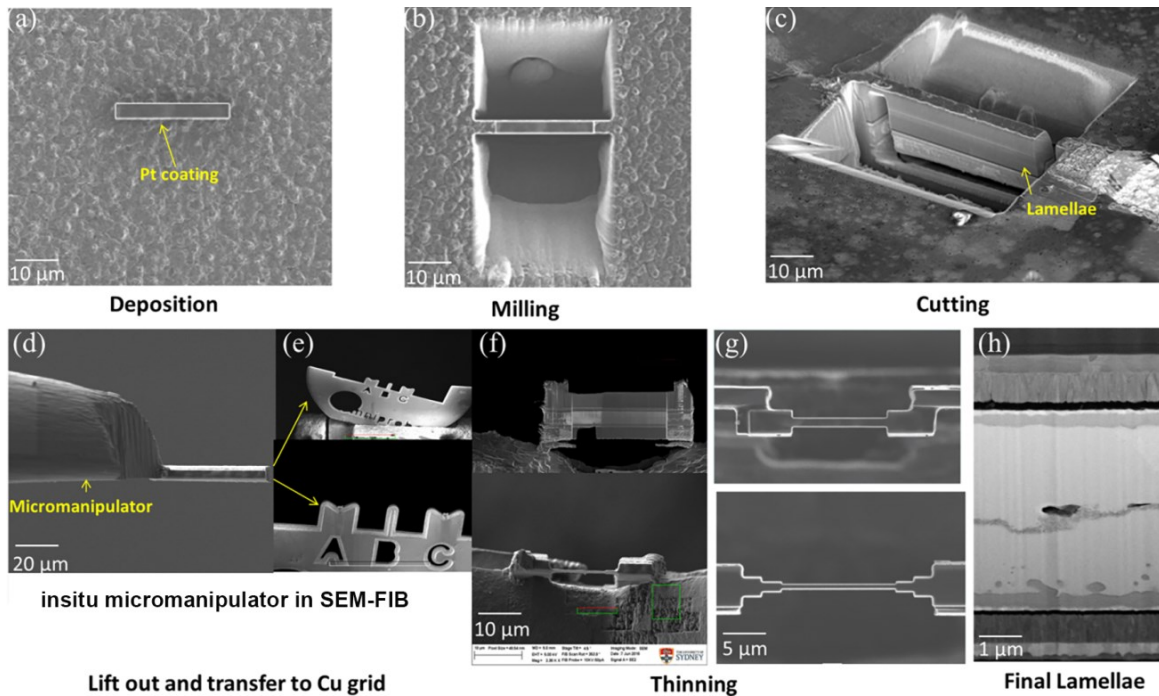
Figure 3.1 Sample preparation steps in FIB-prepared lamella.

88
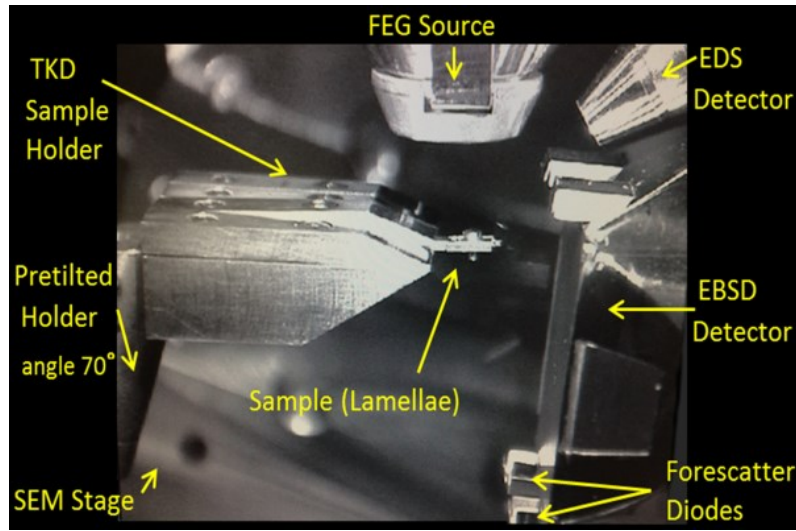
Figure 3.2 SEM-based TKD experimental setup.

Instruments	Specifications	Purpose
Vertical LED Chip	GaN: 440-490 nm	Blue Light
Zeiss Auriga SEM-FIB	10 kV-30 kV/ 50 pA-2 nA	Milling
Zeiss Ultra plus FEG-SEM	12-30 kV/ 1-3 nA WD: 6-8 mm Oxford Intr. AZTec Nordlys-nano EBSD detector system	EDS+TKD
JEOL TEM 2200FS	200 kV	STEM+EDS

Table 3.1 Experimental details

3.4 Results and Discussion

3.4.1 SEM-TKD with EDX Analysis on Metallic Bonding

In Figure 3.3(a), SEM-EDX chemical analysis across the ROI (marked in red dotted lines) confirms that Au and Sn are involved in eutectic and thermocompression bondings. However, Au majorly occupies at the thermocompression bonding interface (Figure 3.3(b) and (c)). The phase analysis indicates the occurrence of Au, AuSn, and Au_9Sn phases (Figure 3.3(d)). Figure 3.3(e) is provided to clarify the elemental and phase's distribution,

particularly across eutectic and thermocompression bonding regions. Also, SEM-EDX phase acquisition analysis provides crystallographic parameters, e.g., crystal structure, lattice vectors, and space group of each phase, as summarized in Table 3.2.
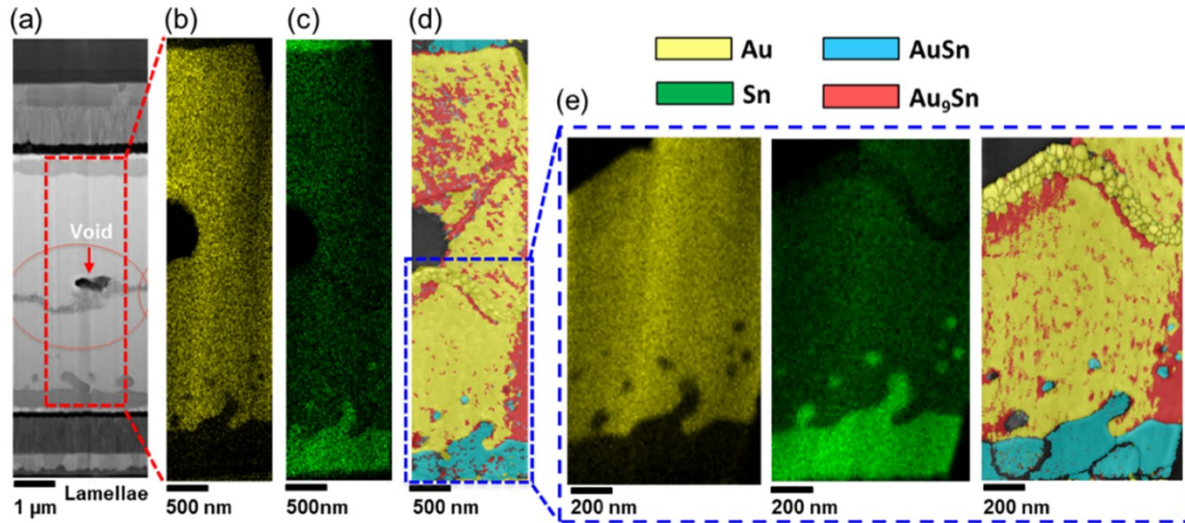
Figure 3.3 SEM-based chemical analyses across eutectic and Au-Au bonding interface.

Table 3.3 SEM-EDX phase acquisition analysis

Phases	a=b	c	Alpha=Beta	Gamma	Space Group
Au	4.08 Å	4.08 Å	90.00 °	90.00 °	225 (F m^{-3} m)
AuSn (δ)	4.32 Å	5.52 Å	90.00 °	120.00 °	194 (P6$_3$/mmc)
Au$_9$Sn (ζ)	2.91 Å	4.79 Å	90.00 °	120.00 °	194 (P6$_3$/mmc)

Table 3.4 SEM-EDX quantitative analysis

Zone	At.%	Wt.%	Phases
Eutectic Bonding	75.82 Au 24.18 Sn	83.6 Au 16.4 Sn	AuSn (δ) + Au$_9$Sn (ζ)
Thermocompression Bonding	85.41 Au 14.59 Sn	90.67 Au 9.33 Sn	Au + Au$_9$Sn (ζ)

SEM-EDX data discerns that at thermocompression bonding interface, Au phase is prominent with face-centered cubic (fcc) crystal structure and lies in space group of 225 (F m^{-3} m). On the other hand, the main alloy for eutectic bonding is AuSn (δ) phase with hexagonal (hcp) crystal structure and lies in space group of 194 (P6$_3$/mmc). However, it is interesting to notice the existence of a new Au$_9$Sn phase at both eutectic and thermocompression metallic bonding zones (Figure 3.3(e)). Table 3.5 shows that similar to AuSn (δ), Au$_9$Sn has hcp crystal structure and lies in space group of 194 (P6$_3$/mmc). In fact, Au$_9$Sn is a type of ζ (or zeta) phase and its further properties can be found in references [165], [190]–[193].

To further quantify the concentration of our metallic bonding zones, EDX quantitative results (Table III) provide at.% and wt.%. of Au and Sn. Our EDX results for eutectic bonding region show that the Sn concentration is ~24.18 at.% (or 16.4 wt.%), which is slightly lower than the standard eutectic composition, i.e., Sn concentration of 29 at.% (or 20 wt.%). The reason is that while performing thermocompression (Au-Au) bonding process, inside bonding chamber a melting temperature of 310-400°C was applied across wafers. However, the temperature of 310°C (or 400°C) was above the eutectic melting point of ~278°C (at 29 at.% Sn), as depicted in phase diagram (Figure 3.4), this caused eutectic AuSn sublayer to be melted as well. Once the AuSn sublayers melted, some of the Sn from either side of AuSn sublayers (CW and DW) diffused into the Au sublayers of thermocompression bonding. Thus, the concentration of Sn in AuSn sublayer decreased.

This lower concentration of Sn resulted in the higher melting temperature of AuSn layers. As it is believed that for every 1% a decrement in the Sn concentration, the melting temperature of the Au/Sn alloy increases by ~30°C [177], [194]. It means that if the Sn concentration was decreased to 3-4%, then the eutectic temperature of 278°C had been raised to ~400°C (which was actually the bonding temperature for thermocompression). Under such conditions, the liquid Au-Sn phase came into equilibrium with initially Au-rich hcp phase of ζ, i.e., ζ + L (liquid) phases form. With decreasing the temperature, Au/Sn alloy during solidification formed two-phase mixture eutectic structure of AuSn (δ) and the ζ. However, here it must be noted that while being in the vicinity of surplus Au (Au rich area), the ζ is not expected to convert into lower melting point phases (e.g. Au$_5$Sn or ζ')

91

[191], [194]. Massalski and King group also reported similar behavior that ζ phase melted at 522°C and was assumed stable down to -5°C (depending on Au concentration) [190]. Also, Yost *et al.* determined that the ζ phase had the lowest shear modulus (E, G) and Vicker's hardness among the Au-rich Au/Sn phases, which means that it has greatest ability to absorb stresses thermomechanically [191].
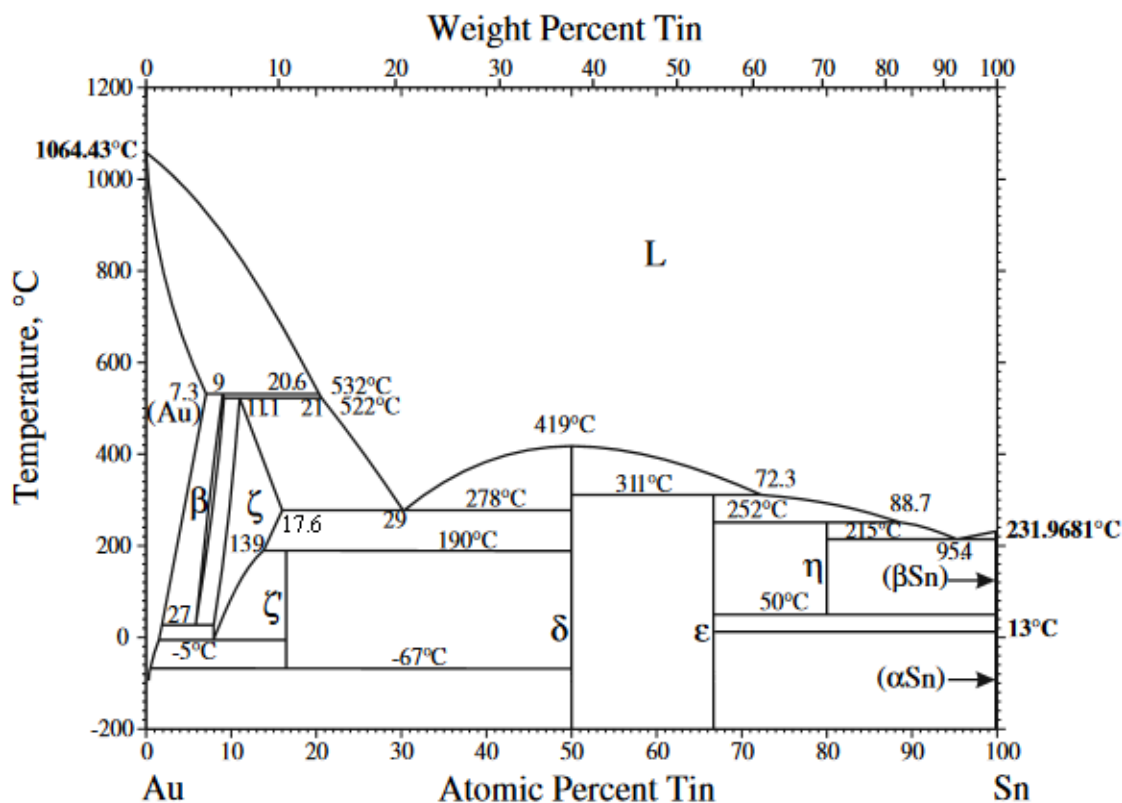
Figure 3.4 Au-Sn phase diagram [17].

In addition, EDX results determine that the concentration of Sn is ~14.59 at.% (9.33 wt.%) at the thermocompression bonding layer, which exactly lies in ζ phases range, i.e., Au82.4-92 at.% Sn17.6-8 at.%. This is because ζ phases exist from the peritectic β+L ←→ ζ at 9.1 at.% Sn at 522°C to 17.6 at.% Sn at 278°C, and from 8 at.% Sn at -5°C to 13.9 at.% Sn at 190°C, as depicted in phase diagram (Figure 3.4) [168]. Therefore, based on our EDX experimental results, it is reasonable to deduce that Sn diffused from eutectic An/Sn alloy,

and formed an Au_9Sn (ζ) phase, which was randomly distributed in eutectic solder and Au-Au bonding interface (Figure 3.3(e)). The distribution of Au_9Sn is believed to be valuable as it contributes in long-term stability to metallic WB, e.g., in SLID bonding [169], [192]. In summary, our SEM-EDX experimental results verified that the eutectic zone consisted of two hcp phases: AuSn (δ) and Au_9Sn (ζ), where AuSn (δ) is the dominant phase. Contrarily, thermocompression bonding zone formed Au and Au_9Sn (ζ) phases, where Au phase prevailed. Hence, such SEM-based EDX qualitative and quantitative results make it possible to relate the observed bonding composition (phases) to processing parameters (materials history), i.e., how was the bonding processed, cast, and ultimately how was it fabricated or produced in a final shape? Thus, SEM-based EDX chemical compositional results are quite fascinating to provide vital insight into metallic WB chemistry and assess the quality of the bonding process.

Further, to investigate the microstructures in eutectic and thermocompression bondings, SEM-based TKD analysis has been performed. SEM-TKD is able to provide cross-sectional morphology and nano-structural characterization of crystalline material. SEM-TKD has identified key microstructural features at the bonding interface, such as band contrast (BC), grain size, GBs, special TBs, inverse pole figure (IPF), texture or pole figures (PFs) and Kikuchi diffraction patterns, as shown in Figure 3.5.

To elucidate the microstructural features of Au-Au thermocompression bonding interface, magnified images of this region have been taken from Figure 3.5(b), as represented by dotted blue lines, and are shown in Figure 3.5(f). In pattern quality images, BC reveals microstructure in a certain qualitative fashion (orientation contrast) [195]. In Figure 3.5(b), BC for Au-Au bonding interface tends to have light contrast (high pattern quality), while underlying eutectic region appears dark (low pattern quality). This is due to electron backscattering patterns (EBSP) produced in the SEM-TKD system, for instance, EBSP along GBs tends to be visible as dark (low pattern quality) features.

(a) 1 µm Lamellae   **(b)** 200 nm; BC+GB   **(c)** 200 nm; BC+IPF_X+GB   **(d)** 200 nm; BC+IPF_Y+GB   **(e)** 200 nm; BC+IPF_Z+GB   IPF coloring legend

(f) Au-Au bonding interface

= 100 nm; BC+GB>10° ; Step=2nm; Grid286x167

= 100 nm; BC+Phase+GB; Step=2nm; Grid286x167

= 100 nm; Special CSL TBs (red); Step=2nm; Grid286x167

= 200 nm; BC+IPF_Z+GB; Step=2nm; Grid286x167

IPF _Z coloring legend

Pole Figures   Kikuchi Patterns

Au   {100}   {110}   {111}   Min=0.03   Max=3.82

Au_9Sn {0001}   {10$\bar{1}$2}   {10$\bar{1}$0}   Min=0.00   Max=106.92

Figure 3.5 SEM-TKD on the metallic bonding. (b) Band contrast (BC). (c)-(e) Inverse pole figures (IPF) in *x, y, z* directions. (f) Au-Au bonding interface: grain boundary (GB), phase mapping, special twin boundaries (TBs) marked red lines with Σ3 60° orientation graphs, pole figures, and Kikuchi patterns.

In grain size analysis, it is manifested that eutectic solder has fine grains with a grain size ~120-240 nm, while Au-Au bond interface is constituted by nanocrystalline grains with the mean grain size < 50-80 nm at a step size of 2-3 nm. The formation of ultrafine grains at eutectic solder is because AuSn is the dominant phase, and such microstructure depends on eutectic alloy composition and temperature cycles. Further detailed information regarding phase transformation can be found in references [165], [196], [197]. However, in Au-Au TCB, the reason behind the formation of peculiar nanocrystalline grains is solid-state (metal) diffusion process. In fact, when two metal bonding surfaces are brought in contact by applied pressure; a plastic deformation occurs, which allows the diffusion of metal atoms (atomic motion). As that diffusion continues, hence the grain growth prevails across the bond interface. The grain growth rate depends on the initial microstructure, i.e., if the microstructures are very fine, grains grow rapidly. To further enhance the deformation for a given pressure, heating the metals not only accelerates the diffusion rate but also slightly softens the metals, as well. Hence, Au diffusion bonding is based on Au atoms migration, and its grain growth depends on the bonding applied force, temperature and duration.

Further, in GB orientation analysis, most grains at Au-Au bonding interface have high-angle GBs (> 10°) and special TBs, as shown in Figure 3.5(f), where high-angle GBs are marked in black and TBs in red lines. SEM-TKD data identifies these special TBs at Au-Au bonding interface as coherent site lattice (CSL) with Sigma-value three ($\Sigma3$) at 60° misorientation angle, as indicated in Figure 3.5(f) Sigma-value and misorientation graphs. In orientation mapping, inverse pole figures (IPFs) in *x, y, z* directions (Fig. 6(c)-(e)) show the existence of grains with different crystallographic orientations by appearing in different colors (colors according to the orientation triangle for fcc and hcp; legends for IPF maps are displayed). In addition, PFs and Kikuchi diffraction patterns show that Au and Au_9Sn phases have fcc and hcp structures, respectively. However, their PFs exhibited a weak preferred crystallographic orientation. Particularly at Au-Au bonding interface (Figure 3.5(f)), a subset with detection of almost ~200 grains have been taken into account, and it is manifested that the Au-Au interface grains have no specific texture or less pronounced <111> texture, i.e., in {111} plane. This suggests that Au film might require a lower

applied stress to initiate plastic deformation because it has shown random crystallographic orientations (anisotropic nature), as shown by TKD IPF maps (Figure 3.5(c)-(e)).

Hence, SEM-TKD concludes that AuSn (eutectic solder) has ultrafine grains; while Au-Au (TCB) interface has nanocrystalline grains with special (Σ3) CSL twin boundaries misoriented at 60° but possess weak <111> texture. On that account, SEM-TKD with EDX technique has substantial potential in providing a detailed microstructural characterization of metallic bonding. Further, it facilitates to associate the observed microstructural features to the structure-property-performance relationship, which is explained in the discussion part of this work.

3.4.2 HR-STEM Analysis on the Metallic Bonding

Figure 3.6(a) shows the cross-sectional STEM image of the Au-Au bonding interface, which also reveals voids at the nanoscale with polygranular structures. Further, HR-bright-field images and diffraction patterns manifest that nano-grains had special twinning of Σ3 (111) TBs obtained under [1-10] direction (Figure 3.6(b)-(d)). In fact, these TBs at Au-Au interface were induced by stacking faults, i.e., deformation lamellae [198], as shown in Figure 3.6(c) (the region marked in red dotted lines).
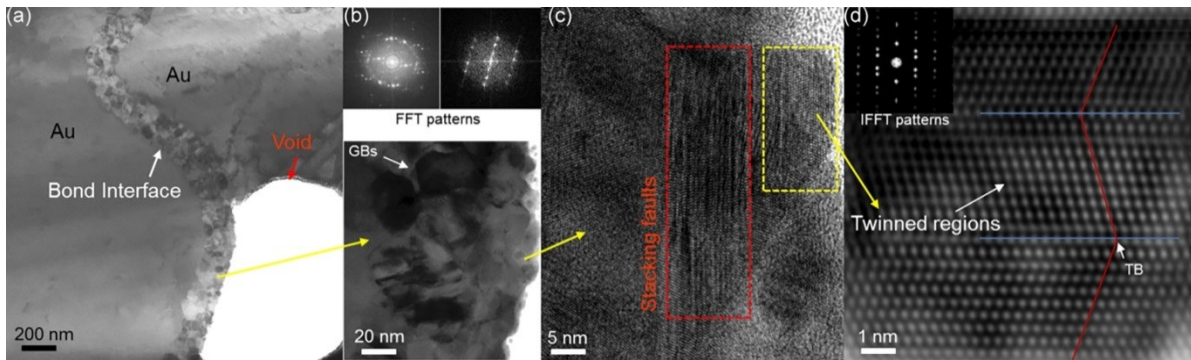
Figure 3.6 (a) Cross-sectional STEM images across the Au-Au thermocompression metallic bonding. (b) Diffraction patterns and nanoscale grain boundaries (GBs). (c) Stacking faults (red dotted lines), and (d) special Σ3 CSL twin boundary (TB) with twinned regions (blue and red).
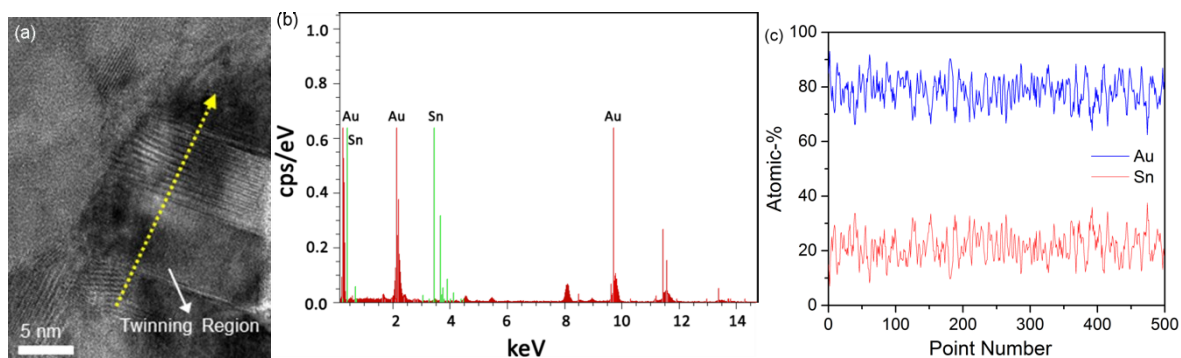
Figure 3.7 TEM-EDS-based chemical analyses across Au-Au bonding interface. (a) Line scan (yellow). (b), (c) Band spectrum and atomic-% of Au and Sn elements.

Twinning in fcc metals often occurs during deformation across the slip planes due to their low stacking fault energies. This shows that Au-Au bonding interfaces fuse together due to atomic interaction (plastic deformation) under the applied pressure and heat. And, such bonds basically involve three steps: 1) interface formation (surface diffusion), 2) crystal misfit accommodation, and 3) grain growth with special TBs formation. These TBs are a special class of GBs in which the grains on either side of the boundary are related by mirror symmetry, as shown in Figure 3.6(d). Such TB symmetrical structure reduces the free volume and GB energy and may provide an Au-Au bonding with unique combinations of high strength and good ductility, conductivity, and thermal stability.

In Figure 3.7(a)-(c), TEM-EDX line-scan chemical analysis across the Au-Au bonding interface confirms the diffusion of Sn with ~10-18 at.% Sn. Such distribution of Sn contents in Au-rich bonding zone corresponds to ζ phase (Au82.4-92 at.% Sn17.6-8 at.%) as per Au-Sn phase diagram (Figure 3.4). These TEM-EDX results are quite consistent with SEM-EDX measurements that Sn migrates from eutectic AuSn sublayers into Au-Au bonding interface. Hence, SEM and TEM results proved that Sn diffuses into Au-Au TC bonding, and forms a ζ phase. Thus, TEM results revealed surface (atomic) diffusion and special TB reactions across the Au-Au bonding interface, which plays a vital role in the failure or success of TC bonding.

3.4.3 Correlating SEM and TEM Results

SEM-TKD and STEM results are quite beneficial as they contribute to relating observed microstructural features to the grain size have inverse relationship, microstructure-properties-processing-performance paradigm. For instance, in context of correlating grain morphology analysis to material properties and metallic WB performance, it is evident that grain size at metallic bonding will impact the thermal, electrical, mechanical or optical properties of thin film LED. This effect is mainly attributed to the mechanism of atomic diffusion, electron (charge) or photon trapping related to the GBs. For instance, according to Hall-Petch law for yield stress dependence on grain size, the yield strength and grain size have an inverse relationship, i.e., yield strength increases with decreasing grain size as $d^{1/2}$ (where d is the grain size) [199]. Here, the ultrafine grains at the eutectic joint promote high yield strength; however, Au-Au bonding interface has slightly more yield strength as of nanocrystalline grains. Also, small grain size means more GB areas or diffusion paths exist, thus improves Au atoms diffusion across the bonding interface.

In addition, the angle of orientation also influences the metallic WB properties as well, such as thermal conductivity, since anisotropic oriented grains have higher conductivity compared to random or isotropic oriented grains [198]. Our TKD IPF maps (Figure 3.5(c)-(e)) vindicated that Au-based interface has an anisotropic behavior, which reflects its high conductivity. In parallel, the angle of orientation impacts WB strength and electrical properties. Besides, it is known from previous studies that to enhance material's strength, HAGBs are required because they are more resistant to dislocation motions [200]. In our metallic bonding case, Au-Au thermocompression bonding interface holds prominent HAGBs (>10°) (Figure 3.5(f)). Thus, a combination of fine grain size with HAGBs evaluates metallic bonding strength [200], [201]. However, it should also be noted that in microelectronic devices, HAGBs are more electrical resistant with the exception of the special type of high angle Σ3 twin boundaries (TBs) [202], [203]. In fact, special TBs with less interfacial energy have low electrical resistance and less mobility compared to HAGB. Interestingly, such TBs have formed at Au-Au thermocompression bonding (Figure 3.5(f) and Figure 3.6(d)). The reason is that it is the tendency of fcc metals to form TBs, which is related to the TB energy, i.e., those with low TB interfacial energy forms twins [204]. Such

special high angle Σ3 (60°) TBs at Au-Au bonding interface have significant advantages: 1) they are considered to be poor pathways for electromigration (EM) voiding [205], [206], 2) TBs with relatively low mobility contributes in a high degree of microstructural stability, 3) TBs improve electrical conductivity because of their low resistance [207]. Nevertheless, TBs have already shown an increase in the strength in other fcc metals (Cu, Al, Ni, Ag, etc.) by acting as barriers to the transmission of dislocations [208], [209]. Moreover, such special TBs have significant benefits on electrical properties, which will imperatively contribute towards the lifetime of the indispensable metallic WB layers in the VLED. Thus, the robust technique of SEM-TKD facilitates us to understand the GB engineering at metallic WB interfaces.

Furthermore, in context of correlating microstructural characterization with possible failure, our combined results from SEM-TKD and STEM with EDX tools enabled us to provide reasons for the concern three points mentioned in section 2 of this paper. Regarding the first finding, our fabricated eutectic joints (AuSn sublayers) are stable and have no Kirkendall voids. Besides, in previous works, such voids have been substantially reported as an issue in these types of eutectic joints [187], [192], [210]. For instance, Kirkendall voids located in between AuSn (δ) and Au_5Sn (ζ') phases [187]. The fact is that for typical eutectic joints a mixture of AuSn (δ) and Au_5Sn (ζ') microstructures are mostly formed. However, AuSn (δ) has a hexagonal crystal structure, while Au_5Sn (ζ') has a trigonal crystal structure. Such varied combination of crystal structures might cause lattice mismatch and furthermore on thermal stresses (heating cycle). That creates vacancies, which might result in void formation in such type of eutectic solders. On the other hand, EDX measurements of our stable eutectic bond showed that it consisted of two AuSn (δ) and Au_9Sn (ζ) phases, and both have hcp crystal structure to mitigate lattice mismatch. Additionally, Zakel *et al.* and other previous studies on properties of Au/Sn phases reported that contrary to ζ' phase, ζ phases have the greatest capability to absorb stresses thermomechanically, and also acts as diffusion barrier for Kirkendall void formation, thus promotes stability of the eutectic bonds [192], [193].

In relation to grain morphology, eutectic (AuSn) layer has somewhat coarse grains (larger grain size) compared to Au-Au bonding interface (Figure 3.5). In such coarse grains, small

99

GB areas (or narrow diffusive paths) are available, which contribute in stability of the diffusion barriers. As coarse grains are most effective either in filling voids/holes at HAGBs or in reducing sources of vacancies, thus, yields in higher median time to failure (MTTF) [208]. Apart from that, coarse grains help in minimizing hillocks (short circuit) formation and reduce film resistivity (less scattering of charge carriers). Further, electromigration (EM) lifetime is highly influenced by the grain size distribution and the texture [212]–[214]. Because EM normally occurs via diffusion along GBs, hence to reduce the GB area for diffusion, grain size needs to be increased. This minimizes the trapping of charge or photons since there are fewer sources of vacancies or less fast diffusion paths will be available for them. Moreover, asymmetry in PFs of Au-Au TCB implied that their grains have weaker or non-existent preferred orientation (texture). For instance, lack of strong <111> texture at Au-Au interface degrades the lifetime, i.e., a lower mean time between failures of the metallic bonding [215].

3.5 Issues Addressed in Metallic Bonding

Regarding the other two issues, i.e., formation of the micro-voids and zig-zag interface at Au-Au TCB are induced by low applied bonding pressure and high temperature. Although in previous literature, studies on Al-Al or Cu-Cu TCB also reported similar defects (voids) and zig-zag interface as a result of low bonding pressure and high temperature, respectively [173], [216]. However, possible reasons in Au-Au TCB are as below:

(1) Micro-voids reflect incomplete bonded interface because of low bonding pressure. Since during the bonding mechanism, Au atoms acquire sufficient energy to diffuse rapidly and Au grains begin to grow. In order to obtain higher bond strength, Au diffusion must happen across the bonding interface and the grain growth also needs to progress across the interface. If the applied pressure is too low or bonding duration is less (e.g. < 5 minutes), the inter-diffusion of Au atoms across the bonding interface is limited. Hence, Au grain formation stops at the bonding interface, which generates micro-gaps in form of voids, thus will reduce bonding strength. More importantly, less Au grains formation across the bonding interface will also reduce the number of GB's or less number of paths

will be available for diffusion, which will impact the thermal conductivity of the Au-Au bonding interface. However, by increasing the uniform pressure, GB sliding could assist in reducing the voids at the interface.

(2)   Void formation at the Au-Au interface also might be due to the production and motion of dislocations under applied thermocompressive stress. Gondcharton et al. observed similar void formation resulting from the Cu-Cu bonding and explained a possible mechanism involves thermocompressive stress [217]. In addition, when the structure is bonded at the higher temperature, the interface between two metal surfaces (Au-Au) develops zig-zag GB (path) due to the diffusive creep, i.e., at high temperature, metal becomes extremely soft that results in reorientation of the interface GBs.

(3)   Moreover, voids or zig-zag interfaces might be on account of surface roughness, which induces non-uniform bonding pressure. Because, once the surfaces are brought together by the application of pressure but due to surface roughness, bonds initially form where the surfaces touch at asperity contacts. Simply, the bonding will occur only on some areas due to non-homogeneous force distribution. Therefore, some portion of surface remains un-bonded, which ultimately leads towards low dicing yield or weak bond strength.

Thus, such micro-voids or zig-zag interfaces act as points of failure and impact the thermal or electrical conductivity of metallic WB, consequently degrade the overall performance of the VLED.

In summary, with the insights provided by such images from SEM-TKD and STEM, material engineers can manipulate the chemistry (via doping) or remove the defects (through the process control) to design high-quality wafer bonding interface. Further, these microscopy results open new approaches and optimization perspective to standardize wafer bonding mechanism.

3.6 Prospective Optimization

To achieve high quality and reliable metallic wafer bonding, prospective optimizations are:

(1) Although, so far eutectic AuSn bonding has been recognized as superior high-temperature performance, high mechanical strength, fluxless bonding, and excellent electrical and thermal conductivity. However, maintaining the desired eutectic composition requires extreme accuracy and close control of temperature. This is because for every 1% decrement in the Sn concentration, increases the melting point of the solder by ~30°C, thus makes it unstable solder. Alternatively, high thermal (HT) stable interconnect techniques such as SLID, also known as transient liquid phase (TLP) bonding can be used for wide-bandgap packages [169], [218], [219].

(2) Bonding parameters such as temperature control, pressure uniformity, surface roughness, bonding equipment, wafers alignment system, and more importantly diffusion rate as a function of metal type need to be optimized. For instance, the high temperature or pressure could damage underlying thin films of the VLED. Hence, for Au-Au diffusion bonding, a temperature around 300-310°C will be quite suitable to achieve a successful bond [175]. The reduced maximum temperature can be attributed to the increased thermal conductivity of Au as compared with that of AuSn; 317 W/m-K versus 57 W/m-K [191]. Also, wafer bonding on metal alloy substrates can be an alternative approach that can provide a very high thermal conductivity of 400 W/m.K [54], [220].

(3) To rectify the issues of voids or zig-zag interface formation, very low pressure or too short bonding duration and the high temperature should be avoided. Their low/high threshold values need to be determined depending on properties of metal being used [221]. Also, surface contamination and wafer bow are the critical factors that affect the bonding uniformity. Thus, prior to the bonding process, surface treatment should be performed to remove organic contaminations. In addition, surface roughness must be tested and measured by AFM or SPM tools to get smooth metal surfaces for diffusion bonding.

(4) Also, the thickness of bond film needs to be considered in W-W bonding, e.g., using a thin metal film as a bond medium necessitates high bond pressures to ensure elastic deformation of the wafers for achieving conformal void-free bonding [189]. However, high bond pressures produce surplus residual stress on wafer surfaces, which can result in defects. Further, the thin bond medium is normally sensitive to wafer flatness and total thickness variation therefore can leave gaps or voids at the bond interface because of wafer surface imperfections and non-uniformities. Hence, selection of the optimum thickness of bond medium is critical for high yield W-W bonding.

(5) In the selection of wafers substrates, the difference of coefficients of thermal expansion (CTE) between substrate and chip must be evaluated. Since the metal diffusion requires a good control of the CTE differences between the two wafers to prevent thermal stresses. In addition, for VLED devices, laser lift-off or chemical lift-off should be substituted with natural substrate lift-off techniques to mitigate tensile stresses [222].

(6) Even though, diffusion barriers (Ni/Ti/Pt/W or Ti/TaW) are used to protect active layers of DW or substrate of CW [177], [223]. However, these barrier layers should also be incorporated in between eutectic and Au-Au bonding regions to avoid Sn-related diffusions and other contaminations. Also, such thin barriers or cavities would reduce thermal or mechanical stress failures [224], [225]. Non-metallic diffusion barriers (e.g., SiO_xN_y, SiCN) would have a significant edge over metallic barriers because of their closely matched CTE to dielectric (substrate) materials.

(7) Moreover, in thermocompression bonding, an addition of tertiary element with traits of high thermal or low electrical resistivity (e.g., alloys of Au-Au-Cu/Ag) would mitigate electromigration-voiding issues. Alternatively, Ag-Ag thermocompression bonding can be used because of its higher thermal conductivity and lower bonding cost [226].

(8) In terms of GB engineering, more fine grains and special nano-TBs should be promoted by applying uniform pressure. Fostering high-density twins significantly

improve the mechanical strength of the Au/Ag-based bonding interface, which might make Au/Ag metals more attractive for various industrial applications, such as in microelectronics.

(9) In parallel, new microscopy and failure analysis tools should be introduced for bond characterization, e.g., atom-probe tomography [31] would provide 3D atomic-scale insight into microstructures of W-W bonding, which helps in better understanding of bonding defects. Thus, it enables design engineers to improve the bonding yields, ultimately promotes the production of high-power and high-efficient VLEDs in the market.

3.7 Conclusion and Future Outlook

In summary, a detailed microstructural characterization and analysis on metallic bonding of vertical LED have been performed by applying SEM-TKD and TEM techniques. SEM-TKD combined with EDX tool identified the elemental segregation, grain size distribution, grain orientation, special twin boundaries, and phases at metallic bonding. Robust SEM-TKD proved to be an effective technique in correlating grain morphology and texture analysis to device failure, which contributes towards performance optimization for enhancing the efficiency and lifetime of the VLED product. Subsequent TEM results also validated the SEM-TKD data and exhibited detailed characterization of bonding interface-related defects and nano-twinned boundaries.

Thus, the results from SEM-TKD and TEM are quite beneficial in understanding the origin of microstructure formation, especially the existence of nanocrystalline grains with special twin boundaries at Au-Au interface will attribute towards twin-induced strengthening mechanism in wafer bonding. In addition, microstructural features obtained from SEM-TKD and TEM are significantly important in associating them to the structure-property-process-performance relationship, which helps in the better discernment of materials design paradigm. We believe that our correlative microscopy results provide a valuable contribution to the improvement of wafer bonding in electronic production processes. Further, based on these results, new opportunities will be opened for scientists and

material's engineers in the field of optimization of microelectronic materials, and devices, particularly in the prototyping of metallic bonding in optoelectronics sector.

Chapter Four

Insights into the Silver Reflection Layer of a Vertical LED for Light Emission Optimization
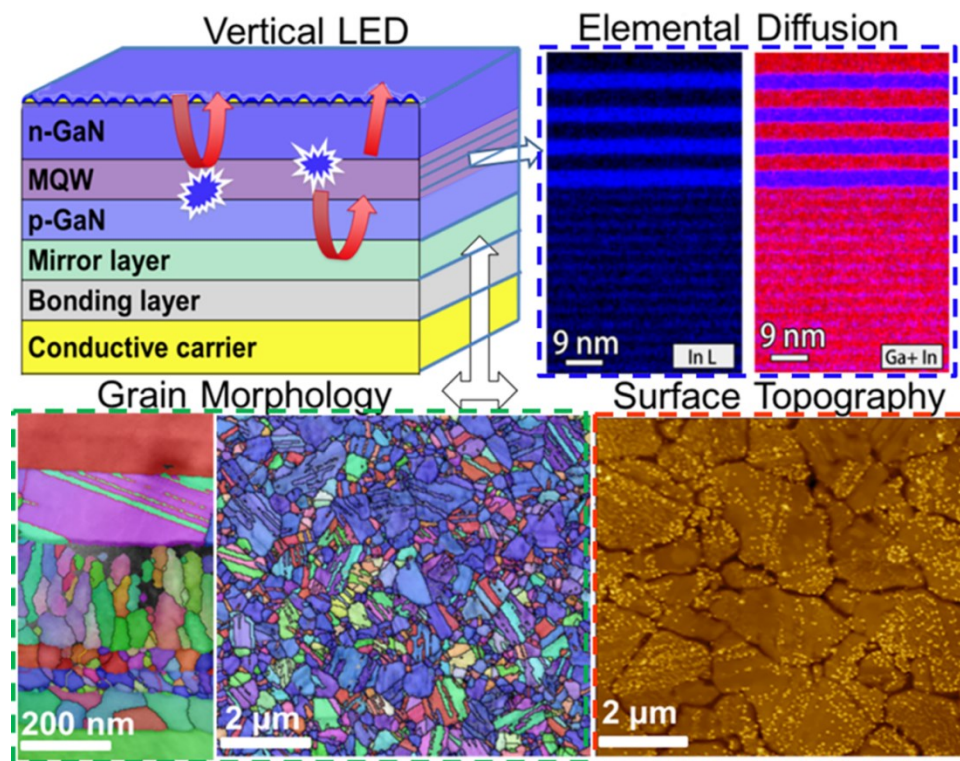
4.1 Functionality of a Silver layer in Vertical LEDs?

As discussed in Chapter 1 of this thesis that the 2014 Nobel Prize in Physics for the invention of efficient blue LEDs enabled bright and energy-saving white light source, which are based GaN VLEDs [227]. Despite VLED possesses superior performance with the efficiency approaching 60- 80%, still it needs improvement, particularly on the luminous efficacy and admittedly EQE. In order to enhance the EQE (η_{EQE}), three factors namely injection efficiency η_{inj}, IQE (η_{IQE}) and the LEE (η_{extr}) are critical because of $\eta_{EQE} = \eta_{inj} \cdot \eta_{IQE} \cdot \eta_{extr}$.

In the context of LEE, extraction of the high count of generated photons from the active region, i.e., MQWs (Figure 4.1), is an essential requirement for high-brightness LED devices. In this regard, a highly reflective mirror incorporated with a textured or scattered surface [5], [48], [228]–[230] has been shown as an effective approach to improve the LEE as compared to other techniques [231]. It is believed that incorporating a reflective coating in nitride-based LEDs increased the light output by about 200% as compared with conventional LED devices (without the reflective layer) [50].

The concept is to confine the light to the GaN layer by a bottom reflective mirror and to extract the light via a textured surface at the top side of an LED chip, as illustrated in Figure 4.1). In this way, the generated photons are reflected from the highly reflective mirror layer at the bottom, and they finally escape from the top textured surface of LED rather than being absorbed by the base substrate or the lead frame in the LED package. Thus, the reflective layers have been widely adopted in the LED chip design to maximize the LEE by major LED vendors [232]–[234]. Among various highly reflective materials, Ag is an ideal choice for green and blue GaN-based light emitters because of the high figure of merits, including electrical resistivity (lowest of all metals), high thermal conductivity (highest of all metals, except nonmetal diamond), low absorption, and the highest optical reflectivity (reflects visible wavelengths ~400 - 650 nm more efficiently than other readily available conductive metals, e.g., copper, aluminum, and gold) [37], [235]. Besides, the Ag layer also acts as the p-electrode, which enhances not only the LEE but also the output power of LEDs [48], [236], [237]. However, the concrete effects of the

interface between GaN and Ag, and the grain morphology of the Ag layer on the LEE are still blurred, which impedes the improvement of the reflective layer in LEDs. Therefore, a detailed systematic investigation of the Ag layer on the atomic scale is essential to facilitate the designing and engineering of high-performance LEDs. Also, such investigations are crucial for optimizing the Ag reflective layer as they will open new opportunities to further improve the luminous efficacy and light output power of LEDs.

In this work, various aspects affecting the Ag reflectivity have been scrutinized, including interfacial diffusions, crystallographic structure and defects, texture, GBs, special boundaries (SBs), interface boundaries, and surface roughness, which have substantial effects on the LEE. Elemental diffusions in and between GaN (semiconductor) and Ag (metal) reflection layers were determined by EDX of SEM and STEM. Grain morphology of the Ag reflective layer was analyzed by SEM-based TKD and EBSD techniques. SEM-TKD, a sophisticated microanalytical technique provided a robust collection of grain orientation, SBs and pattern quality maps at a spatial resolution of 2 - 10 nm, with the significant advantage over other techniques. In parallel, SEM-EBSD facilitated the detailed microstructural characterization of the top surface of the bulk Ag reflective layer. Further, surface topography (surface roughness) was examined by AFM. Finally, on the basis of these correlative microscopy results, suggestions are presented for performance optimization of GaN-based VLEDs.

4.2 Materials and Methods

As explained in Section 2.1 of this thesis that the process flow of fabricating VLEDs involved mainly four steps [38], [57], [238]: (1) MOCVD of epitaxial layers grown on a sapphire substrate, and deposition of a reflective mirror by electron-beam evaporation, diffusion barrier, adhesive, and bonding metal layers; (2) wafer bonding to carrier substrate; (3) removal of the sapphire substrate by using laser lift-off technique; and (4) surface structuring on the LED die.

In step (1), usually, to optimize Ag contact in terms of ohmic contact and optical reflectivity, thermal annealing was performed at temperatures of 300−600 °C for 1 min in

N_2 or O_2 ambient. However, the O_2 annealed samples showed better linear ohmic characteristics as compared with N_2 annealed samples (non-linear rectifying behavior) [R]. Also, contrarily to N_2 annealed samples, the reduction of contact resistivity is three orders of magnitude by O_2 annealed samples.

The schematic cross-section of the final VLED device is illustrated in Figure 4.1.
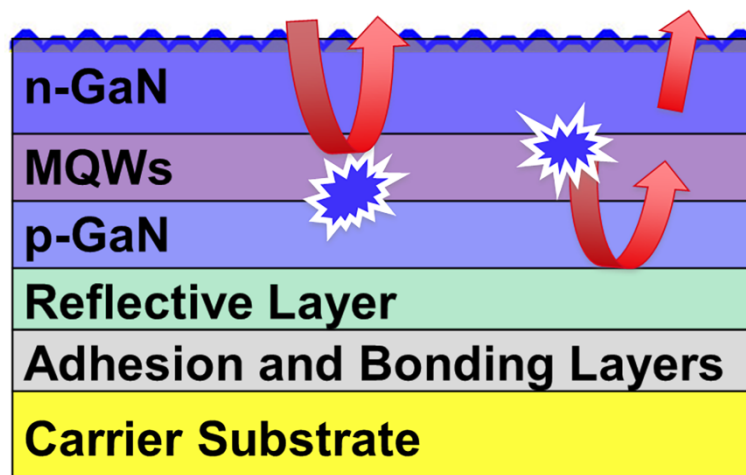
Figure 4.1 Cross-sectional schematic of VLED.

The GaN-based blue VLED sample was analyzed with a set of powerful microscopic techniques as summarized in the supporting information section (Table 4.1S). TEM and SEM-TKD require the region of interest (ROI) on a sample with thickness around 60 -100 nm, and accordingly, lamella specimen was prepared and mounted on a Cu/Mo grid in accordance with the standard TEM foil preparation procedure based on focused ion beam (FIB) lift-out techniques [108], as shown in Figure 4.2. Furthermore, the sample chemistry, surface morphology, compositional variations and crystallographic texture were determined by EDX and Nordlys-nano EBSD detectors, equipped in a single Carl Zeiss Ultra Plus SEM [118]. For TKD analysis, a standard 70° tilted TKD sample holder was used, on which the specimen was mounted on, and experiment was carried out at 20° stage tilt to align the ROI surface at 90° ($70^{\circ} + 20^{\circ} = 90^{\circ}$) toward the EBSD detector, as shown in Figure 4.9S. Thereafter, the TKD patterns were recorded and processed by the Oxford Instruments Aztec software. In addition, the roughness (surface topography) of the Ag reflection layer

and its interface with GaN were further examined by AFM and FEI Titan Themis Z (probe) aberration-corrected STEM at 300kV, respectively.
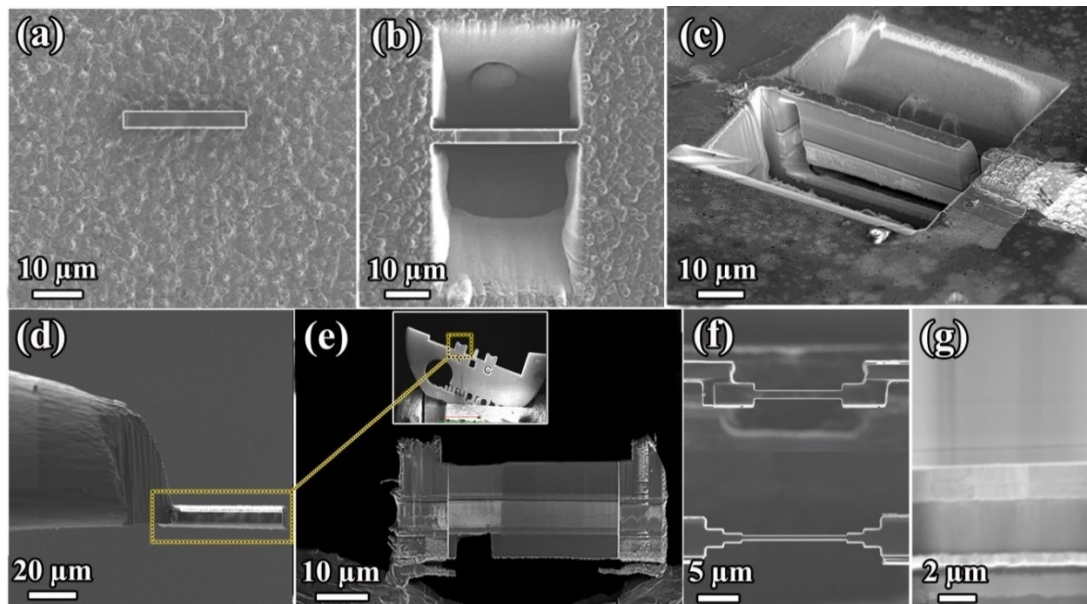
Figure 4.2 Sample preparation by FIB. (a)-(g) for STEM and SEM-TKD analyses.

4.3 Experimental Results and Discussion

4.3.1 Elemental Diffusion

SEM-EDX spectra collected along the yellow marked line in Figure 4.10S provide rapid identification of the quantification of the compositional variations across the multilayered device structure. It indicates that the interface between Ag (metal) and GaN (semiconductor) layers is somewhat diffused. The complete stack of elemental analysis is detailed in the supporting information (Figure 4.10S). Also, Table 4.2S provides the lattice parameters of the phases (Figure 4.11S) identified by the EDX data.

Robust compositional analysis across the multilayered device through SEM-EDX was very beneficial to locate the elemental inter-diffusion on a micron-scale for a broad field of view. However, the spatial resolution of SEM-based EDX was not high enough to investigate the delicate nanostructure of samples involving QWs and elemental inter-diffusion or interfacial diffusion (Ag/-GaN). Therefore, aberration-corrected HR-STEM was employed

to measure the accurate compositions on the atomic-scale. In Figure 3, cross-sectional layers enriched with different elements are differentiated using different colors. In Figure 4.3(a), STEM-EDX mapping shows that Ag reflective layer is followed by epitaxial layers that consist of GaN, Al as the electron blocking layer (EBL), the active region comprising four pairs of InGaN/GaN MQWs, and In-based superlattice with stress release functionality. Given the importance of elemental diffusion occurring within the active region (MQWs) and at Ag-GaN interface, Figure 4.3(a)-(d), STEM-EDX results provide three interesting aspects of diffusion: 1) In and Ga migration into Ag reflective layer, 2) Ag (metal) migration into GaN (semiconductor), especially into active region (MQWs), and 3) Ag-O and Ag-Ga bond formations at the Ag and GaN interface.

1) The STEM-EDX line spectrum (Figure 4.3(b) and (c)) reveals that In is quite diffusive and migrates into the Ag reflection layer. Also, it can be observed from Figure 4.3(c) and (e) that the In distribution in MQW's is inhomogeneous, *i.e.,* two pairs of MQW's towards the Ag side have slightly less atomic% in relationship to other two pairs of MQW's toward the superlattice end. This verifies that the source of In diffusion into the Ag layer is from either InGaN/GaN-based MQWs or In-based superlattice. The reason for In diffusion and In content fluctuations along the MQWs is the well-known thermal variability phenomenon, which is related to the difference in growth temperature between the GaN layers and InGaN wells. The high growth temperature of p-GaN (hole transport layer) and later Ag thermal annealing process at higher temperatures attribute to the In re-evaporation or thermal damage to InGaN/GaN MQWs [239]. Consequently, out-of-plane In diffusion penetrates into Ag mirror layer and the In content in the QWs decreases, particularly for those QWs that are located close to the interface of p-GaN and Ag. This nanoscale inhomogeneous distribution of In will seriously change the potential profile of InGaN/GaN MQWs because of In segregation at the Ag mirror layer. This is because the optoelectronic properties of LEDs are very sensitive to the In content distribution in the InGaN well layers, and any alternation in the In composition profile has both a direct and secondary effects on the LED device band structure [240].Subsequently, this results in the reduced
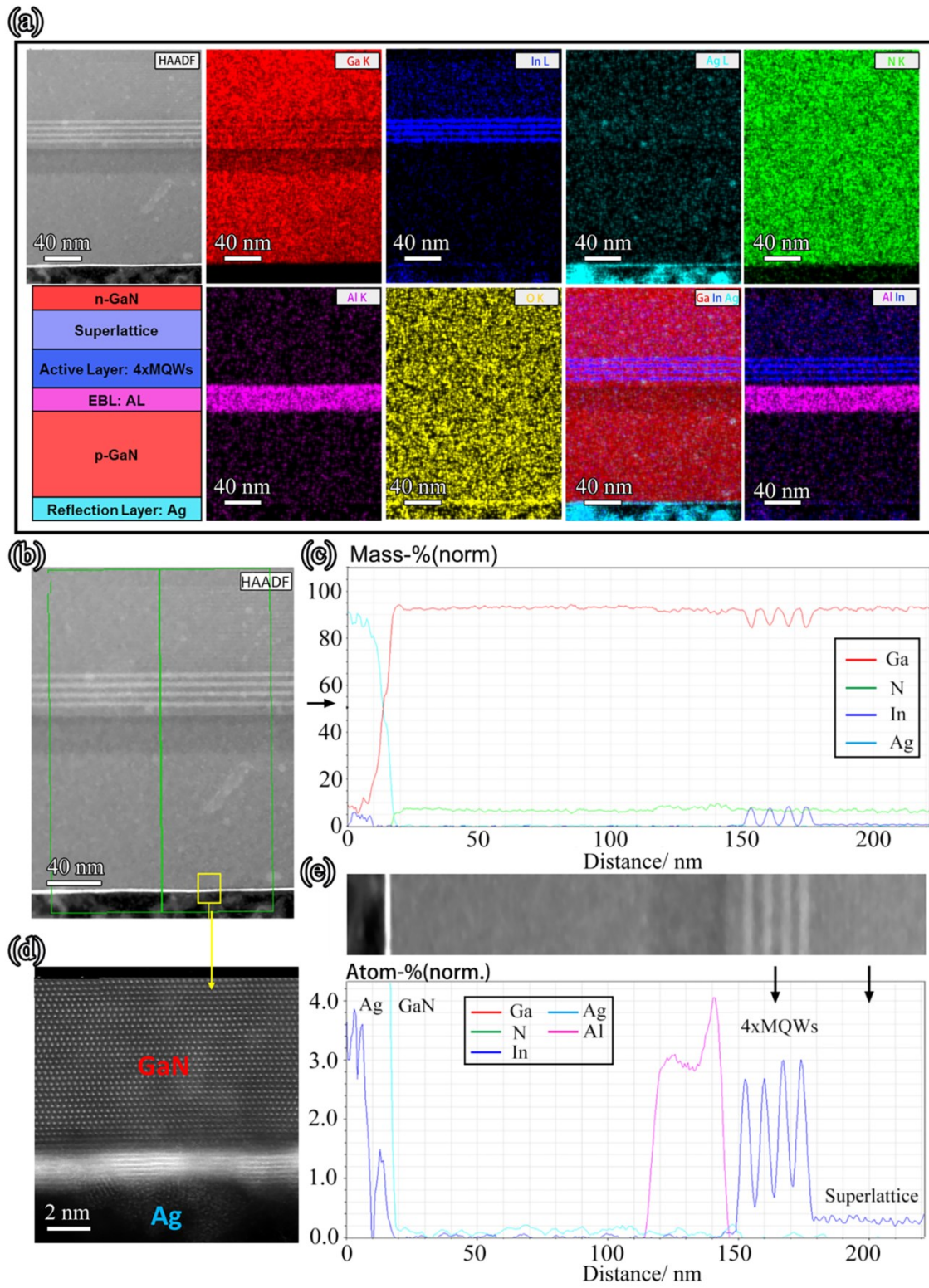
Figure 4.3 (a) STEM-EDX elemental chemical analysis. (b), (d) High-angle annular dark-field (HAADF) images. (c), (e) Line spectrum across the MQWs and GaN-Ag interface.

overlap between the electron and hole wave functions in the InGaN quantum well layer, and thus decreases the IQE. Moreover, In diffusion into the Ag mirror layer will also impact optical (reflectivity) and electrical (resistivity) properties of LED as well. Ag reflectivity gets reduced because of lattice distortion caused by In diffusion [73]. Also, any impurity in the Ag mirror layer degrades its surface quality and hence increases its contact resistivity, which leads to lowering of the wall-plug efficiency (amount of light power produced compared to the electrical power applied) of VLED.

2) It is important to note that the Ag-GaN interface is not abrupt and that the Ag metal gets diffused into the GaN semiconductor layer, as indicated from the STEM-EDX line spectrum (Figure 4.3(b) and (c)). Possible reasons involve poor adhesion between the Ag reflective (metal) and GaN (semiconductor) layers, different thermal annealing (temperature cycle) and lattice mismatch (stress) during the fabrication of GaN and Ag layers [241], [242]. Furthermore, thermal annealing, which is performed in the O_2 ambient environment to lower the contact resistivity of Ag metal, exhibited interdiffusion between Ag and GaN, which disrupts Ag-GaN interface (Figure 4.3(d)) [243]. In this case, interfacial Ga vacancies will be generated substantially, which can degrade the Ohmic contact (metal-semiconductor junction) or change energy levels (e.g., Schottky barrier height) [22], [244]. In addition, dissimilar properties between the Ag metal and GaN semiconductor materials (Table 4.3S) can potentially result in unwanted diffusion and intermixing. For instance, lattice mismatch (strain) and different miscibility between different materials can cause Ag atoms into the upper layer of GaN (as no barrier layer exists), which will lead to inhomogeneous distribution of carrier concentration or photon transport at Ag/p-GaN interface and, ultimately influence the optical and electrical performances of VLEDs.

Moreover, the chemical distribution map in Figure 4.4 reveals that Ag further diffused into the QWs (active region), even contaminated and disrupted the In-based superlattice layer. Such excessive Ag diffusion into the GaN region will mainly affect the crystal quality of QWs, as shown in Figure 4.4(b) (yellow marked circles). The degradation of the crystal quality of InGaN/GaN MQWs will decrease the efficiency of the active region in generating photons by varying the energy levels (bandgap). This additional reliability issue
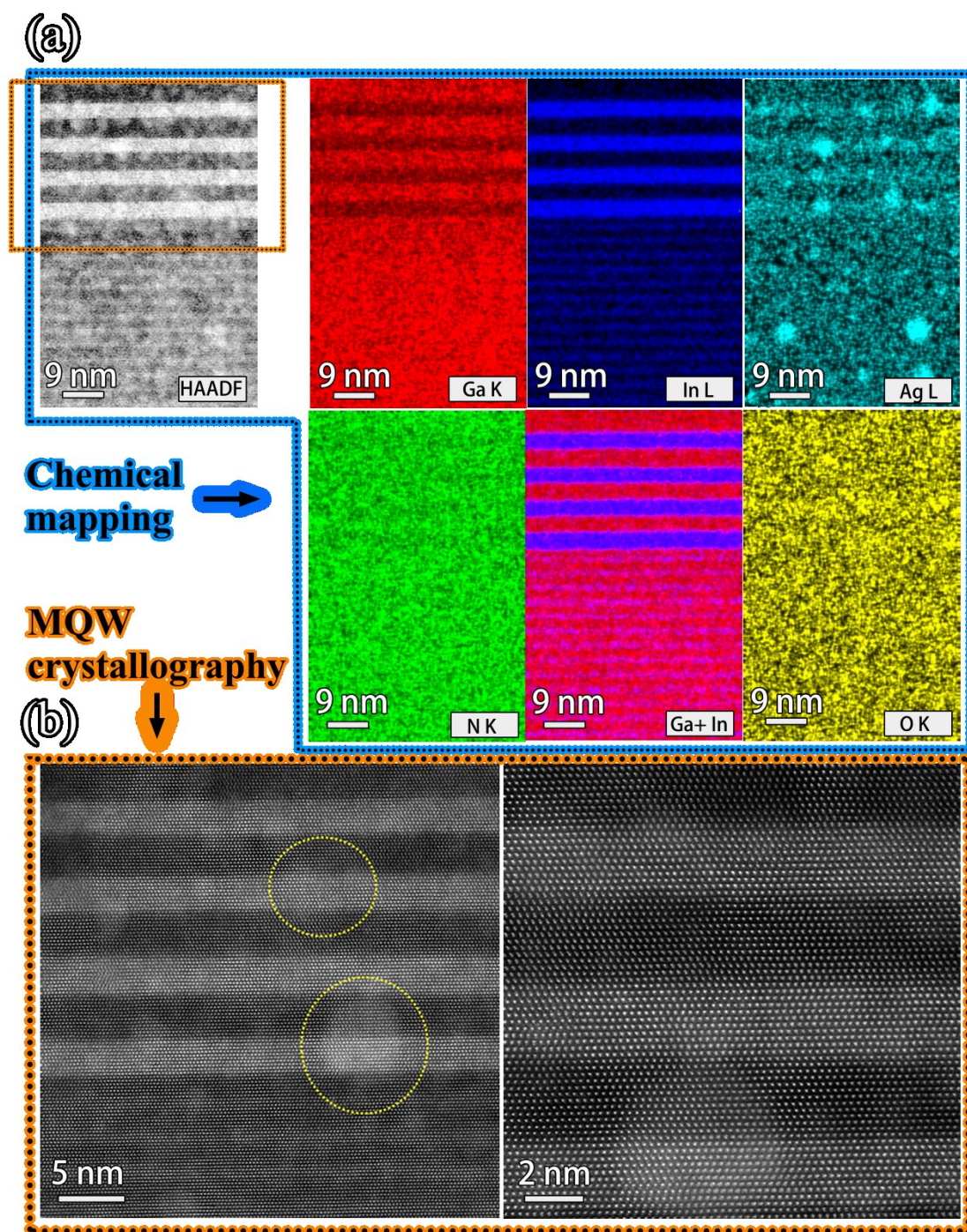
Figure 4.4 (a) STEM-EDX analysis showing Ag diffusion into InGaN/GaN-based MQWs. (b) HR-STEM HAADF images showing the Ag particles contamination (yellow marked) into quantum wells making their interfaces non-abrupt**.**

of the Ag is due to its electromigration property, and such interfacial reactions between the Ag metal and GaN were also addressed by other groups using the secondary-ion mass spectrometry (SIMS) technique [242], [243], wherein Ag diffused into the light-producing

active region (MQWs), thereby creating deep levels in the GaN semiconductor material and hindering the light output [46]. Furthermore, Ag migration inside of the MQWs serves as a non-radiative recombination centers that can shift the spectrum (optical wavelength) of a particular blue LED device by impairing the carrier confinement and transport mechanism at the active region of the LED. Consequently, diffusion of Ag (metal) into GaN (semiconductor) or MQWs (active region) will not only reduce the IQE but also the overall EQE of the VLED device.

3) In Figure 4.3(a), STEM-EDX analysis indicates Ag oxidization at the Ag-GaN interface, which is consistent with previous reports regarding the Ag thermal instability issues, such as Ag oxidization post-annealing, void formation, and agglomeration due to thermal annealing process (500-600 °C) performed in O_2 ambient environment [245], [246]. Also, in Figure 4.3(c), the long diffusion tail of Ga in the Ag layer clearly indicates the dissolution of Ga atoms in Ag. Thus, the formation of Ag-O and Ag-Ga bonds at Ag-GaN interface indicates the oxidation of Ag, and existence of Ag-Ga solid solution, respectively. The reason is that the oxygen molecules, which get incorporated during oxidation annealing result in decomposition of the GaN-Ag interface to form GaO_x rather than GaN because Ga-O has higher bonding strength compared with the Ga-N bond and thus contributes Ga out-diffusion to Ag metal layers. After the oxidation annealing process, while the Ag layer was brought in to make a direct contact with the p-GaN layer, the Ga atoms from the GaN layer dissolved into Ag layer to form Ag-Ga solid solution because of the high solubility of Ga in Ag [242]. In fact, Ag in-diffusion promotes the Ga-out diffusion. Hence, such Ag oxidation and agglomeration degrade the Ag surface morphology and subsequently reduce the reflectivity of the LED device.

In the context of optical reflectivity, Ag is considered as the most common reflector for the GaN-based flip-chip or VLEDs because of its good Ohmic characteristic on p-GaN, and high reflectivity at ultraviolet visible regions. However, the (2) and (3) aspects of Ag

diffusion discern that the Ag reflector undergoes electromigration and thermal degradation issues, such as Ag oxidization and/or agglomeration upon annealing, which lead to the degradation of LED performances.

In summary, In and Ga show out-diffusion into Ag layer, whereas Ag tends to diffuse into the GaN region during the LED manufacturing process. In/Ga diffusion into Ag degrades the reflectivity of the Ag mirror layer, whereas the composition variations or reactions induced by the diffused Ag into the GaN region can compromise the IQE of the LED by forming non-radiative recombination or scattering centers in an active layer. Hence, whether semiconductor material diffuses into the metal layer or vice versa, in either case, it will impact the performance of the finished VLED product.

Overall, these findings from the STEM analysis are critical in exploring the origin of decreased luminous efficiency; for instance, almost 60% of IQE has been achieved so far for the blue LEDs operating at a wavelength (λ)$\sim$ 450 nm [67], and still there is a potential to improve its performance by optimization. Moreover, these results suggest the different diffusion widths that originate from the growth temperature variation (between GaN, InGaN and Ag layers), and the non-availability of the diffusion barrier between Ag and GaN interface. To mitigate such in/out-diffusion issues, the Ag-GaN interface needs to be optimized by incorporating appropriate transparent barrier layers, for example, tin-zinc oxide interlayer [244]. Also, the formation of Ag–O and Ag alloy (Ag–Ga) during the thermal annealing process can be suppressed by having a multilayer stack of Me/Ag/Ru/Ni/Au (where Me = Ni, Ir, Pt or Ru) contacts or barriers for high-power GaN-based VLEDs [242]. Further suggestions are listed in the optimization section.

4.3.2 Grain Morphology

4.3.2.1 Vertical Thin Sample (SEM-TKD)

Another factor that affects the quality of the Ag layer and the LEE is the grain morphology. The grain morphology of the Ag mirror layer needs to be scrutinized to correlate its impact on transport related properties, such as electrical resistivity, reflectivity, mass transport, and thermal conductivity [201], [212], [247].

In this regard, powerful SEM-based TKD with a spatial resolution of 2-15 nm provides key nanostructural information, such as orientation mapping (OM), grain size analysis, poles figures (PFs, texture), and Kikuchi diffraction patterns [118]. SEM-based TKD and EBSD techniques have a significant advantage over other counterparts because of their automated analysis of grain morphology with diffraction system [248], [249]. Automated analysis of grain morphology is inevitable because grains and their GBs occupy a considerable volume in the LED structure. Figure 4.12S shows the complete picture of cross-sectional grain morphology, PFs and crystallographic information obtained from the TKD mapping data across the multi-layered structure of the VLED. However, for a particular ROI, i.e., GaN (semiconductor) and Ag (metal) layer/interface is shown in Figure 4.5.
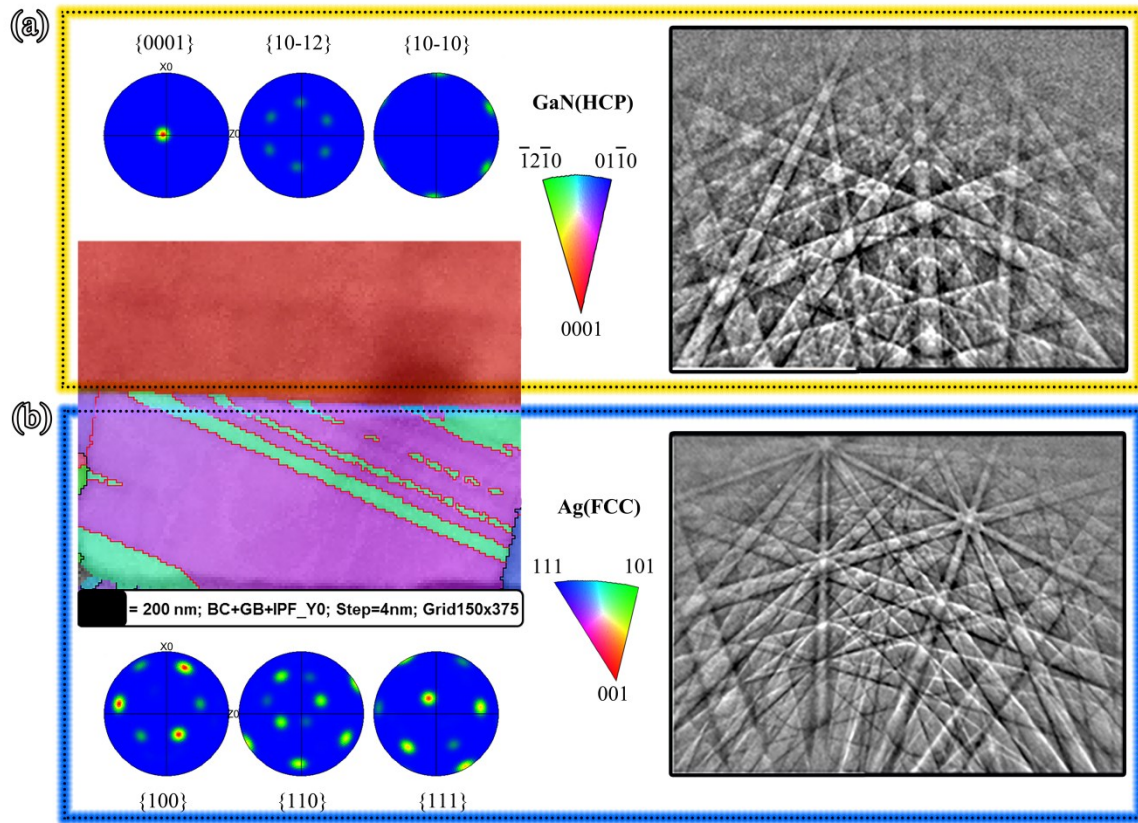
Figure 4.5 Cross-sectional SEM-TKD analysis. (a) GaN. (b) Ag having twin boundaries with their respective pole figures (PFs) and Kikuchi diffraction patterns.

In grain morphology, OM analysis identifies GaN as a mono-crystalline material with no GBs (Figure 4.5(a)). However, beneath the GaN layer, the Ag metal reflective layer has

special GBs oriented in a specific direction, as shown in Figure 4.5(b). Aztec software processed TKD data also reveal that most of the Ag mirror region is dominated by the high-angle grain boundaries (HAGBs) but with a special type of boundary called Sigma 3 ($\Sigma3$) TBs that are shown in red diagonal-shaped lines (Figure 4.5(b)). TKD analysis discerns that $\Sigma3$ TBs were found abundant in the Ag reflective layer (~80.9%); however, a few were also identified at barrier/adhesion layers, i.e., Pt (~9.36%) and W (0.65%), as marked in red (Figure 4.12S). The tendency of face-centered-cubic (FCC) metals to form TBs is related to the TB energy, i.e., those with low TB interfacial energy, such as Ag easily form twins. Contrary to that, metals with high TB energy interferes with twins formation; thus, twins are quite rare there, e.g., Pt, W.

In the context of correlating these GB orientations with the material properties, it has been reported that to enhance the material's strength, HAGBs are required because they are more resistant to dislocation motions [198]. However, it is also noted in microelectronic devices that HAGBs are more electrically resistant than low-angle grain boundaries (LAGBs, subgrain) boundaries with the exception of a special type of high-angle $\Sigma3$ (TBs) [202], [207]. Special TBs at the Ag mirror layer will impact its electrical resistivity and mobility [202]. In fact, special TBs with less interfacial energy have low electrical resistance and less mobility compared with HAGBs [206]. Moreover, contrary to HAGBs, special $\Sigma3$ TBs are considered to be poor pathways for electromigration voiding or mass transport [57], [206].

Interestingly, OM also highlights the position of special TBs and it can be observed that the width of twins (diagonal lines) at the Ag layer gets sharp while moving towards Ag-GaN interface, i.e., narrow twins are slightly toward the upper GaN layer (Figure 4.5(b)). The measured average twin spacing in the Ag film found to be ~10 nm. Here, identifying such special TBs at the cross-sectional layers of VLEDs is important for the following aspects: 1) Such narrow (nano) and dense twins toward the GaN layer may influence the reflectivity of the Ag mirror layer, consequently enhancing the LEE of the LED device, 2) TBs with relatively low mobility contribute to a high degree of microstructural stability [208], [250], 3) TBs improve the electrical conductivity because of their low resistance, 4) TBs provides better thermal stability [209], [251], 5) also, it enables us to associate TBs with origin of

118

defects (light loss) in a reflective layer of VLEDs, which may act as barriers for other HAGBs during growth and lead to the initiation of points of failure, and 6) TBs with less energy will provide poor diffusivity paths for electromigration mass transport while appearing at the Ag metal reflective layer of the VLED [205]. Nevertheless, TBs have shown the capability to increase the strength in other fcc metals (Cu, Al, Ni, *etc.*) by acting as barriers to the transmission of dislocations [208], [252]. However, such special TBs have a significant impact on electrical properties, which imperatively contributes toward the lifetime of the indispensable Ag reflective layer in the VLED.

In addition, the grain size also influences the Ag reflectivity because the existence of any fine or coarse grain size induces certain type of diffusion paths, i.e., their GBs, which might result in either scattering paths or defective (trapping) points in photon and electron transportation. Our TKD cross-sectional grain size analysis of Ag reflective layer showed that it has an average fine grain size of ~ 90-110 nm (including TBs). Also, Figure 4.5(a) shows the PFs (degree of preferred orientation), and Kikuchi diffraction patterns from the topmost GaN layer indicate that it has a wurtzite crystal hexagonal close-packed (HCP) structure with strong {0001} texture in the growth direction (c-axis). In Figure 4.5(b), the PFs obtained from the cross-sectional layer of Ag hold peculiar shaped texture at {100}, {110} and {111} with fcc diffraction patterns owning to the special TBs. Because a twining relationship between the two component grains occurs, i.e., in between any two strong component grains there exists a weak component grain and vice versa.

Hence, such a variety of grain size and texture across different layers of VLED (Figure 4.12S) might exhibit unusual properties in light emission operation. For instance, the resistivity of a coarse-grained sample is lower than that of a fine-grained one because the former has a smaller number of GBs [198]. Similarly, in the case of Ag metal reflective layer, the grain size and texture (grain orientation) impact the electrical and optical properties of thin-film LEDs. This effect is mainly attributed to the mechanism of charge or photon trapping and scattering at the GBs. For instance, EM lifetime is highly influenced by the grain size distribution and texture [253]. The reason is that the EM normally occurs via diffusion along GBs; hence, grain size needs to be increased to reduce the GB area for diffusion. This minimizes the metal diffusion and trapping of charge or photons because

there are fewer sources of vacancies or less fast diffusion paths will be available for them. Also, point defects (vacancies and impurities) and extended defects (GBs) scatter the photons and electrons, thus shortening their mean free paths. On account of the photon and electron scattering at the GBs, a polycrystal has lower thermal and electrical conductivities than a single crystal. In the case of W or Pt (Figure 4.12S), coarse grains contribute to the stability of diffusion barriers because they are most effective in filling voids or holes at HAGBs (reducing sources of vacancies), and hence yields higher median times to failure (MTTF) [254]. Apart from that, coarse grains would help in minimizing hillocks (short circuit) formation, reducing film resistivity (less scattering of charge carriers), and thereby better controlling Ag mirror reflectivity by protecting it from chemical etching, diffusions, or contaminations during the deposition or photolithography process.

In summary, SEM-TKD provides valuable pattern quality maps, grain size and orientation mapping, texture, and Kikuchi diffraction patterns from cross-sectional layers of VLEDs. Also, in general, coarse-grained materials with LAGBs are preferred in semiconductor devices; however, promoting certain grain structures with particular orientation depends on the functionality of each material (layer or interface) in that specific device. For instance, in coarse-grained metals with LAGBs, the increased thermal stability, electrical conductivity, and ductility merits are accompanied by the loss in strength. Contrary to that, in nanocrystalline metals with HAGBs, the increased strength is accompanied by the loss in thermal stability, electrical conductivity, and ductility. However, a special case of nanotwinned or TB materials (such as in the Ag mirror layer) exhibits high tensile strength with good ductility, thermal stability, and electrical conductivity [209], [251]. Therefore, in prospective electronic devices, these nanotwinned structures may express distinctive properties in comparison to coarse-grained and nanocrystalline metals.

4.3.2.2 Planar Bulk Sample (SEM-EBSD)

Nevertheless, SEM-TKD or transmission EBSD (t-EBSD) has a better spatial resolution (2-15 nm) compared with conventional EBSD technique (30-100 nm).[118] However, SEM-TKD cannot be performed on a bulk or thick specimen, as it requires electron transparent
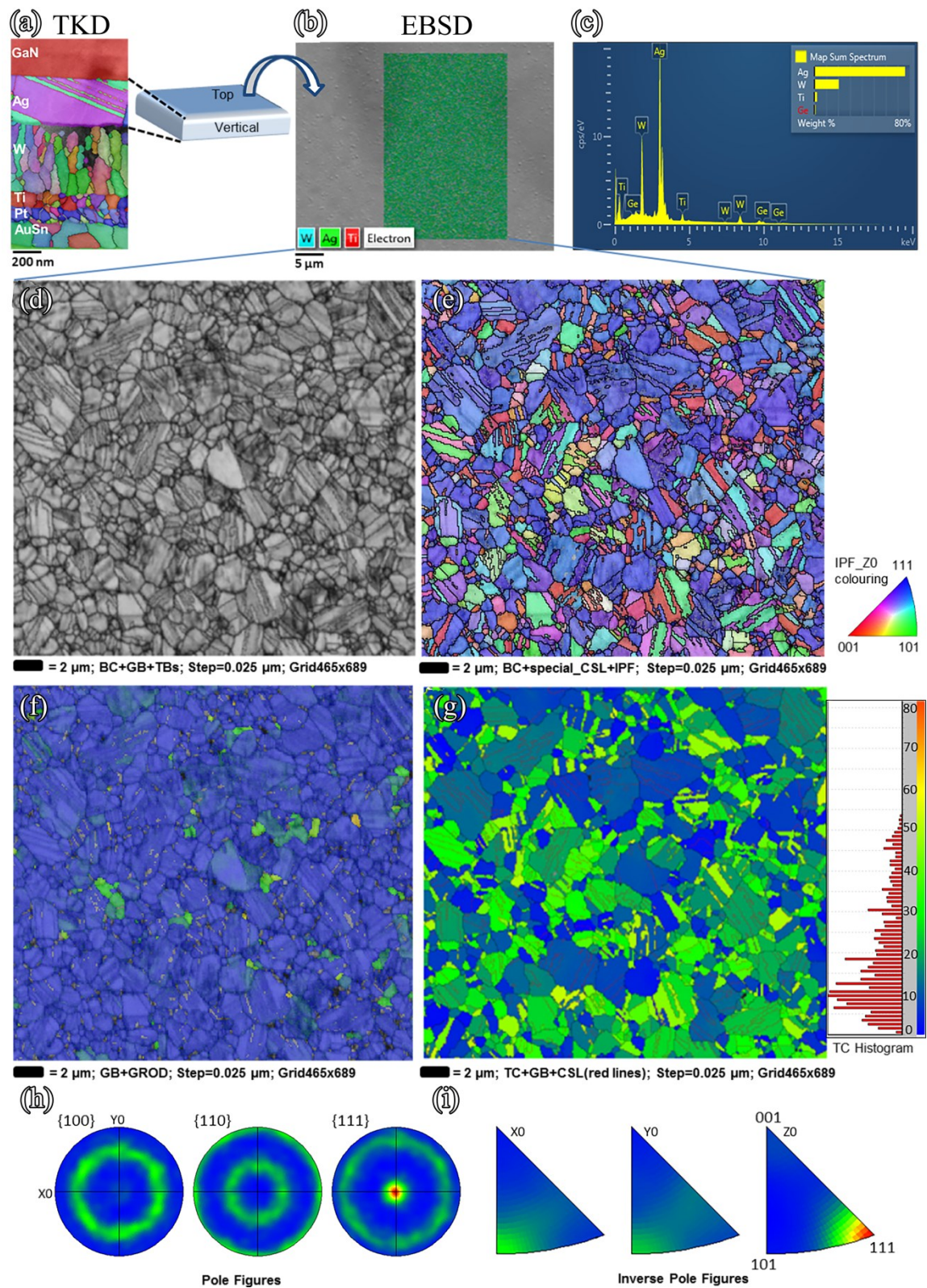
Figure 4.6 SEM-EBSD analysis. (a)-(i) On the top (bulk) surface of the Ag reflection layer.

thin samples. Although robust SEM-TKD results reveal interesting special TB's features (Figure 4.5(b) and Figure 4.6(a)) at the thin Ag mirror layer (in a cross-sectional view), it is equivalently important to further investigate the nature of the top bulk surface of the Ag mirror layer by applying SEM-EBSD and AFM techniques (in a planar view). Figure 4.6(b) shows the SEM-EBSD analysis on the top bulk surface of the mirror layer, and its spectrum verifies the presence of Ag (Figure 4.6(c)). Note that SEM-EBSD was performed on the top (bulk) surface of the Ag mirror layer, whereas SEM-TKD analysis was applied on the vertical (thin) sample of the Ag mirror layer (Figure 4.5).

On the top bulk surface of the Ag layer, almost 2000 grains were detected by SEM-EBSD in a scan area of 5 x 5 μm^2 at a step size of 25 nm, and the average grain size was found to be ~300 nm (Figure 4.13S). Such compact fine grains promote better reflectivity compared with the coarse grain structure because coarse grains involve larger micro area for more loss of light by absorption rather than reflection [255]. Also, Figure 4.6(d) shows SEM-EBSD-based BC and GB analysis of bulk Ag mirror layer, which verifies enrichment of TBs. Figure 4.6(e) reveals in detail the microstructural analysis, i.e., the grain morphology and twinning structures (black marked lines) indicate special TBs for the bulk (planar) surface of the Ag reflective layer. Figure 4.6(f) map shows the grain reference orientation deviation (GROD) analysis, which displays the misorientation angle of a point from the grain's average orientation. It can be seen that all misorientation angles are less than 2°; so, the visible deformation is really quite small, i.e., majority of the grains are in the same color. GROD map has a significant role in the interpretation of the local accommodation of deformation within the microstructure.

In Figure 4.6(g), another OM component called the texture component (TC) shows a map of misorientation relevant to the reference point (here, grains with {111} direction), and indicates that most of the mapped area is within the ideal orientation (the only peak of 10° deviation is found in the TC inset histogram). In the scope of mirror layer reliability, such texture has its advantages, as it indicates the higher mean time between failures (MTBF, circuit life) and higher density of GB pathways that are inactive for EM mass transport [206]. To further explain that texture, PFs, and inverse PFs provide considerable lines of evidence of texture in the {111} direction parallel to the Z-axis (axial direction). The high

exposure densities (red regions) are shown at the center of the {111} PF (Figure 4.6(h)) and the {111} corner of the Z-axis (Figure 4.6(i)) indicates a strong fiber texture. Hence, the Ag reflective mirror layer holds strong <111> fiber texture in the Z-axis (normal to the bulk surface plane).

In addition, EBSD data analysis further manifested that Ag layer has a specific class of TBs, i.e., coincident site lattice (CSL) boundaries with dominant Σ3-value and misorientation angle of 60° (rotation about <111>), as evident from Figure 4.13S graphs. The Σ3 <111> CSL boundaries in Ag (fcc) metal typically provide lower electrical resistivity, lowest TB energy, higher strength and inherently more thermal stability properties. Such a combination of properties is ideal for reducing the effects of EM, and hence promoting low-contact and highly reflective p-contact mirrors in VLEDs. Furthermore, once the MQW generated source light hits such TBs of an Ag layer; light will adopt a certain reflection path depending on these special TBs because they possess specific mirror lattice symmetry operation. Therefore, the role of twin structures at the Ag mirror layer in the enhancement of photons scattering (light reflectivity) can be correlated with top textured (structured) surface of the GaN layer or the bottom PS layer. Because they normally improve the light extraction of LED by generating specific escape cones (twin-shaped), a major portion of light reflects back or scattered out rather than being absorbed by the base substrates [139], [256], [257]. Thus, these EBSD results from the highly reflective mirror layer are significant in failure and optimization analysis because GB engineering substantially relies upon CSL analysis.

4.3.3 Surface Topography

Apart from GB engineering at the Ag mirror layer, the surface roughness also impacts the reflectivity of light, i.e., reflectivity degrades because of increase in the surface roughness [255], [44]. To evaluate the roughness (micro surface topography index), AFM analysis was conducted on the bulk surface of the Ag-based mirror sample, and the RMS roughness value was measured to be ~3-4 nm (Figure 4.7). This value indicates that the Ag surface is flat (smooth), which is better for the quality of Ag reflectivity. Notably, SEM-EBSD provides grain morphology (grain size, GBs or TBs), whereas AFM assists in surface
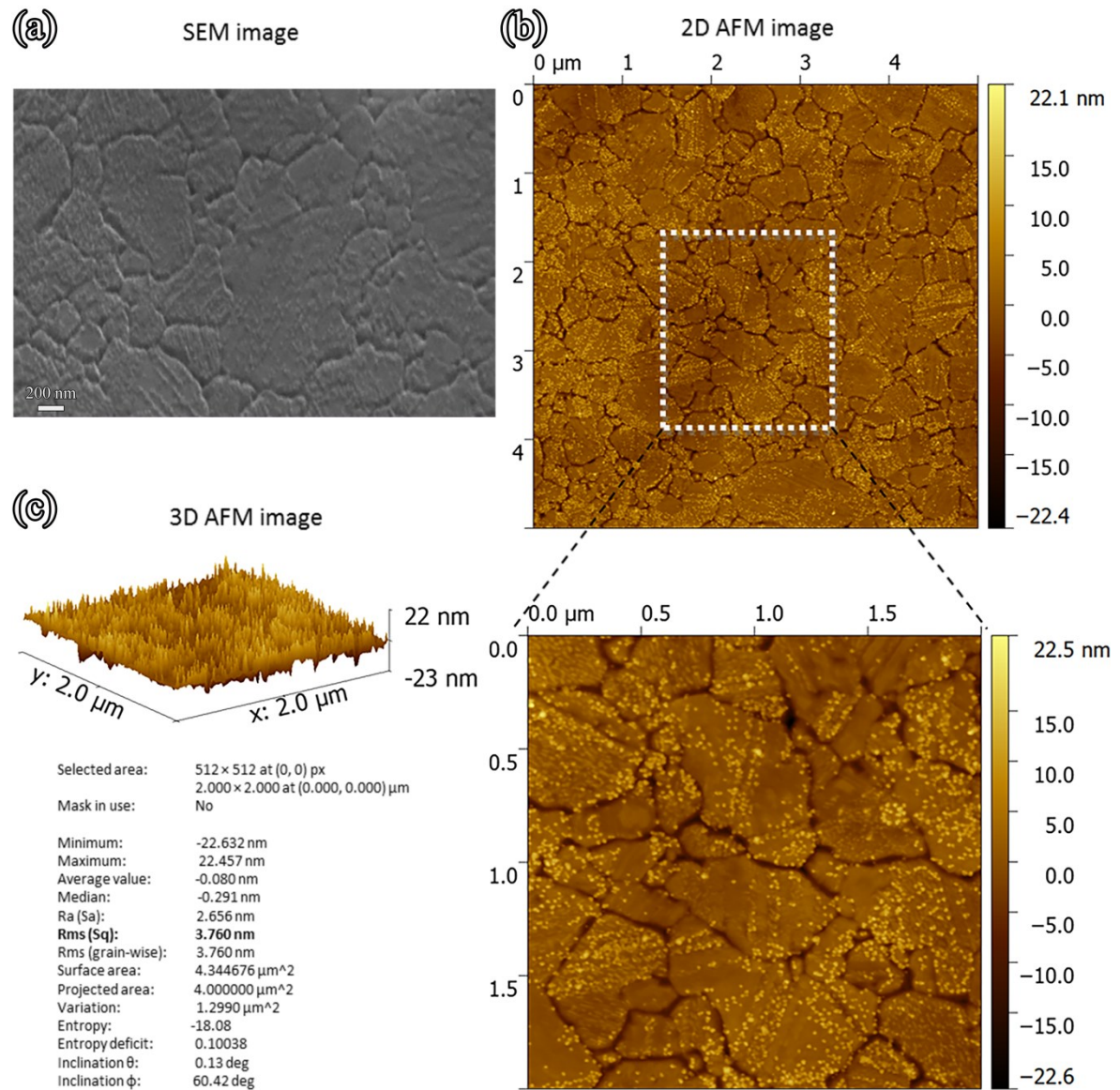
Figure 4.7 (a) SEM image. (b) 2D AFM. (c) 3D AFM analysis on the top bulk surface of the Ag mirror layer.

topography (roughness). Collective data analysis from EBSD (grain morphology) and AFM (surface topography) reveal that the Ag reflective layer possesses a fine-grained structure ~300 nm with TBs, and a smooth surface of ~3-4 nm. Such fine grains with lower roughness results in enhancement of the total optical light output of the VLED device [50], [258]. Also, previous research about the structure of reflective metal surfaces stated that metal surfaces are highly reflective if their microstructure consists of crystallites smaller than the wavelength of visible light, i.e., $\lambda < 400nm$ [255]. On that account, our SEM-

124

EBSD and AFM data are quite consistent in identifying the nano-morphology of the Ag layer, i.e., grain morphology (grain size of ~300 nm) and surface topography (roughness of ~3-4nm), respectively. Thus, the finest (smaller) grain size with special TB's and a flat surface are necessary features to maximize the reflectivity of the Ag layer.
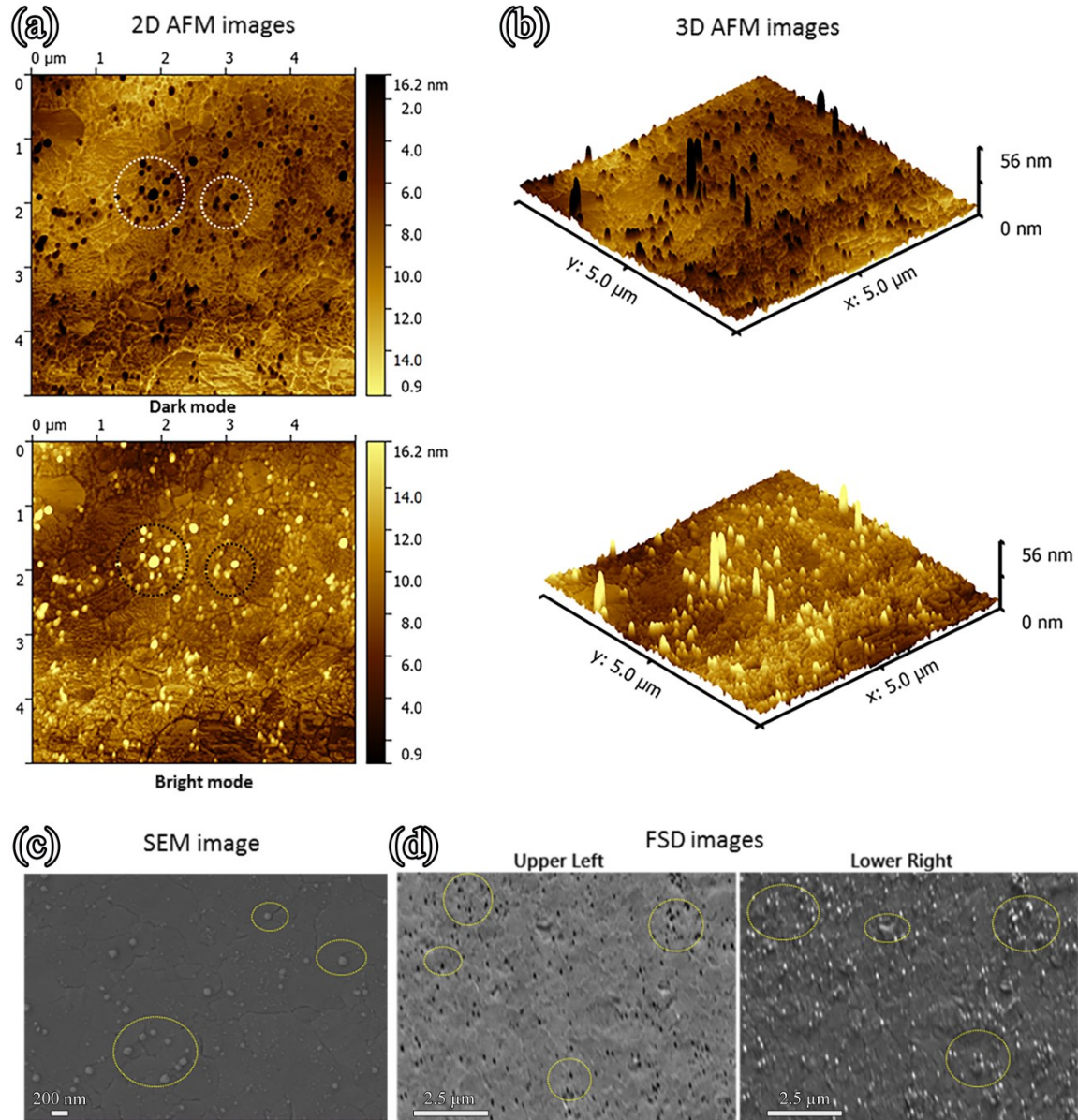
Figure 4.8 Images of the Ag mirror surface from: (a),(b) AFM. (c), (d) SEM and FSD (detectors for characterizing material microstructures in SEM) showing whisker formation marked in yellow dotted circles.

However, in Figure 4.8, it can also be discerned from AFM, SEM and forward scatter detector (FSD) images that protrusions in the form of whiskers (such as prills or bubble particles) exist at the Ag mirror layer. The formation of these whiskers is related to agglomeration phenomena that occur in Ag films during the thermally assisted O_2 annealing process, which involves the evolution of capillary instabilities [245], [246]. Such Ag agglomeration and/or Ag oxidization will increase the roughness of the micro-surface of Ag up to 10-15 nm, leading to a decrease of reflectance over the whole spectral range. The reason is that a rougher surface not only has a larger micro area to reflect light but there is also more loss of light by absorption, thus decreasing the reflectance which eventually leads to a drop in luminous efficiency [255]. Also, these whiskers might become a source of pits for trapping of light.

Further, AFM results are also consistent with TEM-EDX results (Figure 4.3), which verify the presence of O at Ag interface that leads to Ag agglomeration or oxidisation. Interestingly, EBSD and AFM analyses of the Ag film identify that these whiskers or agglomeration forms mostly along the GB or TBs (defective paths), as shown in Figure 4.7(b) and Figure 4.14S. To mitigate that, thermal annealing temperature needs to be optimized to obtain a smooth Ag microsurface.

Hence, application of SEM-EBSD and AFM techniques on nanotwinned Ag metal is exciting because this combination provides a better understanding of the physics of failure (PoF) in the methodology of Ag fabrication. Thus, the smaller the grain size and smoother the surface, the better the quality of Ag for reflection purposes.

4.4 Prospective Optimization

In the context of optimization for device performance enhancement in terms of LEE and output power, factors such as nanostructural composition, selection of metallic elements at reflection, barrier or adhesion, and wafer bonding layers need to be considered in correlation with electrical resistivity, CTE or mechanical stress, fabrication methodology and grains morphological parameters. On the basis of analysis and results, possible optimization suggestions are given as follows:

1) GB engineering, i.e., grain structure, SB (TBs), and texture orientation need to be well controlled as electron or photon scattering mechanism and electromigration lifetime are highly dependent on the grain size distribution [201], [203], [206].

2) Nano-twinned metals, e.g., Ag, should be promoted as these structures exhibit distinctive properties (e.g., high tensile strengths, good ductility, thermal stability, and electrical conductivity) as compared to the nanocrystalline or ultrafine-grained metals [207], [208].

3) To mitigate issues of Ag diffusion into the GaN or active region and In/Ga out-diffusion into the Ag mirror layer, high thermal treatments should be avoided on Ag and p-GaN layers to prevent metal-semiconductor diffusions [239], [243]. Ni/Ag/TiW metal stack is found to tolerate high-temperature annealing [259].

4) To reduce thermal stress between GaN and metal-alloy-based interfaces, the tunable incorporation of diamond-like carbon (DLC) layers on the reflective layer has the distinct capability to match its CTE with GaN and hence enhances the thermal diffusion [260], [261].

5) The GaN-Ag interface needs diffusion barrier layers such as tin-zinc oxide (TZO) [244] and nickel-titanium (NiTi) related alloys that can effectively block Ag diffusion [262]. Alternatively, nickel-vanadium (NiV) as a diffusion barrier can be used to increase the mirror reflectivity in high power led chips [263].

6) Although thermal annealing in O_2 ambient produces a low resistivity Ag-based ohmic contact as compared to N_2 ambient, O_2 annealing still causes Ag to be oxidized and/or agglomerated, leading to degradation in both reflectance and adhesion to GaN and overlaid metals. To suppress the Ag oxidization (Ag-O), a multilayer stack of Me/Ag/Ru/Ni/Au (where Me= Ni, Ir, Pt or Ru) contacts or barriers are required for high-power GaN-based VLEDs [242]. To avoid the Ag agglomeration, i.e., whiskers formation which increases roughness and resistivity of the mirror layer, thermal annealing process should be performed at a low optimum temperature to attain smooth highly reflective mirror contacts [264]. Moreover, the

Ag replacements or combination with other elemental candidates, such as Sn (which forms fewer whiskers than Ag does) or Rh as RhZn/Ag (which has high reflectivity and barrier property), will improve the efficiency of extracting light in LEDs [255], [265].

7) Ag alloys (AgNi/AgCu/AgAl) or SiO_2/TiO_2 dielectric Bragg reflectors (DBRs) combined with highly the reflective Ag layer could overcome the limitation of LEE [49], [266].

8) In addition, selection of adhesion or barrier materials and their film thicknesses should also be considered in terms of fabrication cost. For instance, rather multiple thick layered structure of Pt or Pt/W on both device and carrier wafers, and a single thin layer of Ti or Ti/W only at the device wafer will be substantially less expensive approach [38]. In parallel, fine grains at adhesion layers will reduce the cost of manufacturing blue VLED. Thus, optimal agitation parameters should be established for each particular layer to achieve the best micro uniformity.

9) Contrary to metallic barriers, non-metal barriers (e.g., SiO_xN_y, SiCN or TaN) would have a significant edge because of their closely matched CTE to dielectric materials (e.g., substrates) [253], [267].

10) In VLEDs, the top small surface (n-GaN) and the large backside reflective mirror (p-contacts) normally cause current crowding issue, to mitigate this, a highly transparent conducting layer (TCL) or graphene current spreading layers are used to increase the light output power and wall-plug efficiency [47]. However, the trade-off between optical transmittance and electrical conductivity must be addressed as well.

11) Selecting a suitable position for the Ag reflection layer also affects the LEE of the VLED because the overall LED LEE quite sensitive to the location of the mirror layer and the base substrate height [268].

12) To enhance the optical output power of GaN-based LEDs graded In composition QWs and on-top layers nanoparticle-assembled or nanowires (ZnO) can be used [85], [269].

13) Influence of laser lift-off (LLO) or chemical lift-off (CLO) on optical and structural properties of InGaN/GaN vertical blue LED should be minimized with alternative approaches, such as natural substrate lift-off (NSLO), and plastic substrates [222], [270] The reason is that CLO and LLO can produce adverse effects involving etching non uniformity and tensile strain, which will lead to piezoelectric polarization (strain-induced electric fields in III-V nitrides). Such electric fields hinder the electron and hole recombination for photon generation, and a behavior termed as a quantum-confined Stark effect (QCSE) can be produced similar to the cases of LLEDs. QCSE reduces the recombination efficiency and increases wavelength shifts [271].

14) New microscopy technique of atom probe tomography (APT) can assist in better understanding of key interfaces (*e.g.,* Ag-GaN) of the VLED by providing 3D chemical compositions [31].

15) Introduction of new chips design such as OSRAM: UX3 [5] and integration of GaN-on-Si technology LEDs with high-electron-mobility transistors (HEMT), and CMOS-MEMS may open emerging paths in prospective smart solid-state lighting.

Hence, optimizing the Ag reflective layer is crucial to further improve the luminous efficacy and light output power of LEDs.

4.5 Conclusions

In this work, the compositional variation (elemental diffusion), grain morphology (grain structure/orientation), and surface topography (surface roughness) of the Ag reflective mirror layer of GaN-based blue VLEDs have been systematically investigated with advanced microscopes for performance optimization, and their corresponding results are as follows:

1) STEM-EDX analysis at the key interface of Ag-GaN (metal-semiconductor) determined that In and Ga from GaN (semiconductor) region out-diffuses into the Ag (metal) layer, whereas the Ag (metal) diffuses into the GaN (semiconductor) region. Ag migration occurs not only in the p-GaN layer but also into the InGaN/GaN QWs and In-based superlattice, as well. Further, the formation of Ag-O (Ag oxidation), Ga-O and Ag-Ga bonds lead to a non-abrupt Ag-GaN interface. Such interfacial diffusion between the Ag (metal) and GaN (semiconductor) degrades both the electrical and optical properties of the LED.

2) SEM-based TKD combined with EDX as a sophisticated technique provided vital information for each cross-sectional layer of VLED, i.e., grain structures (size), GBs, SBs, crystallographic orientation (textures), defects and phases that exist in between semiconductor (epitaxial) layers, and metal (adhesion, barrier, and reflecting) layers. SEM-TKD results for a thin specimen of Ag reflectivity layer discerned that it has special nano-TBs.

3) Further, SEM-EBSD analysis on the top bulk surface of an Ag reflective layer depicted its surface morphology that consists of fine-grained structures (~300nm) and more importantly possesses special CSL TBs with a strong fiber texture. Such a nano-morphology of Ag with specific texture is vital for highly reflective materials to design efficient LED light sources.

4) Moreover, the surface topography of an Ag reflective layer with an average 3-4nm roughness was determined by AFM, and shows Ag has a smooth (flat) surface. However, results also indicated that the presence of whiskers induced by the thermal annealing process (in the O_2 ambient environment) increases the micro surface roughness, consequently, deteriorating the reflectivity of the Ag mirror layer.

5) On the basis of these correlative microscopy analyses and results, feasible suggestions on performance optimization are proposed, which can be integrated into prospective VLED device scaling and modeling.

In summary, the quality of the Ag reflective layer is strongly dependent on the control of interfacial diffusions, grain morphology, and surface topography. Abrupt Ag-GaN interface and compact smaller (fine) grains with a smooth surface (low roughness) are essential criteria for the better reflectivity of light at the Ag mirror layer. Hence, these results are critical in understanding the origin of diminution in IQE and EQE, which will assist to significantly enhance the overall light emission efficiency of the VLED devices.

4.6 Future Outlook

We believe that our correlative microscopy results will open new opportunities for optimization of enhancing LED performances by controlling the GB, especially by controlling the nano-TBs. In fact, these results could have direct effects on the "Application of Ag material in the micro-optoelectronics industry" because the special nano-TBs at the Ag reflective layer might have peculiar attributes toward the enhancement of the critical LEE factor. Furthermore, these attributes only make Ag an attractive model system not only for the study of TB formation and twin-induced strengthening mechanisms in LEDs but also for other organic solar cells or organic photovoltaic (OPV) and OLED devices, where Ag serves diverse functionality as a contact electrode, reflection, or wafer bonding layer [272]–[274].

Moreover, SEM-based TKD and EBSD techniques will facilitate us in the improvement of grain alignment by correlating it with GB engineering, and subsequently, further structure-properties-process-performance relationship (material design paradigm) can be determined. Although SEM-based TKD and EBSD is less beam-damaging compared with TEM (30kV vs 300kV), there are still are certain limitations, such as time-consuming FIB preparation of thin samples for TKD or requisite of a smooth (flat) surface for EBSD analysis, and certain difficulty in obtaining patterns or textures for very thin (narrow) film layers (below <10 nm). Nevertheless, integration of different characterization techniques (SEM-TKD/EBSD, TEM, APT, AFM and RS,) can mitigate it and help further in understanding the PoF for the concerned investigated LED device.

4.7 Supporting Information

Table 4.1S Experimental methods and details

Instruments		Specifications	Purpose
Vertical LED Chip		GaN: 440-490 nm, ɳ_{opt} : 50%	Blue Light
Zeiss Auriga SEM-FIB		5 kV-30 kV 50 pA-2 nA	Milling
Zeiss Ultra plus FEG-SEM		10-30 kV	EDX
		1-3 nA	EBSD
		WD: 6-10 mm Oxford Intr. AZTec Nordlys-nano EBSD detector system	TKD
TEM	JEOL 2200FS	200 kV	STEM
	FEI Titan Themis Z aberration-corrected with Super-X EDX	300 kV	EDX
Bruker SPM/AFM		Dimension ICON SPM with ScanAsyst® image system	AFM
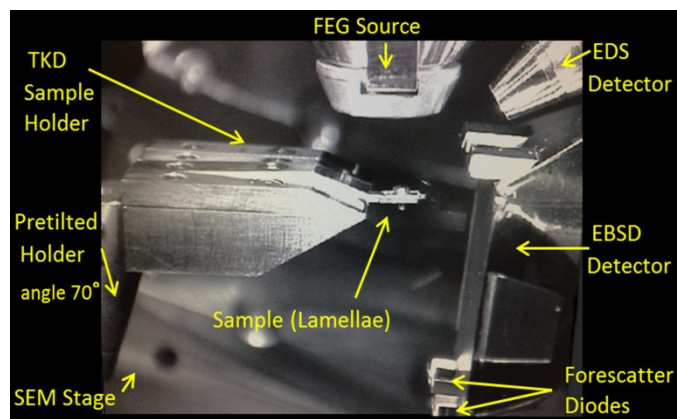
Figure 4.9S Experimental setup of SEM-TKD with EDX [57].
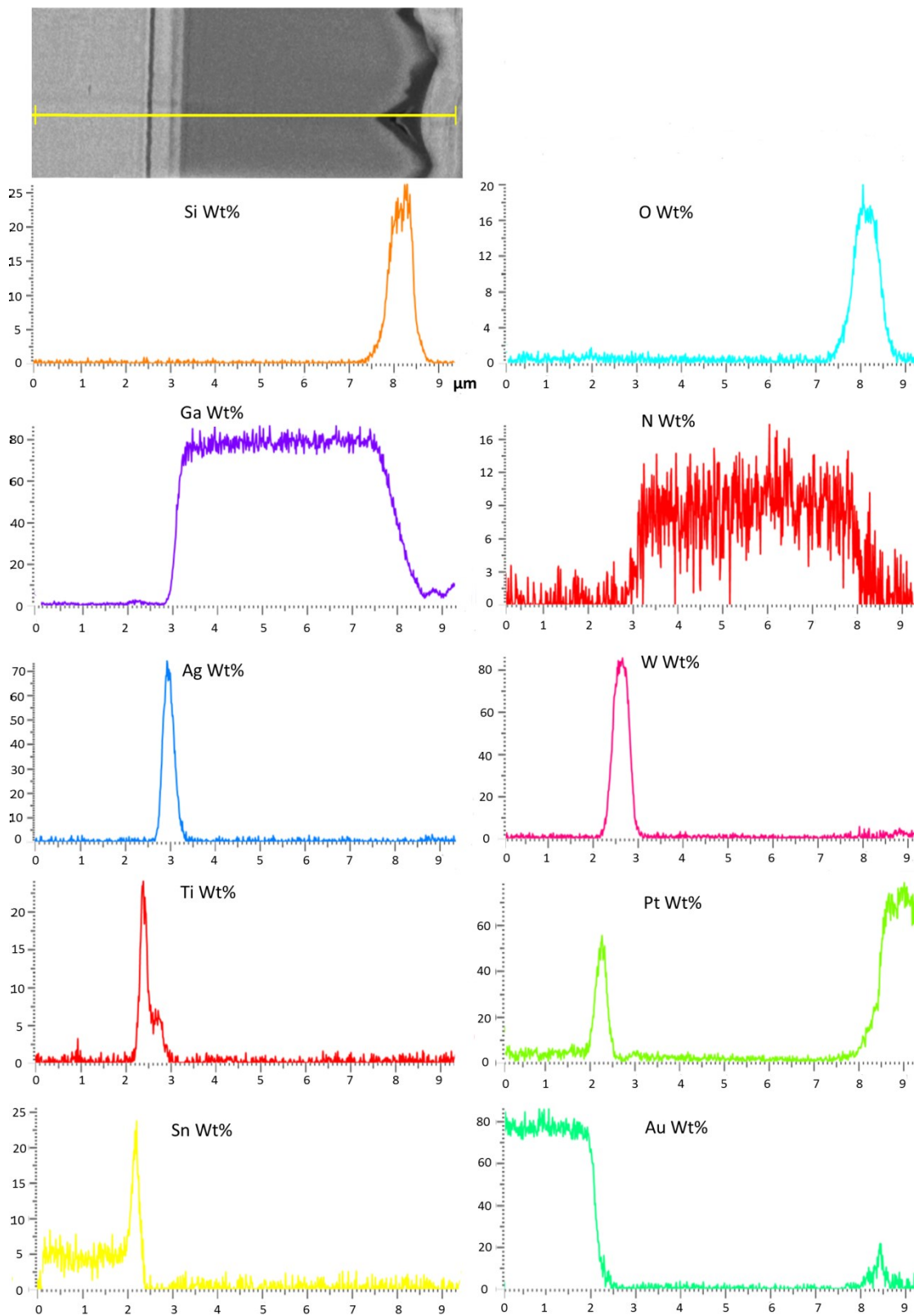
Figure 4.10S SEM-EDX line scan mapping.

Table 4.2S SEM-EDX phase acquisition data.

Phase	a	b	c	Alpha=Beta	Gamma	Space Group
Ga N	3.19 Å	3.19 Å	5.18 Å	90.00 °	120.00 °	186
Ag	4.09 Å	4.09 Å	4.09 Å	90.00 °	90.00 °	225
W	3.19 Å	3.19 Å	3.19 Å	90.00 °	90.00 °	229
Ti-Hex	2.95 Å	2.95 Å	4.73 Å	90.00 °	120.00 °	0
Pt	3.92 Å	3.92 Å	3.92 Å	90.00 °	90.00 °	225
Au Sn	4.32 Å	4.32 Å	5.52 Å	90.00 °	120.00 °	194
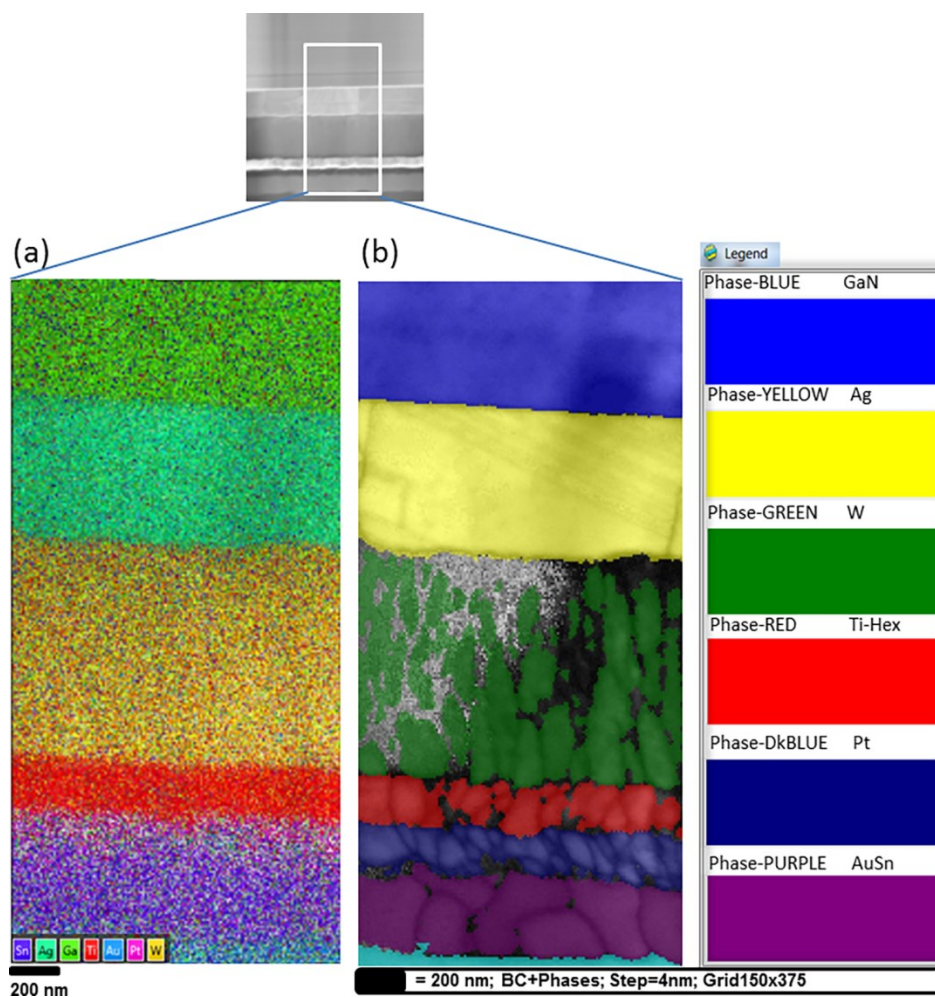
Figure 4.11S (a) SEM elemental EDX. (b) Phase mapping of cross-sectional layers of VLED.

Discussion for Figure 4.10S and Figure 4.11S

SEM-EDX allows us for rapid identification of quantification of the compositional variations across multilayered device structure. The complete stack of elemental analysis is detailed in the Figure 4.10S. In Figure 4.10S and Figure 4.11S, SEM-EDX spectra collected along the yellow marked line clearly reveals that the vertical LED top textured surface is composed of elemental silicon (Si) and oxygen (O), i.e., SiO_2 passivation layer is used for enhancement of light extraction [45], [275]–[277]. The top epitaxial layer of VLED is composed of GaN as a semiconductor (SC) [278]–[280]. Beneath the GaN layer, Ag phase (200 nm) is found as a mirror reflective layer and p-contact [281]–[286]. Usually, the mirror is produced from a highly reflective metal (e.g., Ag) by electron beam (e-beam) evaporation or sputtering techniques [98], [287]–[290]. Also, prior to wafer bonding, tungsten (W) as a diffusion barrier, titanium (Ti) as adhesion and platinum (Pt) as encapsulation layers have been deposited on the Ag mirror layer. Table S2 provides lattice parameters of the phases (Figure 4.11S) identified by the EDX data.

Such robust elemental analysis in the first instance through SEM-EDX is also very beneficial to locate device chemistry, i.e., elemental diffusions within the wide field of view (FOV) in microns for the multilayered device. In Figure 4.10S, the line scan at ~2.8-3.5 μm indicates that interface between GaN (semiconductor) and Ag (metal) layer is not abrupt contrarily to underlying W/Ti/Pt (diffusion/adhesion/encapsulation) layers. This is because no barrier layer between GaN and Ag layer exists. However, on the other end of Ag layer, W is used as diffusion barrier layer to prevent the penetration of material from the Ti adhesion layer into the Ag mirror layer. Also, while performing the wafer bonding mechanism [291], Pt layer is necessary to block Sn diffusion from the eutectic bonding layer (AuSn) into Ag mirror layer. Therefore, it is essential to have stable diffusion barriers to protect the reflective layer, as any metal diffusion (e.g., Sn diffusion during eutectic bond formation) into Ag mirror layer might degrade the reflectivity and/or increase the contact resistivity of Ag mirror layer [292].

SEM-EDX analysis are robust and useful to analyze the compositions without the sample being damaged by the high-electron beam and to crosscheck the existence of

contaminations at a specific region, i.e., any residual or by-products left during the LED fabrication process [205], [293].

Table 4.3S Material properties of GaN and Ag.

Properties	GaN	Ag
Class	Semiconductor	Metal
Crystal structure	Wurtzite (HCP)	FCC
Lattice Constant (°A)	a_o (c_o) 3.189 (5.186)	4.09
Refractive Index@450 nm	2.49	0.135
Dielectric Constant	9.5	-5.65
CTE (10^{-6}/K)@20°C	3.1	18
Thermal Conductivity (W/m.K)	130-225	430
Electrical Resistivity (cmΩ)	$1x10^6$	$1.6 x10^{-6}$
Young Modulus (GPa)	180-200	83
Melting Point (°C)	>2500	961
Yield Strength (MPa)	100-200	55
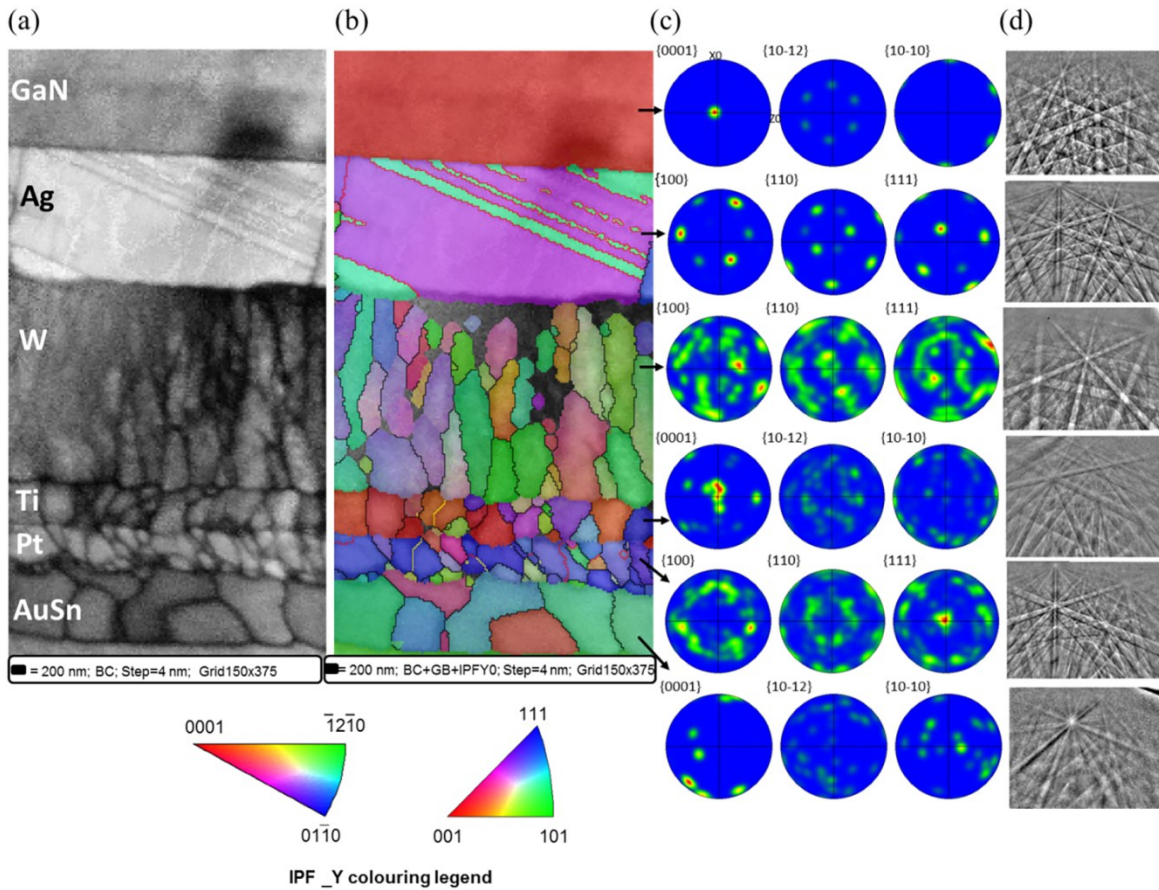
Figure 4.12S SEM-TKD analysis across different layers of the vertical LED. (a) Band contrast (BC). (b) Grain morphology with orientation mapping (OM) showing high-angle boundaries (HAGB) >10° in black and Sigma-3 CSL in red at Pt and Ag reflective layer. (c) Poles figures. (d) Kikuchi diffraction patterns.

Discussion for Figure 4.12S

In Figure 4.12S, TKD measurements were carried out across different regions of thin lamella (electron transparent) sample of VLED in order to determine the grain morphology, and orientation relationship between GaN (semiconductor) and base (metal) layers. Figure S4a shows the pattern quality images calculated by AZtecHKL software from respective multilayered structure [249]. The cross-sectional morphology from the SEM-based TKD analysis indicates that light region is composed of GaN, the shinning white region as Ag mirror layer. This is because of electron backscattering patterns (EBSPs) produced in the SEM-based TKD system [294]. In pattern quality images, band contrast (BC) is EBSP quality factor that reveals microstructure in a certain qualitative fashion (orientation contrast). For instance, Figure 4.12S(a) shows that Ag tends to show light BC (high pattern

quality) while EBSPs along GBs tend to visible as dark (low pattern quality) linear features. Figure 4.12S (b) shows that the grain size of diffusion barrier (W) ~65 nm, the adhesion layer (Ti) ~45 nm, encapsulation layer (Pt) ~50nm and eutectic bonding (AuSn) ~90-120 nm. Notably, the coarse grains promote better stability of diffusion barriers (W, Pt) by filling voids or holes, as of small GB areas [295]. Whereas, fine grains at adhesion or bonding layers (Ti, AuSn) provide better fusion and strength properties because smaller grains have large GB area or diffusion paths to form good adhesive joints between two metals [198], [200], [224], [296], [297]. Also, from Figure S4b we can observe that most of the VLED layers have HAGB > 10° (in black). Such, HAGBs at barrier/adhesion (W/Ti/Pt) and bonding layers (AuSn) might be helpful to locate the source of defects in electromigration mechanism [296], [298].

Figure 4.12S(c) and (d) show that PFs for diffusion barrier layer (W) do not have strong <111> texture, thus pay-off in lower mean time between failures (MTBF) [136]. Therefore, it is substantial to have a stable diffusion barrier for reflective layer because any metal diffusion (*e.g.,* Sn diffusion during eutectic bond formation) into Ag mirror layer might degrade the reflectivity or increase the contact resistivity of the Ag mirror layer. Further, PFs for adhesion (Ti) or bonding (AuSn) layers revealed a low degree of <0001> texture. It can be envisaged that such low degree of texture endures lattice mismatch that degrades the performance and reliability of concern layer, consequently impacts the operating life of thin-film LED product because of short MTBF [299]. Moreover, the angle of orientation influences the thermal conductivity, since isotropic oriented grains have lower conductivity compared to anisotropic grains [209], [251], [300].

From this analysis, it can be concluded that most of VLED multilayered structure composed majority of nanocrystalline grains (1-100 nm) with HAGBs, except Ag reflection layer with special TBs [203], [300], [301]. In summary, SEM-based TKD helps us to investigate the cross-sectional morphology and nano-structural characterization of crystalline material in the VLED. In this context, nano-scale characterization of the complete stack of VLED layers will assist material's engineers to figure out possible solutions to design efficient and low-cost LED technology.
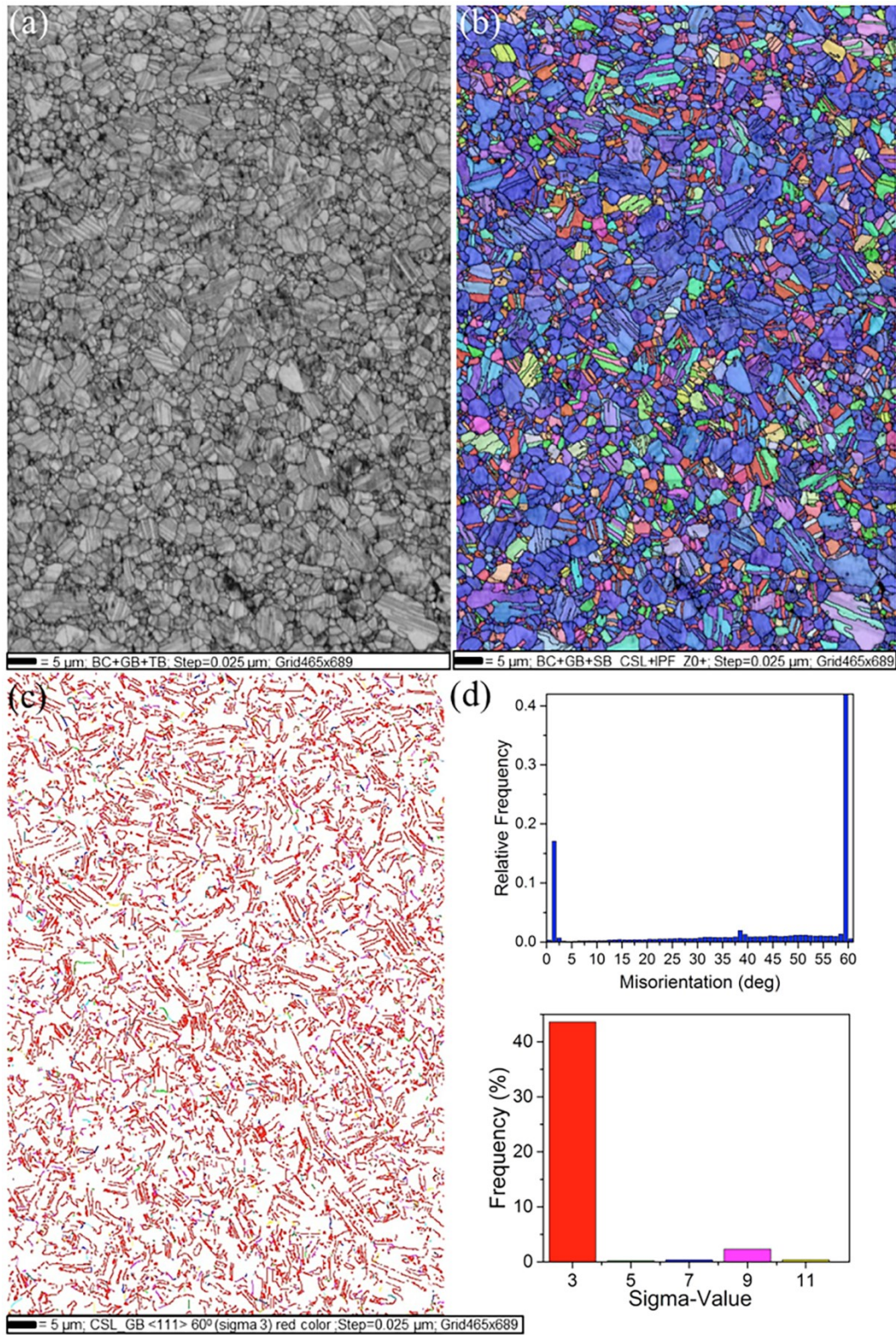
Figure 4.13S SEM-EBSD analysis on the top bulk surface of Ag mirror layer (area 5x5 µm) with the majority

of Sigma-value 3 CSL boundaries (marked in red) with 60° misorientation angle.
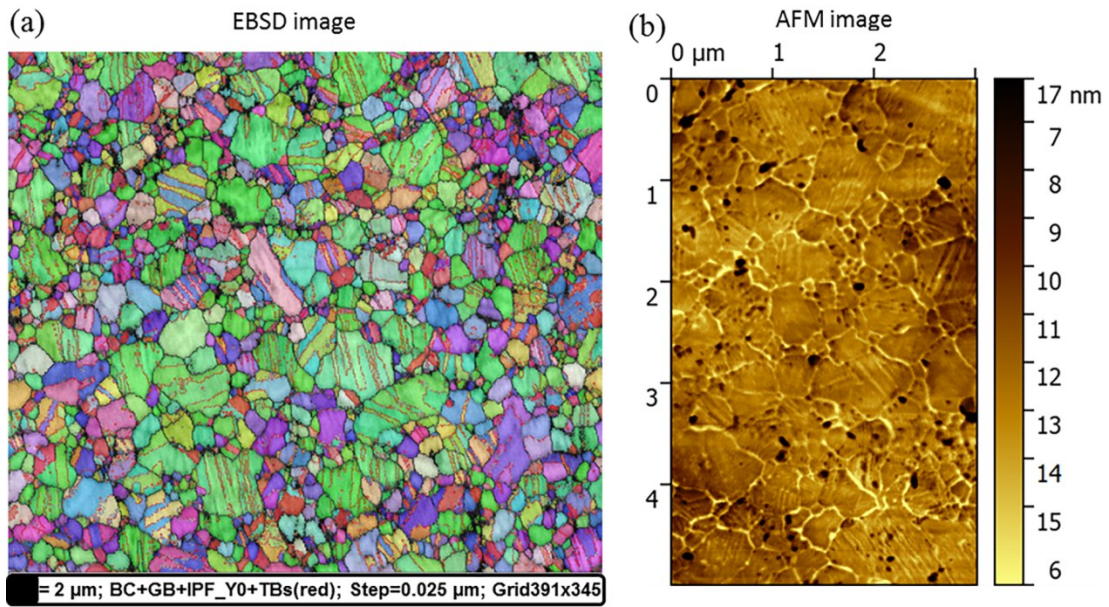
Figure 4.14S (a) SEM-EBSD and (b) AFM analysis on the top bulk surface of Ag mirror layer showing grain morphology and surface topography with twinning structures. Whiskers formation (black particles) around the GB areas.
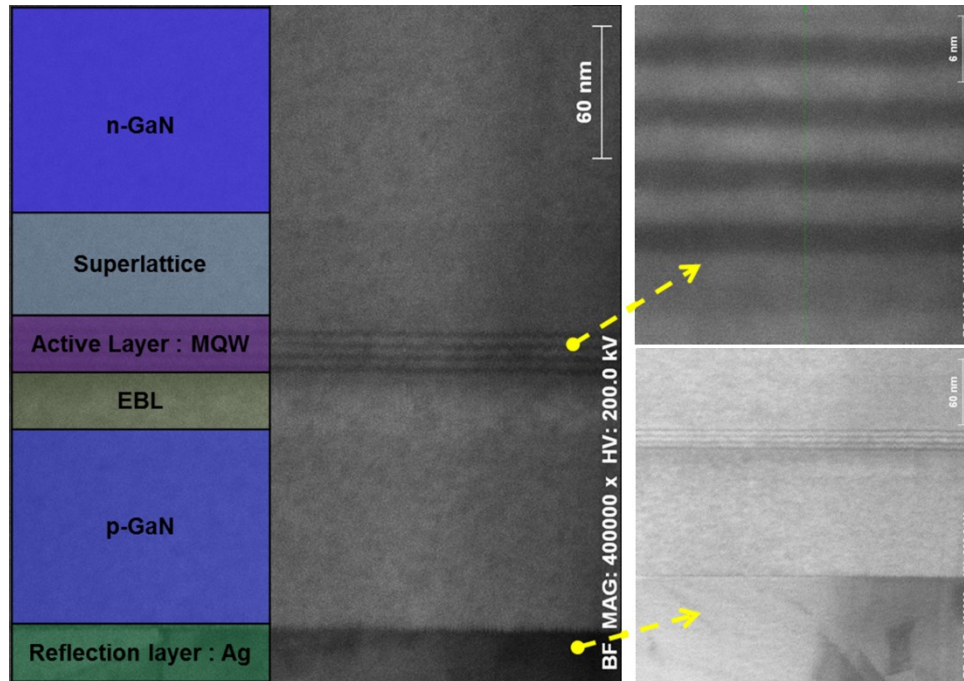
Figure 4.15S JEOL2200FS bright-field (BR) STEM images of GaN epitaxial layers and GaN-Ag interface.

Chapter Five

Insight into Multiple Quantum Wells of GaN-based Vertical LED using Aberration-Corrected Electron Microscopy
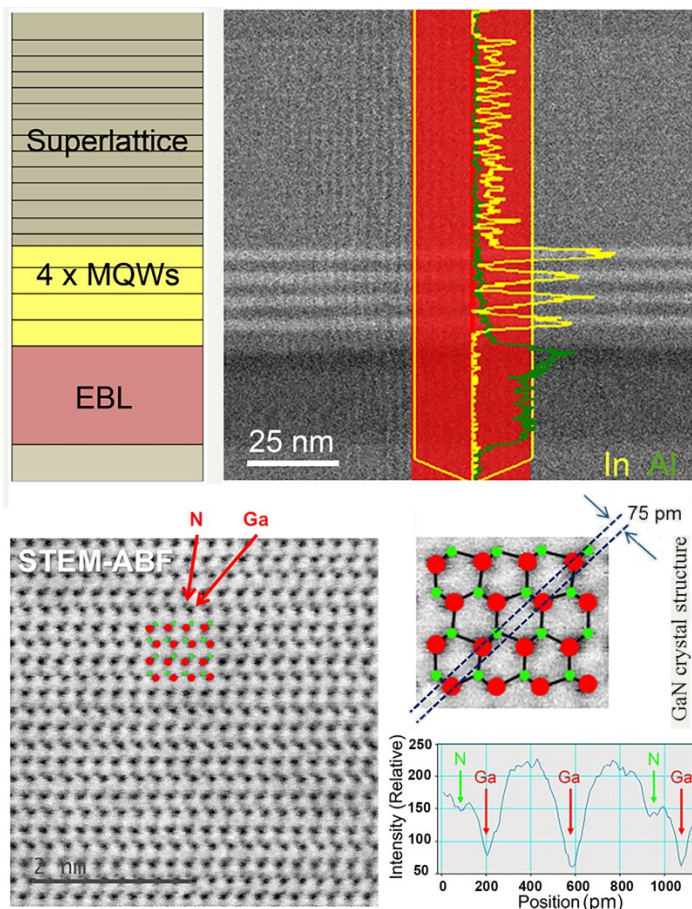
5.1 GaN-based MQWs for Blue LEDs

The 2014 Nobel Prize was awarded to the invention of efficient blue LEDs, which enabled bright and energy-saving white light sources [11]. A modern white LED lightbulb converts more than 50% of the electricity remarkably superior to its incandescent counterparts with 4% conversion efficiency, and therefore is regarded as a green solution to counter the global energy crisis [15]–[17]. With 20-30% of the world's electricity used for lighting, it's been estimated that optimal use of LED lighting could reduce this to 4% [18]. The potential for solid-state lighting based on LED technology to reduce energy usage is made possible through the development of GaN and its alloys. GaN is a fundamental material for a vast range of optoelectronic devices because it demonstrated prominent light emission capabilities ranging from ultra-violent (undoped) to green and red (doped with indium or aluminum) [12], [22]. GaN as a wide bandgap material can be integrated with other compound semiconductors such as InGaN and InGaAlP to form MQWs, which generate active regions to produce LEDs and laser diodes [24], [25].

Particularly, InGaN/GaN-based LEDs are the dominating candidates in illumination market with merits of saving over 10% of worldwide electricity usage and reduction in global warming by decreasing at least 10% in fuel consumption and CO_2 emissions from power stations [3], [35]. Although InGaN/GaN-based QWs for blue LEDs can produce IQE of 90% and EQE of 70-80% [59], [62], [63], there exist many key challenges, for instance, the efficiency droop (the substantial decrease of quantum efficiency with increasing drive current) [61], [64], [65], the green gap (the relatively low efficiency of green LEDs in comparison to blue) [65], [66], the quantum-confined Stark effect (large piezo-electric and polarization fields arising at polar interfaces) [67], carrier (electrons and holes) injection efficiency [68], [69], Auger recombination [70], [71], carrier delocalization [72], impurity diffusion [52], [73], structural and crystal defects (lattice mismatch, dislocations) [74]–[76]. Therefore, further optimization is required in producing high- performance LEDs to fully replace traditional incandescent and compact fluorescent technologies. In this regard, atomic or nanoscale characterization of the light emitting active region is critical to understand the detailed morphology, chemical composition, elemental diffusion, atomic structure with polarity, interfaces abruptness and carrier localization mechanism.

142

5.2 Atomic-scale Characterization of MQWs of LED by Aberration-Corrected STEM

Over the past years, various microscopic techniques have been performed by many research groups, including SEM, TEM, SIMS, APT, Raman spectroscopy, CL, AFM, XRD, and so on, to address above stated issues [76], [112], [302]–[304]. Among these techniques, electron microscopy or TEM has a unique capability by providing crystallographic information, high lateral spatial resolution for high-fidelity imaging along with compositional information from the EELS and EDX [121]–[123]. Precisely, HR-STEM showed better spatial resolution (atomic-planes) compared to APT [31], [124]. Furthermore, these complementary techniques (TEM and APT) are combined to correlate the analytical sensitivity and three-dimensionality of APT with TEM spatial fidelity [125], [126].

Specifically, development of AC-STEM provides new dimensions to state-of-the-art electron microscopy, enabling to perform a structural analysis at a sub-angstrom resolution [127]–[129]. The evolution of aberration correctors has improved the sensitivity and spatial resolution of both phase contrast imaging in HR-TEM and Z-contrast imaging in STEM [130], [131]. This peculiar capability of AC-STEM has opened a new realm to understand materials properties by correlating their atomic-scale changes in composition with the structure of interfaces and defects [132]. For instance, by HAADF STEM method, a resolution of sub-50-pm was achieved on Ge and Si, where 47-pm separated Ge-Ge dumbbells and 45-pm separated Si-Si dumbbells imaging were performed [133]. Also, for the light elements, the sub-angstrom distance between Si-N atomic columns in a β-Si3N4 sample was resolved by an ABF imaging technique [305], [306].

In this work, the MQWs of a GaN-based blue VLED was systematically investigated by the AC-STEM technique equipped with EDX at a true atomic resolution of 0.7 Å. The results across MQW region indicated the compositional inhomogeneity of indium distribution, structural defects, and nanoscale interfacial chemical migration. STEM-based EDX results revealed that InGaN is a random alloy, which causes indium composition fluctuations at both MQWs and short-period superlattice (SL) layers. Also, Al-based electron blocking layer (EBL) at the p-GaN side showed non-uniform profile. Moreover, high-resolution

STEM HAADF and BF images determined that inhomogeneity of indium distribution leads to the QW width variations and random indium fluctuations on account of its compositional pulling effect. In addition, ultra-high-resolution STEM images show that InGaN QWs and GaN QBs interfaces are fairly abrupt and have few interface-related defects. Moreover, the Ga-Ga atomic columns separated by 75 pm was resolved by HAADF STEM whereas the ABF is utilized for a light element (N) imaging with sub-angstrom resolution. Subsequently, AC-STEM HAADF and ABF images of GaN active region identified that it has the hcp-wurtzite crystal structure with validation of N-polarity. Furthermore, our electron microscopy results are correlated with various aspects of degradation in LED performance, which leads towards to understand the origin of efficiency droop, QCSE, carrier delocalization, current leakage, dislocations and impurity diffusion issues. Lastly, based on our AC-STEM nanostructural characterization and analytical results, further prospective optimization and remedies are suggested to mitigate critical issues of efficiency droop, QCSE and structural defects for performance enhancement of LEDs.

5.3 Materials and Methods

GaN-based blue vertical LED structure was fabricated on a 2-inch (0001) sapphire wafer using metal-organic vapor-phase epitaxy (MOVPE) method and the cross-sectional schematic diagram is shown in Figure 5.1. In the growth process, trimethyl gallium (TMGa), trimethyl indium (TMIn), bis-cyclopentadienyl magnesium (Cp$_2$Mg), silane (SiH$_4$), and ammonia (NH$_3$) were used as sources for Ga, In, Mg, Si, and N, respectively.
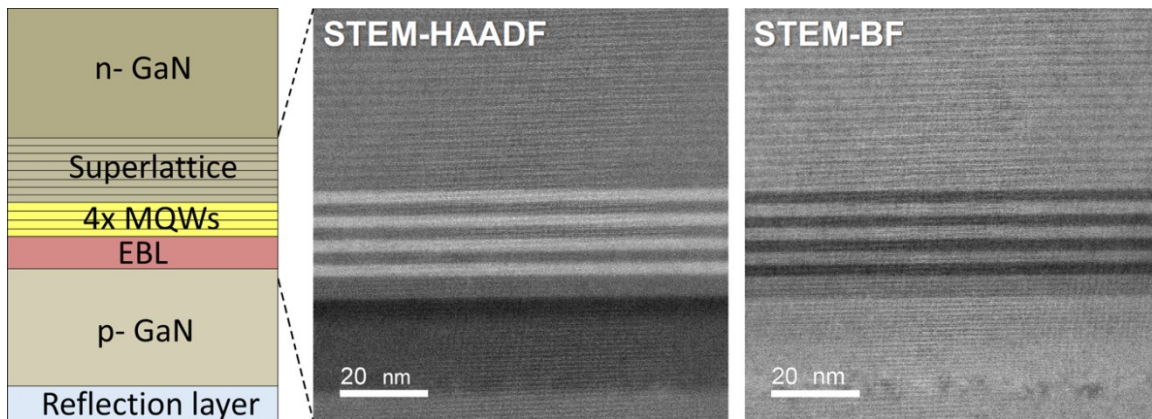
Figure 5.1 Schematic diagram of vertical LED structure with corresponding STEM images.

Prior to the growth of GaN epitaxial layers, the sapphire wafer was exposed to H_2 gas at 1100 °C to remove surface contamination. Firstly, the 25-nm-thick GaN nucleation layer was deposited at 550 °C, followed by the growth of a 2.5-μm-thick undoped GaN and a 3-μm-thick Si-doped n-type GaN layer. A 60-nm-thick superlattice (SL) containing alternating layers of InGaN/GaN (1nm/1nm), and four periods of InGaN QWs with 2.5-nm-thick wells each separated by 3.5-nm-thick GaN quantum barriers (QB) were used for blue light emission in the wavelength of ~455-470 nm. The growth temperature for four pairs of InGaN QWs and GaN QBs were kept between 750 and 850 °C, respectively. On the top of InGaN/GaN-based MQWs, a 20-nm-thick p-AlGaN electron blocking layer (EBL) was incorporated, and finally, a deposition of 200-nm-thick Mg-doped p-type GaN constitutes the layer of the device wafer. Afterward, the device and carrier wafers were bonded together, followed by a laser lift-off step to remove sapphire substrate from a device wafer [57], [98]. Lastly, the exposed n-GaN surface was roughened by a KOH solution for efficient light extraction and LED structure was then processed in a type of vertical current injection with chip dimensions of 1×1 mm^2 [177], [307], [308].

TEM specimen was prepared by standard focused ion beam (FIB) and argon (Ar)-ion milling techniques [107], [309], the steps are summarized in Figure 5.2. A lamella of the MOVPE grown epitaxial layers was prepared by deposition of protective metal (Pt) layer followed by FIB milling with a Ga-ion beam at 30 kV and 5 kV. Subsequent Ar-ion milling by JEOL EM-09100IS Ion Slicer at 1-2 kV was performed for final thinning of the lamella to 60-80 nm and to minimize the FIB-induced damages or artefacts. Further, the lamella was examined under JEOL JEM-ARM300F and FEI Titan Themis Z300 AC-STEMs to obtain the crystallographic structure, high lateral spatial resolution for high-fidelity imaging and chemical compositional information from the key epitaxial layers of the GaN-based blue VLED.

5.4 Results and Discussion

The STEM-based EDX mapping is an essential step to locate the area of interest at high resolution and identify elemental composition across the region of interest (in our case active layers of the VLED). Figure 5.3(a)-(d) provides elemental compositional analysis
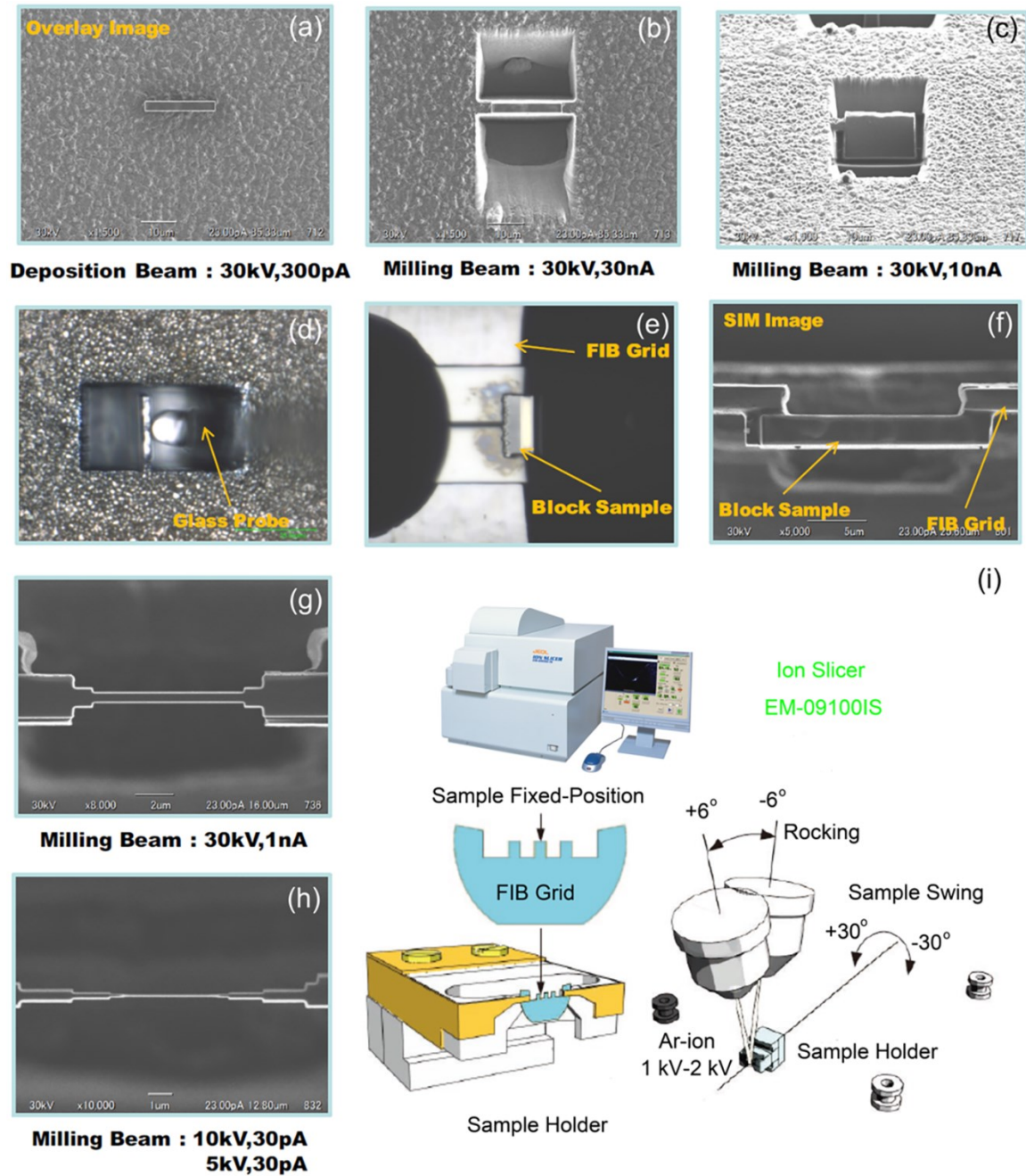
Figure 5.2 Vertical LED TEM-lamella preparation steps: (a)-(h) in FIB and (i) Ar-ion milling.

with HAADF-STEM, where EDX mapping shows that epitaxial layers consist mainly of Ga, N, In and Al elements. In Figure 5.3(d), EDX line profile identifies 21 indium-rich short-periods SL and 4 MQWs are formed by InGaN/GaN compound semiconductors, whereas EBL is composed of an AlGaN material.
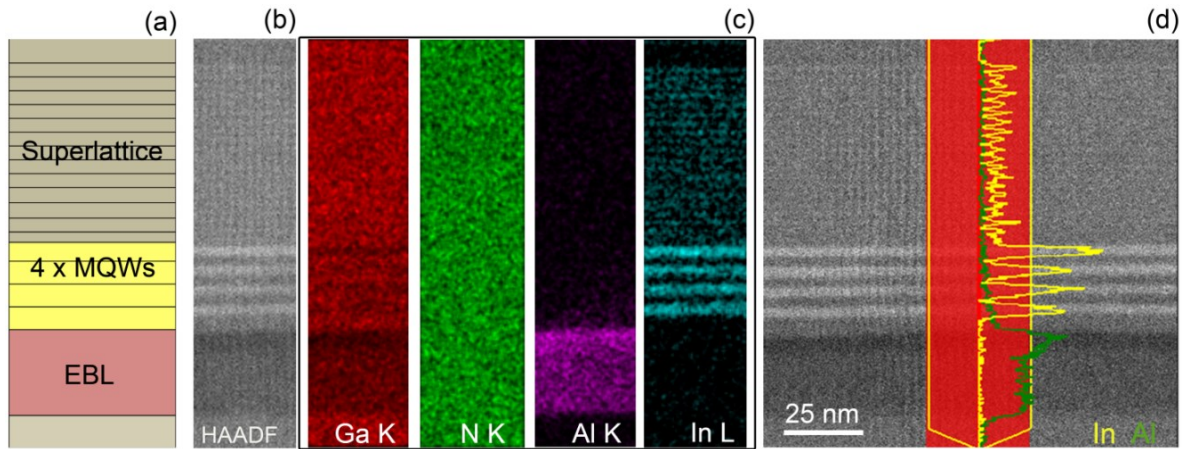
Figure 5.3 (a)-(d) STEM-based EDX elemental chemical analysis across p-n junction of the vertical LED structure.

Interestingly, it can be clearly seen in Figure 5.3(d) that SL, MQW, and EBL layers exhibit diffused interfaces, where indium distribution is apparently nonuniform across SL structures and MQWs. It can be observed that indium has inhomogeneous satellite peaks, i.e. the first QW towards SL or n-GaN side have higher satellite peaks (with 3.2 at.%) compared to other QWs located towards EBL or p-GaN side (with 2.8 at.%). Moreover, Al-based EBL situated between the active region and p-GaN also shows sporadic profile trend, where its lower interface towards p-GaN side has a broad profile with 3.0 at.% concentration while upper interface (toward MQW side) has narrow sharp edge with 4 at.%. From EDX profile (Figure 5.3(d)) we can analyze from that there is overall compositional degradation trend while moving from n-GaN (left) towards the p-GaN (right) growth layers.

To further investigate these issues, high-resolution STEM-HAADF and BF images reveal that the width of QWs is asymmetric, as shown in Figure 5.4. The width of first QW (towards n-GaN side) is 2.47 ± 0.02 nm, while last QW (towards EBL side) has a narrow width with a thickness of 1.66 ± 0.02 nm. Similarly, the width of GaN QB layers between these 4 MQWs is also varied, which means that the QW width variation influenced the subsequent growth of LED epitaxial layers and expected to depend on the growth conditions of the fabrication process.
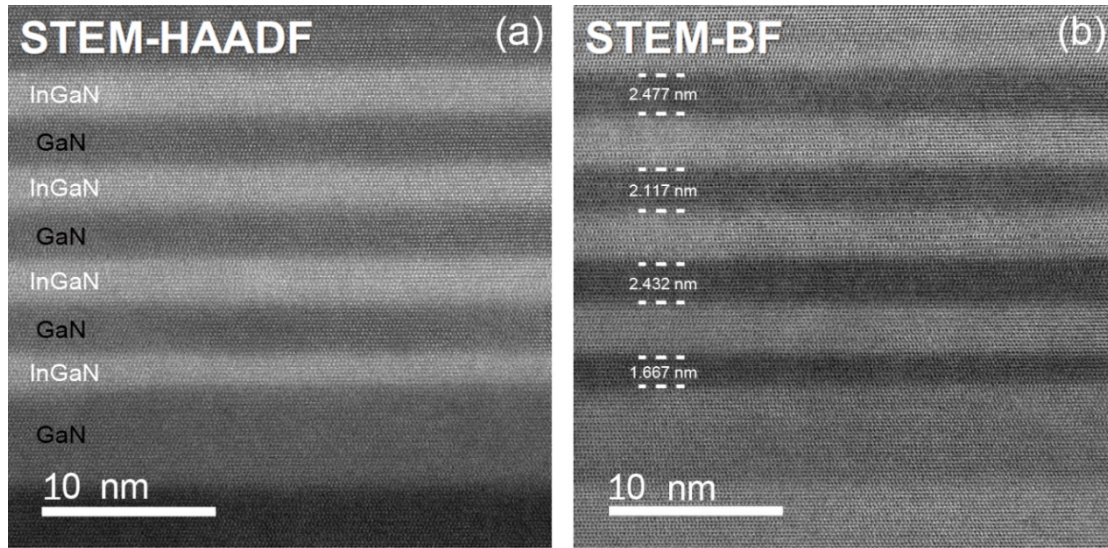
Figure 5.4 (a) STEM-HAADF and (b) BF images across the active region of the vertical LED structure.

In addition, high contrast between InGaN QW and GaN QB layers indicates that the abrupt interface is not destroyed. However, it can be also observed that InGaN QW interfaces have somewhat protrusions towards GaN QB layers as in Figure 5.5, thereby shows that the interface quality is not perfectly sharp, which is due to the fact that InGaN and GaN material systems have poor miscibility (between InN and GaN) and lattice mismatch (InGaN QW strained on GaN QB) [62]. Also, the indium content in the wide QW wells deviates from the others due to the compositional pulling effect [310]–[312], which states that indium atoms trend away from the InGaN/GaN interface to reduce the deformation energy in order to mitigate lattice mismatch.
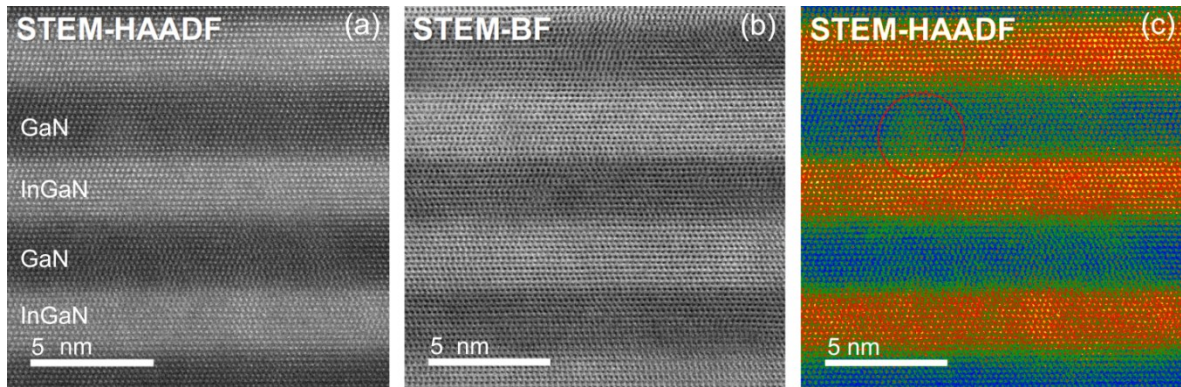
Figure 5.5 (a)-(c) High-resolution STEM-HAADF and BF images across the active region of the vertical LED structure.

Thus, the amount of indium will be increased along the growth direction of wide QWs (towards n-GaN side) because of the compositional pulling effect. This also manifests EDX result of Figure 5.3(d) that InGaN is a random alloy, where In replacing Ga randomly, i.e., upper InGaN/GaN interface (QWs towards n-GaN) and lower InGaN/GaN interface (QWs towards p-GaN) have different satellite peaks. Our results agree with previous reports on that such degree of chemical inhomogeneity in InGaN QWs has atomic height interface steps, resulting in QW width variations and random indium fluctuations on an atomic-scale, and eventually plays a vital role in carrier localization at the InGaN/GaN MQWs [66], [313].

Additionally, from Figure 5.3(d) and Figure 5.4, we can notice that the last InGaN QW (towards p-GaN side) has the narrowest well width and lowest indium satellite peaks, which indicates that variation of indium contents is attributed to epitaxial layers growth conditions. The reason is that QW, which is grown nearby p-GaN interface, faces not only residual strain (lattice mismatch between InGaN and GaN) but also additional thermal stress as well, i.e., on the top of it an high-temperature post-growth p-GaN hole transport layer causes further indium re-evaporation [62], resulting in significantly high indium diffusion from that InGaN QW into next higher InGaN/GaN QWs (towards n-GaN side). Hence, compositional inhomogeneity of indium contents is highly correlated with lattice strain and thermal stress conditions.

Moreover, AC-STEM images at atomic resolution from GaN active region determine that it has an hcp-wurtzite crystal structure with N-face polarity in [$1\bar{2}10$] zone axis, as shown in Figure 5.6. This key result is attributed to powerful high-resolution AC-STEM capability, where Ga-Ga atomic columns separated by 75 pm is resolved by HAADF imaging, whereas the ABF technique is utilized for a light element (N) imaging with sub-angstrom resolution. Also, HR-ABF image (Figure 5.6(b)) shows that the N-atomic columns are above the Ga-atoms, corresponding to the VLED being N-polar. Based on these HAADF and ABF images, GaN crystallographic model is designed (Figure 5.6(c)). Further, the N polarity is more clearly evident in the intensity plot (Figure 5.6(d) and (f)) at each pixel along the trace line marked in Figure 5.6(b), where N-atoms are visible just above the dark Ga-atoms.
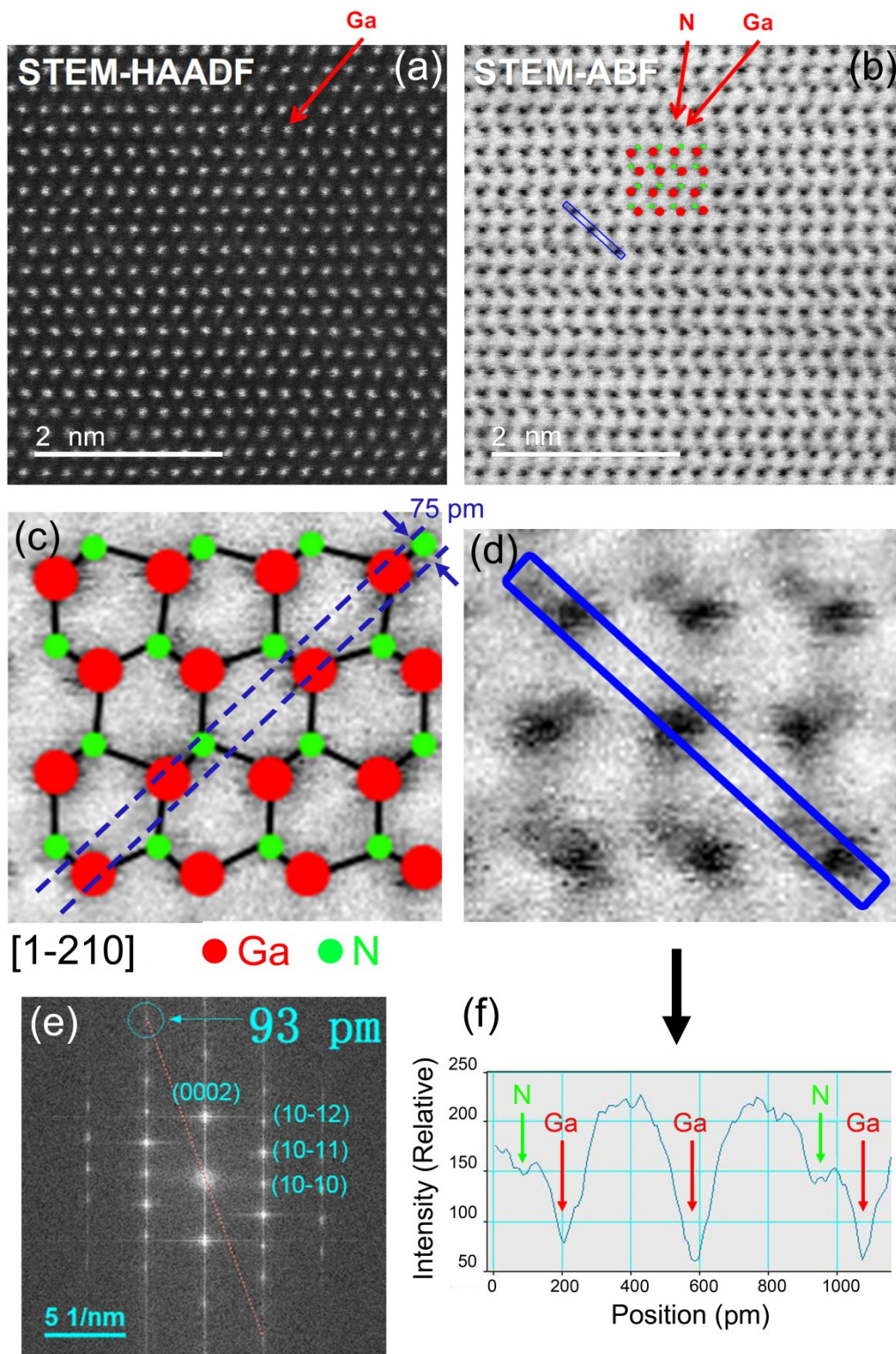
Figure 5.6 UHR atomic-scale STEM images across QWs. (a) and (b) 2D lattice fringes for HAADF and ABF showing Ga, N positions with zone axis. (c) Overlaid GaN crystal model. (d)- (f) Power spectrum revealing

lattice resolution of 93 pm and the plot of the pixel intensity as a function of position along the trace marked in (b) illustrates N-polarity, where N column just above darker Ga column.

The simultaneously recorded HAADF and ABF images enable us to confirm the polarity of the sample by establishing the location of the lighter element (N), thus eliminating ambiguity in the identification of heavier element (Ga) as well. Moreover, Fourier-transform simulations on AC-STEM atomic-scale imaging revealed no stacking faults or major dislocations, e.g., Lomer edge dislocations, which are common interface-related defects for group III-V-based materials [143], [198]. Such dislocations are located at the InGaN QW and GaN QB interface and act as non-radiation recombination centers resulting efficiency droop in the device. In the context of correlating our AC-STEM results with the performance of LED, i.e., the asymmetric QW width, In composition fluctuations at MQWs and SL, and nonuniform EBL profile severely impact the efficiency of the VLED. The reasons are:

1) QWs with narrow well width will maximize the carrier density in the active region, which increases the Auger recombination, resulting in the efficiency droop (or non-thermal rollover) [143], [198].

2) Contrary to thinner QWs, QWs with wide well width will have charges with long dwell time (the time an electron spends over the QW) and high probability of carrier-injection/capture efficiency [314], subsequently contributes to high IQE.

3) Although wide QWs provide high a probability of carrier-injection/capture efficiency (enhances IQE at high current), they still have disadvantages of degradation in radiative recombination and strong quantum-confined Stark effect (QCSE) because of large polarization-related spontaneous and piezoelectric fields, which results in a reduction of spontaneous emission rate of VLED [67]. Also, due to QCSE, the ground-state energy level of electrons in wide QWs is lower than narrow QW, therefore injected carriers (electrons) from n-GaN will prefer to accumulate at widest QW (in Figure 5.4, first grown QW towards n-GaN), which can lead to strong Auger recombination and result in droop effect [315]. Thus, the difference in ground-state energy levels between the QWs with different thickness will hinder electrons

tunneling into the narrow ones, while holes with large effective and low mobility not able to penetrate deeper into the wide QWs, resulting in non-uniform carrier distribution and impedes radiative recombination rate within the QWs, which ultimately causes the efficiency droop [316], [317].

4) In asymmetric QWs, graded-thickness of QWs may induce different degree on stress/strain on the InGaN/GaN lattice system and impacts the composition pulling effect [310], [318], consequently the indium segregation will be slightly increased due to variations of indium contents [240]. This generates strong asymmetry in carrier concentration and mobility across p-n junction of the LED, which is considered to be the dominant reason for the efficiency droop. Further, the optoelectronic properties, which are sensitive to indium content, will deteriorate because of the QWs with different indium content (varied satellite peaks in Figure 5.3(d) tend to emit their own characteristic colors thus degrade light emission for a particular wavelength.

5) Also, the fluctuations in indium composition or varied QW thickness creates localized potential minima within the QW plane [319], [320]. At low current, the injected carrier concentration is small, so they are able to remain confined to the potential minima, however, at high currents, the localized potential minima get filled and carriers will be delocalized (released). Such delocalization of carriers undergoes to interact with non-radiative centers, hence degrades the efficiency of LED. Previous studies also showed that indium fluctuations across MQWs significantly impact the LED's IQE, forward voltage and droop behavior [313].

6) In Figure 5.3(d), it can be depicted that QWs are not in perfect rectangular-shaped rather a potential profile of satellite-shaped QWs are formed. The deformation in the potential profile of QWs is due to the lattice mismatch in the InGaN QW and GaN QB materials. Because of this lattice mismatch, the indium composition in QWs is non-uniform and resulting diffused InGaN QW and GaN QB will induce additional discontinuous polarization-related internal electric fields. These discontinuities in polarization cause a build-up of sheet charges at the interfaces, producing an electric field that bends the energy bands. This band banding directs the electron and hole

wave functions in opposite direction, leading to spatial separation of confined carriers that can reduce recombination rates [25]. Furthermore, the band bending decreases the transition energy of the bound states, which can shift emission spectrum towards longer wavelength, i.e., ascribed to QCSE. This QCSE impacts the optoelectrical properties of the device and is even worse for QWs with higher indium compositions due to increased lattice mismatch [73], causing the LED to exhibit a low IQE on account of decreased electron-hole pair overlap within the titled potential wells.

7) Non-uniform Al-EBL makes it difficult to ascertain whether its role is to fully confine electrons in the active region (suppress electron leakage) or hinder hole transport (poor hole injection efficiency). Because, the increased Al content nearer to GaN QB interface (Figure 5.3(d)) will raise the barrier for electrons, thereby also increases polarization mismatch with respect to GaN, i.e., due to differences in spontaneous and piezoelectric polarization between InGaN/GaN-MQWs and AlGaN-EBL layer [321]. For polar LED structures, this polarization mismatch further induces positive and negative sheet charges, which will strongly impact the energy-band diagram. Consequently, the positive sheet charge develops on EBL (in between GaN QB and Al-EBL interface), which attracts electrons and lower downs the conduction band, leading to reduce the effective barrier height for electrons confinement. Thus, electrons (having high mobility than holes) may escape from QWs into the p-GaN region, thus incite recombination process outside the active region and results in current leakage that accounts for substantial efficiency droop, hence determines ineffective EBL or potential barrier to suppress fully electron leakage or efficiency droop issue [322].

8) Figure 5.1 and Figure 5.3(d) show indium-rich 21 short-period structures (each of 1 nm ± 0.2 with indium concentration range from 0.5 at.% to 1 at.%) towards n-GaN side forms SL, which is another nanostructural feature similar to MQW and idea is to increase number of QWs to have a carrier delocalization among the QWs [323], [324], leading to more uniform electron and hole distribution across the active region and reduced peak carrier densities. Apart from that, SL plays diverse roles such as active light emitting region, or a low-resistance layer for charge flow, or a stress relief layer

for MQWs to compensate crystal lattice defects (dislocations) and associated polarization fields, or as a distributed Bragg reflector to direct photon generation [325], [326]. Therefore, SL number of multiple periods or spacing between each period like factors need to be considered while growing it on epitaxial layers of VLED.

9) GaN most applicable crystal structure of hexagonal wurtzite phase has either Ga or N-polarity along c-axis [22]. In Figure 5.6, we can notice that our sample has N-polarity, however, at the initial stage of the epitaxial layers growth process (i.e., from n- to p-side), it actually has Ga-polarity. In fact, as explained in Section 2.1 of this thesis that during the final stage of the vertical LED fabrication, the device wafer was flipped (Figure 2.1(e)), bonded to carrier wafer and laser lift-off (to remove sapphire substrate) steps were performed [57], [98]. Simply, at the initial stage of epitaxial layers growth, the Ga-polarity exists, however, after the wafer bonding steps, the final VLED product holds an N-polarity on which structure will operate. The determination of this polarity is critical information as it causes internal electrical fields in a different direction, subsequently impacts the electrical (e.g., current spreading from n-GaN towards p-GaN), material growth and optical properties of III-V semiconductor devices [327]. Also, our Ga-face grown layers/interfaces showed good quality of interfaces (as in Figure 5.5, clear bright and dark contrast between InGaN/GaN MQWs). This result agrees with previous reports, which found that the interfaces of both Ga-face and N-face heterostructures are chemically abrupt at the monolayer scale; however, Ga-face interfaces are rather uniform and flat whereas rough in the N-face [328].

10) In summary of above, AC-STEM results across n-GaN, SL, MQW, EBL and p-GaN assist in understanding the mechanism of non-radiative carrier loss that can occur either inside or outside of the active region. Because three types of non-radiative recombination processes normally occur and are: (a) defects related Shockley-Read-Hall (SRH) and (b) Auger recombination occur inside the MQWs, whereas (c) carrier leakage generates non-radiative recombination outside the MQWs. These three non-radiative recombination processes are illustrated in Figure 5.7.

154
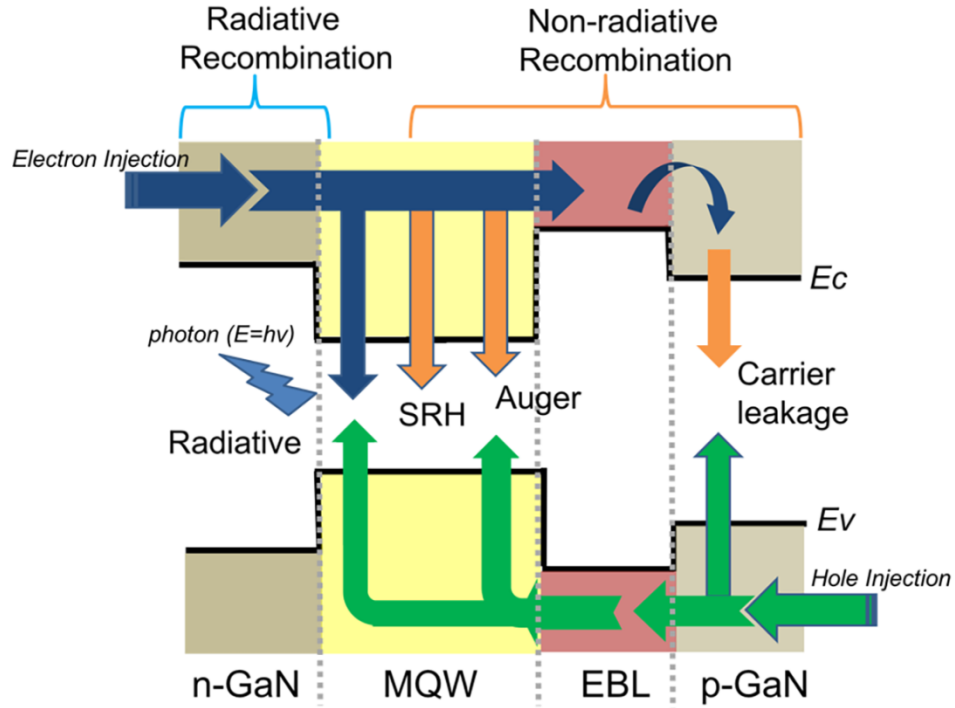
Figure 5.7 Schematic illustration of the radiative recombination and three non-radiative recombination mechanisms.

Hence, we can conclude from our AC-STEM analytical results that asymmetry in carrier transport across p-n junction plays a crucial role in efficiency droop. In the context of these results, optimization prescriptions are as below.

5.5 Prospective Optimization

Based on our AC-STEM results, optimization suggestions are shared for the primary objective of high performance VLED by mitigating efficiency droop, QCSE, carrier delocalization mechanism, impurity diffusions, structural and crystal defects or dislocations issues. The proposed remedies are as below:

1. To alleviate the efficiency droop, reduced carrier densities within the QWs can be obtained by increasing the QW thickness or increasing the QW number or enlarging the chip area or thin-film approach or 3D core-shell nanorods [64], [329], [330]. The improvements are attributed to reduced Auger recombination, smaller electron leakage and improved lateral current spreading [331]. However, the optimal QW

155

thickness depends on substrate dislocation density (DD) and varies from 3 nm (for high DD sapphire substrate) to 18 nm (for low DD free-standing GaN substrate) [62].

2. To reduce the QCSE, thinner QWs are normally employed but that adverse the QWs efficiency (IQE) because of reduced carrier injection/capture capability. To fully suppress the QCSE induced by polarization effects, reversed-polarization (by either inverted epitaxy or growing N-face LED structure) or having crystal orientation in m-plane, a-plane or any other growth of semipolar and nonpolar light-emitting heterostructures need to be designed and fabricated [83]. The reduction of polarization field in InGaN/GaN MQW causes less band bending, higher radiative recombination rate, and less electron leakage from the active region, leading to higher emission energy.

3. Incorporating the p-InGaN layer as a hole injection layer (instead of p-GaN) can diminish strain in the InGaN QWs, resulting in the mitigation of QCSE. This is because ternary alloy materials such as InGaN and AlGaN have large lattice mismatch to GaN, thus piezoelectric effects need to be considered [67].

4. In addition, employing polarization-matched AlGaInN quaternary QBs (instead of GaN) with respect to InGaN QWs in the active region results in mitigation of efficiency droop [332].

5. Thick QWs with high indium contents suffers from poor material quality and reduced efficiency, thus increasing the QW number or by employing short-period multiple SL structures are suggested as alternative solutions [329].

6. In the context of better electron confinement, InAlN EBL (instead of AlGaN) is suggested to counteract electron leakage. This improvement is attributed to increasing conduction band offset (≈ 0.4 eV greater than for $Al_{0.2}Ga_{0.8}N$ EBL) and enhance potential barrier for electrons [333], [334]. Also, InAlN/GaN or AlGaN/GaN SL EBLs or graded-EBL with uniform and triangular-shaped Al profiles can be engineered for enhancing hole-injection capability [269], [335].

7. To mitigate indium segregation at InGaN QWs, indium pre-deposition (IP) methodology before InGaN well growth can be used to obtain the uniform spatial distribution of indium content across MQWs [240], which contributes to increasing the IQE.

8. The growth conditions of MQWs and QBs are crucial in the structural (crystallization quality) and light properties of LED, because temperature difference between InGaN QWs and GaN QBs, and post-growth high-temperature p-GaN hole transport layer induces indium re-evaporation and segregation at the interfaces of QWs, consequently leads to indium diffusion from InGaN QWs into GaN QBs, even into Ag reflection layer [52], [336]. Hence, the reduced growth temperature of p-GaN is necessary to enhance IQE by better interface quality of InGaN/GaN MQWs.

9. Also, efficiency droop behavior is minimized more effectively by inserting low-temperature insertion layers between n-GaN and MQWs [83]. Also, engineering the quantum barriers such as using InGaN QBs (instead of GaN) and graded QBs show better performance in hole density distribution and reducing polarization effect between the QB and QW across the active region [34], [337].

Although AC-STEM has ease of sample preparation and large field of view as compared to APT [31], and provides crucial insights into the active region of LED at the atomic level, it still requires further research to improve the accuracy of atomic locations or atomic arrangement in a material, lower beam energy to minimize sample damage and 3D chemical doping profile. It will be better to prototype a standalone AC-STEM tool that can integrate unique features from different microscopes, e.g., robust TKD patterns from SEM [119], [338], 3D chemical composition from APT [115], [142], and so on. This approach will assist scientist to perform failure analysis, and material's engineers to determine nanostructure-property-process-performance paradigm in order to design high-power and high efficient smart LEDs in illumination market.

5.6 Conclusion

Light-emitting region of the GaN-based blue vertical LED is systematically investigated using the powerful technique of AC-STEM. AC-STEM having an atomic resolution of 0.7 Å with EDX combination has demonstrated a parallel insight into InGaN/GaN-based MQW's by providing morphology, chemical composition, structural defects, polarity and nanoscale interfacial chemical migration. AC-STEM-based EDX analysis reveals that InGaN is a random alloy and causes indium fluctuations across four MQWs and SL layers. HR-STEM results show that compositional inhomogeneity of indium distribution resulted in QW width variations and random indium fluctuations, which impacts the carrier localization at the MQWs. In addition, HR-STEM images show that InGaN QWs and GaN QBs interfaces are not atomically smooth, which is likely due to interdiffusion. Also, results show that Al-based EBL at the p-GaN side has a non-uniform profile and makes it ineffective for blocking electron leakage.

Further, AC-STEM HAADF and BF images of GaN active region successfully determine that it has wurtzite crystal structure with N-face polarity. The Ga-Ga atomic columns separated by 75 pm is resolved by STEM-HAADF imaging whereas the ABF technique is utilized for a light element imaging with sub-angstrom resolution, which confirms the N-face polarity of the vertical LED.

We believe that our results from AC-STEM extract critical information across the active region (p-n junction) of the vertical LED, which encompasses SL, QWs, QBs, and EBL layers along with unprecedented picometer metrology of atomic structures in GaN material. Consequently, these results at atomic resolution lead us towards to understand the origin of efficiency droop, QCSE, carrier delocalization, current leakage, structural defects, polarity and impurity diffusion issues. Thus, AC-STEM is an essential technique that assists in providing main reasons for degradation in IQE and EQE of LEDs. In addition, based on our AC-STEM results optimization suggestions are proposed, which will further facilitate design engineers to optimize device physics and fabrication methodology to have better light management in upcoming smart LED products.

Chapter Six

Non-destructive Analysis on Nano-Textured Surface of the Vertical LED for Light Enhancement
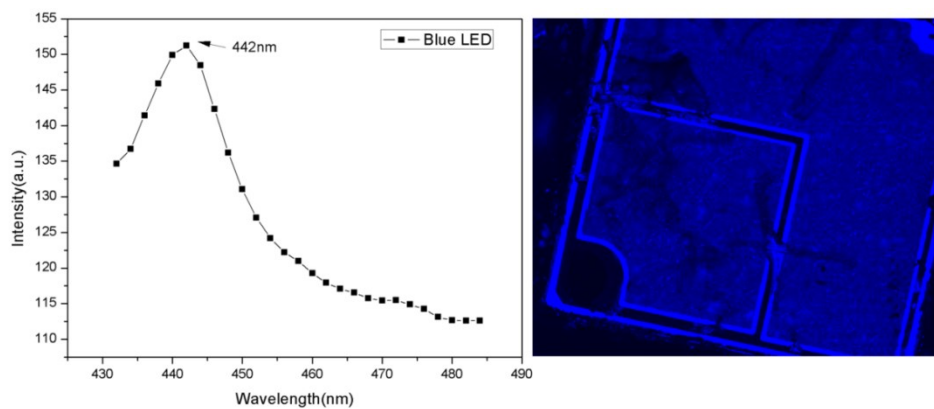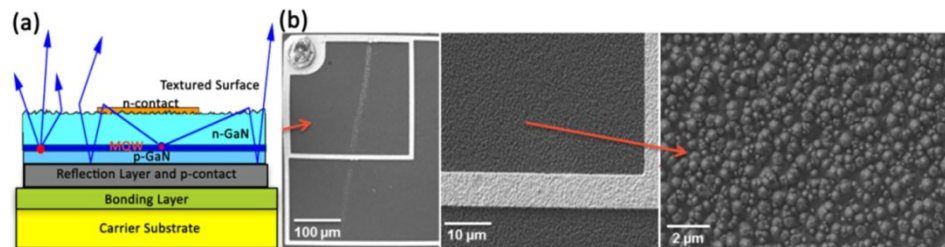
6.1 Introduction to Surface Engineering

Light-emitting diode (LED) is an eco-friendly electroluminescence device, which converts electricity into visible light for illumination. LED technology has many advantages over traditional light sources in terms of compact size, lifetime, variable intensity control, low voltage requirement, instant on/off, high energy saving capability, and so forth [3]–[6]. Due to the superb figure of merits among various III-nitrides system, GaN-based LEDs has attracted tremendous attention in various industrial applications including back-lighting for smart phones and liquid crystal displays, traffic signals, automotive lights, and other outdoor commercial full-color displays [7], [8], [11], [12], [35]. In recent years, GaN-based LEDs market is booming fast and has demonstrated high IQE of 90% by developing good epitaxy or high crystalline quality MQWs [15], [58], [59]. However, their EQE, which is equal to IQE × LEE, has achieved only 60-80% and there are still room for further improvement. To achieve the required benchmark for next-generation solid-state lighting, vertical LEDs are facing major challenges of LEE and high cost [60], [61].

In the vertical injection LED (VLED), light output efficiency is mainly controlled by two interfaces: (1) semiconductor/air interface, and (2) semiconductor/metal interface [52], [230]. The main reason for the low LEE in LEDs is a total internal reflection (TIR) of light at the semiconductor/air interface, which results from the large difference in refractive indices between the semiconductor and air [339]. According to Snell's law, the critical angle for GaN (n_s=2.5) and air (n_{air}=1) interface is 23.6°, so any light ray incident from MQWs with an angle of more than 24° on the GaN/air interface has will be trapped inside the semiconductor [22], and consequently does not contribute to illumination. In this regard, variety of methods have been employed till now, such as surface roughening [276], [340], [341], hexagonal cones [342], photonic crystals [343], [344], nanorods [339], highly reflective metal (Ag) mirror layer [51], [228], air prism array [345], patterned sapphire substrates (PSSs) [346], [347], and graded refractive index materials [348], and so on. In these approaches, top textured-surface on a bottom highly-reflective metal mirror layer has been considered to be a prominent candidate in VLED structures due to its versatility in reducing TIR and processing cost, improving the current spreading and heat dissipation,

and maximizing optical output [230], [349]–[351]. Compared to non-etched LED, the light output power of the textured LED has been increased by 30-50%, and the wall-plug efficiency has been improved by 33% at an injection current of 20 mA [352]–[355]. Therefore, it is indispensable to perform surface analysis of the VLED for further performance optimization and light enhancement without damaging or degrading its top topography and surface morphology.

In this report, surface analysis of nano-textured structure in the VLED is characterized by NDT consisting of SEM, AFM, Raman spectroscopy, PL and XRD for performance optimization and light enhancement. These techniques provided noncontact, local, and nondestructive, hence prevent damage to the nano-textured surface of the VLED. Surface morphology and topographical (roughness) information of textured surface were analyzed by SEM and AFM. Stress by texturing on the n-GaN surface was determined by Raman spectroscopy, whereas emission property and crystal quality of textured surface were examined by PL and XRD. Furthermore, SEM-based TKD/EDX, and AC-STEM tools were used to investigate the influence of texturing engineering on underneath layers (n-GaN and quantum wells). Finally, the framework of NDT provided parallel insight into texture engineering and on the basis of these correlatives NDT results, suggestions are presented on optimization of surface engineering for better light extraction efficiency in VLEDs.

6.2 Materials and Methods

The fabrication of the GaN-based VLED constitutes four steps [52], [57], [177]: (1) growth of epitaxial layers by MOCVD on a 2 inch sapphire (0001 oriented) substrate and deposition of a reflective mirror (silver) by electron-beam evaporation, (2) integration of device wafer with carrier wafer by wafer bonding technique, (3) removal of temporary grown sapphire substrate from the device wafer by laser lift-off (LLO) method, and (4) to improve the light output power and LEE of the VLEDs, a random abraded pyramid-shaped textured surface was formed on the n-GaN layer by using a KOH solution at 80°C and final
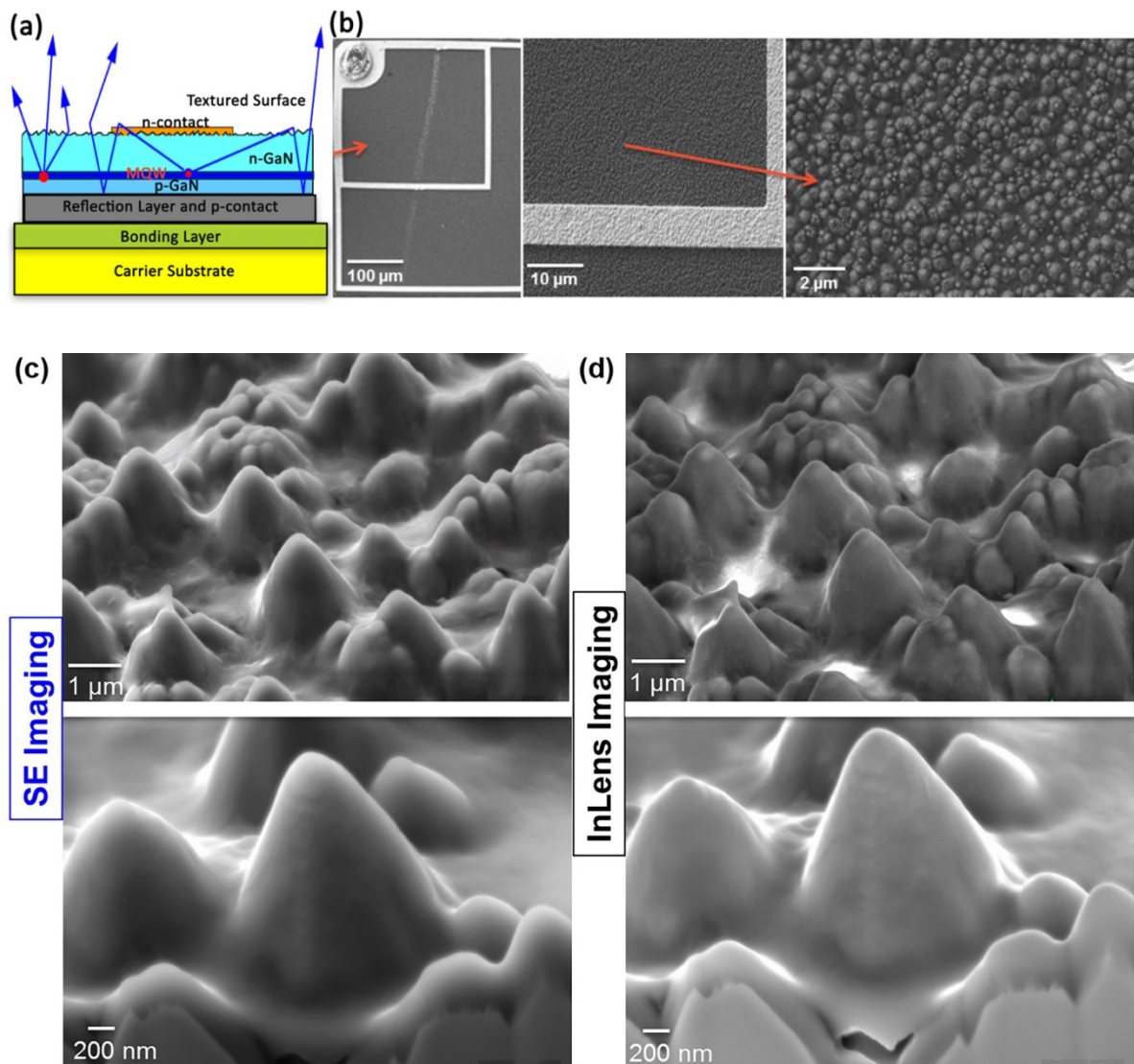
Figure 6.1 (a) Cross-sectional schematic layers of the VLED. (b) SEM micrographs of the top textured surface. (c) SE2 and (d) In-lens cross-sectional imaging of the textured surface of the VLED.

SiO$_2$ as passivation layer was deposited by plasma-enhanced chemical vapor deposition (PECVD). Figure 6.1(a) shows the cross-sectional schematic of the VLED. Surface morphology and topography of the sample was investigated with Zeiss ULTRA Plus FEG-SEM and Bruker Dimension ICON AFM, respectively. High-resolution Renishaw Raman spectroscopy and Schimadzu XRD 6000 were used to evaluate the stress state and crystalline quality of the top textured n-GaN layer. PL measurement was performed at room temperature to characterize the emission properties of the textured surface. Furthermore, SEM-based EDX with TKD and JEOL JEM-ARM300F AC-STEM were used to assess the

cross-sectional view, chemical composition and impact of a textured surface on the underlying active region, i.e., the crystalline quality of MQWs of the VLED.

6.3 Results and Discussion

6.3.1 Surface Morphology and Topographical Information

SEM with low e-beam at 5kV was applied to avoid damaging the top surface of VLED. In Figure 6.1(b)-(d), SEM micrographs show that wet etching of GaN using KOH solution formed pyramid shaped nanorods structures with sizes ranging from 100 nm to 900 nm, (diameter of the tip surface) having height of ~1.0 to 2.5 μm, and are randomly located on the top surface of the VLED. Light extraction is enhanced by hindering TIR with these random textured n-GaN surface [356], because the light is successively reflected by the sidewalls of the pyramid structures and after each reflection their departure angle decreases, until the critical angle of the GaN (~24°). Thus, most of light can exit instead get trapped in the pyramid cones or semiconductor material, as illustrated in Figure 6.1. These random textured n-GaN surface of the wet-etched VLED scattered the light in a non-specific direction and mostly forms a typical Lambertian emission pattern [342]. Also, in SEM, imaging by SE2 and in-lens detectors depict different contrast of the textured surface in a cross-sectional view, as shown in Figure 6.1(c) and (d).

To further investigate the surface topography of the textured surface of VLED, AFM analysis was performed. AFM results reveal that pyramid structures are not uniform in height with a root-mean-square (RMS) surface roughness value of ~ 300 nm, as shown in Figure 6.2. Interestingly, it is worth to note that these pyramid-shaped microstructures have a surface roughness less than the wavelength of visible light, that is, $\lambda < 400$ nm, thus the variability of roughness (height of pyramid cones) need to considered during surface engineering for light emission in a specific wavelength. The variability of surface roughness strongly depends on the etching rate, so etching needs to be optimized.

Also, in Figure 6.2, we can observe that the shape of the imprints is roughly pyramid with curved edges and is in random spatial distribution. The roughness of surface provides better angular redistribution of light, i.e., roughness randomly scatters photons and distributes

them in arbitrary directions for better light extraction, in agreement with previous literature on the textured surfaces, which states that the rough surface improves light extraction and output power of the LED [357], [358]. Although a rough surface promotes high light extraction and output power, high roughness is achieved at the cost of over-etching (higher depth) [358], [359]. This results in damaging the n-GaN or active layers (MQWs) and the probability of more loss of light by absorption exits (because of dislocations induced by over-etching or high-stress conditions), which decreases the reflection of light and eventually causes a drop in the luminous efficiency.
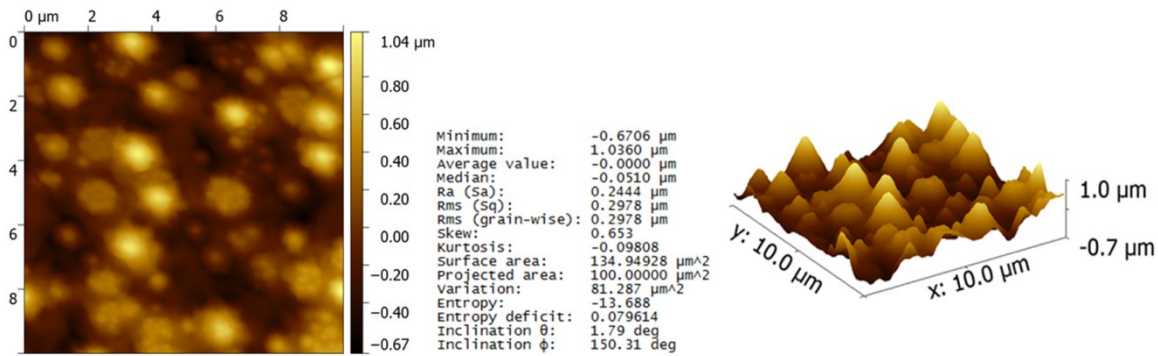
Figure 6.2 2D and 3D AFM analysis on the top textured surface of the VLED.

6.3.2 Stress-State on Textured GaN Surface?

Furthermore, Raman scattering was conducted to evaluate the stress-state of the textured rough surface of the VLED. Raman spectra, intensity profiles, and 2D mapping are shown in Figure 6.3.

In GaN films, the E_2 high (E_2^H) and A_1 longitudinal optical (LO) phonon modes are widely used to evaluate the stress-related property of III-nitrides, particularly the E_2^H phonon peak at $\sim$565–568 cm^{-1} is associated to the residual stress inside the GaN layer [135], [94]. In Figure 6.3(a) and (c), Raman spectroscopy revealed that the E_2^H phonon peak is shifted to high wavenumbers at 569 cm^{-1} with respect to the peak of stress-free GaN at 567.5 $\pm$ 0.5 cm^{-1} [138], which shows that the textured n-GaN layer is under the stress because of the Raman shift of 1.5 is observed.

164
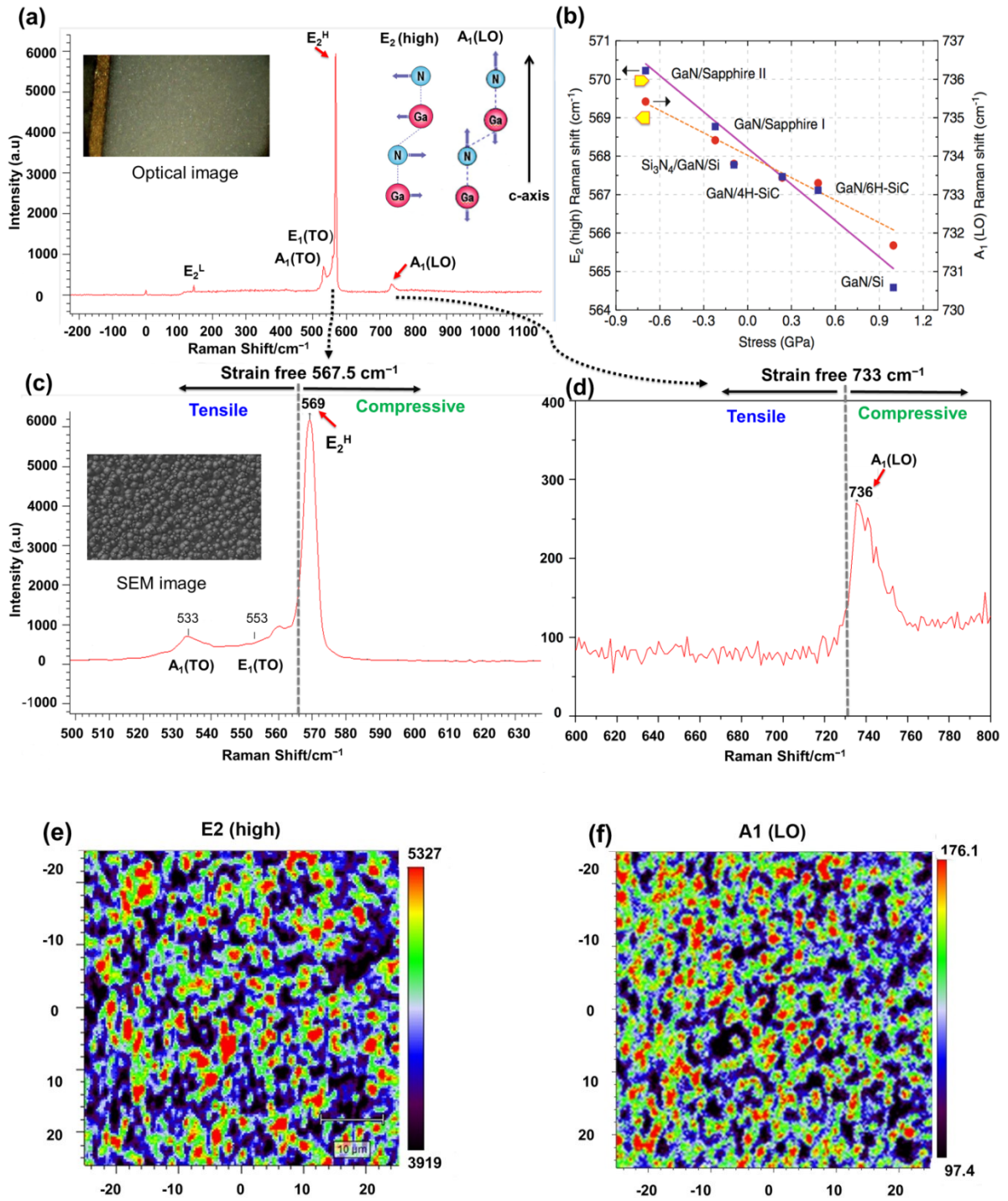
Figure 6.3 (a)-(d) Micro-Raman spectra on texture surface of VLED. Raman peaks of E_2^H at 569 cm^{-1} and A$_1$(LO) at 736 cm^{-1} are ascribed to the compressive GaN. The dashed line indicates the stress-free GaN with $E2$ peak at 567.5 cm^{-1} and A$_1$(LO) at 733cm^{-1}. (b) Room temperature Raman shifts versus corresponding residual stresses. Our Raman measurements of both E_2^H and A$_1$(LO) mode relations are displayed as yellow marked, respectively. The solid line is the fitting of E$_2$(high) frequencies whereas the dashed line is the result

of A$_1$(LO) frequencies [138]. (e), (f) Two-dimensional micro-Raman intensity mapping of the $E_2{}^H$ and A$_1$(LO) peaks in an area of 10 μm × 10 μm

To validate it mathematically, the stress can be measured by ω ($E_2{}^H$) = ω0 + Cσ, or σ = Δω/C, where ω0 is the Raman shift for stress-free GaN (567.5 cm^{-1}), Δω is the shift of the $E_2{}^H$ phonon peak, C is the biaxial strain coefficient (−2.25 cm^{-1} GPa^{-1} for GaN), and σ is the in-plane (c-plane) compressive stress [97], [360], and estimated to be -0.667 GPa (negative value indicates that the residual stress is compressive). This result reveals that textured surface induces more compression than tensile stress on the n-GaN layer, thus verified that the textured surface is under the compressive stress state. In fact, this compressive stress is due to the lattice and thermal mismatch with the sapphire substrate. In fact, the thermal expansion coefficient of sapphire is much larger than that of GaN, which is responsible for the highly compressive residual stress in GaN [22].

The A$_1$(LO) phonon mode corresponds to atomic oscillations along the c-axis and is affected by free carrier concentration or different doping levels. As shown in Figure 6.3(a) and (d), like $E_2{}^H$ mode, the A$_1$(LO) phonon peak is also shifted to high wavenumber at 736 cm^{-1} with respect to a stress-free GaN peak at 734.2 ± 0.5 cm^{-1} [95], [138], indicating a stress state at -0.667 GPa, which is consistent with the $E_2{}^H$ shift and with previous reports [94], [360]–[362], as illustrated below in Figure 6.3b. Thus, Raman spectroscopy is a sophisticated tool for optical characterization of stress conditions ($E_2{}^H$), and impact of free carrier concentration or doping levels (A$_1$(LO) mode) in heteroepitaxial material and device structures.

Moreover, 2D Raman mapping and intensity profiles at $E_2{}^H$ (569 cm^{-1}) and A$_1$(LO) (736 cm^{-1}) modes (Figure 6.3(e) and (f)) depicted that the blue regions with the lowest intensity correspond to the center parts of the textured surface, i.e. pointed rods of pyramid patterns; meanwhile, the green, yellow and red regions with the highest intensity refer to the rest part of the patterns. The different intensity is due to the fact that nano-textured GaN epilayer is subjected to biaxial compressive stress, because of three reasons: (1) prior to laser-lift out, GaN was grown on sapphire substrate, which shrinks more than GaN because of different coefficient of thermal expansion [76], (2) etching could have influenced stress on the top

GaN epilayer while forming textured surface in the last stages of LED fabrication process, and (3) stress might be induced during passivation of SiO_2 by PECVD on the top textured surface [363], [364].

6.3.3 Emission Property and Crystal Quality of Textured GaN Surface

Furthermore, PL and XRD measurements were taken to verify Raman spectroscopy results. PL can also assess the variations of stress level in the GaN since the energy band gap is strongly sensitive to the state of stress [138], [139]. As shown in PL spectra in Figure 6.4, emission peak of the blue LED is shifted to 442 nm rather its expected reference emission wavelength of 450 nm (depending on indium concentration and QW width as shown in Figure 1.7). This result validates the Raman spectroscopy analysis that nano-textured structures on the GaN layer demonstrate a stress, leading to a blue shift of the emission peak wavelength, subsequently impacts the optical efficiency of the VLED. Hence, Raman and PL measurements, an accurate assessment of the slope of stress versus frequency or energy shift is feasible.
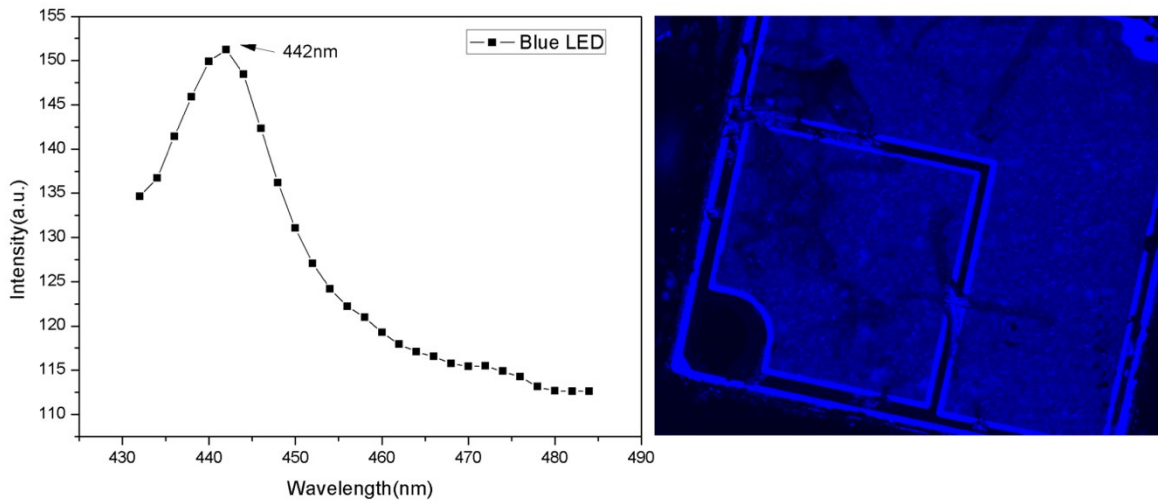
Figure 6.4 Photoluminescence spectrum obtained from the top textured surface of the VLED.

In Figure 6.5, XRD data obtained through X-ray source with a rotating Cu anode indicates that the GaN material holds not superior but good crystalline quality with 2-θ values at 35.0, 35.4, 38.6, 39.0, 40.5, 44.0, 45.2, 51.1, 65.4, 74.9, 78.4, where peaks of 35.0 and 35.4 represent InGaN (MQWs) and GaN (0002), and 74.9 peaks are for GaN (0004) planes,

respectively. Normally, significant reflection by the hexagonal GaN (0002) is at 34.6°, but in our case GaN peak it is at 35.4, indicating a stress state in the textured n-GaN layer, consistent with PL and Raman results. The absence of XRD peaks for SiO_2 in this material suggests that the deposited passivation layer on the nano-textured surface is amorphous. Thus, the nice agreement between the results from different NDT methods provides confidence in the analyzed data. Such results from NDT are very crucial, because the increase in the energy band gap of GaN results from the compressive stress, whereas it decreases with an applied tensile stress. In fact, strain engineering in semiconductor-based thin films can be employed to obtain desired physical and electronic properties of VLEDs [22].
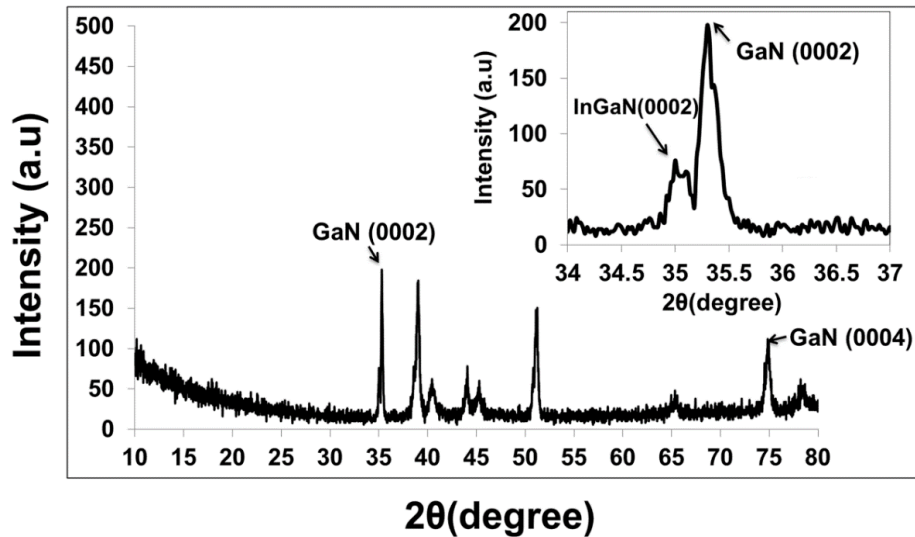
Figure 6.5 XRD analysis of the top textured surface of the VLED.

6.3.4 Impact of Textured Surface on n-GaN and MQWs layers

After NDT analysis, to further scrutinize the impact of the top textured surface on underlying n-GaN and active (MQWs) layers of the VLED, the possibility is to apply destructive techniques of SEM-FIB and STEM. Figure 6.6(a) presents a cross-sectional (view) SEM image obtained on a specimen prepared by focused-ion beam (FIB) technique. SEM-based EDX depicts chemical composition of top surface and across the top cross-sectional region (Figure 6.6(b) and (c)), where VLED top nano-textured pyramids (with
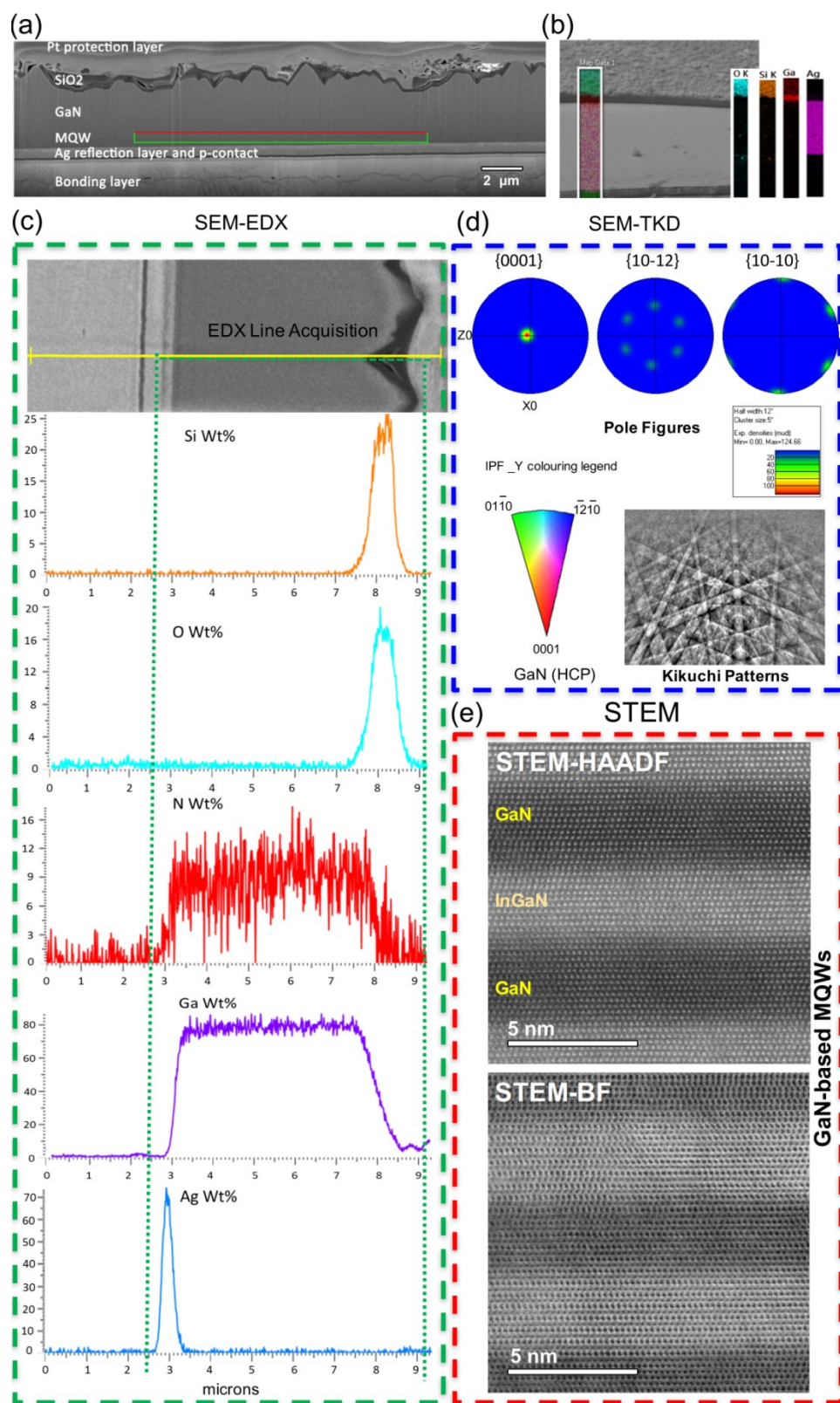
Figure 6.6 (a) Cross-sectional view of the SEM micrograph. (b) and (c) SEM-based EDX line scan analysis. (d) SEM-based TKD analysis on the GaN layer. (e) AC-STEM imaging on MQWs.

etch depth of ~1-2 μm) are covered by the 200 nm thick SiO_2 film with 20-25 wt.%, which resulted in a hemispherical textured n-GaN surface. Passivation of SiO_2 on the nano-textured is vital to increase the critical angle (reduces TIR) and provide a gradual change in refractive index (GaN=2.5, SiO_2=1.46, air=1), thus further enhances light scattering and output power of the VLED [364], [365]. Also, previous reports showed that white VLEDs having a SiO_2 layer exhibit an 8.1% higher luminous efficacy than white VLEDs with no layer at an injection current of 350 mA [275]. Table 6.1 illustrates refractive index of n-GaN, air, SiO_2 and other passivation materials in relation to the critical angle.

Table 6.1 Refractive index and the critical angle of materials (interfaces and passivation layers) used in the VLED [365], [366].

Material Interface (Passivation)	Refractive Index (n2/n1)	Critical Angle (degrees)
Air/GaN	1/2.5	23.6
Air/ITO	1/2.19	27.2
Air/SiO$_2$	1/1.46	43.2
Air/Al$_2$O$_3$	1/1.76	34.3
SiO$_2$/GaN	1.46/2.5	35.7
MgO/GaN	1.73/2.5	43.8
ZnO/GaN	1.94/2.5	50.9
MgO/ZnO	1.73/1.94	63.1

In addition, to investigate the crystal quality of underlying n-GaN and active (MQWs) layers, a thin TEM lamella (prepared by FIB) is analyzed under SEM-TKD and AC-STEM

The crystallographic texture of n-GaN layer is determined by SEM-TKD and structural morphology of active region on the atomic scale is studied by AC-STEM. Using SEM-TKD, pole figures (degree of preferred orientation) and Kikuchi diffraction patterns obtained from the pyramids structures on the GaN layer reveal that they exhibit a wurtzite crystal (HCP structure) with strong {0001} texture in the growth direction (c- axis). However, the grown structures are not perfectly aligned in the <0001> direction and the surrounded six-fold rotational symmetric features appeared at {10-12} and {10-10} planes are also not well aligned and sharp, which shows that GaN layer is under certain minimum stress (Figure 6.6(d)) [360], [367], [368]. This result is in agreement with NDT analysis and validates that the GaN layer (just beneath the top textured surface) is influenced by KOH etching process, resulting in a stress-induced GaN layer. On the other hand, the active region (4-5 μm away from the top textured surface) has smooth morphology and stress-free MQWs interface, i.e., InGaN/GaN, as shown in atomic-imaging in Figure 6.6 (e). Also, no major stalking faults or dislocations are noticed in the active region of the VLED. This result also substantiates that in the vertical LEDs, all the surface engineering, which occurs on the n-GaN layer (> 2-3 μm and much thicker than p-GaN) does not affect the underneath light emitting active regions, i.e., MQWs. Contrarily, in case of lateral LEDs, surface texturing is difficult because the top p-GaN layer is too thin for surface texturing and sensitive to electrical deterioration and etching or plasma damage [358].

6.4 Prospective Optimization

On the basis of above results, following optimization are suggested:

1. In competitive or failure analysis of LEDs, NDT need to be applied prior to other destructive characterization techniques, such as FIB, SIMS, TEM, and APT to prevent damage to sample.
2. NDT can be used to evaluate the actual lifetime and reliability of LED to identify variations of the top surface of n-GaN after lighting up LED for certain hours to estimate its lifetime duration.
3. During fabricating the LED device, the distance between GaN/air interface and MQW or GaN/Ag interface need to be optimized for better light extraction [369].

4. The etching mechanism or methodology need to efficient and effective. For instance, in case of wet etching, KOH etching rate need to be considered as different degrees of surface morphology and surface roughness can be achieved by varying etching rate and temperature. Different groups reported that the pyramid dimensions and pyramidal distribution density is inversely proportional to the etching time, and impacts both LEE and output power [340], [370]–[372].

5. Less-damaging and low-cost etching methods need to be introduced, such as natural lithography or direct printing and subsequent inductive coupled plasma etching can be used [373], [374]. Also, hexagonally close-packed micrometer array or GaN circular nano-cones structures can effectively increase the LEE by utilizing all different components of light [342], [375]. Furthermore, such texture engineering can also be done in organic LEDs and solar cells, as well.

6. It is known that the concept of the random textured surface is light scattering (in a random direction) to hinder TIR but lacks waveguide coupling. Hence, for light scattering in a specific direction, periodic cones in form of the micropatterned array (Figure 6.7) or nanopillar structures will further enhance the LEE of VLED by enlargement of the photon escape cone [376]–[378].
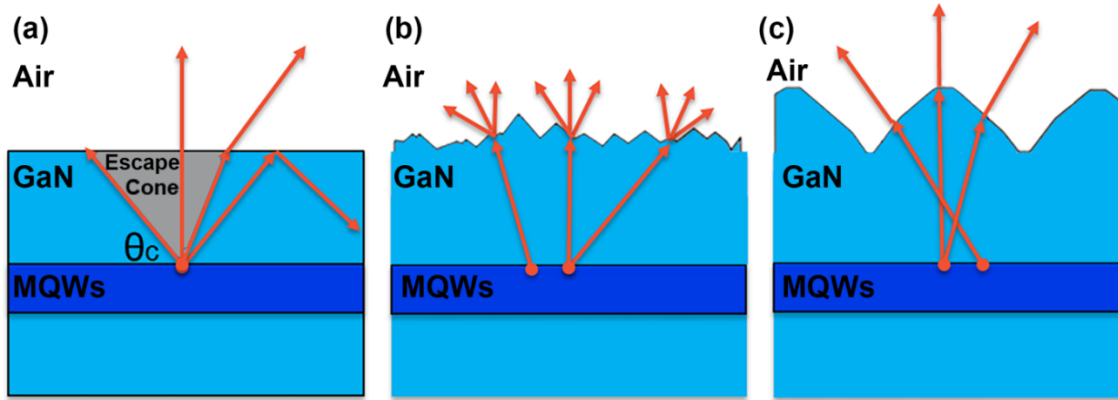
Figure 6.7 (a) Schematic of (a) the unpatterned, (b) wet-etched, and (c) micropatterned VLED [342].

7. Nevertheless, texturing the surface is an efficient way to improve the light output power because of multiple chances of light escape from the surface. However, the random scattering probability will increase with compact patterns, which shows that

LEE strongly dependent on distance/size parameter of pyramids, i.e., if the distance/size parameter decreases, the number of pyramid pattern increases, hence will have more chances of random scattering at the n-GaN/air interface [357]. Compact patterns also enhance light output power and are attributed to the scattering effect at the textured surface. Thus, more compact patterns are required for better LEE and output power. In this regard, nanoparticle-assembled on-top layers or nanowires (e.g., ZnO) or thin-film flip chip methodologies can also be used [277], [379]–[381].

8. Stress/strain-free GaN films are necessary to produce high power and high optical output LEDs for emerging smart lighting products. To achieve that, natural substrate lift-off or plastic substrates can be used rather a laser or chemical lift-off during the fabrication process to avoid the non-uniform etching or tensile stress, resulting in reducing the piezoelectric polarization electric fields (i.e., quantum-confined Stark effect), which leads to high recombination efficiency and fewer wavelength shifts in VLEDs.

9. Normally, the Raman data represents a volume average of the stress through the GaN layer (with a thickness in the order of 1–2 mm). On the other hand, micro-PL shows the stress near the surface of the GaN, for instance, the photon penetration depth of the He–Cd 325-nm of the order of 80–90 nm [138]. Also, the AFM provides only top surface topography. Thus, a combination of these NDT techniques needs to be implemented because they offer complementary information to reveal the through-thickness variation of stress in the GaN epilayer without contacting or damaging its surface.

10. To optimize surface engineering of VLED, new passivation layers need to be explored that can reduce TIR by increasing the critical angle (Table 6.1) so that plasma or etching-induce damage can be minimized [365], [370], [382]. Also in VLEDs, the top (small area) textured n-type electrode and backside (large area) reflective mirror or p-contacts normally have current crowding issue, to mitigate that, highly transparent conducting layer or graphene current spreading layers can be incorporated to improve light output power and wall-plug efficiency [47], [383]. However, the trade-off between optical transmittance and electrical conductivity must be addressed as well.

6.5 Summary and Conclusion

In summary, GaN-based vertical LED with pyramid-shaped textured structure was grown, fabricated and characterized by non-destructive surface analysis techniques. Impact of a textured surface on the stress state and crystalline quality of the GaN were analyzed by advanced powerful microscopy tools of SEM, AFM, Raman, PL, and XRD. SEM and AFM results showed that the surface topography of nano-textured surface on VLED has a roughness of ~300 nm. Raman spectroscopy revealed that the stress state of the nano-textured surface in compression stress of 0.667 GPa with E_2^H and A_1(LO) phonon peak values at 569 cm^{-1} and 736 cm^{-1}, respectively. Also, PL and XRD measurements agree with Raman data and manifest that because of the stress state, the blue VLED has emission peak wavelength of 442 nm rather 450 nm. To further examine the influence of texturing on underneath layers, SEM-based TKD and AC-STEM results depicted that n-GaN and MQWs have a smooth surface morphology in a good crystalline quality, thus validated the etch-induced damage caused by texture engineering do not affect the active region of the VLED. Furthermore, on the basis of these results, prospective optimizations are suggested on surface engineering for light enhancement in VLEDs.

Hence, surface analysis using NDT is crucial because of non-contact, local, and non-destructive material characterization techniques adequate for measuring surface roughness and stress in VLEDs. Also, surface analysis using NDT helps in understanding the structure-property of nano-textured pyramids of the VLED without destructing or damaging the material. NDT will help the design engineers in a deep understanding of surface engineering to alleviate decreased LEE and enables them to find the relationship of luminous intensity and efficiency in corresponding to different degrees of surface roughness and stress state. The reason is that on one hand, more roughness in surface increases the optical output, while it also induces stress on the n-Ga layer on the other hand, which leads to degradation of the LEE. Thus, the optimized textured surface should be promising for the future applications of solid-state lighting.

6.6 Future Outlook

A unified framework of NDT in a standalone microscopy needs to be developed, where complimentary results from SEM, AFM, Raman spectroscopy, PL and XRD techniques can be obtained in parallel. This will facilitate device engineers to investigate the actual cause of low LEE, and other current challenges of the VLED structures facing, such as efficiency drop and green gap issues. Also, this standalone NDT will not only perform failure analysis but also optimizes texture engineering to produce stress-free GaN films, which are necessary to generate high power and high optical output LEDs for emerging smart lighting products.

Chapter Seven

Conclusions and Perspectives

7.1 Summary and Conclusions

Figure 7.1 provides a compact summary of keys results of this dissertation.
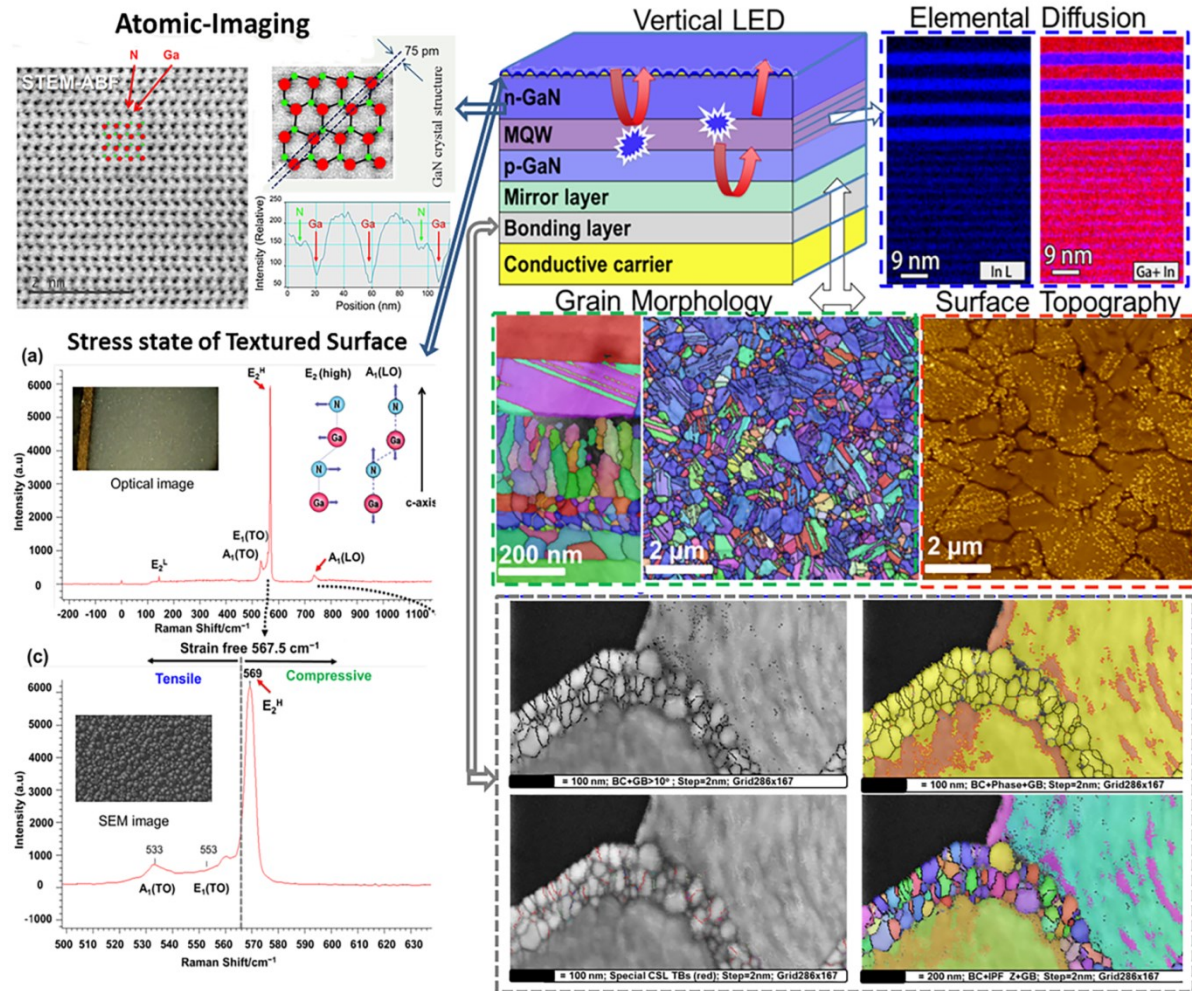
Figure 7.1 Summary of key findings in the understanding of the light extraction efficiency and reliability of the Vertical LED

In this dissertation, atomic or nano-scale characterization of the LED stack layers is systematically performed to understand their microstructure-property relationship, and to address the current challenges of efficiency droop and reliability issues. In order to explore the answer to the key question that what are possible causes of efficiency droop in the LED, advance microscopy techniques have been employed to characterize it at the nano or

atomic-scale. Later, the qualitative and quantitative 2D/3D characteristics were analyzed to optimize LED device for performance enhancement.

In this context, different properties such as surface morphology, compositional variation, elemental diffusion, and surface topography, stress-state, and interface-related reliability characteristics have been systematically investigated under the powerful high-resolution microscopy tools of SEM, FIB, TEM, AFM, Raman spectroscopy, XRD and PL, and their corresponding results are as follows:

1. SEM technique has provided surface morphology of the top surface and cross-sectional layers of the VLED. Combined SEM-based EBSD/TKD with the EDX analyses revealed elemental segregation, grain morphology (grain size, grain orientation, and grain boundary types) and crystallographic (texture) orientations of the LED stack layers. At the preliminary stage of the VLED investigation, the combination of SEM-TKD/EBSD with EDX proved to be robust and sophisticated methodology for nanocharacterization of the LED. On the other hand, TEM technique on the VLED exhibited its unique capability to reveal the structural and chemical properties of devices at atomic-scale resolution.

2. Combine results from SEM-TKD and TEM techniques exhibited detailed characterization of metallic bonding interface-related defects and nano-twinned boundaries. The correlative results are quite beneficial in understanding the origin of microstructure formation, especially the existence of nanocrystalline grains with special twin boundaries at Au-Au interface attribute towards twin-induced strengthening mechanism in wafer bonding.

3. Also in case of mirror layer of VLED, combine results from SEM-based TKD/EBSD/EDX, AC-STEM and AFM techniques provided unprecedented insights into the Ag reflection layer of VLED. The results revealed that Ag quality is strongly dependent on the control of interfacial diffusions, grain morphology, and surface topography. Abrupt Ag-GaN interface and compact smaller (fine) grains with a smooth surface (low roughness) are essential criteria for the better reflectivity

178

of light at the Ag mirror layer. Such peculiar results are critical in understanding the origin of diminution in IQE and EQE, which will assist to significantly enhance the overall light emission efficiency of the VLED devices.

4. In addition, AC-STEM having atomic resolution of 0.7 Å with EDX combination has demonstrated a parallel insight into InGaN/GaN-based MQW's by providing morphology, chemical composition, structural defects, polarity and nanoscale interfacial chemical migration. AC-STEM-based EDX analysis reveals that InGaN is a random alloy and causes indium fluctuations across four MQWs. HR-STEM results show that compositional inhomogeneity of indium distribution resulted in QW width variations and random indium fluctuations, which impacts the carrier localization at the MQWs. Also, HR-STEM images showed that InGaN QWs and GaN QBs interfaces are not atomically smooth, which is likely due to interdiffusion. Also, results show that Al-based electron blocking layer at the p-GaN side has a non-uniform profile and makes it ineffective for blocking electron leakage.

5. Furthermore, AC-STEM HAADF and BF images of GaN active region successfully determined that it holds wurtzite crystal structure with N-face polarity. The Ga-Ga atomic columns separated by 75 pm was resolved by STEM-HAADF imaging whereas the ABF technique utilized for a light element imaging with sub-angstrom resolution, which confirms the N-face polarity of the vertical LED. Thus, results from AC-STEM extract critical information across the active region (p-n junction) of the vertical LED, which encompasses QWs, QBs, and EBL layers along with picometer metrology of atomic structures in the GaN material. Consequently, these results at atomic resolution lead us to understand the origin of efficiency droop, QCSE, carrier delocalization, current leakage, structural defects, polarity and impurity diffusion.

6. In addition to above stated advanced microscopy techniques, surface analysis of the VLED using NDT of SEM, AFM, Raman spectroscopy, XRD, and PL provided surface morphology, surface topography, stress-state, phase identification of a crystalline material, and emission properties, respectively. For instance, AFM

results showed that the surface topography of nano-textured surface on VLED has a roughness of ~300 nm whereas Raman spectroscopy, XRD, and PL revealed that the stress-state of the nano-textured surface in a compressive stress. In parallel, XRD and PL techniques validated Raman spectroscopy results by indicating that the quality of crystal in a stress-state, resulting in blue VLED emission peak wavelength of 442 nm rather 450 nm. Thus, NDT will help the design engineers in a deep understanding of surface engineering to alleviate decreased LEE and enables them to find the relationship of luminous intensity and efficiency in corresponding to different degrees of surface roughness and stress state.

7. Surface analysis using NDT is necessary because of non-contact, local, and non-destructive material characterization adequate for measuring accurate surface topography (roughness) and stress-state in VLEDs.

8. Indeed, microscopy techniques are capable of performing component-level and device-level analysis, and offers unique information for LED optimization to play a vital role in the electronic materials industries. In general, microscopy characterization on the VLED demonstrated that the interface quality strongly influences the properties of the epitaxial layers, and interfaces are linked to hetero-structure properties, such as carrier density or mobility and recombination rates, which directly affect the efficiency droop of the VLED. Nonetheless, microscopy analysis is essential to map chemical composition, surface morphology, elemental diffusion or impurity levels, surface topography, and GBs that impact the electronic properties of the device under test (DUT).

9. Microstructural features interpreted from microscopy techniques are significantly important in associating them to the structure-property-process-performance relationship, which helps in the better discernment of materials design paradigm.

10. Atomic or nano-scale characterization of VLED facilitates quality analysis and quality control in the LED fabrication process, resulting in new process developments and optimization engineering.

In summary, in-depth analysis of wafer (metallic) bonding, the silver reflection layer, an active region (MQWs) and top-textured layers provided critical evidences in relation to failure analysis, and will assist device engineers in optoelectronics sector to identify the actual cause of efficiency droop in the LED. Nevertheless, the nanostructural study of the LED devices via powerful advanced microscopy tools resulted in optimization suggestions to enhance the light extraction efficiency and to improve the lifetime of the future smart LED devices.

7.2 Future Directions

7.2.1 Organic Solar Cells

Sunlight is a promising clean and readily available energy source compared to conventional fossil fuels on earth. To utilize that energy, solar cells are the devices that convert solar energy into electricity. However, today's solar cells generated electricity is less than 1.3% of the world's total energy consumption [384]. Although the 1st and 2nd generation solar cells, such as crystalline Si, III-V single junction, CdTe, and other inorganic solar cells, exist, still they are not pertinent devices for most desired applications due to their high temperature processing, high quality of Si or dependence on scare resources and complex engineering requirements [385]. The 3rd generation photovoltaic cells, such as Perovskite, quantum dot and organic solar cells (OSC) are emerging thin-film cells because they have potential to overcome Shockley-Queisser limit and are based on novel semiconductors [386], [387].

In OSC, polymer-based solar cells show great potential due to their low material cost, lightweight, mechanical flexibility, and swift processiblity. Also, they provide an attractive approach to increase solar cell efficiencies because their bandgaps and energy levels can be engineered by varying chemical structure [388], [389]. Nevertheless, the power conversion efficiency has been the main criterion for the OSC performance and is approaching 8-15%
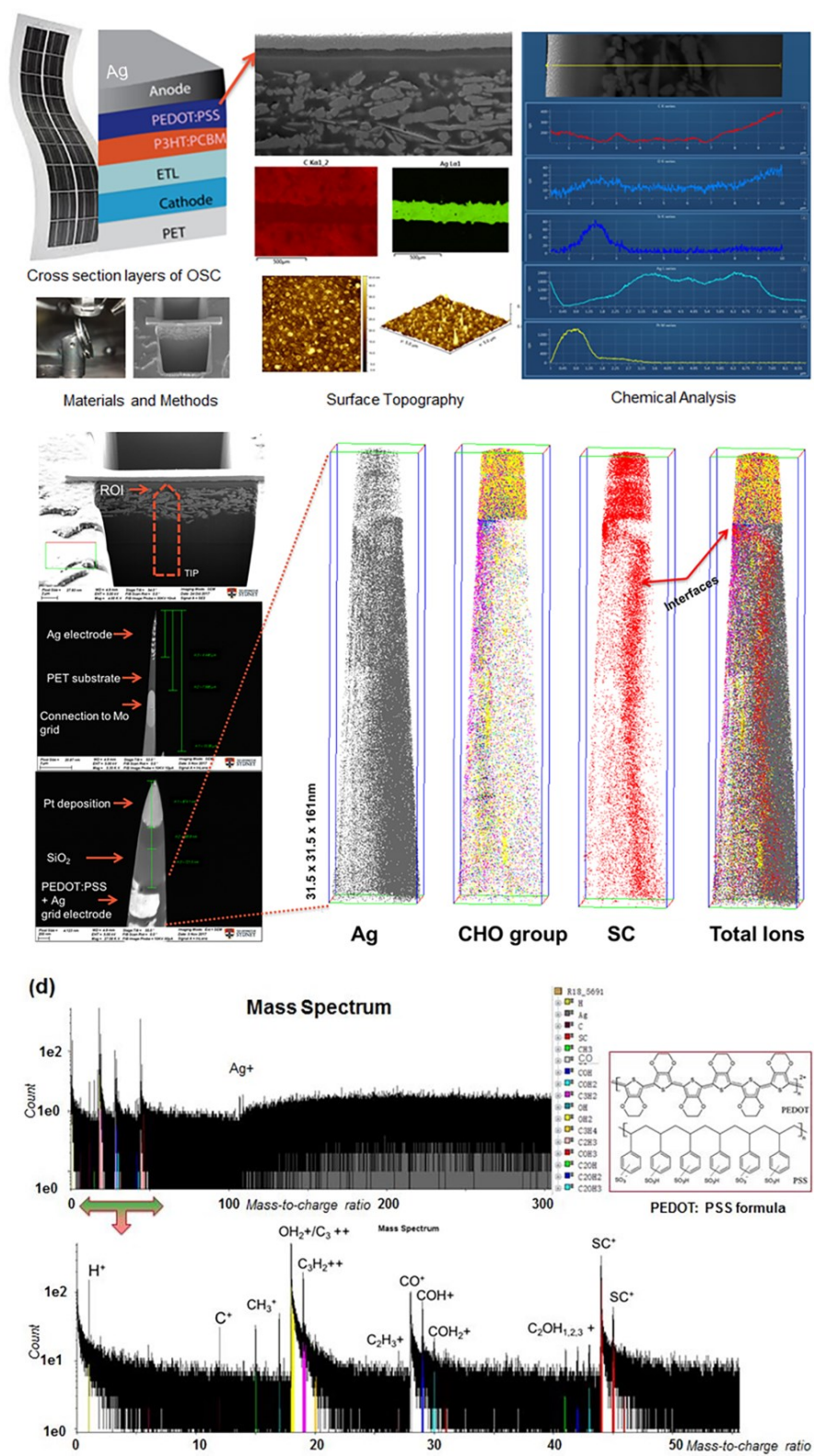
Figure 7.2. Nanocharacterization of Polymer Solar cells by SEM, EDX, and APT

in today's market products with the stability of almost one year [390]–[392], but the scope of further improvement exists. Thus, to understand their underlying fundamental mechanisms a detailed nanostructural characterization is necessary. In this regard, although SEM and STEM have been done, APT characterization is still rarely available [393]–[395]. This is because of challenging sample preparation (APT tips) of organic material under less damaging beam environment.

In this context, we have done preliminary work on the flexible polymer-based OSC and few attempts have been made to systematically analyze them under the powerful microscopic tools, specifically APT. The methodology of sample preparation via FIB and APT characterization are under consideration. So far, few initial results have been collected and are summarized in Figure 7.2 However, still there is potential to perform analytical nanocharacterization on organic materials to investigate the issues of efficiency and stability in OSC and organic LEDs (OLEDs).

7.2.2 Organic LEDs and optical CMOS-MEMS devices

For future work, atomic-scale characterization should broaden its versatility to organic electronics technologies (OLEDs) and Micro-Electro-Mechanical Systems (MEMS). The monolithic integration of the CMOS and MEMS technology, i.e., MEM Specific Integrated Circuit (MEMSIC), drives the need for "Everything on a Single IC". Although few groups have started work on these devices [253], [273], [396], [397], still to realize a given product of OLED and MEMSIC, considerable challenges remain unexplored in achieving a high-quality yield factor. Hence, it is suggested that the power of APT and AC-STEM technologies should not only be exploited for ICs but also for a variety of novel organic materials (OLED, OFET, OSC and smart MEMS devices (MEMS accelerometers, digital MEMS microphones, CMOS-MEMS thermoelectric micro-generators, optical MEMS, and MEMS RF resonators. Also, in future, it is expected that correlative microscopy by combining both APT and ET can be used to characterize the compositional and structural information of complex devices in three or four-dimensions at the atomic-scale. Consequently, this concept will facilitate the prototyping of organic and MEMS devices.

Further, there is a need to combine all the capabilities and features of different microscopy techniques into one standalone microscopy, namely "structure-properties microscopy". For instance, SEM or TEM in that prospective microscopy will contribute in: (a) imaging (the verification of internal and external shape, size and morphology of the DUT), (b) diffraction (from TEM) and Kikuchi patterns (from SEM-TKD) (the verification of atomic structure, amorphous or crystalline nature of each region of the DUT), and (c) analysis (credentials of any general composition of phases). Hence, integration of SEM or TEM (ET) and APT into one benchmark instrument can perform sophisticated device analysis.

7.3 Closing Thoughts

Having worked over five years on inorganic semiconductor devices, I am optimistic that field of organic semiconductor devices will become a dominant solution not only to issues of inorganic devices, such as scare resources, cost of fabrication and engineering complexity, and so on, but also able to mitigate the world energy crisis as well. It is also possible that light generating (OLED) and light absorbing (OSC) get integrated, thus, the potential of organic semiconductor devices is tremendous because of their non-renewable resources, flexibility, low fabrication cost, eco-friendly, sophisticated process and optimization engineering. I believe that atomic-scale characterization on organic semiconductor devices, such as OLED and OSC helps scientists, researchers and design engineers to investigate their chemical composition, surface topography, and interface diffusions between the active region and the related stack of thin layers. The focus of that vital research will be to present a competitive and failure analysis of by characterizing them at the nanoscale for performance optimization in efficiency and stability aspects.

References

[1]   S. Nakamura, M. Senoh, and T. Mukai, "P-GaN/N-InGaN/N-GaN Double-Heterostructure Blue-Light-Emitting Diodes," *Jpn. J. Appl. Phys.*, vol. 32, no. 1A, p. L8, Jan. 1993.

[2]   S. Nakamura, "Present performance of InGaN-based blue/green/yellow LEDs," in *Photonics West'97*, 1997, pp. 26–35.

[3]   S. Pimputkar, J. S. Speck, S. P. DenBaars, and S. Nakamura, "Prospects for LED lighting," *Nat. Photonics*, vol. 3, no. 4, pp. 180–182, Apr. 2009.

[4]   J. Y. Tsao *et al.*, "Toward Smart and Ultra-efficient Solid-State Lighting," *Adv. Opt. Mater.*, vol. 2, no. 9, pp. 809–836, Sep. 2014.

[5]   B. Hahn, B. Galler, and K. Engl, "Development of high-efficiency and high-power vertical light emitting diodes," *Jpn. J. Appl. Phys.*, vol. 53, no. 10, p. 100208, Sep. 2014.

[6]   T. Q. Khan, P. Bodrogi, Q. T. Vinh, and H. Winkler, *LED Lighting: Technology and Perception*. John Wiley & Sons, 2014.

[7]   A. V. Ortega and I. N. da Silva, "Technique for application of hi-bright LED in automobile industry through intelligent systems," presented at the Neural Networks, 2002. IJCNN '02. Proceedings of the 2002 International Joint Conference on, 2002, vol. 3, pp. 2674–2679.

[8]   G. Harbers, S. J. Bierhuizen, and M. R. Krames, "Performance of High Power Light Emitting Diodes in Display Illumination Applications," *J. Disp. Technol.*, vol. 3, no. 2, pp. 98–109, Jun. 2007.

[9]   R. Shriram, M. Sundhararajan, and N. Daimiwal, "Application of high & low brightness LEDs to human tissue to capture photoplethysmogram at a finger tip," presented

at the Convergence of Technology (I2CT), 2014 International Conference for, 2014, pp. 1–5.

[10]   T. Q. Khan, P. Bodrogi, Q. T. Vinh, and H. Winkler, *LED Lighting: Technology and Perception*. John Wiley & Sons, 2014.

[11]   "The Nobel Prize in Physics 2014." [Online]. Available: https://www.nobelprize.org/nobel_prizes/physics/laureates/2014/. [Accessed: 27-Sep-2017].

[12]   S. P. DenBaars, S. Nakamura, and J. S. Speck, "Gallium nitride based light emitting diodes (LEDs) for energy efficient lighting and displays," in *Electronics, Communications and Photonics Conference (SIECPC), 2013 Saudi International*, 2013, pp. 1–13.

[13]   "Top LED Technology Trends at Light+ Building 2016 - LEDinside." [Online]. Available:
http://www.ledinside.com/showreport/2016/3/top_led_technology_trends_at_light_building
_2016. [Accessed: 21-Jun-2017].

[14]   "Semiconductor Today." [Online]. Available: http://www.semiconductor-today.com/news_items/2011/JUNE/KOREAPHOTONICS_040611.html. [Accessed: 15-Jun-2016].

[15]   Y. Narukawa, M. Ichikawa, D. Sanga, M. Sano, and T. Mukai, "White light emitting diodes with super-high luminous efficacy," *J. Phys. Appl. Phys.*, vol. 43, no. 35, p. 354002, Aug. 2010.

[16]   K. T. Bicanic *et al.*, "Design of Phosphor White Light Systems for High-Power Applications," *ACS Photonics*, vol. 3, no. 12, pp. 2243–2248, Dec. 2016.

[17]   J. Cho, J. H. Park, J. K. Kim, and E. F. Schubert, "White light-emitting diodes: History, progress, and future," *Laser Amp Photonics Rev.*, vol. 11, no. 2, Mar. 2017.

[18]   G. S. B. Ganandran, T. M. I. Mahlia, H. C. Ong, B. Rismanchi, and W. T. Chong, "Cost-Benefit Analysis and Emission Reduction of Energy Efficient Lighting at the Universiti Tenaga Nasional," *The Scientific World Journal*, 2014. [Online]. Available:

https://www.hindawi.com/journals/tswj/2014/745894/. [Accessed: 28-Sep-2017].

[19]   M. A. Khan *et al.*, "Effects of a recessed camel-gate head structure on normally-off ALGaN/GaN HEMTs," *J. Korean Phys. Soc.*, vol. 62, no. 5, pp. 787–793, Mar. 2013.

[20]   Q. Rudiger, *Gallium Nitride Electronics*, 1st ed., vol. 96. Berlin, Heidelberg: Springer Berlin Heidelberg, 2008.

[21]   M. A. Khan, J.-W. Heo, H.-S. Kim, and H.-C. Park, "Comparison of recessed gate-head structures on normally-off AlGaN/GaN high-electron-mobility transistor performance," *J. Nanosci. Nanotechnol.*, vol. 14, no. 11, pp. 8141–8147, Nov. 2014.

[22]   *Gallium Nitride Electronics*, vol. 96. Berlin, Heidelberg: Springer Berlin Heidelberg, 2008.

[23]   "OSRAM Opto Semiconductors. OSRAM GmbH. Munich, Germany."

[24]   S. Nakamura, M. Senoh, N. Iwasa, and S. Nagahama, "High-Brightness InGaN Blue, Green and Yellow Light-Emitting Diodes with Quantum Well Structures," *Jpn. J. Appl. Phys.*, vol. 34, no. Part 2, No. 7A, pp. L797–L799, Jul. 1995.

[25]   S. P. DenBaars *et al.*, "Development of gallium-nitride-based light-emitting diodes (LEDs) and laser diodes for energy-efficient lighting and displays," *Acta Mater.*, vol. 61, no. 3, pp. 945–951, Feb. 2013.

[26]   D. Zhu, D. J. Wallis, and C. J. Humphreys, "Prospects of III-nitride optoelectronics grown on Si," *Rep. Prog. Phys.*, vol. 76, no. 10, p. 106501, 2013.

[27]   J. Wu *et al.*, "Unusual properties of the fundamental band gap of InN," *Appl. Phys. Lett.*, vol. 80, no. 21, p. 3967, 2002.

[28]   J. Wu *et al.*, "Small band gap bowing in In[sub 1−x]Ga[sub x]N alloys," *Appl. Phys. Lett.*, vol. 80, no. 25, p. 4741, 2002.

[29]   K. Gehrke, K. Perzlmaier, R. Floeter, and C. Schmid, "Optoelectronic semiconductor chip and method for producing an optoelectronic semiconductor chip,"

8816373, 26-Aug-2014.

[30]   J. P. Dakin and R. G. W. Brown, *Handbook of Optoelectronics (Two-Volume Set)*. CRC Press, 2010.

[31]   M. A. Khan, S. P. Ringer, and R. Zheng, "Atom Probe Tomography on Semiconductor Devices," *Adv. Mater. Interfaces*, Apr. 2016.

[32]   S. Nakamura, "III–V nitride based light-emitting devices," *Solid State Commun.*, vol. 102, no. 2–3, pp. 237–248, Apr. 1997.

[33]   S. Pimputkar, J. S. Speck, S. P. DenBaars, and S. Nakamura, "Prospects for LED lighting," *Nat. Photonics*, vol. 3, no. 4, pp. 180–182, Apr. 2009.

[34]   Y.-K. Kuo, J.-Y. Chang, M.-C. Tsai, and S.-H. Yen, "Advantages of blue InGaN multiple-quantum well light-emitting diodes with InGaN barriers," *Appl. Phys. Lett.*, vol. 95, p. 011116, Jul. 2009.

[35]   E. F. Schubert and J. K. Kim, "Solid-State Light Sources Getting Smart," *Science*, vol. 308, no. 5726, pp. 1274–1278, May 2005.

[36]   D. Kang *et al.*, "Comparison of the Performance of Lateral and Vertical InGaN/GaN-Based Light-Emitting Diodes with GaN and AlN Nucleation Layers," *ECS J. Solid State Sci. Technol.*, vol. 5, no. 2, pp. Q1–Q6, Jan. 2016.

[37]   C.-F. Chu *et al.*, "High Brightness GaN Vertical Light-Emitting Diodes on Metal Alloy for General Lighting Application," *Proc. IEEE*, vol. 98, no. 7, pp. 1197–1207, Jul. 2010.

[38]   Z. Chen and T. T. C. Inc, *Buffer layer for GaN-on-Si LED*. 2011.

[39]   S.-J. Lee, K. H. Kim, J.-W. Ju, T. Jeong, C.-R. Lee, and J. H. Baek, "High-Brightness GaN-Based Light-Emitting Diodes on Si Using Wafer Bonding Technology," *Appl. Phys. Express*, vol. 4, no. 6, p. 066501, May 2011.

[40]   K.-J. Byeon, J.-Y. Cho, J. O. Song, S. Y. Lee, and H. Lee, "High-Brightness

Vertical GaN-Based Light-Emitting Diodes With Hexagonally Close-Packed Micrometer Array Structures," *IEEE Photonics J.*, vol. 5, no. 6, pp. 8200708–8200708, Dec. 2013.

[41]   C.-H. Cheng *et al.*, "Growing GaN LEDs on amorphous SiC buffer with variable C/Si compositions," *Sci. Rep.*, vol. 6, p. srep19757, Jan. 2016.

[42]   C.-H. Cheng *et al.*, "Transferring the bendable substrateless GaN LED grown on a thin C-rich SiC buffer layer to flexible dielectric and metallic plates," *J. Mater. Chem. C*, vol. 5, no. 3, pp. 607–617, Jan. 2017.

[43]   "SEOULVIOSYS."   [Online].   Available: http://www.seoulviosys.com/eng/technology/technology05.asp. [Accessed: 15-Jun-2016].

[44]   O. Hunderi and D. Beaglehole, "On the reflectivity of rough metal surfaces," *Phys. Lett. A*, vol. 29, no. 6, pp. 335–336, Jun. 1969.

[45]   I. Schnitzer, E. Yablonovitch, C. Caneau, T. J. Gmitter, and A. Scherer, "30% external quantum efficiency from surface textured, thin-film light-emitting diodes," *Appl. Phys. Lett.*, vol. 63, no. 16, pp. 2174–2176, Oct. 1993.

[46]   Q. a Ding, K. Li, F. Kong, X. Chen, and J. Zhao, "Improving the Vertical Light-Extraction Efficiency of GaN-Based Thin-Film Flip-Chip LEDs With p-Side Deep-Hole Photonic Crystals," *J. Disp. Technol.*, vol. 10, no. 11, pp. 909–916, Nov. 2014.

[47]   S. Palakurthy, S. Singh, S. Pal, and C. Dhanavantri, "Design and comparative study of lateral and vertical LEDs with graphene as current spreading layer," *Superlattices Microstruct.*, vol. 86, pp. 86–94, Oct. 2015.

[48]   R.-H. Horng *et al.*, "Performance of GaN-based light-emitting diodes fabricated using GaN epilayers grown on silicon substrates," *Opt. Express*, vol. 22, no. S1, p. A179, Jan. 2014.

[49]   H. Kim and S.-N. Lee, "Performance characteristics of GaN-based light-emitting diodes fabricated with AgNi, AgCu, and AgAl-alloy reflectors," *J. Vac. Sci. Technol. B Microelectron. Nanometer Struct.*, vol. 29, no. 1, p. 011032, 2011.

[50]   M. cheol Yoo, "Method of making diode having reflective layer," US8236585 B2, 07-Aug-2012.

[51]   F.-R. Chien, S.-J. Hon, and M.-J. Lai, "Light emitting semiconductor device having reflection layer structure," US6492661 B1, 10-Dec-2002.

[52]   M. A. Khan *et al.*, "Insights into the Silver Reflection Layer of a Vertical LED for Light Emission Optimization," *ACS Appl. Mater. Interfaces*, vol. 9, no. 28, pp. 24259–24272, Jul. 2017.

[53]   H. Chen *et al.*, "Enhanced Performance of GaN-Based Light-Emitting Diodes by Using Al Mirror and Atomic Layer Deposition-TiO $_2$ /Al $_2$ O $_3$ Distributed Bragg Reflector Backside Reflector with Patterned Sapphire Substrate," *Appl. Phys. Express*, vol. 6, no. 2, p. 022101, Feb. 2013.

[54]   T. Doan *et al.*, "Vertical GaN based Light Emitting Diodes on Metal Alloy Substrate for Solid State Lighting Application," presented at the Integrated Optoelectronic Devices 2006, 2006, p. 61340G–61340G–6.

[55]   P. Kopperschmidt, S. Senz, G. Kästner, D. Hesse, and U. M. Gösele, "Materials integration of gallium arsenide and silicon by wafer bonding," *Appl. Phys. Lett.*, vol. 72, no. 24, p. 3181, 1998.

[56]   M. Alexe and U. Gösele, Eds., *Wafer Bonding*, vol. 75. Berlin, Heidelberg: Springer Berlin Heidelberg, 2004.

[57]   M. A. Khan, P. W. Trimby, H. W. Liu, and R. K. Zheng, "On the metallic bonding of GaN-based vertical light-emitting diode," *Mater. Sci. Semicond. Process.*, vol. 63, pp. 237–247, Jun. 2017.

[58]   T. Sano *et al.*, "High Internal Quantum Efficiency Blue-Green Light-Emitting Diode with Small Efficiency Droop Fabricated on Low Dislocation Density GaN Substrate," *Jpn. J. Appl. Phys.*, vol. 52, no. 8S, p. 08JK09, May 2013.

[59]   M.-A. Tsai, H.-W. Wang, P. Yu, H.-C. Kuo, and S.-H. Lin, "High Extraction

Efficiency of GaN-Based Vertical-Injection Light-Emitting Diodes Using Distinctive Indium–Tin-Oxide Nanorod by Glancing-Angle Deposition," *Jpn. J. Appl. Phys.*, vol. 50, no. 5R, p. 052102, May 2011.

[60]   C. Weisbuch, M. Piccardo, L. Martinelli, J. Iveland, J. Peretti, and J. S. Speck, "The efficiency challenge of nitride light-emitting diodes for lighting," *Phys. Status Solidi A*, vol. 212, no. 5, pp. 899–913, May 2015.

[61]   M.-H. Kim *et al.*, "Origin of efficiency droop in GaN-based light-emitting diodes," *Appl. Phys. Lett.*, vol. 91, no. 18, p. 183507, Oct. 2007.

[62]   Q. Zhou, M. Xu, and H. Wang, "Internal quantum efficiency improvement of InGaN/GaN multiple quantum well green light-emitting diodes," *Opto-Electron. Rev.*, vol. 24, no. 1, pp. 1–9, 2016.

[63]   "High Internal Quantum Efficiency Blue-Green Light-Emitting Diode with Small Efficiency Droop Fabricated on Low Dislocation Density GaN Substrate," *Jpn. J. Appl. Phys.*, vol. 52, no. 8S, p. 08JK09, May 2013.

[64]   J. Cho, E. F. Schubert, and J. K. Kim, "Efficiency droop in light-emitting diodes: Challenges and countermeasures," *Laser Photonics Rev.*, vol. 7, no. 3, pp. 408–421, May 2013.

[65]   C. Weisbuch, M. Piccardo, L. Martinelli, J. Iveland, J. Peretti, and J. S. Speck, "The efficiency challenge of nitride light-emitting diodes for lighting," *Phys. Status Solidi A*, vol. 212, no. 5, pp. 899–913, May 2015.

[66]   C. J. Humphreys *et al.*, "The atomic structure of polar and non-polar InGaN quantum wells and the green gap problem," *Ultramicroscopy*, vol. 176, pp. 93–98, May 2017.

[67]   J. H. Ryou *et al.*, "Control of Quantum-Confined Stark Effect in InGaN-Based Quantum Wells," *IEEE J. Sel. Top. Quantum Electron.*, vol. 15, no. 4, pp. 1080–1091, Jul. 2009.

[68]   Y.) Zhao *et al.*, "Mechanism of hole injection enhancement in light-emitting diodes by inserting multiple hole-reservoir layers in electron blocking layer," *J. Appl. Phys.*, vol. 119, no. 10, p. 105703, Mar. 2016.

[69]   S. Choi *et al.*, "Efficiency droop due to electron spill-over and limited hole injection in III-nitride visible light-emitting diodes employing lattice-matched InAlN electron blocking layers," *Appl. Phys. Lett.*, vol. 101, no. 16, p. 161110, Oct. 2012.

[70]   E. Kioupakis, P. Rinke, K. T. Delaney, and C. G. Van de Walle, "Indirect Auger recombination as a cause of efficiency droop in nitride light-emitting diodes," *Appl. Phys. Lett.*, vol. 98, no. 16, p. 161107, Apr. 2011.

[71]   Y. C. Shen, G. O. Mueller, S. Watanabe, N. F. Gardner, A. Munkholm, and M. R. Krames, "Auger recombination in InGaN measured by photoluminescence," *Appl. Phys. Lett.*, vol. 91, no. 14, p. 141101, Oct. 2007.

[72]   J. Wang, L. Wang, W. Zhao, Z. Hao, and Y. Luo, "Understanding efficiency droop effect in InGaN/GaN multiple-quantum-well blue light-emitting diodes with different degree of carrier localization," *Appl. Phys. Lett.*, vol. 97, no. 20, p. 201112, Nov. 2010.

[73]   Z. Yong-Ping *et al.*, "Effect of In Diffusion on the Property of Blue Light-Emitting Diodes*," *Chin. Phys. Lett.*, vol. 32, no. 6, p. 064207, Jun. 2015.

[74]   J. Hader, J. V. Moloney, and S. W. Koch, "Density-activated defect recombination as a possible explanation for the efficiency droop in GaN-based diodes," *Appl. Phys. Lett.*, vol. 96, no. 22, p. 221106, May 2010.

[75]   J. S. Speck and S. J. Rosner, "The role of threading dislocations in the physical properties of GaN and its alloys," *Phys. B Condens. Matter*, vol. 273–274, pp. 24–32, Dec. 1999.

[76]   H.-Y. Shih *et al.*, "Ultralow threading dislocation density in GaN epilayer on near-strain-free GaN compliant buffer layer and its applications in hetero-epitaxial LEDs," *Sci. Rep.*, vol. 5, p. 13671, Sep. 2015.

[77] I. Vurgaftman and J. R. Meyer, "Band parameters for nitrogen-containing semiconductors," *J. Appl. Phys.*, vol. 94, no. 6, p. 3675, 2003.

[78] S. Nakamura and G. Fasol, "Physics of Gallium Nitride and Related Compounds," in *The Blue Laser Diode*, Springer Berlin Heidelberg, 1997, pp. 21–34.

[79] S. Nakamura, "InGaN/AlGaN blue-light-emitting diodes," *J. Vac. Sci. Technol. A*, vol. 13, no. 3, pp. 705–710, May 1995.

[80] H. Sugawara, K. Itaya, and G. Hatakoshi, "Emission Properties of InGaAlP Visible Light-Emitting Diodes Employing a Multiquantum-Well Active Layer," *Jpn. J. Appl. Phys.*, vol. 33, no. Part 1, No. 10, pp. 5784–5787, Oct. 1994.

[81] S. Nakamura, M. Senoh, N. Iwasa, and S. Nagahama, "High-Brightness InGaN Blue, Green and Yellow Light-Emitting Diodes with Quantum Well Structures," *Jpn. J. Appl. Phys.*, vol. 34, no. Part 2, No. 7A, pp. L797–L799, Jul. 1995.

[82] G.-L. D. Bona, N. D. Buchan, W. Heuberger, and P. D. Röntgen, "Improved AlGaInP diodes emitting visible light," EP0540799 A1, 12-May-1993.

[83] T.-Y. Seong, Jung Han, Hiroshi Amano, and Hadis Morkoc, Eds., *III-Nitride Based Light Emitting Diodes and Applications*. Springer Netherlands, 2013.

[84] L.-Y. Su and J. Huang, "Methods of Improving GaN based LED Luminous Efficiency," *Appl Phys Lett*, vol. 91, no. 18, p. 181109, 2007.

[85] Y.-C. Yao *et al.*, "Enhanced external quantum efficiency in GaN-based vertical-type light-emitting diodes by localized surface plasmons," *Sci. Rep.*, vol. 6, p. 22659, Mar. 2016.

[86] K. J. Lee, S.-J. Kim, J.-J. Kim, K. Hwang, S.-T. Kim, and S.-J. Park, "Enhanced performance of InGaN/GaN multiple-quantum-well light-emitting diodes grown on nanoporous GaN layers," *Opt. Express*, vol. 22, no. 104, pp. A1164–A1173, Jun. 2014.

[87] A. d. Giddings, T. j. Prosa, D. Olson, P. h. Clifton, and D. j. Larson, "Reverse Engineering at the Atomic Scale: Competitive Analysis of a Gallium-Nitride-Based

Commercial Light-Emitting Diode," *Microsc. Today*, vol. 22, no. 05, pp. 12–19, Sep. 2014.

[88] P. Peres, A. Merkulov, S. Y. Choi, F. Desse, and M. Schuhmacher, "Characterization of LED materials using dynamic SIMS," *Surf. Interface Anal.*, vol. 45, no. 1, pp. 437–440, Jan. 2013.

[89] "Dopant monitoring in LED devices with CAMECA Dynamic SIMS tools." [Online]. Available: http://www.cameca.com/markets/energy-materials/dopant-monitoring-led-sims. [Accessed: 23-Jan-2018].

[90] J. Kim *et al.*, "Principle of direct van der Waals epitaxy of single-crystalline films on epitaxial graphene," *Nat. Commun.*, vol. 5, Sep. 2014.

[91] K. Song, G.-Y. Shin, J. K. Kim, S. H. Oh, and C. T. Koch, "Strain mapping of LED devices by dark-field inline electron holography: Comparison between deterministic and iterative phase retrieval approaches," *Ultramicroscopy*, vol. 127, no. Supplement C, pp. 119–125, Apr. 2013.

[92] G. Capuzzo *et al.*, "All-nitride $Al_xGa_{1−x}N$:Mn/GaN distributed Bragg reflectors for the near-infrared," *Sci. Rep.*, vol. 7, p. 42697, Feb. 2017.

[93] Z. Li, Y. Tang, X. Ding, C. Li, D. Yuan, and Y. Lu, "Reconstruction and thermal performance analysis of die-bonding filling states for high-power light-emitting diode devices," *Appl. Therm. Eng.*, vol. 65, no. 1, pp. 236–245, Apr. 2014.

[94] K. Lekhal *et al.*, "Selective-area growth of GaN microrods on strain-induced templates by hydride vapor phase epitaxy," *Jpn. J. Appl. Phys.*, vol. 55, no. 5S, p. 05FF03, Mar. 2016.

[95] T. Jiang *et al.*, "Spatial distribution of crystalline quality in N-type GaN grown on patterned sapphire substrate," *Opt. Mater. Express*, vol. 6, no. 6, pp. 1817–1826, Jun. 2016.

[96] L. Ming-Gang *et al.*, "Performance improvement of GaN-based light-emitting diodes transferred from Si (111) substrate onto electroplating Cu submount with embedded wide p-electrodes," *Chin. Phys. B*, vol. 24, no. 3, p. 038503, 2015.

[97]   J. Ma, X. Zhu, K. M. Wong, X. Zou, and K. M. Lau, "Improved GaN-based LED grown on silicon (111) substrates using stress/dislocation-engineered interlayers," *J. Cryst. Growth*, vol. 370, no. Supplement C, pp. 265–268, May 2013.

[98]   W. S. Wong *et al.*, "Fabrication of thin-film InGaN light-emitting diode membranes by laser lift-off," *Appl. Phys. Lett.*, vol. 75, no. 10, pp. 1360–1362, Sep. 1999.

[99]   A. Cerezo and M. G. Hetherington, "VISUALISATION AND ANALYSIS OF 3-DIMENSIONAL ATOM PROBE DATA," *J. Phys. Colloq.*, vol. 50, no. C8, pp. C8-523-C8-528, Nov. 1989.

[100]   D. J. Larson, P. P. Camus, J. L. Vargas, T. F. Kelly, and M. K. Miller, "Specimen Preparation and Atom Probe Field Ion Microscopy of BSCCO-2212 Superconductors," *J. Phys. IV*, vol. 06, no. C5, pp. C5-271-C5-276, Sep. 1996.

[101]   T. Philippe *et al.*, "Clustering and nearest neighbour distances in atom-probe tomography," *Ultramicroscopy*, vol. 109, no. 10, pp. 1304–1309, Sep. 2009.

[102]   B. Gault *et al.*, "Advances in the reconstruction of atom probe tomography data," *Ultramicroscopy*, vol. 111, no. 6, pp. 448–457, May 2011.

[103]   D. j. Larson, B. p. Geiser, T. j. Prosa, S. s. a. Gerstl, D. a. Reinhard, and T. f. Kelly, "Improvements in planar feature reconstructions in atom probe tomography," *J. Microsc.*, vol. 243, no. 1, pp. 15–30, Jul. 2011.

[104]   G. Da Costa, H. Wang, S. Duguay, A. Bostel, D. Blavette, and B. Deconihout, "Advance in multi-hit detection and quantization in atom probe tomography," *Rev. Sci. Instrum.*, vol. 83, no. 12, p. 123709, Dec. 2012.

[105]   S. Nakahara, "Recent development in a TEM specimen preparation technique using FIB for semiconductor devices," *Surf. Coat. Technol.*, vol. 169–170, pp. 721–727, Jun. 2003.

[106]   K. Thompson, B. Gorman, D. Larson, B. van Leer, and L. Hong, "Minimization of Ga Induced FIB Damage Using Low Energy Clean-up," *Microsc. Microanal.*, vol. 12, no.

Supplement S02, pp. 1736–1737, Aug. 2006.

[107] M.-H. Lee and K.-H. Kim, "Post-thinning using Ar ion-milling system for transmission electron microscopy specimens prepared by focused ion beam system: POST-THINNING TECHNIQUE FOR FIBED TEM SPECIMENS," *J. Microsc.*, vol. 261, no. 3, pp. 243–248, Mar. 2016.

[108] L. A. Giannuzzi, J. L. Drown, S. R. Brown, R. B. Irwin, and F. A. Stevie, "Focused Ion Beam Milling and Micromanipulation Lift-Out for Site Specific Cross-Section Tem Specimen Preparation," *MRS Proc.*, vol. 480, Jan. 1997.

[109] S. E. Thompson and S. Parthasarathy, "Moore's law: the future of Si microelectronics," *Mater. Today*, vol. 9, no. 6, pp. 20–25, Jun. 2006.

[110] "Intel® 14 nm Technology," *Intel*. [Online]. Available: https://www.intel.com/content/www/us/en/silicon-innovations/intel-14nm-technology.html. [Accessed: 10-Jan-2018].

[111] K. Kim and G.-S. Park, "Landscape for semiconductor analysis: Issues and challenges," in *Physical and Failure Analysis of Integrated Circuits (IPFA), 2011 18th IEEE International Symposium on the*, 2011, pp. 1–9.

[112] X. Wei, L. Zhao, J. Wang, Y. Zeng, and J. Li, "Characterization of nitride-based LED materials and devices using TOF-SIMS," *Surf. Interface Anal.*, vol. 46, no. S1, pp. 299–302, Nov. 2014.

[113] M. Bosman *et al.*, "The distribution of chemical elements in Al- or La-capped high-κ metal gate stacks," *Appl. Phys. Lett.*, vol. 97, no. 10, p. 103504, Sep. 2010.

[114] B. P. Gorman, A. G. Norman, D. Lawrence, T. Prosa, H. Guthrey, and M. Al-Jassim, "Atomic scale characterization of compound semiconductors using atom probe tomography," in *Photovoltaic Specialists Conference (PVSC), 2011 37th IEEE*, 2011, pp. 003357–003359.

[115] T. F. Kelly, "3D atomic scale imaging methods," US8670608 B2, 11-Mar-2014.

[116] M. K. Miller, A. Cerezo, M. G. Hetherington, and G. D. W. S. FRS, *Atom Probe Field Ion Microscopy*. Clarendon Press | Monographs on the Physics and Chemistry of Materials 52, 1996.

[117] B. Gault, M. P. Moody, J. M. Cairney, and S. P. Ringer, *Atom Probe Microscopy*, vol. 160. New York, NY: Springer New York, 2012.

[118] P. W. Trimby *et al.*, "Characterizing deformed ultrafine-grained and nanocrystalline materials using transmission Kikuchi diffraction in a scanning electron microscope," *Acta Mater.*, vol. 62, pp. 69–80, Jan. 2014.

[119] P. W. Trimby, "Orientation mapping of nanostructured materials using transmission Kikuchi diffraction in the scanning electron microscope," *Ultramicroscopy*, vol. 120, pp. 16–24, Sep. 2012.

[120] P. W. Trimby, "Orientation mapping of nanostructured materials using transmission Kikuchi diffraction in the scanning electron microscope," *Ultramicroscopy*, vol. 120, pp. 16–24, Sep. 2012.

[121] J. M. Zuo and J. C. H. Spence, *Advanced Transmission Electron Microscopy*. New York, NY: Springer New York, 2017.

[122] D. J. Smith, "Ultimate resolution in the electron microscope?," *Mater. Today*, vol. 11, pp. 30–38, 2008.

[123] C. Hetherington, "Aberration correction for TEM," *Mater. Today*, vol. 7, no. 12, pp. 50–55, Dec. 2004.

[124] M. K. Miller and R. G. Forbes, "The Local Electrode Atom Probe," in *Atom-Probe Tomography*, Springer US, 2014, pp. 229–258.

[125] M. Herbig, P. Choi, and D. Raabe, "Combining structural and chemical information at the nanometer scale by correlative transmission electron microscopy and atom probe tomography," *Ultramicroscopy*, vol. 153, pp. 32–39, Jun. 2015.

[126] T. F. Kelly, "The Many Connections Between Atom Probe and Electron Microscopy," *Microscopy and Microanalysis*, Jul-2017. [Online]. Available: /core/journals/microscopy-and-microanalysis/article/many-connections-between-atom-probe-and-electron-microscopy/3B70D24AEAD359F2CE43DCF85D7E819C. [Accessed: 27-Sep-2017].

[127] P. E. Batson, N. Dellby, and O. L. Krivanek, "Sub-ångstrom resolution using aberration corrected electron optics," *Nature*, vol. 418, no. 6898, pp. 617–620, Aug. 2002.

[128] A. I. Kirkland, S. Haigh, and L.-Y. Chang, "Aberration corrected TEM: current status and future prospects," *J. Phys. Conf. Ser.*, vol. 126, no. 1, p. 012034, 2008.

[129] U. Dahmen, R. Erni, V. Radmilovic, C. Ksielowski, M.-D. Rossell, and P. Denes, "Background, status and future of the Transmission Electron Aberration-corrected Microscope project," *Philos. Trans. R. Soc. Lond. Math. Phys. Eng. Sci.*, vol. 367, no. 1903, pp. 3795–3808, Sep. 2009.

[130] P. A. Midgley and M. Weyland, "3D electron microscopy in the physical sciences: the development of Z-contrast and EFTEM tomography," *Ultramicroscopy*, vol. 96, no. 3–4, pp. 413–431, Sep. 2003.

[131] A. B. Yankovich *et al.*, "Thickness Variations and Absence of Lateral Compositional Fluctuations in Aberration-Corrected STEM Images of InGaN LED Active Regions at Low Dose," *Microscopy and Microanalysis*, Jun-2014. [Online]. Available: /core/journals/microscopy-and-microanalysis/article/thickness-variations-and-absence-of-lateral-compositional-fluctuations-in-aberrationcorrected-stem-images-of-ingan-led-active-regions-at-low-dose/A89ADEF5A2BE548358E440C0B272D02F. [Accessed: 25-Aug-2017].

[132] N. Tanaka, "Present status and future prospects of spherical aberration corrected TEM/STEM for study of nanomaterials *," *Sci. Technol. Adv. Mater.*, vol. 9, no. 1, p. 014111, Jan. 2008.

[133] D. J. Smith, T. Aoki, J. Mardinly, L. Zhou, and M. R. McCartney, "Exploring

aberration-corrected electron microscopy for compound semiconductors," *Microscopy*, vol. 62, no. suppl 1, pp. S65–S73, Jun. 2013.

[134] "Tapping Mode AFM," *Bruker AFM Probes Announcements*. .

[135] P. Puech *et al.*, "GaN nanoindentation: A micro-Raman spectroscopy study of local strain fields," *J. Appl. Phys.*, vol. 96, no. 5, pp. 2853–2856, Sep. 2004.

[136] M. Ohring and L. Kasprzak, *Reliability and Failure of Electronic Materials and Devices*. Academic Press, 2014.

[137] "Photoluminescence - an overview | ScienceDirect Topics." [Online]. Available: https://www.sciencedirect.com/topics/biochemistry-genetics-and-molecular-biology/photoluminescence. [Accessed: 25-Jan-2018].

[138] O. Ueda and S. J. Pearton, Eds., *Materials and Reliability Handbook for Semiconductor Optical and Electron Devices*. New York, NY: Springer New York, 2013.

[139] W. D. van Driel and X. Fan, *Solid State Lighting Reliability: Components to Systems*. Springer Science & Business Media, 2012.

[140] M. K. Miller and R. G. Forbes, "The Local Electrode Atom Probe," in *Atom-Probe Tomography*, Springer US, 2014, pp. 229–258.

[141] D. Cullen and D. Smith, "Preparation of AlGaN-based High Electron Mobility Transistor Devices using Focused Ion Beam Milling," *Microsc. Microanal.*, vol. 14, no. Supplement S2, pp. 1030–1031, Aug. 2008.

[142] L. Rigutti, B. Bonef, J. Speck, F. Tang, and R. A. Oliver, "Atom probe tomography of nitride semiconductors," *Scr. Mater.*, Jan. 2017.

[143] D. J. Smith, J. Lu, T. Aoki, M. R. McCartney, and Y. H. Zhang, "Observation of compound semiconductors and heterovalent interfaces using aberration-corrected scanning transmission electron microscopy," *J. Mater. Res.*, pp. 1–7, Aug. 2016.

[144] B. Gault, M. P. Moody, J. M. Cairney, and S. P. Ringer, "Atom probe

crystallography," *Mater. Today*, vol. 15, no. 9, pp. 378–386, Sep. 2012.

[145]　G. Haberfehlner *et al.*, "Four-dimensional spectral low-loss energy-filtered transmission electron tomography of silicon nanowire-based capacitors," *Appl. Phys. Lett.*, vol. 101, no. 6, p. 063108, 2012.

[146]　S. Van Aert, K. J. Batenburg, M. D. Rossell, R. Erni, and G. Van Tendeloo, "Three-dimensional atomic imaging of crystalline nanoparticles," *Nature*, vol. 470, no. 7334, pp. 374–377, Feb. 2011.

[147]　M. Herbig, P. Choi, and D. Raabe, "Combining structural and chemical information at the nanometer scale by correlative transmission electron microscopy and atom probe tomography," *Ultramicroscopy*, vol. 153, pp. 32–39, Jun. 2015.

[148]　D. Blavette and S. Duguay, "Atom probe tomography in nanoelectronics," *Eur. Phys. J. Appl. Phys.*, vol. 68, no. 1, p. 10101, Oct. 2014.

[149]　A. Grenier *et al.*, "3D analysis of advanced nano-devices using electron and atom probe tomography," *Ultramicroscopy*, vol. 136, pp. 185–192, Jan. 2014.

[150]　T. T. Tsong, "Field penetration and band bending near semiconductor surfaces in high electric fields," *Surf. Sci.*, vol. 81, no. 1, pp. 28–42, Feb. 1979.

[151]　A. Grenier *et al.*, "Three dimensional imaging and analysis of a single nano-device at the ultimate scale using correlative microscopy techniques," *Appl. Phys. Lett.*, vol. 106, no. 21, p. 213102, May 2015.

[152]　M. Miller and T. Kelly, "The Atom TOMography (ATOM) Concept," *Microsc. Microanal.*, vol. 16, no. Supplement S2, pp. 1856–1857, Jul. 2010.

[153]　T. Kelly *et al.*, "Toward Atomic-Scale Tomography: The ATOM Project," *Microsc. Microanal.*, vol. 17, no. Supplement S2, pp. 708–709, Jul. 2011.

[154]　T. F. Kelly, M. K. Miller, K. Rajan, and S. P. Ringer, "Atomic-Scale Tomography: A 2020 Vision," *Microsc. Microanal.*, vol. 19, no. 03, pp. 652–664, Jun. 2013.

[155] P. Dannberg, L. Erdmann, A. Krehl, C. Wächter, and A. Bräuer, "Integration of optical interconnects and optoelectronic elements on wafer-scale," *Mater. Sci. Semicond. Process.*, vol. 3, no. 5–6, pp. 437–441, Oct. 2000.

[156] V. Dragoi, E. Cakmak, and E. Pabo, "Wafer bonding with metal layers for MEMS applications," 2009, pp. 215–218.

[157] C. Colinge, *Semiconductor Wafer Bonding 11: Science, Technology, and Applications - In Honor of Ulrich Gösele*. The Electrochemical Society, 2010.

[158] V. Dragoi, P. Lindner, M. Tischler, and C. Schaefer, "New challenges for 300mm Si technology: 3D interconnects at wafer scale by aligned wafer bonding," *Mater. Sci. Semicond. Process.*, vol. 5, no. 4–5, pp. 425–428, Aug. 2002.

[159] P. Garrou, "Introduction to 3D Integration," in *Handbook of 3D Integration*, P. Garrou, C. Bower, and P. Ramm, Eds. Wiley-VCH Verlag GmbH & Co. KGaA, 2008, pp. 1–11.

[160] C.-T. Ko and K.-N. Chen, "Wafer-level bonding/stacking technology for 3D integration," *Microelectron. Reliab.*, vol. 50, no. 4, pp. 481–488, Apr. 2010.

[161] J.-W. Yoon, H.-S. Chun, J.-M. Koo, and S.-B. Jung, "Au–Sn flip-chip solder bump for microelectronic and optoelectronic applications," *Microsyst. Technol.*, vol. 13, no. 11–12, pp. 1463–1469, May 2007.

[162] N. Belov *et al.*, "Thin-layer Au-Sn solder bonding process for wafer-level packaging, electrical interconnections and MEMS applications," in *2009 IEEE International Interconnect Technology Conference*, 2009, pp. 128–130.

[163] V. Dragoi, G. Mittendorfer, J. Burggraf, and M. Wimplinger, "Metal Thermocompression Wafer Bonding for 3D Integration and MEMS Applications," 2010, pp. 27–35.

[164] R.-H. Horng, C.-H. Chen, W.-C. Kao, and D.-S. Wuu, "High-yield thin GaN LED using metal bonding and laser lift-off technology," 2012, p. 84841H.

[165]   J. Ciulik and M. R. Notis, "The Au☐Sn phase diagram," *J. Alloys Compd.*, vol. 191, no. 1, pp. 71–78, Jan. 1993.

[166]   W. Kim, Q. Wang, K. Jung, J. Hwang, and C. Moon, "Application of Au-Sn eutectic bonding in hermetic RF MEMS wafer level packaging," in *9th International Symposium on Advanced Packaging Materials: Processes, Properties and Interfaces, 2004. Proceedings*, 2004, pp. 215–219.

[167]   Z. Ling *et al.*, "Development of advanced AuSn alloy plating technology for semiconductor application," in *2014 15th International Conference on Electronic Packaging Technology (ICEPT)*, 2014, pp. 113–116.

[168]   H. Okamoto, "Au-Sn (Gold-Tin)," *J. Phase Equilibria Diffus.*, vol. 28, no. 5, pp. 490–490, Oct. 2007.

[169]   T. A. Tollefsen *et al.*, "Au-Sn SLID Bonding: A Reliable HT Interconnect and Die Attach Technology," *Metall. Mater. Trans. B*, vol. 44, no. 2, pp. 406–413, Apr. 2013.

[170]   J. Wu, S. X. Jia, Y. X. Wang, and J. Zhu, "Study on the Gold-Gold Thermocompression Bonding for Wafer-Level Packaging," *Adv. Mater. Res.*, vol. 60–61, pp. 325–329, 2009.

[171]   N. Malik, K. Schjolberg-Henriksen, E. Poppe, and T. G. Finstad, "Al-Al thermocompression bonding for wafer-level MEMS packaging," 2013, pp. 1067–1070.

[172]   M. M. V. Taklo, P. Storås, K. Schjølberg-Henriksen, H. K. Hasting, and H. Jakobsen, "Strong, high-yield and low-temperature thermocompression silicon wafer-level bonding with gold," *J. Micromechanics Microengineering*, vol. 14, no. 7, p. 884, May 2004.

[173]   N. Malik, P. A. Carvalho, E. Poppe, and T. G. Finstad, "Interfacial characterization of Al-Al thermocompression bonds," *J. Appl. Phys.*, vol. 119, no. 20, p. 205303, May 2016.

[174]   A. Fan, A. Rahman, and R. Reif, "Copper Wafer Bonding," *Electrochem. Solid-State Lett.*, vol. 2, no. 10, pp. 534–536, Oct. 1999.

[175] C. H. Tsau, M. A. Schmidt, and S. M. Spearing, "Characterization of Low Temperature, Wafer-Level Gold-Gold Thermocompression Bonds," *MRS Online Proceedings Library Archive*, Jan-1999. [Online]. Available: /core/journals/mrs-online-proceedings-library-archive/article/characterization-of-low-temperature-wafer-level-gold-gold-thermocompression-bonds/554794A9323DD1E36FAC8FE5EB7C6B5E.   [Accessed: 13-Nov-2016].

[176] V. Dragoi and E. Pabo, "Wafer Bonding Process Selection," 2010, pp. 509–517.

[177] Z. Chen, "Buffer layer for GaN-on-Si LED," US8686430 B2, 01-Apr-2014.

[178] C. H. Tsau, S. M. Spearing, and M. A. Schmidt, "Fabrication of wafer-level thermocompression bonds," *J. Microelectromechanical Syst.*, vol. 11, no. 6, pp. 641–647, Dec. 2002.

[179] C. H. Tsau, S. M. Spearing, and M. A. Schmidt, "Characterization of wafer-level thermocompression bonds," *J. Microelectromechanical Syst.*, vol. 13, no. 6, pp. 963–971, Dec. 2004.

[180] D.-S. Wuu, S.-C. Hsu, S.-H. Huang, C.-C. Wu, C.-E. Lee, and R.-H. Horng, "GaN/Mirror/Si Light-Emitting Diodes for Vertical Current Injection by Laser Lift-Off and Wafer Bonding Techniques," *Jpn. J. Appl. Phys.*, vol. 43, no. 8R, p. 5239, Aug. 2004.

[181] T.-H. Lin, S.-J. Wang, and C.-H. Hung, "Enhanced light extraction of GaN-based vertical LEDs with patterned trenches and nanostructures," *Mater. Sci. Semicond. Process.*, vol. 57, pp. 77–82, Jan. 2017.

[182] R.-H. Horng, S.-H. Huang, D.-S. Wuu, and Y.-Z. Jiang, "Characterization of Large-Area AlGaInP/Mirror/Si Light-Emitting Diodes Fabricated by Wafer Bonding," *Jpn. J. Appl. Phys.*, vol. 43, no. 5R, p. 2510, May 2004.

[183] D. Lauvernier, D. Van Thourhout, C. DETAVERNIER, and R. Baets, "Metal bonding with ultra-thin layer for optical applications," in *Proceedings of the 12th Annual Symposium of the IEEE/LEOS Benelux Chapter*, 2007, pp. 79–82.

[184]   A. A. Bajwa, Y. Qin, R. Reiner, R. Quay, and J. Wilde, "Assembly and Packaging Technologies for High-Temperature and High-Power GaN Devices," *IEEE Trans. Compon. Packag. Manuf. Technol.*, vol. 5, no. 10, pp. 1402–1416, Oct. 2015.

[185]   M. A. Schmidt, "Wafer-to-wafer bonding for microstructure formation," *Proc. IEEE*, vol. 86, no. 8, pp. 1575–1585, Aug. 1998.

[186]   K. Scheerschmidt, D. Conrad, A. Belov, and D. Timpel, "Enhanced semi-empirical potentials in molecular dynamics simulations of wafer bonding," *Mater. Sci. Semicond. Process.*, vol. 3, no. 1–2, pp. 129–135, Mar. 2000.

[187]   J. Y. Tsai, C. W. Chang, Y. C. Shieh, Y. C. Hu, and C. R. Kao, "Controlling the microstructure from the gold-tin reaction," *J. Electron. Mater.*, vol. 34, no. 2, pp. 182–187, Feb. 2005.

[188]   H. Ji, Y. Ma, M. Li, and C. Wang, "Effect of the Silver Content of SnAgCu Solder on the Interfacial Reaction and on the Reliability of Angle Joints Fabricated by Laser-Jet Soldering," *J. Electron. Mater.*, vol. 44, no. 2, pp. 733–743, Feb. 2015.

[189]   A. Chitnis, "Permanent wafer bonding using metal alloy preform discs," US20080096365 A1, 24-Apr-2008.

[190]   T. B. Massalski and H. W. King, "The lattice spacing relationships in close-packed α and ζ phases based on gold," *Acta Metall.*, vol. 8, no. 10, pp. 677–683, Oct. 1960.

[191]   F. G. Yost, M. M. Karnowsky, W. D. Drotning, and J. H. Gieske, "Thermal expansion and elastic properties of high gold-Tin Alloys," *Metall. Trans. A*, vol. 21, no. 7, pp. 1885–1889, Jul. 1990.

[192]   T. A. Tollefsen, A. Larsson, O. M. Løvvik, and K. Aasmundtveit, "Au-Sn SLID Bonding—Properties and Possibilities," *Metall. Mater. Trans. B*, vol. 43, no. 2, pp. 397–405, Apr. 2012.

[193]   E. Zakel and H. Reichl, "Au-Sn bonding metallurgy of TAB contacts and its influence on the Kirkendall effect in the ternary Cu-Au-Sn," *IEEE Trans. Compon. Hybrids*

Manuf. Technol., vol. 16, no. 3, pp. 323–332, May 1993.

[194]   E. Gusev, E. Garfunkel, and A. Dideikin, *Advanced Materials and Technologies for Micro/Nano-Devices, Sensors and Actuators*. Springer, 2010.

[195]   "EBSD Oxford Instruments - Home." [Online]. Available: http://www.ebsd.com/. [Accessed: 17-Nov-2016].

[196]   R. R. Chromik, D.-N. Wang, A. Shugar, L. Limata, M. R. Notis, and R. P. Vinci, "Mechanical Properties of Intermetallic Compounds in the Au–Sn System," *J. Mater. Res.*, vol. 20, no. 08, pp. 2161–2172, Aug. 2005.

[197]   A. Garnier, X. Baillin, and F. Hodaj, "Solidification and interfacial interactions in gold–tin system during eutectic or thermo-compression bonding for 200 mm MEMS wafer level hermetic packaging," *J. Mater. Sci. Mater. Electron.*, vol. 24, no. 12, pp. 5000–5013, Dec. 2013.

[198]   W. D. Callister and D. G. Rethwisch, *Materials Science and Engineering: An Introduction, 9th Edition: Ninth Edition*. 2013.

[199]   S. Khamsuk, N. Park, S. Gao, D. Terada, H. Adachi, and N. Tsuji, "Mechanical Properties of Bulk Ultrafine Grained Aluminum Fabricated by Torsion Deformation at Various Temperatures and Strain Rates," *Mater. Trans.*, vol. 55, no. 1, pp. 106–113, Jan. 2014.

[200]   Y. H. Zhao *et al.*, "Tougher ultrafine grain Cu via high-angle grain boundaries and low dislocation density," *Appl. Phys. Lett.*, vol. 92, no. 8, p. 081903, Feb. 2008.

[201]   M. Öztas, "Influence of grain size on electrical and optical properties of InP films," *Chin. Phys. Lett.*, vol. 25, no. 11, p. 4090, 2008.

[202]   Z. Ikonić, G. P. Srivastava, and J. C. Inkson, "Electronic properties of twin boundaries and twinning superlattices in diamond-type and zinc-blende-type semiconductors," *Phys. Rev. B*, vol. 48, no. 23, pp. 17181–17193, Dec. 1993.

[203]   M. J. Demkowicz, O. Anderoglu, X. Zhang, and A. Misra, "The influence of ∑3 twin boundaries on the formation of radiation-induced defect clusters in nanotwinned Cu," *J. Mater. Res.*, vol. 26, no. 14, pp. 1666–1675, Jul. 2011.

[204]   T.-H. Yang, C. Jin, H. Zhou, R. J. Narayan, and J. Narayan, "Role of twin boundaries in semiconductor to metal transition characteristics of VO2 films," *Appl. Phys. Lett.*, vol. 97, no. 7, p. 072101, Aug. 2010.

[205]   H. M. Breitling and R. E. Hummel, "Electromigration in thin silver, copper, gold, indium, tin, lead and magnesium films," *J. Phys. Chem. Solids*, vol. 33, no. 4, pp. 845–852, Jan. 1972.

[206]   C.-U. Kim, *Electromigration in Thin Films and Electronic Devices: Materials and Reliability*. Elsevier, 2011.

[207]   H. Li, X. Liu, Z. Du, and B. Yang, "Twin boundaries enhanced current transport in 14.4%-efficient CdTe solar cells by RF sputtering," presented at the Photovoltaic Specialist Conference (PVSC), 2015 IEEE 42nd, 2015, pp. 1–4.

[208]   D. Bufford, H. Wang, and X. Zhang, "High strength, epitaxial nanotwinned Ag films," *Acta Mater.*, vol. 59, no. 1, pp. 93–101, Jan. 2011.

[209]   D. Bufford, H. Wang, and X. Zhang, "Thermal stability of twins and strengthening mechanisms in differently oriented epitaxial nanotwinned Ag films," *J. Mater. Res.*, vol. 28, no. 13, pp. 1729–1739, Jul. 2013.

[210]   H. Xu *et al.*, "Wafer-level SLID bonding for MEMS encapsulation," *Adv. Manuf.*, vol. 1, no. 3, pp. 226–235, Sep. 2013.

[211]   J. H. Anderson, T. G. Maple, and W. P. Cox, "Aging Effects in Gold Thermocompression Bonds to Complex Metallizations," *IEEE Trans. Reliab.*, vol. R-19, no. 1, pp. 32–34, Feb. 1970.

[212]   R. Ahmed, C. Simbrunner, M. A. Baig, and H. Sitter, "Grain Size and Interface Dependence of Bias Stress Stability of n-Type Organic Field Effect Transistors," *ACS Appl.*

Mater. Interfaces, vol. 7, no. 40, pp. 22380–22384, Oct. 2015.

[213]   M. Krause, M. Muller, M. Petzold, S. Wiese, and K.-J. Wolter, "Scaling effects on grain size and texture of lead free interconnects #x2014; investigations by electron backscatter diffraction and nanoindentation," in *Electronic Components and Technology Conference, 2008. ECTC 2008. 58th*, 2008, pp. 75–81.

[214]   M. A. Khan and R. K. Zheng, "Nanostructural Analysis of CMOS-MEMS-based Digital Microphone for Performance Optimization."

[215]   M. A. Khan and R. K. Zheng, "Nanostructural Analysis of CMOS-MEMS-based Digital Microphone for Performance Optimization," *IEEE Trans. Nanotechnol.*, pp. 1–1, 2016.

[216]   P. Gondcharton, B. Imbert, L. Benaissa, F. Fournel, and M. Verdier, "Effect of Copper–Copper Direct Bonding on Voiding in Metal Thin Films," *J. Electron. Mater.*, vol. 44, no. 11, pp. 4128–4133, Nov. 2015.

[217]   P. Gondcharton, B. Imbert, L. Benaissa, and M. Verdier, "Voiding Phenomena in Copper-Copper Bonded Structures: Role of Creep," *ECS Trans.*, vol. 64, no. 5, pp. 357–367, Aug. 2014.

[218]   K. E. Aasmundtveit, T. A. Tollefsen, T. T. Luu, A. Duan, K. Wang, and N. Hoivik, "Solid-Liquid Interdiffusion (SLID) bonding #x2014; Intermetallic bonding for high temperature applications," in *2013 Eurpoean Microelectronics Packaging Conference (EMPC)*, 2013, pp. 1–6.

[219]   H.-K. Sung, C. Wang, and N.-Y. Kim, "Reliability study of Au-in solid-liquid interdiffusion bonding for GaN-based vertical LED packaging," *J. Micromechanics Microengineering*, vol. 25, no. 12, p. 127002, Nov. 2015.

[220]   C.-F. Chu *et al.*, "High Brightness GaN Vertical Light-Emitting Diodes on Metal Alloy for General Lighting Application," *Proc. IEEE*, vol. 98, no. 7, pp. 1197–1207, Jul. 2010.

[221]   G. G. Zhang, X. F. Ang, Z. Chen, C. C. Wong, and J. Wei, "Critical temperatures in thermocompression gold stud bonding," *J. Appl. Phys.*, vol. 102, no. 6, p. 063519, Sep. 2007.

[222]   C.-Y. Lee *et al.*, "Natural substrate lift-off technique for vertical light-emitting diodes," *Appl. Phys. Express*, vol. 7, no. 4, p. 042103, Mar. 2014.

[223]   M. D. Henry and C. R. Ahlers, "Platinum Diffusion Barrier Breakdown in a-Si/Au Eutectic Wafer Bonding," *IEEE Trans. Compon. Packag. Manuf. Technol.*, vol. 3, no. 6, pp. 899–903, Jun. 2013.

[224]   J. H. Anderson, T. G. Maple, and W. P. Cox, "Aging Effects in Gold Thermocompression Bonds to Complex Metallizations," *IEEE Trans. Reliab.*, vol. R-19, no. 1, pp. 32–34, Feb. 1970.

[225]   Y.-C. Hu and K.-N. Chen, "A Novel Bonding Approach and Its Electrical Performance for Flexible Substrate Integration," *IEEE J. Electron Devices Soc.*, vol. 4, no. 4, pp. 185–188, Jul. 2016.

[226]   A. Q. A. Qureshi, S. Colpo, D. A. Vasilache, S. Girardi, P. Conci, and B. Margesin, "Thermocompression bonding for 3D RF MEMS devices using gold and silver as intermediate layer," in *CAS 2012 (International Semiconductor Conference)*, 2012, vol. 1, pp. 183–186.

[227]   "The 2014 Nobel Prize in Physics - Press Release." [Online]. Available: https://www.nobelprize.org/nobel_prizes/physics/laureates/2014/press.html. [Accessed: 04-May-2016].

[228]   S.-K. Kim *et al.*, "Metal mirror assisting light extraction from patterned AlGaInP light-emitting diodes," *Appl. Phys. Lett.*, vol. 94, no. 10, p. 101102, 2009.

[229]   V. Haerle *et al.*, "Light extraction technologies for high-efficiency GaInN-LED devices," 2003, vol. 4996, pp. 133–138.

[230]   H. Kim *et al.*, "Enhanced light extraction of GaN-based light-emitting diodes by

using textured n-type GaN layers," *Appl. Phys. Lett.*, vol. 90, no. 16, p. 161110, Apr. 2007.

[231]   A. I. Zhmakin, "Enhancement of light extraction from light emitting diodes," *Phys. Rep.*, vol. 498, no. 4–5, pp. 189–241, Feb. 2011.

[232]   T. Okahis, "Light emitting device," EP2843718 A1, 04-Mar-2015.

[233]   J. K. Park, S. G. Lee, K. T. Han, and S. Y. Han, "Light emitting diode package with metal reflective layer and method of manufacturing the same," US7687292 B2, 30-Mar-2010.

[234]   M. Peter *et al.*, "Reflective contact layer system for an optoelectronic component and method for producing same," US9196789 B2, 24-Nov-2015.

[235]   M. Bartek, J. H. Correia, and R. F. Wolffenbuttel, "Silver-based reflective coatings for micromachined optical filters," *J. Micromechanics Microengineering*, vol. 9, no. 2, p. 162, 1999.

[236]   J. Jonathan J. Wierer, M. R. Krames, S. L. Rudaz, and L. Lumileds Lighting U. S., *Multi-layer highly reflective ohmic contacts for semiconductor devices*. 1999.

[237]   M. Kim and J. Kwak, "Reflective electrode and compound semiconductor light emitting device including the same," US7973325 B2, 05-Jul-2011.

[238]   C.-K. Lin, H. Liu, C.-K. Lin, and H. Liu, *Light emitting diodes with smooth surface for reflective electrode*. 2008.

[239]   L. Sun *et al.*, "Influence of p-GaN annealing on the optical and electrical properties of InGaN/GaN MQW LEDs," *Phys. E Low-Dimens. Syst. Nanostructures*, vol. 60, pp. 166–169, Jun. 2014.

[240]   Z. Deng *et al.*, "Indium segregation measured in InGaN quantum well layer," *Sci. Rep.*, vol. 4, 2014.

[241]   B. P. Yonkee, E. C. Young, S. P. DenBaars, S. Nakamura, and J. S. Speck, "Silver free III-nitride flip chip light-emitting-diode with wall plug efficiency over 70% utilizing a

GaN tunnel junction," *Appl. Phys. Lett.*, Nov. 2016.

[242]   H. W. Jang, J. H. Son, and J.-L. Lee, "Formation of High-Quality Ag-Based Ohmic Contacts to p-Type GaN," *J. Electrochem. Soc.*, vol. 155, no. 8, pp. H563–H568, Aug. 2008.

[243]   L. Liu, L. X. Zhao, Z. G. Yu, J. X. Wang, Y. P. Zeng, and J. M. Li, "The diffusion of Ag in GaN-based surface plasmon light-emitting diodes under different temperature annealing," in *2014 11th China International Forum on Solid State Lighting (SSLCHINA)*, 2014, pp. 125–128.

[244]   H.-G. Hong *et al.*, "Formation of High-Quality Ag-Based Ohmic Contact to p-Type GaN for UV LEDs Using a Tin-Zinc Oxide Interlayer," *Electrochem. Solid-State Lett.*, vol. 8, no. 10, p. G280, 2005.

[245]   D. Adams, T. L. Alford, and J. W. Mayer, *Silver Metallization: Stability and Reliability*. Springer Science & Business Media, 2007.

[246]   A. R. Shugurov, A. V. Panin, H.-G. Chun, and V. A. Loginov, "Grain growth and thermal stability of Ag thin films," 2005, pp. 528–531.

[247]   K.-B. Kim, G. Jin, M. Kim, S. Kim, and C.-W. Jeon, "Effects of Grain Size in Sequential Lateral Solidification Processed on Active Matrix Organic Light Emitting Diode Displays," *ECS Solid State Lett.*, vol. 3, no. 8, pp. R40–R43, Jan. 2014.

[248]   L. Palasse and D. Goran, "Large area orientation mapping on nanoscale materials using SEM," in *European Microscopy Congress 2016: Proceedings*, Wiley-VCH Verlag GmbH & Co. KGaA, 2016.

[249]   M. Abbasi, D.-I. Kim, H.-U. Guim, M. Hosseini, H. Danesh-Manesh, and M. Abbasi, "Application of Transmitted Kikuchi Diffraction in Studying Nano-oxide and Ultrafine Metallic Grains," *ACS Nano*, vol. 9, no. 11, pp. 10991–11002, Nov. 2015.

[250]   M. Shatzkes, P. Chaudhari, A. A. Levi, and A. F. Mayadas, "Twin Boundary Resistivity: Application to Silver," *Phys. Rev. B*, vol. 7, no. 12, p. 5058, Jun. 1973.

[251]   X. Zhang and A. Misra, "Superior thermal stability of coherent twin boundaries in nanotwinned metals," *Scr. Mater.*, vol. 66, no. 11, pp. 860–865, Jun. 2012.

[252]   L. Lu, Y. Shen, X. Chen, L. Qian, and K. Lu, "Ultrahigh strength and high electrical conductivity in copper," *Science*, vol. 304, no. 5669, pp. 422–426, Apr. 2004.

[253]   M. A. Khan and R. Zheng, "Nanostructural Analysis of CMOS-MEMS-Based Digital Microphone for Performance Optimization," *IEEE Trans. Nanotechnol.*, vol. 15, no. 6, pp. 849–855, Nov. 2016.

[254]   J. Cho and C. V. Thompson, "Grain size dependence of electromigration-induced failures in narrow interconnects," *Appl. Phys. Lett.*, vol. 54, no. 25, pp. 2577–2579, Jun. 1989.

[255]   Z. Xu, S. Kumar, J. P. Jung, and K. K. Kim, "Reflection characteristics of displacement deposited Sn for LED lead frame," *Mater. Trans.*, vol. 53, no. 5, pp. 946–950, 2012.

[256]   Ya-Ju Lee, Chia-Jung Lee, and Chih-Hao Chen, "Effect of Surface Texture and Backside Patterned Reflector on the AlGaInP Light-Emitting Diode: High Extraction of Waveguided Light," *IEEE J. Quantum Electron.*, vol. 47, no. 5, pp. 636–641, May 2011.

[257]   J. K. Kim, H. Luo, Y. Xi, J. M. Shah, T. Gessmann, and E. F. Schubert, "Light Extraction in GaInN Light-Emitting Diodes using Diffuse Omnidirectional Reflectors," *J. Electrochem. Soc.*, vol. 153, no. 2, p. G105, 2006.

[258]   U. Beck, G. Reiners, and K. Witt, "Decorative hard coatings: advances in optical characterization techniques," *Thin Solid Films*, vol. 236, no. 1–2, pp. 184–190, Dec. 1993.

[259]   N. Hasanov *et al.*, "Improved performance of InGaN/GaN flip-chip light-emitting diodes through the use of robust Ni/Ag/TiW mirror contacts," *J. Vac. Sci. Technol. B Nanotechnol. Microelectron. Mater. Process. Meas. Phenom.*, Dec. 2015.

[260]   R.-H. Horng, W.-C. Kao, S.-L. Ou, and D.-S. Wuu, "Effect of diamond like carbon layer on heat dissipation and optoelectronic performance of vertical-type InGaN light

emitting diodes," *Appl. Phys. Lett.*, vol. 101, no. 17, p. 171102, 2012.

[261] P.-Y. Tsai, H.-K. Huang, C.-M. Sung, M.-C. Kan, and Y.-H. Wang, "High-Power LED Chip-on-Board Packages With Diamond-Like Carbon Heat-Spreading Layers," *J. Disp. Technol.*, vol. 12, no. 4, pp. 357–361, Apr. 2016.

[262] J. Hu, M. H. Le, S. Nijhawan, and T. B. Sapirman, "Nickel-Titanium and Related Alloys as Silver Diffusion Barriers," US20150091032 A1, 02-Apr-2015.

[263] C. Carter-Coman, G. Hofler, and F. A. K. Jr, "Diffusion barrier for increased mirror reflectivity in reflective solderable contacts on high power led chip," US6593160 B2, 15-Jul-2003.

[264] K. L. June and J. Tak, "Suppression of Ag Agglomeration in Pt capped ITO/Ag Reflectors for Vertical-type Light-Emitting Diodes," *J. Korean Phys. Soc.*, vol. 55, no. 4, p. 1615, Oct. 2009.

[265] P. Seong-Han, J. Joon-Woo, S. Tae-Yeon, and O. Jeong-Tak, "Thermally Stable and Reflective RhZn/Ag Ohmic Contacts to p-type GaN for Near-UV Flip-chip Light-emitting Diodes," *J. Korean Phys. Soc.*, vol. 59, no. 1, p. 156, Jul. 2011.

[266] S.-K. Kim and H.-G. Park, "Coherent vertical beaming using Bragg mirrors for high-efficiency GaN light-emitting diodes," *Opt. Express*, vol. 21, no. 12, p. 14566, Jun. 2013.

[267] Z.-C. Wu, Y.-C. Lu, and S.-M. Jang, "Method of a non-metal barrier copper damascene integration," US7151315 B2, 19-Dec-2006.

[268] X. Jin and G. Chavoor, "Position of Ag reflection layer and its effect on GaN LED light extraction efficiency," in *2015 IEEE 15th International Conference on Nanotechnology (IEEE-NANO)*, 2015, pp. 409–411.

[269] H. Y. Chung, K. Y. Woo, S. J. Kim, and T. G. Kim, "Improvement of blue InGaN/GaN light-emitting diodes with graded indium composition wells and barriers," *Opt. Commun.*, vol. 331, pp. 282–286, Nov. 2014.

[270] J. H. Seo *et al.*, "A Simplified Method of Making Flexible Blue LEDs on a Plastic Substrate," *IEEE Photonics J.*, vol. 7, no. 2, pp. 1–7, Apr. 2015.

[271] M.-H. Chang, D. Das, P. V. Varde, and M. Pecht, "Light emitting diodes reliability review," *Microelectron. Reliab.*, vol. 52, no. 5, pp. 762–782, May 2012.

[272] Y. J. Chen, C. C. Chang, H. Y. Lin, S. C. Hsu, and C. Y. Liu, "Fabrication of vertical thin-GaN light-emitting diode by low-temperature Cu/Sn/Ag wafer bonding," *Microelectron. Reliab.*, vol. 52, no. 2, pp. 381–384, Feb. 2012.

[273] J.-L. Lee and I. Lee, "Highly transparent see-through OLED using a thin Ag electrode," in *Light, Energy and the Environment*, 2014, p. JW6A.39.

[274] J. H. Kim *et al.*, "Transparent Conductive ITO/Ag/ITO Electrode Deposited at Room Temperature for Organic Solar Cells," *J. Electron. Mater.*, vol. 46, no. 1, pp. 306–311, Jan. 2017.

[275] S. H. Kim *et al.*, "Enhanced luminous efficacy in phosphor-converted white vertical light-emitting diodes using low index layer," *Opt. Express*, vol. 21, no. 5, pp. 6353–6359, Mar. 2013.

[276] Chia-Feng Lin, Zhong-Jie Yang, Jing-Hui Zheng, and Jing-Jie Dai, "Enhanced light output in nitride-based light-emitting diodes by roughening the mesa sidewall," *IEEE Photonics Technol. Lett.*, vol. 17, no. 10, pp. 2038–2040, Oct. 2005.

[277] C. H. Chao, W. H. Lin, C. H. Chen, C. H. Changjean, and C. F. Lin, "Tunable light extraction efficiency of GaN light emitting diodes by ZnO nanorod arrays," *Semicond. Sci. Technol.*, vol. 24, no. 10, p. 105017, Oct. 2009.

[278] M. Kneissl, "A Brief Review of III-Nitride UV Emitter Technologies and Their Applications," in *III-Nitride Ultraviolet Emitters*, vol. 227, M. Kneissl and J. Rass, Eds. Cham: Springer International Publishing, 2016, pp. 1–25.

[279] A. Rockett, *The Materials Science of Semiconductors*. Boston, MA: Springer US, 2008.

[280] T. Doan *et al.*, "Vertical GaN based Light Emitting Diodes on Metal Alloy Substrate for Solid State Lighting Application," presented at the Integrated Optoelectronic Devices 2006, 2006, p. 61340G–61340G–6.

[281] M. Bergmann *et al.*, *LED structure with enhanced mirror reflectivity*. 2011.

[282] R. H. Haitz and F. A. K. Jr, "Highly reflective contacts for light emitting semiconductor devices," US5917202 A, 29-Jun-1999.

[283] Y. Kondoh, S. Watanabe, Y. Kaneko, S. Nakagawa, and N. Yamada, "Semiconductor light emitting device having a silver p-contact," US6900472 B2, 31-May-2005.

[284] C. F. Shen *et al.*, "Nitride-based high power flip-chip near-UV leds with reflective submount," *IET Optoelectron.*, vol. 1, no. 1, pp. 27–30, Feb. 2007.

[285] L. Zhou, "Reflective electrode for a semiconductor light emitting apparatus," US7612384 B2, 03-Nov-2009.

[286] J. O. Song, J. S. Ha, and T. Y. Seong, "Ohmic-Contact Technology for GaN-Based Light-Emitting Diodes: Role of P-Type Contact," *IEEE Trans. Electron Devices*, vol. 57, no. 1, pp. 42–59, Jan. 2010.

[287] M. cheol Yoo and Y. M. Cheol, *Method of fabricating vertical structure compound semiconductor devices*. 2004.

[288] C.-F. Chu *et al.*, "Study of GaN light-emitting diodes fabricated by laser lift-off technique," *J. Appl. Phys.*, vol. 95, no. 8, pp. 3916–3922, Apr. 2004.

[289] M. S. Cho, K. Y. Park, S. Y. Song, S. H. Lee, and P. J. Choi, "Vertical structure led device and method of manufacturing the same," US20100200867 A1, 12-Aug-2010.

[290] D.-S. Wuu, S.-C. Hsu, S.-H. Huang, C.-C. Wu, C.-E. Lee, and R.-H. Horng, "GaN/Mirror/Si Light-Emitting Diodes for Vertical Current Injection by Laser Lift-Off and Wafer Bonding Techniques," *Jpn. J. Appl. Phys.*, vol. 43, no. 8R, p. 5239, Aug. 2004.

[291]   A. E. Plößl *et al.*, "(Invited) Wafer Bonding for the Manufacture of High-Brightness and High-Efficiency Light-Emitting Diodes," *ECS Trans.*, vol. 33, no. 4, pp. 613–624, Oct. 2010.

[292]   W. Lee, J. Limb, J.-H. Ryou, D. Yoo, T. Chung, and R. D. Dupuis, "Effect of thermal annealing induced by p-type layer growth on blue and green LED performance," *J. Cryst. Growth*, vol. 287, pp. 577–581, Jan. 2006.

[293]   M. H. Doan, S. Kim, J. J. Lee, H. Lim, F. Rotermund, and K. Kim, "Influence of laser lift-off on optical and structural properties of InGaN∕GaN vertical blue light emitting diodes," *AIP Adv.*, vol. 2, no. 2, p. 022122, 2012.

[294]   J. A. Venables and C. J. Harland, "Electron back-scattering patterns—A new technique for obtaining crystallographic information in the scanning electron microscope," *Philos. Mag.*, vol. 27, no. 5, pp. 1193–1200, May 1973.

[295]   M. Krause, M. Muller, M. Petzold, S. Wiese, and K.-J. Wolter, "Scaling effects on grain size and texture of lead free interconnects- investigations by electron backscatter diffraction and nanoindentation," in *Electronic Components and Technology Conference, 2008. ECTC 2008. 58th*, 2008, pp. 75–81.

[296]   R. Kapoor, N. Kumar, R. S. Mishra, C. S. Huskamp, and K. K. Sankaran, "Influence of fraction of high angle boundaries on the mechanical behavior of an ultrafine grained Al–Mg alloy," *Mater. Sci. Eng. A*, vol. 527, no. 20, pp. 5246–5254, Jul. 2010.

[297]   K. . Kumar, H. Van Swygenhoven, and S. Suresh, "Mechanical behavior of nanocrystalline metals and alloys," *Acta Mater.*, vol. 51, no. 19, pp. 5743–5774, Nov. 2003.

[298]   L. Cao *et al.*, "Analysis of grain structure by precession electron diffraction and effects on electromigration reliability of Cu interconnects," in *Interconnect Technology Conference (IITC), 2012 IEEE International*, 2012, pp. 1–3.

[299]   J. N. Lalena and D. A. Cleary, "Transport Properties," in *Principles of Inorganic Materials Design*, John Wiley & Sons, Inc., 2005, pp. 179–205.

[300] O. Anderoglu, A. Misra, H. Wang, and X. Zhang, "Thermal stability of sputtered Cu films with nanoscale growth twins," *J. Appl. Phys.*, vol. 103, no. 9, p. 094322, May 2008.

[301] S. Ni *et al.*, "The effect of dislocation density on the interactions between dislocations and twin boundaries in nanocrystalline materials," *Acta Mater.*, vol. 60, no. 6–7, pp. 3181–3189, 2012.

[302] S. E. Bennett *et al.*, "Mg dopant distribution in an AlGaN/GaN p-type superlattice assessed using atom probe tomography, TEM and SIMS," *J. Phys. Conf. Ser.*, vol. 209, no. 1, p. 012014, 2010.

[303] T. j. Prosa, D. Olson, A. d. Giddings, W. Lefebvre, P. h. Clifton, and D. j. Larson, "Atom Probe Tomography Analysis of a Gallium-Nitride-Based Commercial Light-Emitting Diode," *Microsc. Microanal.*, vol. 19, no. Supplement S2, pp. 1014–1015, Aug. 2013.

[304] M.-H. Doan and J. Lee, "Spatially Resolved Cathodoluminescence in the Vicinity of Defects in the High-Efficiency InGaN/GaN Blue Light Emitting Diodes," *Advances in Condensed Matter Physics*, 2014. [Online]. Available: https://www.hindawi.com/journals/acmp/2014/671210/. [Accessed: 28-Sep-2017].

[305] S. D. Findlay, N. Shibata, H. Sawada, E. Okunishi, Y. Kondo, and Y. Ikuhara, "Dynamics of annular bright field imaging in scanning transmission electron microscopy," *Ultramicroscopy*, vol. 110, no. 7, pp. 903–923, Jun. 2010.

[306] R. Ishikawa, E. Okunishi, H. Sawada, Y. Kondo, F. Hosokawa, and E. Abe, "Direct imaging of hydrogen-atom columns in a crystal by annular bright-field electron microscopy," *Nat. Mater.*, vol. 10, no. 4, pp. 278–281, Apr. 2011.

[307] "The fabrication of GaN-based light emitting diodes (LEDs)," *Adv. Nat. Sci. Nanosci. Nanotechnol.*, vol. 1, no. 2, p. 025015, Aug. 2010.

[308] H. Kim, K.-K. Kim, S.-N. Lee, and K.-H. Baik, "Design and fabrication of vertical-

injection GaN-based light-emitting diodes," *Opt. Express*, vol. 19, no. 104, pp. A937–A942, 2011.

[309]   S. Nakahara, "Recent development in a TEM specimen preparation technique using FIB for semiconductor devices," *Surf. Coat. Technol.*, vol. 169–170, pp. 721–727, Jun. 2003.

[310]   M. Hao, H. Ishikawa, T. Egawa, C. L. Shao, and T. Jimbo, "Anomalous compositional pulling effect in InGaN/GaN multiple quantum wells," *Appl. Phys. Lett.*, vol. 82, no. 26, pp. 4702–4704, Jun. 2003.

[311]   S. Pereira *et al.*, "Compositional pulling effects in In x Ga 1 − x N / G a N layers: A combined depth-resolved cathodoluminescence and Rutherford backscattering/channeling study," *Phys. Rev. B*, vol. 64, no. 20, Nov. 2001.

[312]   Y. Inatomi *et al.*, "Theoretical study of the composition pulling effect in InGaN metalorganic vapor-phase epitaxy growth," *Jpn. J. Appl. Phys.*, vol. 56, no. 7, p. 078003, Jul. 2017.

[313]   Y.-R. Wu, R. Shivaraman, K.-C. Wang, and J. S. Speck, "Analyzing the physical properties of InGaN multiple quantum well light emitting diodes from nano scale structure," *Appl. Phys. Lett.*, Aug. 2012.

[314]   M. F. Schubert and E. F. Schubert, "Effect of heterointerface polarization charges and well width upon capture and dwell time for electrons and holes above GaInN/GaN quantum wells," *Appl. Phys. Lett.*, vol. 96, no. 13, p. 131102, Mar. 2010.

[315]   J. Fu, L. Zhao, N. Zhang, J. Wang, and J. Li, "Influence of electron distribution on efficiency droop for GaN-based light emitting diodes," *J. Solid State Light.*, vol. 2, no. 1, p. 5, Dec. 2015.

[316]   X. Ni, Q. Fan, R. Shimada, Ü. Özgür, and H. Morkoç, "Reduction of efficiency droop in InGaN light emitting diodes by coupled quantum wells," *Appl. Phys. Lett.*, vol. 93, no. 17, p. 171113, Oct. 2008.

[317] R. Charash *et al.*, "Carrier distribution in InGaN/GaN tricolor multiple quantum well light emitting diodes," *Appl. Phys. Lett.*, vol. 95, no. 15, p. 151103, Oct. 2009.

[318] Y.-L. Li, Y.-R. Huang, and Y.-H. Lai, "Efficiency droop behaviors of InGaN/GaN multiple-quantum-well light-emitting diodes with varying quantum well thickness," *Appl. Phys. Lett.*, vol. 91, no. 18, p. 181113, Oct. 2007.

[319] S. Nakamura, "The Roles of Structural Imperfections in InGaN-Based Blue Light-Emitting Diodes and Laser Diodes," *Science*, vol. 281, no. 5379, pp. 956–961, Aug. 1998.

[320] G. F. Neumark, I. L. Kuskovsky, and H. Jiang, Eds., *Wide Bandgap Light Emitting Materials and Devices*. Weinheim, Germany: Wiley-VCH Verlag GmbH & Co. KGaA, 2007.

[321] D.-Y. Lee *et al.*, "Effect of an electron blocking layer on the piezoelectric field in InGaN/GaN multiple quantum well light-emitting diodes," *Appl. Phys. Lett.*, vol. 100, no. 4, p. 041119, Jan. 2012.

[322] S.-H. Han *et al.*, "Effect of electron blocking layer on efficiency droop in InGaN/GaN multiple quantum well light-emitting diodes," *Appl. Phys. Lett.*, vol. 94, no. 23, p. 231123, Jun. 2009.

[323] J. Piprek, "Efficiency droop in nitride-based light-emitting diodes," *Phys. Status Solidi A*, vol. 207, no. 10, pp. 2217–2225, Oct. 2010.

[324] D. A. Zakheim, A. S. Pavluchenko, and D. A. Bauman, "Blue LEDs - way to overcome efficiency droop," *Phys. Status Solidi C*, vol. 8, no. 7–8, pp. 2340–2344, Jul. 2011.

[325] Y. LIU *et al.*, "Improved performance of GaN-based light-emitting diodes by using short-period superlattice structures," *Prog. Nat. Sci. Mater. Int.*, vol. 20, pp. 70–75, Nov. 2010.

[326] S. J. Lee, D. H. Oh, K. H. Kim, and C. S. Han, "Light emitting diode having barrier layer of superlattice structure," US8093583 B2, 10-Jan-2012.

[327] A. Roshko *et al.*, "Comparison of convergent beam electron diffraction and annular bright field atomic imaging for GaN polarity determination," *Journal of Materials Research*, Mar-2017. [Online]. Available: /core/journals/journal-of-materials-research/article/comparison-of-convergent-beam-electron-diffraction-and-annular-bright-field-atomic-imaging-for-gan-polarity-determination/55897D4F5F4AA27A1057692CEEE3D9F1. [Accessed: 25-Aug-2017].

[328] E. Sarigiannidou *et al.*, "Comparison of the structural quality in Ga-face and N-face polarity GaN/AlN multiple-quantum-well structures," *Semicond. Sci. Technol.*, vol. 21, no. 5, p. 612, 2006.

[329] Y.-S. Yoo, J.-H. Na, S. J. Son, and Y.-H. Cho, "Effective suppression of efficiency droop in GaN-based light-emitting diodes: role of significant reduction of carrier density and built-in field," *Sci. Rep.*, vol. 6, p. srep34586, Oct. 2016.

[330] B. Hahn, A. Weimar, M. Peter, and J. Baur, "High-power InGaN LEDs: present status and future prospects," presented at the Light-Emitting Diodes: Research, Manufacturing, and Applications XII, 2008, vol. 6910, p. 691004.

[331] G. Verzellesi *et al.*, "Efficiency droop in InGaN/GaN blue light-emitting diodes: Physical mechanisms and remedies," *J. Appl. Phys.*, vol. 114, no. 7, p. 071101, Aug. 2013.

[332] M. F. Schubert *et al.*, "Polarization-matched GaInN/AlGaInN multi-quantum-well light-emitting diodes with reduced efficiency droop," *Appl. Phys. Lett.*, vol. 93, no. 4, p. 041102, Jul. 2008.

[333] S. Choi *et al.*, "Improvement of peak quantum efficiency and efficiency droop in III-nitride visible light-emitting diodes with an InAlN electron-blocking layer," *Appl. Phys. Lett.*, vol. 96, no. 22, p. 221105, May 2010.

[334] R. B. Chung *et al.*, "The reduction of efficiency droop by $Al_{0.82}In_{0.18}N$/GaN superlattice electron blocking layer in (0001) oriented GaN-based light emitting diodes," *Appl. Phys. Lett.*, vol. 101, no. 13, p. 131113, Sep. 2012.

219

[335] Y.-Y. Zhang and G.-R. Yao, "Performance enhancement of blue light-emitting diodes with AlGaN barriers and a special designed electron-blocking layer," *J. Appl. Phys.*, Nov. 2011.

[336] W. Lee, J. Limb, J.-H. Ryou, D. Yoo, T. Chung, and R. D. Dupuis, "Influence of growth temperature and growth rate of p-GaN layers on the characteristics of green light emitting diodes," *J. Electron. Mater.*, vol. 35, no. 4, pp. 587–591, Apr. 2006.

[337] C. H. Wang *et al.*, "Hole transport improvement in InGaN/GaN light-emitting diodes by graded-composition multiple quantum barriers," *Appl. Phys. Lett.*, vol. 99, no. 17, p. 171106, Oct. 2011.

[338] C. Trager-Cowan *et al.*, "Characterization of nitride thin films by electron backscatter diffraction," *J. Microsc.*, vol. 205, no. Pt 3, pp. 226–230, Mar. 2002.

[339] B.-U. Ye *et al.*, "Enhancing Light Emission of Nanostructured Vertical Light-Emitting Diodes by Minimizing Total Internal Reflection," *Adv. Funct. Mater.*, vol. 22, no. 3, pp. 632–639, Feb. 2012.

[340] J. H. Kang *et al.*, "Comparison of various surface textured layer in InGaN LEDs for high light extraction efficiency," *Opt. Express*, vol. 19, no. 4, pp. 3637–3646, Feb. 2011.

[341] C. A. Tran and T. T. Doan, "Light emitting diodes (LEDs) with improved light extraction by roughening," US7186580 B2, 06-Mar-2007.

[342] K.-J. Byeon, J.-Y. Cho, J. O. Song, S. Y. Lee, and H. Lee, "High-Brightness Vertical GaN-Based Light-Emitting Diodes With Hexagonally Close-Packed Micrometer Array Structures," *IEEE Photonics J.*, vol. 5, no. 6, pp. 8200708–8200708, Dec. 2013.

[343] A. David *et al.*, "Photonic-crystal GaN light-emitting diodes with tailored guided modes distribution," *Appl. Phys. Lett.*, vol. 88, no. 6, p. 061124, Feb. 2006.

[344] J. Jewell *et al.*, "Double embedded photonic crystals for extraction of guided light in light-emitting diodes," *Appl. Phys. Lett.*, vol. 100, no. 17, p. 171105, Apr. 2012.

[345] V. V. Lysak, J. Hye Kang, and C.-H. Hong, "Conical air prism arrays as an embedded reflector for high efficient InGaN/GaN light emitting diodes," *Appl. Phys. Lett.*, vol. 102, no. 6, p. 061114, Feb. 2013.

[346] S.-F. Yu *et al.*, "Characteristics of InGaN-Based Light-Emitting Diodes on Patterned Sapphire Substrates with Various Pattern Heights, Characteristics of InGaN-Based Light-Emitting Diodes on Patterned Sapphire Substrates with Various Pattern Heights," *J. Nanomater. J. Nanomater.*, vol. 2012, 2012, p. e346915, Jul. 2012.

[347] W.-C. Ke, F.-W. Lee, C.-Y. Chiang, Z.-Y. Liang, W.-K. Chen, and T.-Y. Seong, "InGaN-Based Light-Emitting Diodes Grown on a Micro/Nanoscale Hybrid Patterned Sapphire Substrate," *ACS Appl. Mater. Interfaces*, vol. 8, no. 50, pp. 34520–34529, Dec. 2016.

[348] J.-Q. Xi *et al.*, "Optical thin-film materials with low refractive index for broadband elimination of Fresnel reflection," *Nat. Photonics*, vol. 1, no. 3, p. 176, Mar. 2007.

[349] R. Windisch *et al.*, "Impact of texture-enhanced transmission on high-efficiency surface-textured light-emitting diodes," *Appl. Phys. Lett.*, vol. 79, no. 15, pp. 2315–2317, Oct. 2001.

[350] T. Fujii, Y. Gao, R. Sharma, E. L. Hu, S. P. DenBaars, and S. Nakamura, "Increase in the extraction efficiency of GaN-based light-emitting diodes via surface roughening," *Appl. Phys. Lett.*, vol. 84, no. 6, pp. 855–857, Feb. 2004.

[351] C.-F. Chu *et al.*, *Vertical light emitting diode (VLED) dice having confinement layers with roughened surfaces and methods of fabrication*. 2013.

[352] V. Haerle *et al.*, "Light extraction technologies for high-efficiency GaInN-LED devices," presented at the Light-Emitting Diodes: Research, Manufacturing, and Applications VII, 2003, vol. 4996, pp. 133–139.

[353] H. C. Lee, J. B. Park, J. W. Bae, P. T. T. Thuy, M. C. Yoo, and G. Y. Yeom, "Effect of the surface texturing shapes fabricated using dry etching on the extraction efficiency of

vertical light-emitting diodes," *Solid-State Electron.*, vol. 52, no. 8, pp. 1193–1196, Aug. 2008.

[354]   Y. L. Hsieh, S. Y. Kuo, and F. I. Lai, "Enhancement in the extraction efficiency of GaN-based LED with naturally textured surface," in *2009 Conference on Lasers Electro Optics The Pacific Rim Conference on Lasers and Electro-Optics*, 2009, pp. 1–2.

[355]   W. Zhou, *Nanoimprint Lithography: An Enabling Process for Nanofabrication*. Berlin, Heidelberg: Springer Berlin Heidelberg, 2013.

[356]   A. I. Zhmakin, "Enhancement of light extraction from light emitting diodes," *Phys. Rep.*, vol. 498, no. 4–5, pp. 189–241, Feb. 2011.

[357]   H. Kim *et al.*, "Light-extraction enhancement of vertical-injection GaN-based light-emitting diodes fabricated with highly integrated surface textures," *Opt. Lett.*, vol. 33, no. 11, pp. 1273–1275, Jun. 2008.

[358]   H.-S. Kwack *et al.*, "Experimental study of light output power for vertical GaN-based light-emitting diodes with various textured surface and thickness of GaN layer," *AIP Adv.*, vol. 2, no. 2, p. 022127, May 2012.

[359]   Y. C. Chiang, B. C. Lin, K. J. Chen, C. C. Lin, P. T. Lee, and H. C. Kuo, "Enhanced performance of nitride-based ultraviolet vertical-injection light-emitting diodes by non-insulation current blocking layer and textured surface," *Nanoscale Res. Lett.*, vol. 9, Dec. 2014.

[360]   Y. Tian *et al.*, "Direct growth of freestanding GaN on C-face SiC by HVPE," *Sci. Rep.*, vol. 5, p. 10748, Jun. 2015.

[361]   F. C. Wang, C. L. Cheng, Y. F. Chen, C. F. Huang, and C. C. Yang, "Residual thermal strain in thick GaN epifilms revealed by cross-sectional Raman scattering and cathodoluminescence spectra," *Semicond. Sci. Technol.*, vol. 22, no. 8, p. 896, 2007.

[362]   D. Christy, A. Watanabe, and T. Egawa, "Influence of strain induced by AlN nucleation layer on the electrical properties of AlGaN/GaN heterostructures on Si(111)

substrate," *AIP Adv.*, vol. 4, no. 10, p. 107104, Oct. 2014.

[363]   Y. Li *et al.*, "Plasma-induced damage in GaN-based light emitting diodes," presented at the Solid State Lighting and Solar Energy Technologies, 2008, vol. 6841, p. 68410X.

[364]   S.-Y. Jung, J. Choe, M.-S. Seok, Q.-H. Park, and T.-Y. Seong, "Improving the light output power of GaN-based light-emitting diodes through the use of SiO2 cones," *Mater. Sci. Semicond. Process.*, vol. 16, no. 3, pp. 582–586, Jun. 2013.

[365]   C.-M. Yang, D.-S. Kim, Y. S. Park, J.-H. Lee, Y. S. Lee, and J.-H. Lee, "Enhancement in Light Extraction Efficiency of GaN-Based Light-Emitting Diodes Using Double Dielectric Surface Passivation," vol. 2012, Sep. 2012.

[366]   J. H. Son, H. K. Yu, and J.-L. Lee, "MgO nano-pyramids structure for enhancement of light extraction efficiency in vertical light-emitting diodes," *Opt. Express*, vol. 18, no. 103, pp. A403–A410, Sep. 2010.

[367]   K. Lekhal *et al.*, "Controlled morphology of regular GaN microrod arrays by selective area growth with HVPE," *J. Cryst. Growth*, vol. 447, pp. 55–61, Aug. 2016.

[368]   R. Ravash *et al.*, "Impact of AlN seeding layer growth rate in MOVPE growth of semi-polar gallium nitride structures on high index silicon," *Phys. Status Solidi B*, vol. 248, no. 3, pp. 594–599, Mar. 2011.

[369]   E. H. Li, C.-C. Chan, and P. C. K. Kwok, "Optimization of textured-surface light emitting diode," in *Electron Devices Meeting, 1998. Proceedings. 1998 IEEE Hong Kong*, 1998, pp. 6–9.

[370]   J. H. Kang *et al.*, "Improvement of Light Output Power in InGaN/GaN Light-Emitting Diodes with a Nanotextured GaN Surface Using Indium Tin Oxide Nanospheres," *Jpn. J. Appl. Phys.*, vol. 48, no. 10R, p. 102104, Oct. 2009.

[371]   H. Huamao, H. Jinyong, and W. Hong, "GaN-based light-emitting diodes with hybrid micro/nano-textured indium-tin-oxide layer," *J. Semicond.*, vol. 35, no. 8, p. 084006,

2014.

[372]   Z. Huaiwen *et al.*, "Light extraction efficiency enhancement in light-emitting diodes with indium tin oxide nano-craters," *J. Semicond.*, vol. 33, no. 5, p. 054009, 2012.

[373]   H. C. Chen *et al.*, "A novel randomly textured phosphor structure for highly efficient white light-emitting diodes," *Nanoscale Res. Lett.*, vol. 7, no. 1, p. 188, Mar. 2012.

[374]   R. H. Horng, S. H. Huang, C. C. Yang, and D. S. Wuu, "Efficiency Improvement of GaN-Based LEDs with ITO Texturing Window Layers Using Natural Lithography," *IEEE J. Sel. Top. Quantum Electron.*, vol. 12, no. 6, pp. 1196–1201, Nov. 2006.

[375]   Z. Yin, X. Liu, Y. Wu, X. Hao, and X. Xu, "Enhancement of light extraction in GaN-based light-emitting diodes using rough beveled ZnO nanocone arrays," *Opt. Express*, vol. 20, no. 2, p. 1013, Jan. 2012.

[376]   Z. Liu *et al.*, "Light emitting enhancement and angle-resolved property of surface textured GaN-based vertical LED," *J. Opt.*, vol. 45, no. 1, pp. 81–86, Mar. 2016.

[377]   Y. Ou *et al.*, "Efficiency enhancement of InGaN amber MQWs using nanopillar structures," *Nanophotonics*, vol. 7, no. 1, pp. 317–322, 2018.

[378]   M. H. Mustary and V. V. Lysak, "High efficient vertical LED with pattern surface texture," in *2013 International Conference on Advanced Optoelectronics and Lasers (CAOL 2013)*, 2013, pp. 166–168.

[379]   G. Lozano, S. R. Rodriguez, M. A. Verschuuren, and J. G. Rivas, "Metallic nanostructures for efficient LED lighting," *Light Sci. Appl.*, vol. 5, no. 6, p. e16080, Jun. 2016.

[380]   Q. a Ding, K. Li, F. Kong, X. Chen, and J. Zhao, "Improving the Vertical Light-Extraction Efficiency of GaN-Based Thin-Film Flip-Chip LEDs With p-Side Deep-Hole Photonic Crystals," *J. Disp. Technol.*, vol. 10, no. 11, pp. 909–916, Nov. 2014.

[381]   Y. C. Chiang, C. C. Lin, and H. C. Kuo, "Novel thin-GaN LED structure adopted

micro abraded surface to compare with conventional vertical LEDs in ultraviolet light," *Nanoscale Res. Lett.*, vol. 10, 2015.

[382] H. Y. Liu, Y. C. Yang, G. J. Liu, and R. C. Huang, "Improved Light Extraction Efficiency of GaN-Based Ultraviolet Light-Emitting Diodes by Self-Assembled MgO Nanorod Arrays," *IEEE Trans. Electron Devices*, vol. 64, no. 12, pp. 5006–5011, Dec. 2017.

[383] C.-Y. Cho, S.-H. Hong, K.-H. Park, W.-K. Park, and S.-J. Park, "Improvement of Optical and Electrical Properties of Indium Tin Oxide Layer of GaN-Based Light-Emitting Diode By Surface Plasmon in Silver Nanoparticles," *Meet. Abstr.*, vol. MA2015-01, no. 23, pp. 1479–1479, Apr. 2015.

[384] "Solar energy | Renewable energy | Statistical Review of World Energy | Energy economics | BP," *bp.com*. [Online]. Available: https://www.bp.com/en/global/corporate/energy-economics/statistical-review-of-world-energy/renewable-energy/solar-energy.html. [Accessed: 23-Oct-2017].

[385] C. J. Traverse, R. Pandey, M. C. Barr, and R. R. Lunt, "Emergence of highly transparent photovoltaics for distributed applications," *Nat. Energy*, p. 1, Oct. 2017.

[386] B. P. Rand and H. Richter, *Organic Solar Cells: Fundamentals, Devices, and Upscaling*. CRC Press, 2014.

[387] C. Zhan, G. Yu, Y. Lu, L. Wang, E. Wujcik, and S. Wei, "Conductive polymer nanocomposites: a critical review of modern advanced devices," *J. Mater. Chem. C*, vol. 5, no. 7, pp. 1569–1585, 2017.

[388] D. Angmo and F. C. Krebs, "Over 2 Years of Outdoor Operational and Storage Stability of ITO-Free, Fully Roll-to-Roll Fabricated Polymer Solar Cell Modules," *Energy Technol.*, vol. 3, no. 7, pp. 774–783, Jul. 2015.

[389] M. Helgesen, R. Søndergaard, and F. C. Krebs, "Advanced materials and processes for polymer solar cell devices," *J. Mater. Chem.*, vol. 20, no. 1, pp. 36–60, 2010.

[390]   M. A. Green, K. Emery, Y. Hishikawa, W. Warta, and E. D. Dunlop, "Solar cell efficiency tables (Version 45)," *Prog. Photovolt. Res. Appl.*, vol. 23, no. 1, pp. 1–9, Jan. 2015.

[391]   Y. Liu *et al.*, "High Efficiency Tandem Thin-Perovskite/Polymer Solar Cells with a Graded Recombination Layer," *ACS Appl. Mater. Interfaces*, vol. 8, no. 11, pp. 7070–7076, Mar. 2016.

[392] Z. Li *et al.*, "9.0% power conversion efficiency from ternary all-polymer solar cells," *Energy Environ. Sci.*, vol. 10, no. 10, pp. 2212–2221, Oct. 2017.

[393]   S. L. P. Kostrna, T. J. Mengelt, M. Ali, D. J. Larson, T. F. Kelly, and S. L. Goodman, "Creating Polymer Microtip Specimens for Atom Probe Tomography," *Microsc. Microanal.*, vol. 11, no. Supplement S02, pp. 874–875, Aug. 2005.

[394]   Y. Zhou, M. Eck, and M. Krüger, "Bulk-heterojunction hybrid solar cells based on colloidal nanocrystals and conjugated polymers," *Energy Environ. Sci.*, vol. 3, no. 12, pp. 1851–1864, 2010.

[395]   D. W. Steuerman, A. Garcia, M. Dante, R. Yang, J. P. Löfvander, and T.-Q. Nguyen, "Imaging the Interfaces of Conjugated Polymer Optoelectronic Devices," *Adv. Mater.*, vol. 20, no. 3, pp. 528–534, Feb. 2008.

[396]   W.-Y. Chen, Y.-C. Ling, B.-J. Chen, H.-H. Shih, and C.-H. Cheng, "Diffusion study of multi-organic layers in OLEDs by ToF-SIMS," *Appl. Surf. Sci.*, vol. 252, no. 19, pp. 6594–6596, Jul. 2006.

[397]   M. B. Jaskot, A. P. Proudian, D. Diercks, B. P. Gorman, and J. D. Zimmerman, "Unraveling the Effects of OLED Active Layer Morphology on Degradation Using Atom Probe Tomography," in *Light, Energy and the Environment (2017), paper STu1C.4*, 2017, p. STu1C.4.